Crystal Engineering with
Metal-Organic Frameworks

Cover illustration:

Crystal Engineering with Metal-Organic Frameworks

Proefschrift

ter verkrijging van de graad van doctor
aan de Technische Universiteit Delft,
op gezag van de Rector Magnificus prof. ir. K.C.A.M. Luyben;
voorzitter van het College voor Promoties,
in het openbaar te verdedigen op
8 Juli 2015 om 15:00 uur

door

Maarten Gérard Goesten
Scheikundig Ingenieur
geboren te Johannesburg, Zuid-Afrika

Dit proefschrift is goedgekeurd door de promotoren:
Prof. dr. F. Kapteijn
Prof. dr. J. Gascon

Samenstelling promotiecommissie:

Rector Magnificus
Prof. dr. F. Kapteijn
Prof. dr. J. Gascon

Onafhankelijke leden:
Prof. em. dr. G. Ferey, Université de Versailles Saint-Quentin
Prof. dr. P. van der Voort, Universiteit Gent
Prof. dr. F. Mulder, Technische Universiteit Delft
Dr. C. Fonseca Guerra, Vrije Universiteit Amsterdam
Prof. em. dr. H. van Bekkum

Prof. dr. J. van Esch, Technische Universiteit Delft

This research, as reported herein, has been conducted in the *Catalysis Engineering* section of the *ChemE* department of the faculty of *Applied Sciences* of the *Delft University of Technology*. I acknowledge financial support for this research by the Dutch Technology Foundation STW, which is part of the Netherlands Organisatoin for Scientific Research (NOW) and partly funded by the Ministry of Economic Affairs (project number 11044).

Proefschrift, Technische Universiteit Delft

Met samenvatting in het Nederlsnds/Including summary in Dutch

Cover design: Maarten G. Goesten
Printed by: Wohrmann Print Service B.V.

To Nastya

C'est par la logique qu'on démontre, c'est par l'intuition qu'on invente.

Poincaré (1900)

CONTENTS

Part I Coordination chemistry of MOFs

Part II Molecular pathways in MOF formation

Part III Post-synthetic functionalisation

INTRODUCTION

At the end of the 19th century, the origin of bonds between metal cations and neutral ligands was not fully clear, as no charge stabilization is realised in such bonds; resulting compounds were named ‘double salts’. Alfred Werner was the first to postulate origins of such chemical bonding, defining the terms ‘first valency’ and ‘secondary valency’. It proved the beginning of the field of *coordination chemistry*; by now, first and secondary valency are ‘oxidation state’ and ‘coordination number’, respectively. The current IUPAC recommendation on the description of a coordination compound is the following: *Each coordination compound either is, or contains, a coordination entity (or complex) that consists of a central atom to which other groups are bonded. A coordination compound is any compound that contains a coordination entity. A coordination entity is an ion or neutral molecule that is composed of a central atom, usually that of a metal, to which is attached a surrounding array of other atoms or groups of atoms, each of which is called a ligand.*[1] In the field of coordination chemistry, a metal cation, a Lewis acid, accepts one or more pairs of electrons from basic ligands, into one or more empty orbitals. The orbital interactions and fillings determine the coordination number, and to a large extent the geometry of the coordination complex.

Since Werners discovery, coordination chemistry has served as main backbone for several important fields, such as supramolecular chemistry and homogeneous catalysis. Traditionally regarded as a subfield of inorganic chemistry, coordination chemistry can famously ‘build a bridge’[2] to organic chemistry, in theoretical bonding perspectives such as the isolobal analogy, or in carbon-carbon bond promoting catalysts such as those developed by Suzuki.[3]

Metal-Organic Frameworks, MOFs, are in principle coordination compounds with an enormously large number of ‘central atoms’ (‘infinite nuclearity’). MOFs are made of metal ions or metal clusters (‘nodes’) that accept electrons from bridging ligands (‘linkers’ or ‘struts’), i.e. ligands that bridge one node to another, making up an extended network. Such architectures were initially named *coordination polymers*, their porous counterparts *porous coordination polymers* (PCPs). By now, the IUPAC recommended definition of a Metal-Organic Framework as “*a Coordination Polymer (or alternatively Coordination Network) with an open framework containing potential voids”.*[4]

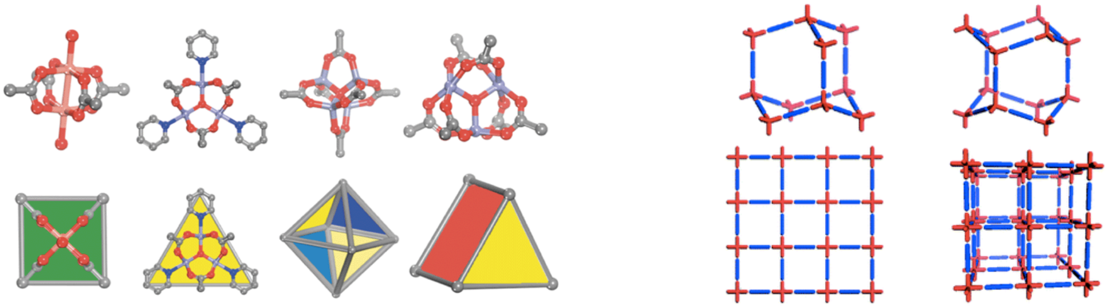

Figure 1 *Left*: MOF ‘nodes’ and their simplified geometries, *right*: nodes connected to each other by linkers/struts, forming an extended network. Images taken from the review from Zaworotko et al.[5]

The earliest reported networks of the 60s differ quite from the MOFs of today, and it is not straightforward to assign the ‘first MOF in history’ (although we will, later in this introduction). What is certain, is that in the mid 1990s and early 2000s, efforts by three main heavyweights, Kitagawa, Férey and Yaghi, in particular those focusing on carboxylate chemistry led to the development of materials with record-breaking porosity, and thermal stability sometimes exceeding 400ºC in argon. The attention this generated was considerable; between 1999 and 2006 almost 3000 new MOF structures were reported,[6] the seminal review of Kitagawa quickly became the most cited paper ever in *Angewandte*

Chemie,[7] and potential use of MOFs is currently eyed ranging from adsorptive and optical to ferroelectric application, and from gas storage, separations, and catalysis to biomedical applications.[8] To understand this sudden popularity, consider the triangle in Figure 2. The triangle is empirical, but represents seemingly well a trade-off between three intrinsic, valuable properties a porous solid can have: crystallinity, stability and tunability. For instance, it is possible to increase the length of the linker in MOFs, which will lead to an increase in tunability, for one has more space and atomic sites to implement chemical functionality, yet an increase in linker spacing goes accompanied by a decrease in crystallinity and thermal stability. If we do not consider MOFs but zeolites, which are built by much smaller subunits, consisting of main group elements, this leads to a considerable increase in stability, but a similar decrease in tunability: zeolites don't have the flexibility of entirely changing the metal element that makes up the node, or the possibility of functionalising an organic linker.

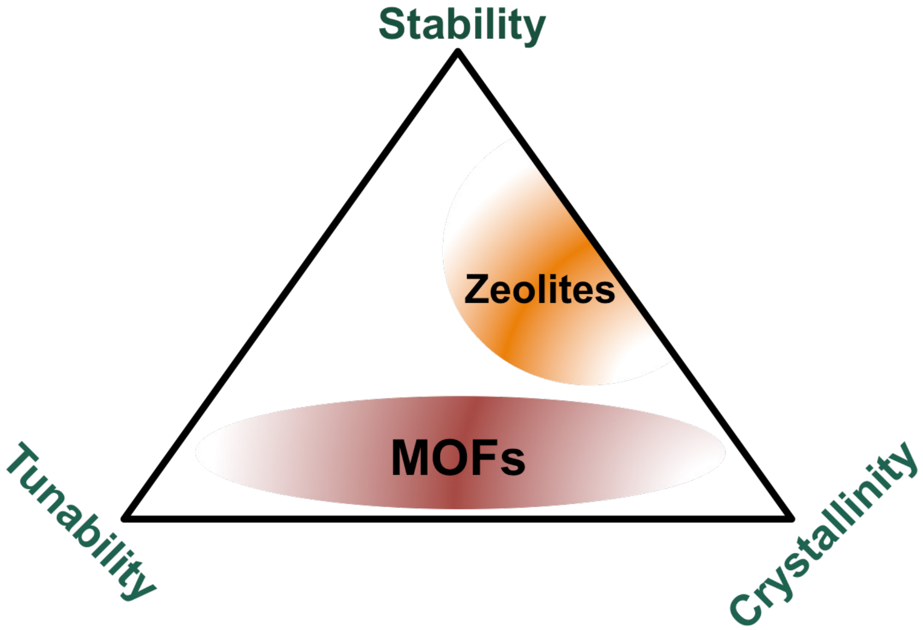

Figure 2 In a trade-off between three intrinsic, valuable properties a solid might have, MOFs find themselves in the tunable, crystalline regime.

It is the position in the triangle, the tunable, crystalline regime that is largely responsible for the attention MOFs have received. More than any other type of solid, MOFs open the door to *crystal engineering*: the 'design' of crystalline materials with specified properties. Indeed, four of the five most cited publications on MOFs have 'design' in their title.[9-12] From this perspective, the first work that should be considered a 'MOF publication' is the work by Hoskins and Robson, who first discuss predictability of PCP architectures by selecting the proper molecular building blocks.[13]

In this PhD thesis, the viability of crystal engineering with MOFs, and its possibilities, are explored. This is done in the frame of an STW project that aims at the application of MOFs in membrane technology. For successful application in membranes, great control over MOF crystal morphology and properties are desired; in essence *applied crystal engineering*.

The thesis consists of three main parts. The first chapter in part I sets the scene for the rest of the thesis; in observing developments and progress made in recent years, we'll come to the conclusion that real design cannot be realised at this stage. The apparent reason for this is the unpredictability generated by the coordination chemistry of the molecular building blocks. We advocate an approach in which the coordination chemistry of the tectonic unit is studied, after which predictive self-assembly can be considered. Chapter 2 in part I discusses Ligand Field Theory and provides the first theoretical basis for 6-coordinate clusters based on group-13 elements.

Part II forms the core of the thesis. Using a combination of *in-situ* techniques, backed up by computational methods, the molecular chain of events in MOF crystallisation is resolved for three of the most popular MOF systems: the aluminium MIL-53 vs. MIL-101 system, ZIF-7, and zirconium/hafnium based UiO-66. Several eye-opening discoveries are presented. Chapter 3 consists of three parts, 3A, 3B and 3C, in which Medium-angle X-ray Scattering (MAXS), Small-angle X-ray Scattering (SAXS) and solid-state NMR dominate the discussion, respectively.

Part III focuses on post-synthetic functionalisation, a method which avoids potential side-effects new functionalities might induce during self-assembly. Two new reactions are introduced and applied.

The thesis reads like a tree, the general advice to the reader is to start with chapter I, after which any chapter can be considered and no chronological order is further required.

REFERENCES

[1] N. G. Connelly, R. S. O. C. Great Britain, I. U. O. P. A. A. Chemistry, **2005**.

[2] R. Hoffmann, *Angew. Chem. Int. Ed.* **1982**, *21*, 711–724.

[3] A. Suzuki, *J. Organometall. Chem.* **1999**, *576*, 147–168.

[4] S. R. Batten, N. R. Champness, X.-M. Chen, J. Garcia-Martinez, S. Kitagawa, L. Öhrström, M. O'Keeffe, M. P. Suh, J. Reedijk, *CrystEngComm* **2012**, *14*, 3001.

[5] J. J. Perry IV, J. A. Perman, M. J. Zaworotko, *Chem. Soc. Rev.* **2009**, *38*, 1400.

[6] J. R. Long, O. M. Yaghi, *Chem. Soc. Rev.* **2009**, *38*, 1213–1214.

[7] S. Kitagawa, R. Kitaura, S. I. Noro, *Angew. Chem. - Int. Ed.* **2004**, *43*, 2334–2375.

[8] H. C. Zhou, J. R. Long, O. M. Yaghi, *Chem. Rev.* **2012**, *112*, 673–674.

[9] H. Li, M. Eddaoudi, M. O'Keeffe, O. M. Yaghi, *Nature* **1999**, *402*, 276–279.

[10] M. Eddaoudi, D. B. Moler, H. Li, B. Chen, T. M. Reineke, M. O'Keeffe, O. M. Yaghi, *Acc. Chem. Res.* **2001**, *34*, 319–330.

[11] M. Eddaoudi, J. Kim, N. Rosi, D. Vodak, J. Wachter, M. O'Keeffe, O. M. Yaghi, *Science* **2002**, *295*, 469–472.

[12] O. M. Yaghi, M. O'Keeffe, N. W. Ockwig, H. K. Chae, M. Eddaoudi, J. Kim, *Nature* **2003**, *423*, 705–714.

[13] B. F. Hoskins, R. Robson, *J. Am. Chem. Soc.* **1989**, *111*, 5962–5964.

PART I

The coordination chemistry of MOFs

The first part of this thesis is divided into two chapters. In the first chapter, developments in crystal engineering of MOFs are reviewed and discussed from a coordination chemistry perspective. The second chapter is more fundamental and exemplary for the complexity and obscurity that surrounds bonding in MOFs and coordination chemistry in general. In this chapter, bonding in coordination complexes is considered from a general perspective, the difference between transition metal and main group metal-based MOF clusters is investigated. Here, the 'hypervalence' of the group 13 elements is discussed and a computational study on this matter is presented.

This part is based on the following publications:

Chapter 1:	*Fascinating chemistry or frustrating unpredictability: observations in crystal engineering of metal–organic frameworks* M. G. Goesten,* F. Kapteijn, J. Gascon,* *CrystEngComm*, 15, 2013, 9249-9257
Chapter 2:	*Six-coordinate group-13 (B, Al, Ga, In, Tl) based complexes: what Is the role of hypervalence?* M. G. Goesten,* C. Fonseca Guerra, F. Kapteijn, J. Gascon, F. M. Bickelhaupt* *submitted*

1

Observations in Crystal Engineering of Metal-Organic Frameworks

Reticular design is a highly attractive concept, but coordination chemistry around the tectonic units of metal-organic frameworks (MOFs) and additional interplay with anionic and solvent species provide for dazzling complexity that effectively rules out structure prediction. We can however study the chemistry around pre-existing clusters, and assemble novel materials correspondingly, using *a priori* information about the connectivity of an investigated metal cluster. Studies, often spectroscopic of nature, have in recent years solved many puzzles in MOF crystallization. The obtained knowledge opens new doors in crystal engineering, but more research on MOF coordination chemistry has to be carried out.

The self-assembly of molecules into an organized network is governed by molecular forces induced by so called tectons, etymologically referring to “building units”, as introduced by Jim Wuest in 1991.[1] Tetrahedral SiO_4 and AlO_4 units, which build up zeolites, are examples of tectons. In these purely inorganic self-assembling structures, small distortions in the metal–oxygen–metal angle allow for a large number of topologies, despite the exclusively tetrahedral nature of the tectons.[2,3] The success of zeolites as catalysts and sorbents is beyond discussion and considerable focus on mimicking this self-assembly in non-purely inorganic structures is a consequence. For organic structures, design of suitable tectons towards self-assembly of highly structured solids has despite several breakthroughs proven to be a serious challenge up until now, as bonding is much less strongly directed.[4]*

It is the inorganic–organic case of metal–organic frameworks (MOFs), where metal–(bridging) ligand bonds extend into one, two or three dimensions, that has led to massive scientific interest into the field of self-assembled, porous structures. As a benchmark ‘first paper’ on MOFs, one may choose a work published in 1989, where Hoskins and Robson proposed that a new and potentially extensive class of solid polymeric materials with unprecedented and possibly useful properties may be afforded by linking together (metal) centers with either a tetrahedral or an octahedral array of valences by rod- like connecting units.[5] After a stint of steady year-by-year increase of publishing on the topic, a wave of scientific interest can be observed towards the late 1990's.[6] The popularity of MOFs as potential candidates for an array of applications much lies in the tunability and versatility of the materials that can be formed upon self-assembly, as potentially desired inorganic and/or organic functionalities can be implemented into a porous structure through appropriate choice of metal precursor and corresponding bridging ligand. In MOFs, tectons come in the form of metal complexes, sometimes referred to as secondary building units (SBUs) and provide virtually infinite possibilities towards connectivity and therefore structure direction. Indeed, this is perhaps the most exciting feature of MOFs, as it matters crystal engineering, the synthesis of crystals with specific and predicted properties, in MOF chemistry sometimes referred to as reticular synthesis or reticular design. ‘Reticul’ is the Latin word for ‘network’, and reticular synthesis represents the targeted retrosynthetic-like

---

* Covalent–organic frameworks (COFs) are sometimes referred to as organic polymers, but may factually represent a case of ‘metalloid–organic frameworks’, since very often these polymers contain boron and its strong directional binding.

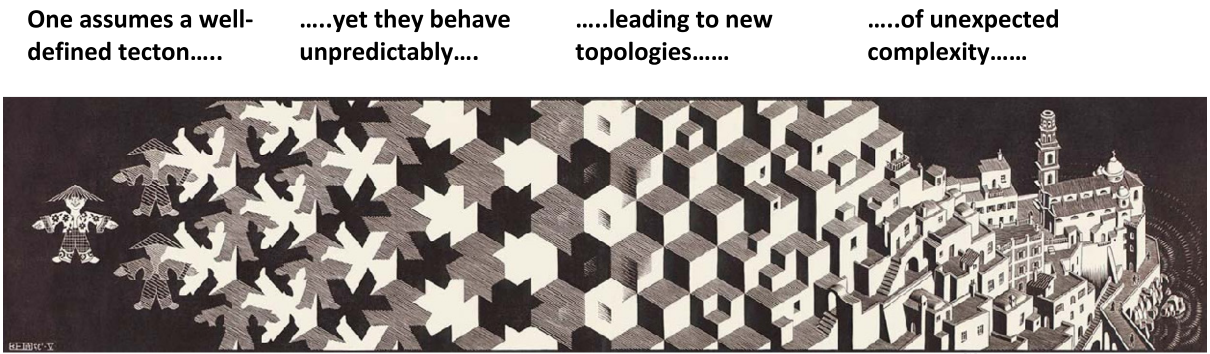

Figure 1.1 Reticular design seems hampered by unpredictability around coordination chemistry.[8]

synthesis of complete networks.[7] One particular example which caught attention was the use of a tetranuclear $Zn_4(\mu_4\text{-}O)L_6$ tecton in which octahedral connectivity leads to a primitive cubic *α-Po* net. Here the six ligands consist of three pairs of aryldicarboxylato syn–syn oxygen, where the aryl species can be varied to deliver a series of isoreticular frameworks, in which chemical properties can be implemented in crystals with predictable topology.[9] Similar observations apply for MOF tectons with different connectivities. Apparently, it seems that if the reaction conditions that lead to the formation of a particular tecton with corresponding connectivity are figured out, then control over the self-assembly towards a desired net is possible. The ideal MOF 'designer' is therefore both an expert in coordination chemistry and crystallography. This attractive idea has, to limited extent been realized, and MOFs have, for instance, been setting records in N_2, H_2, CO_2 and CH_4 sorption ('storage') through the use of dimensionally very long ligands, and display magnetically predictive behaviour through the self-assembly of specific nets.[10-14] Despite these (amongst other) examples, unpredictability is still common and true design is relatively rare. This should not be a surprise, as coordination chemistry around MOF crystallisation is far from being a resolved field within its own specialist domain. The contrary is true: investigations on MOF structures have led to discoveries. An example is the trimeric $Al_3O(BTC)_6L_3$ (BTC: benzene-1,3,5-tricarboxylate, L: H_2O, N) tecton within MIL-96, which will be treated in the text below, a commonly observed moiety for transition metals but a new cluster for a *p*-block metal.[14] Clearly, if the current state of coordination chemistry does not allow us to predict chemistry around the MOF tecton, little prediction in the crystallographic domain can be provided as well, as artistically depicted in Figure 1.1. Thus, MOF crystallisation ought to be investigated more, so that previously unknown events can be revealed for the sake of crystal engineering. This is also a requirement from industrial perspective – the main factor determining whether the MOF 'hype' will turn out to be successful, as MOF applications would require crystals 'shaped' towards functionality, from both morphological and chemical perspective.

This chapter aims at giving insight in progress researchers have made in revealing coordination chemistry around MOFs by selecting different examples rather than at deeply reviewing all MOF synthesis papers published to date. The chapter is divided into three parts. The first part deals with the chemistry around the metal and ligand, the tectons they form with corresponding connectivities, and the topological unpredictability observed in synthesis. The second part deals with the chemistry of the anion that is usually present, and its large influence on MOF crystallization. The third part deals with the yet more unpredictable role of the solvent. The chapter finishes with some final outlook and remarks. It is emphasized that this chapter focuses on the coordination-chemical and synthetic part of crystal engineering with MOFs, an area left relatively unexposed in recent years. For detailed theory into MOF crystallography, the reader is referred to reviews published by Batten and by O'Keefe and Yaghi that, respectively, give insight into unpredictability and predictability within the crystallographic domain.[15,16]

1. Metal and ligand

One of the most apparent claims for reticular design is the development of ZIFs (zeolitic imidazolate frameworks), porous solids where structural binding in zeolites is mimicked in the metal–organic domain by the use of tetrahedrally coordinating ions and imidazolato bridging ligands.[17] The metal ion resembles tetrahedral SiO_4, the ligand displays a bridging angle resembling the Si–O–Si angle in zeolites and self-assembly leads indeed to structures possessing zeolite topologies. Even the crystallization mechanism of one of the members, ZIF-8, was shown to resemble the corresponding mechanism of some high-silica zeolites.[18] This successful claim for rational design is an exception in a field where unpredictability reigns. A first observation is that one is strongly limited in decorating the MOF ligand with functional groups. These groups are either seen to coordinate to the metal themselves, like sulfonate groups, or to inhibit/promote formation of the coordination polymer for ambiguous reasons.[19] For example, we have observed that one can pre-functionalize MIL-101(Cr) with nitro groups, but not with amine groups. For MIL-101(Al) the reverse is true; only the aminated ligand leads to formation of the coordination polymer. We have so far been unable to fully explain this observation. The general consequence of this ligand effect is that researchers have to turn to post-synthetic functionalization of metal–organic frameworks, and this has itself grown into a large field within MOF research.[20-23] It is however the complexity of the tectonic units which generates most uncertainty around crystallization of MOFs. This is actually easily understood if we observe that, as stated in the introduction, simple tectonic units in zeolites already allow for a huge diversity in topologies. In the MOF domain, (often polynuclear) transition metal chemistry governs the self-assembly mechanism, and polynuclear transition metal chemistry is an area in which inorganic chemists, despite numerous attempts, have in general only made limited progress in successfully “designing” coordination clusters.[24] As Ribas Gispert states in his coordination chemistry textbook: *the vast majority of these, including the most relevant and spectacular, have been made as a result of “serendipitous self-assembly”*. In this context coordination chemists have learned the reaction conditions necessary to favour the formation of large polynuclear clusters, however, it currently remains impossible to predict the structure of any new system prepared in this manner. For anyone believing new MOF networks based on new tectons can be self-assembled in predictable manner, this news should be rather demoralising. If chemists cannot predict the structure of a new polynuclear complex, then surely the MOF structure based on this complex can only be guessed.

The enormous diversity of tectonic units within the field of metal–organic frameworks is first of all related with the flexible coordination environment of metal ions, often those with d^{10} configuration such as Zn^{2+}, Ga^{3+}, In^{3+}, Ti^{3+}, Cd^{2+}, Hg^{2+}, Ag^{+}, Cu^{+}. Zinc, in particular, is frequently used as metal ion and can show many coordination geometries besides its commonly observed tetrahedral configuration. For instance, zinc can exist in pentagonal bipyramidal configuration as reported by Kitagawa in 1997, where zinc is coordinated to three 4,4′-bpy ligands and two chelating nitrato ligands (in the next section we shall see that nitrato is on more occasions seen to promote pyramidal coordination geometries),[25] but octahedral and trigonal bipyramidal coordination geometries are seen as well.[26,27] An interesting case present the dinuclear paddlewheel clusters, which are also observed for copper, for instance in CuBTC (HKUST-1). These binuclear clusters are tectons with square connectivity.[28]

For *f*-block elements, unpredictability around the coordination environment is even more pronounced and can lead to exotic tectons such as praesodynium-based or dysprosium square antiprisms leading to lanthanide open-framework structures, and ‘supercubanes’, respectively.[29,30] These examples matter clusters of higher nuclearity, and it are these clusters of that act as even more diverse and unpredictably appearing tectons in self-assembly towards new structures.

We will here consider aluminium-based MOF members of the MIL (Materiel Institut Lavoisier) family, which provide an excellent illustration in this regard. Aluminium is one of the smaller metals available in the periodic system; it is not expected to form bonds with *d*-orbitals (see: chapter 2) and often coordinates in octahedral mode, yet the chemistry around multinuclear Al clusters is extremely diverse and unpredictable. MIL-96(Al), MIL-100(Al) and MIL-110(Al) are all three aluminium benzene-1,3,5-tricarboxylate (BTC, trimesate) based MOFs, containing very different molecular tectonics.† MIL-96 and MIL-100 contain an $Al_3(\mu_3\text{-}O)(BTC)_6L_3$ tecton, a well-known moiety in coordination chemistry for *d*-block elements but here for the first time seen with the *p*-block aluminium. In MIL-96, this cluster and its trigonal connectivity reside within a hexagonal chain made up by μ_2-OH bridged Al chains which are commonly observed in clay chemistry and are known for their high chemical stability.[31,32] In MIL-100(Al), the μ_3-O based cluster oligomerizes to an Al_{12} "super tetrahedron", which bears striking resemblance to SiO_4 tectons from zeolites. As a result, this far bigger analogue directs self-assembly to zeolite MTN topology with gargantuan cage dimensions exceeding 3 nm. MIL-110(Al) does not contain the μ_3-O cluster but its make-up is fascinating nevertheless, as two types of clusters (six with terminal aqua/hydroxido ligands, two without terminal ligands) make up large Al_8 octagonal tectons, which self-assemble towards large hexagonal channels. Looking at Table 1.1, one can conclude that the synthetic conditions do not differ much, as only small changes in pH appear to inflict large structural changes through promotion of these different complexes. This inspired Haouas *et al.* to perform *in-situ* NMR experiments from which they could reconstruct the

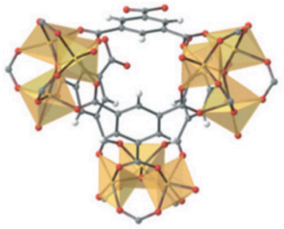

MIL-101

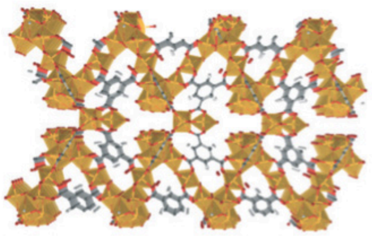

MIL-96

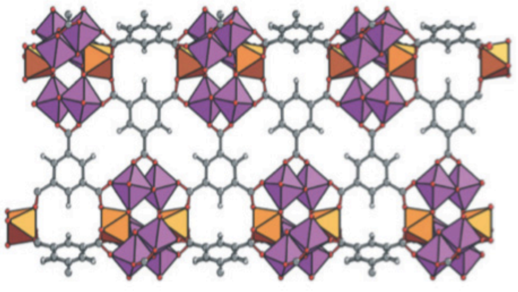

MIL-110

Table 1.1: Different aluminium trimesates and their synthesis conditions

	pH	Synth. *T*/*t* (°C/h^{-1})	Clusters and tecton geometry
MIL-96	1.0-3.0	210/24	$Al_3(\mu_3\text{-}O)O_6L_3$ trigonal $Al_2(\mu_2\text{-}OH)_3O_6$ hexagonal chain
MIL-100	0.5-0.7	210/3-4	$Al_3(\mu_3\text{-}O)O_6L_3$ trigonal
MIL-110	0–0.3 & 3.5–4.0	210/72 & 3	$Al(\mu_2\text{-}OH)_3O_2L$ octamer $Al(\mu_2\text{-}OH)_3O_3$ octamer

---

† MIL-96 and MIL-100 have also been synthesized using Fe, Cr and Sc (only MIL-100).

mechanism, and concluded that identical dinuclear Al–BTC complexes form early on for all three topologies, but small differences in equilibria lead to different topologies.[33] MIL-100(Al) is clearly the kinetic product, and MIL-96(Al) the thermodynamic product, MIL-110(Al) falls in between. It is thus not surprising that upon prolonged heating, MIL-100(Al) can be seen to rearrange towards MIL-110(Al), and to MIL-96(Al) correspondingly.

The complexity and extreme dependence on the chemical environment that MOF tectons show effectively rules out true prediction of a resulting structure. Instead, we are forced to study the coordination chemistry of tectons of reported coordination polymers, and use resulting information in the synthesis of functionalized or adapted structures. This reduced level of predictability can still be satisfactory, as functionalized or adapted frameworks have been rationally designed in this way. As we will see in the succeeding sections, even at this level of 'design', crystallization of MOFs is unpredictable and pervasive.

2. Influence of the anion

As MOFs are generally synthesized from metal salt precursors, anionic species will always be present in solution.[‡] Influence of the anion on the final topology of the MOF is a regularly observed phenomenon.[36-41] Apart from acting as potential mineralizers enhancing crystallinity, anions can act as true structure-directing agents.[42] One of the earliest and perhaps still most striking example dates from 2000 where Min and Sun reported on a silver ethylenediaminetetrapropionitrile (EDTPN) MOF where the choice of precursor, Ag(NO_3), Ag(CF_3SO_3) or Ag(ClO_4) leads to self-assembly towards three completely different nets.[43] EDTPN, displayed in Figure 1.2, is via four cyano and two tertiary ammine ligand sites capable of μ_{2-6} bridging. Interestingly, solely depending on the anion, μ_2 (1), μ_3 (2) or μ_4 (3) bridging is observed. Corresponding coordination geometries and topologies are distorted bipyramidal: linear network, tetrahedral: 2D layer, octahedral: 2D boxlike network, respectively. The EDTPN ligand coordinates to one silver ion through both its ammine ligands, and to one, two or three other silver ions through its cyano ligands.

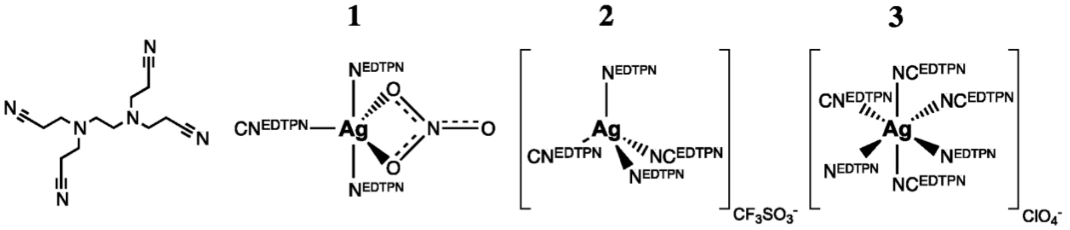

Figure 1.2 A simplified scheme around self-assembly of the silver–EDTPN networks. On the far *left*, the EDTPN ligand, then coordination geometries of silver in the presence of a nitrate (trigonal bipyramid), triflate (tetrahedral), or perchlorate (octahedral) anion, from *left to right*.

The authors also report on the possibility to induce crystal-to-crystal rearrangements upon ion exchange: **1** and **2** can be reversibly transformed into each other, and both can be irreversibly transformed into **3**. This illustrative example shows that the (metal salt) anion can have two structure-directional roles in MOF crystallization: it can act as an anionic terminal ligand, or less definable, as an anionic moiety stabilizing coordination geometry and resulting structure. In the first case, it changes connectivity of the metal-precursor by blocking a coordinative site, and/or by changing coordination geometry as can be seen in structure 1, where a nitrato ligand occupies two silver coordination sites whilst promoting trigonal bipyramid coordination. EDTPN

[‡] Exceptions may always exist, and a few syntheses make use of metallic precursor, such as the synthesis of MIL-100(Cr) as first reported by Ferey[34] and MOFs synthesized via electrochemical synthesis.[35] Anions are however present in both cases, as mineralizing agent and electrolyte species, respectively

can as a result only bridge two silver ions. Depending on lability of the metal–anion bond, such blocking through anion coordination might even affect crystal morphology. One primary example is the synthesis of ZIF-7 microrod crystals through the use of $ZnCl_2$ instead of $Zn(NO_3)_2$, in the presence of a diethyl amine modulator.[44]§ In an attempt at revealing the pathway of the formation of these microrods, we found that the strong Zn–Cl bond inhibits direct replacement of the two chlorido ligands by the benzimidazole bridging ligand, and dimerization of mononuclear Zn benzimidazole clusters is favoured. This rules out growth in tetrahedral direction, as normally induced by a Zn^{2+} tecton, but directs self-assembly towards rod-like structures (in a rather complex manner).[45] As seen with the nitrato ligand in 1 ion co-coordination might also induce an alternate coordination environment by promoting (different) geometry. Surprisingly little has been published about this particular anionic effect on connectivity of the metal cluster in MOFs, whereas it is likely to have significant effect on the structure of the frameworks that crystallize. The anionic effect on connectivity is frequently observed, as we saw in the first part of this review where Zn(II) coordination polymers may display nitrato-induced pentagonal bipyramidal geometry, but for instance also isothiocyanato-induced octahedral coordination geometry (amongst a long list of other examples).[25,46,47] Predicting this particular effect of the anion ligand on cluster connectivity and resulting framework can be a cumbersome affair that requires use of ligand field theory in combination with computational methods. With the latter, further complexities, such as anion-solvent or anion-ligand interactions might be taken into account as well. In the second case, non-coordinate stabilization of a cluster or resulting net by an anion, chemistry is even less predictable. Referring to figure 1.2 again: **2** can rearrange into **3** upon solid-state ion exchange, yet the reverse reaction does not occur. This hints at the silver–EDTPN coordination polymer possessing greater affinity towards the perchlorate anion with respect to the triflate anion. As a matter of fact, in further experiments the authors determine the affinity to follow $ClO_4^- > NO_3^- > CF_3SO_3^- > Cl^-$ and note that this follows the order of the Hofmeister series, a series first proposed in 1888 which ranks the relative influence of anions on macromolecules.** The Hofmeister series is a point of discussion; whereas the anionic influence was originally related to influence on 'water structure' around the macromolecule, recent time-resolved and thermodynamic studies indicate otherwise. Direct ion–macromolecule interactions seem to provide a more realistic rationale for the series.[48]

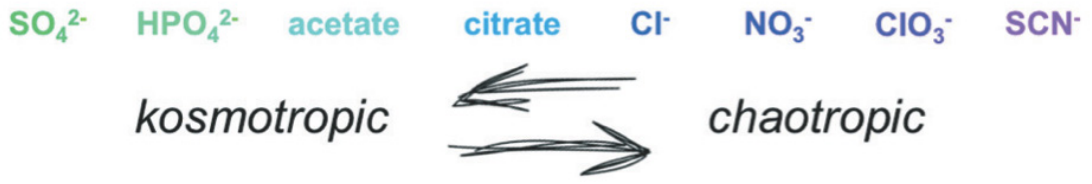

Figure 1.3 The Hofmeister series.

The series is depicted in figure 1.3. Anions in the left part of the Hofmeister series are called kosmotropes, the ones to the right part chaotropes. These terms refer to the anion's ability to alter the hydrogen-bonding network of water. Kosmotropes stabilize 'water structure', and are seen to have a stabilizing (and salting-out) effect on proteins macromolecules. MOFs are often seen to follow the Hofmeister series in anion selectivity, and therefore the series might be used as a rough guideline towards anionic stabilization of MOFs, but nothing more than a rough

---

§ ZIF-7 is based on zinc and benzimidazole.[17]

** Both anions and cations are taken into account, but anions appear to have a much bigger effect. The 'macromolecules' initially investigated were proteins, and the anionic effect on protein folding and 'salting in/out' behavior delivered the Hofmeister series.

guideline, as also anti-Hofmeister and non-Hofmeister selectivities with MOFs are sometimes observed. In an excellent review on this topic (to which the interested reader is certainly referred to), the authors state that *sorely needed at this time are more quantitative studies of anion exchange and separations, including competition experiments, anion-exchange isotherms, thermodynamic and kinetic measurements, and mechanistic investigations of anion transport. Computational studies could also offer valuable information about the energetics of anion binding inside the coordination frameworks, as well as the electronic and steric requirements for optimal anion selectivity*.[49] We can but conclude that, in this peculiar domain of anion–MOF interaction, many events are currently beyond our grasp in terms of general understanding.

3. The ambiguous role of the solvent

Synthesis of MOFs is usually done under solvothermal conditions,[††] and the choice of solvent is shown to be a significant parameter in kinetics of crystallization, network structure and crystal topology. The nature of structure-direction by the solvent is very versatile. Similar to the case of the anion described above, it may influence the structure of the coordination polymer acting as a ligand, or through less defined (often hydrogen-bonding) interaction with the scaffold. Yet in addition, it can promote topologies acting as a true molecular promoter, assist in post-synthetic functionalization or strongly affect crystal morphology, as we will see in this section.
A typical example of solvent structure-direction through coordinating ability is the Cd(II)-4,4′-dipyridyl sulfide MOF system, in which depending on whether one chooses a DMF–dichloromethane, acetonitrile–dichloromethane or methanol–dichloromethane solvent system a 1D, 2D, or 3D network forms, respectively. In the first, 1D $\{[Cd(Py_2S)_2(DMF)_2](ClO_4)_2\}_n$ and the second, 2D $\{[Cd(Py_2S)_2(MeCN)_2](ClO_4)_2\}_n$ case, a pair of solvent ligands are in *trans* positions in octahedrally coordinated Cd(II), whereas in the 3D $\{[Cd_2(Py_2S)_5(MeOH)_2](ClO_4)_4\}_n$, only one site of octahedral Cd(II) is occupied by MeOH solvent, resulting in a chiral 5-connected framework.[51] Many analogous examples can be provided.[52-55] Coordinated solvents can also exert influence over framework topology through steric effects as was shown by Noro et al. in which Lewis base solvents modify the forms of flexible chain motifs in regularity, through steric effect of coordinated solvents.[56]
If we proceed studying the non-coordinate structure-directing ability of solvent, we can take a look at several studies carried out by Dastidar et al. on cadmium coordination polymers. They found that only polar solvents lead to Cd(II) based coordination polymers, but less polar solvents only form complexes of lower nuclearity. They stretched this work to coordination polymers constructed from bis-pyridyl-bis-urea ligands bound to octahedral Zn(II).[57] This specific ligand was chosen for its ability to form hydrogen bonds with solvent (and anionic) species. The authors successfully demonstrated the ability of the solvent to direct structure as they found that ethylene glycol promotes formation of a zig–zag coordination polymer through hydrogen bonding interactions with the urea nitrogen ligand, stabilizing its *syn–syn* conformation.

THF (polar aprotic), acetone (polar aprotic) and 1,4-dioxane (non-polar) were not capable of stabilising *syn–syn* conformation and led to crystallization of a 2D grid-like network instead. The dependence of topology on solvents is truly remarkable, and we have ourselves carried out several studies in this field, initially sparked by the competition between the NH_2–MIL-53(Al) and NH_2–MIL-101(Al) phases in synthesis. Both topologies carry our interest and are investigated for application in our laboratories. NH_2–MIL-53(Al) is a flexible, microporous, highly stable MOF in which μ_2-OH bridged aluminium chains form lozenge-shaped channels. This material presents many interesting properties, such as breathing, selective adsorption, selective separation, and was also shown to be among the first solid-state materials displaying

---

[††] It is technically possible to avoid the presence of anions in MOF mechanosynthesis.[50]

nonlinear optical switching.[58-61] NH_2–MIL-101(Al) contains the μ_3-O centered clusters that, like in MIL-100(Al) make up supertetrahedral tectons that self-assemble towards an MTN topology with huge cages. NH_2–MIL-101(Al) is like MIL-100(Al) mesoporous, and therefore interesting for applications in catalysis, but carries an advantage over MIL-100(Al) in the 2-aminoterephthalato ligand being much more prone to post-synthetic functionalization.[62]‡‡ One may state that NH_2–MIL-53(Al) and NH_2–MIL-101(Al) are the 2-aminoterephthalato analogues of MIL-96(Al) and MIL-100(Al), respectively; NH_2–MIL-53(Al) is the thermodynamic product, and owes its high stability to clay-like μ_2-OH bridged Al chains. NH_2–MIL-101(Al) is the kinetic product and both phases are frequently observed to be in competition with each other. As was stressed in the introduction, optimising synthesis of these materials is a requirement if they are to be implemented in industry, so we decided to place these materials under the microscope.§§ In a Medium/Wide Angle X-Ray Scattering (MAXS/WAXS) study, we were able to calculate the kinetics of formation of both topologies in different solvent compositions, using the Gualtieri model earlier used by Millange and co-authors.[45,64-66] Results are summarized in Table 1.2. Chapters 3A and 3B contain our full studies on this system.

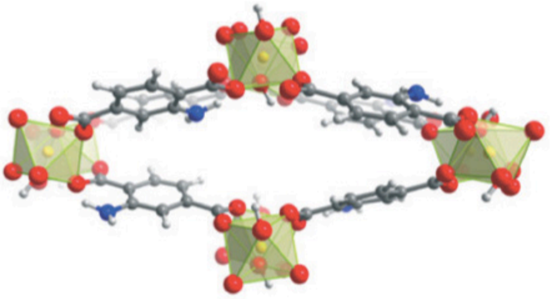

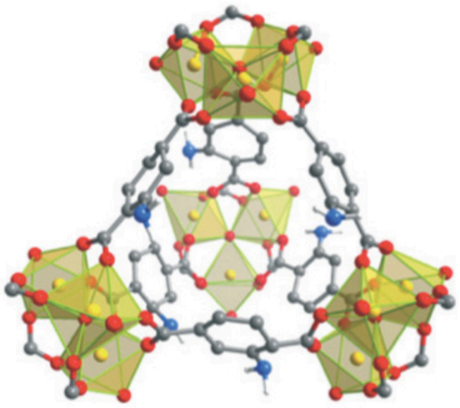

DMF : H_2O molar ratio	k_g (10^{-4} s^{-1})	k_n (10^{-4} s^{-1})	Product
0.00 : 1.00	1.2	45	NH_2-MIL-53(Al)
0.70 : 0.30	14	43	NH_2-MIL-53(Al)
0.90 : 0.10	7.0	23	NH_2-MIL-53(Al)
0.95 : 0.05	4.1	14	NH_2-MIL-53(Al)
1.00 : 0.00	6.3	14	NH_2-MIL-101(Al)

Table 1.2 NH_2–MIL-53(Al), NH_2–MIL-101(Al) along with topologic and kinetic dependency on solvent composition.

DMF imposes a different molecular mechanism as it promotes formation of NH_2–MIL-101(Al), but only when pure DMF is used as solvent, whereas it significantly enhances crystal growth rate of NH_2–MIL-53(Al) in DMF : H_2O mixtures. A small victory in synthetic control was obtained when we used this result to find an optimal solvent composition for the synthesis of NH_2–MIL-53(Al), DMF : H_2O molar ratio of 0.1:0.9, for which the yield is three times as high as in a pure H_2O synthesis. This specific solvent-dependent behaviour was explained through observation of a DMF-promoted intermediate, NH_2–MOF-235(Al).[67] This intermediate is seen to rearrange either towards MIL-101(Al) topology (pure DMF) or to MIL-53(Al) topology (DMF-H_2O mixtures). From SAXS analysis follows indeed that NH_2–MOF-235(Al) crystals form very

---

§§ Their industrial significance is reflected in a BASF patent which effectively claims NH_2–MIL-53(Al) and NH_2–MIL-101(Al).[63]

quickly in DMF containing mixtures. In further research at the molecular scale, DFT confirmed that DMF stabilizes the MOF-235 topology, which bears strong chemical kinship to the MIL-101 topology.[68] *In-situ* NMR studies showed that DMF plays a kinetically promotional role in converting NH_2–MOF-235(Al) to NH_2–MIL-101(Al) in complexating HCl (Table 2).[69] This result is highly interesting, and it is inferred that similar solvent-modulation is a factor in the promotion of many other MOF topologies (Figure 1.4).

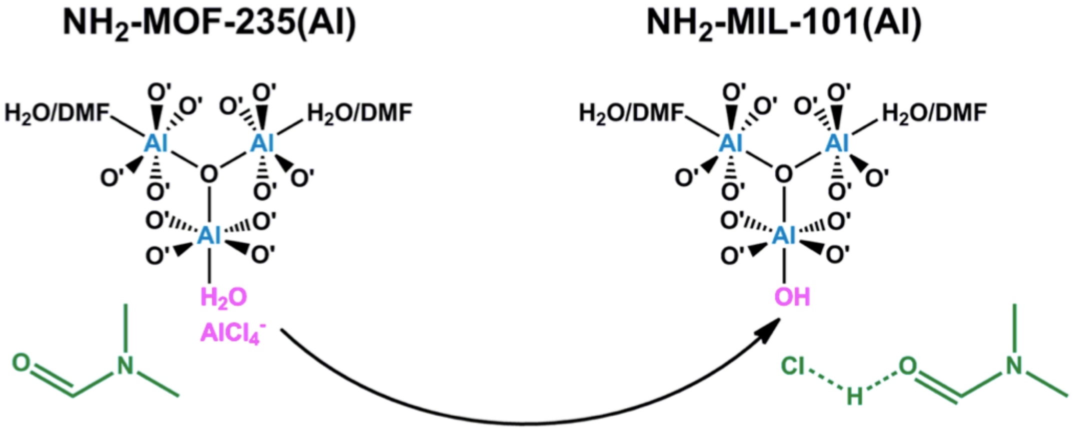

Figure 1.4 Promotional role of DMF in converting NH_2–MOF-235(Al) into NH_2–MIL-101(Al). The oxygen ligands originate from 2-aminoterephthalic acid linkers.

Crystal topology and crystallinity of the resulting material is also highly dependent on the choice of solvent. In a study on efficient encapsulation of phosphotungstic acid (PTA) in MIL-100(Cr), we obtained a xerogel-like MOF with dual porosity, when pure DMF was used.[70] A similar effect of the use of ethanol on MIL-100(Fe) was reported before.[71] Also referred to as metal–organic gels, these materials are investigated for use as solid sorbents.[72]

We thus conclude that the role of the solvent in MOF synthesis is ambiguous and unpredictable. It might act as coordinating agent, (hydrogen-binding) non-coordinating template and even as homogeneous catalyst and gelator.

Final remarks

Reticular design is a tremendously attractive concept as it essentially presents a crystallographic analogue of retrosynthesis, which we know from organic chemistry, but without the tedious step-by-step assembly towards the final structure: it would make use of self-assembly instead. As known by now, the concept of reticular design is a highly controversial one.[73] A must-read 2006 article by Schön and Jansen slams the concept of solid-state chemical design, calling it an illusion, and states about the field of coordination polymers that "*one should critically note that typically, in those cases in which a synthesis is claimed to have been successfully designed, the design and actual synthesis are published in the same paper. This does not strike us as very convincing."* They show that the number of possible structures, which correspond to local minima in energy landscapes, is so large that one is effectively unable to predict anything.[74] This is certainly seen in laboratory practice as the stunning amount of polynuclear tectons that form in near-identical synthetic environments for the aluminium-based frameworks treated in the text above is a testimony towards coordination chemistry unpredictability as described by Ribas Gispert.[24]

As current cognizance within the chemistry field is insufficient to truly design novel crystalline materials that self-assemble from newly designed tectons, one can but conclude that we are left to study the chemistry around pre-existing clusters, and assemble novel materials correspondingly, using *a priori* information about the connectivity of the pre-studied metal cluster. One can take soothe from the fact that this approach has indeed been successful in several cases, and various functionalities have been implemented in MOFs with predictable topology. In this chapter we have seen that progress is being made, and in some cases the full multiscale pathway – from molecular to crystal scale – has been revealed (always *a posteriori*). This obtained knowledge opens the door to a new step in crystal engineering. Yet again it is underlined that this does not mean the obscure prediction and assembly of new materials, but manipulation and adaptation of studied ones in order to design structured sorbents, catalysts, magnetic materials, luminescent materials etc. One particular field that is opening up, as knowledge around the coordination chemistry of MOFs is expanding, is the case where structure-directing moieties are used. The addition of structure-directing agents is common in zeolite synthesis, as many topologies actually require the use of an auxiliary template, yet the mechanistic effect of these structure-directing agents had for long been poorly understood and therefore called for specialist studies on the subject.[75,76] As resulting knowledge of the mechanism of zeolite templation increased over the years, chemists have been able to tune their templates so they are capable of more than just stabilizing a topology. This resulted and is still resulting into some spectacular results, such the hierarchically structured zeolite catalysts presented by Ryong Ryoo in 2009.[77] In the field of MOFs, the first reports on structure-directed synthesis, attempts at obtaining mesoporosity through the use of surfactants are starting to appear.[78-80] True templation and corresponding structure stabilization has been observed for several high-profile MOFs such as the phosphotungstic acid enhanced synthesis of MIL-100(Cr) and Cu- BTC.[82,83] An additional field that is opening up is the use of the solvent as structure-directing agent; it is indeed possible to form specific topologies in which a non-innocent solvent participates in the molecular pathway to MOF formation. An example of this is treated in chapter 3C.

2

Bonding in Metal-Organic Frameworks: transition metals versus group 13 metals

This chapter analyses the difference in bonding between 6-coordinate clusters based on group 13 metal ions and transition metal ions. The analysis is based on relativistic Density Functional Theory (DFT) based quantum-chemical calculations in which a metal ion fragment (B^{3+}, Al^{3+}, Ga^{3+}, In^{3+}, Tl^{3+}, Sc^{3+}) interacts with a hexaaqua ($[H_2O]_6$) fragment. The role of *d*-orbitals and electron-rich, 3-center-4-electron (3c4e) bonds is investigated. We conclude that octahedral clusters based on group 13 ions are primarily held together by 7-center-10-electron patterns, and the role of *d*-orbitals can be safely neglected. This results in high affinity towards small, electronegative, ligands, as well as elongated bonds of considerable ionic character, a consequence carrying through to the macroscopic properties of Metal-Organic Framework materials such as MIL-53(Al,Ga,In). This chapter provides the first general theoretical basis for 6-coordinate molecules based on group 13 elements, a particularly interesting class that bridges traditional fields of coordination chemistry and main group chemistry.

Introduction

A reasonable number of known metal clusters can be synthesized with both transition and main-group metal ions. Metal-Organic Frameworks are very exemplary here; several rather popular MOF topologies exist for both *d*-block and *p*-block elements, such as MIL-53, which can be synthesized using Sc^{3+}, Fe^{3+}, Cr^{3+}, Cu^{3+}, Al^{3+}, Ga^{3+} and In^{3+} as metal ion.[83-87] Although the Periodic Table indicates otherwise, chemistry in such series is often treated as comparable with ion radius and electronegativity acting as dominant parameters.

Any main group element that makes more than four bonds and thus violates the octet rule is considered *hypervalent*. Octahedral, 6-coordinate clusters networking MOFs that are based on Al, Ga and In are thus based on hypervalent connectors.

Linus Pauling had explained hypervalence by involving low-energy *d*-atomic orbitals with a scheme in which main group elements can *expand* their valence shell and form sp^3d^2 hybrids.[88] However, such hybridization was quickly realized to involve large electron promotion energies and in 1951 Rundle and Pimentel proposed another, simple description of hypervalent bonding (figure 2.1).[89]

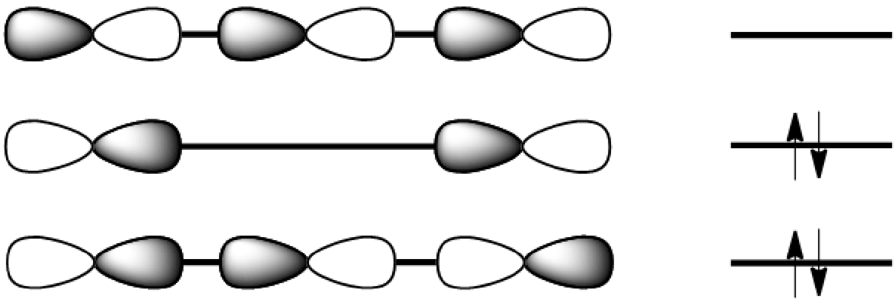

Figure 2.1 The Rundle-Pimentel model of bonding in hypervalent compounds: the 3c4e bond.

The so-called "electron rich" three-center-four-electron (*3c4e*) bond consists of three linear combinations of three *p*-orbitals, two provided by ligands, one by the central atom. The three combinations lead to one bonding, one non-bonding and one antibonding Molecular Orbital (MO). A main implication of the Rundle-Pimentel model is that main group elements do not have to violate the octet rule to make more bonds than their valence suggests; the 'excess' electrons are simply located on the ligands. Jeremy Israel Musher stretched this concept, being the first to work out a general theoretical basis for hypervalent molecules (and as theoretical chemist *n.b.,* the first to synthesize a hypervalent organo-noble compound!).[90] In 1990, remaining ambiguity on the role of *d*-orbitals in bonding of second-row elements – are they necessary in covalent bonding or acting as *functions* improving the wavefunction of the molecule? – was convincingly resolved by Magnusson and von Ragué Schleyer;[91,92] the idea of *d*-orbital involvement was starting to be widely rejected by chemists.

The Rundle-Pimentel model remains accepted as view on hypervalence, but it is not complete: Hoffmann showed that *s,p*-mixing is rather significant for isoelectronic X_3 systems (X-being a main-group element) and destabilizes interactions when moving across the periodic table from right to left,[93] whilst Braïda and Hiberty used their Valence Bond (VB) description of *charge-shift bonding* to explain hypervalent bonding in signature molecule XeF_2.[94] The quest for new hypervalent molecules, in particular those involving 5-coordinate carbon is still alive.[95,96] Recently, the ball-in-a-box model showed for the first time unequivocally, that not the differences in the MO bonding pattern, but rather the small size of carbon is the reason why this element, at contrast to its third-row congener silicon, resists towards binding a fifth substituent.[97-99] In light of this interest, it is surprising that apart from some focus on hypervalent lithium,[100] the role of hypervalence in group 13 based metal clusters has not received extensive theoretical treatment.[***]

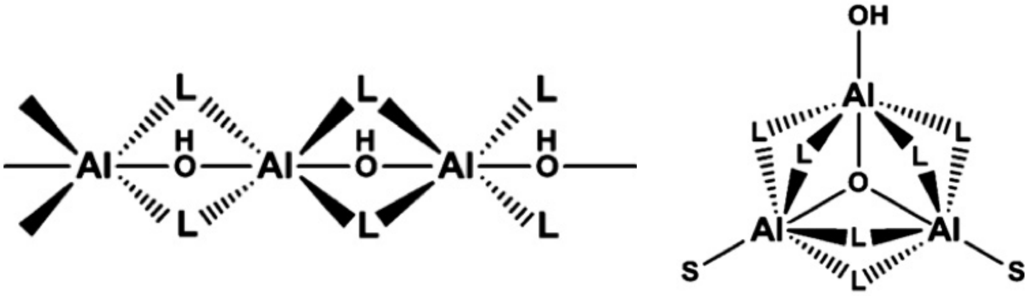

Figure 2.2 Bonding in MIL-53(Al), *left*, and MIL-101(Al), *right*.

It is thus very interesting that several MOF topologies can exist based on either main-group and/or transition metals. It must here be noted that the choice of main-group or transition metal leads to some general differences here: only transition metals lead to a variety of richly coloured powders, and not all transition-metal based MOFs can be synthesized with main group ions. For instance, whereas the μ_2-OH bridged chains that make up MIL-53 are readily formed with both transition-metal and main group-metal ions, μ_3-O clusters that make up highly desired topologies such as MIL-100 and MIL-101 do not easily materialize for the group 13 ions: they are only found for aluminium in some particular cases (see: chapter 1).

The question, with the focus on MOFs, is thus: how do 6-coordinate main group clusters compare to their transition metal analogues from the perspective of bonding and what is the role of hypervalence here?

In this chapter, octahedral hexaaqua complexes for Sc, B, Al, Ga, In, and Tl are investigated using quantum chemical bonding- and energy decomposition analyses (EDA) based on relativistic DFT.

[***] One 2008 study investigates the electronic structure of $[Al(H_2O)]^{3+}$ but mainly focuses on its effect on XANES spectra.[101]

MO perspective

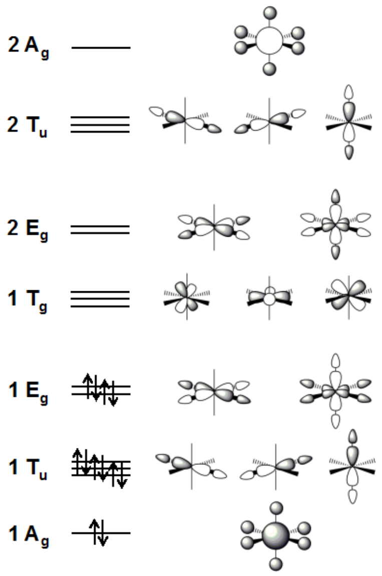

Figure 2.3 Ligand-Field description of a *12e* octahedral complex.

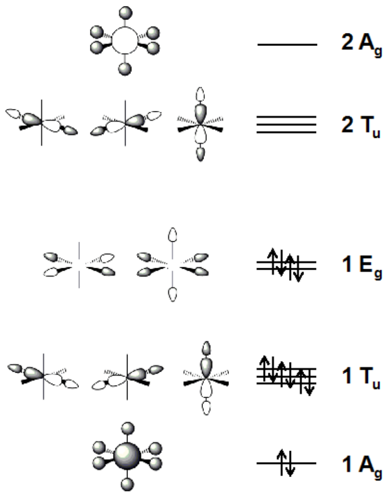

Figure 2.4 MO description of a *12e* hypervalent, octahedral complex

The concept of Crystal Field Theory, introduced in 1932, was one of the first successful attempts at explaining the spectroscopic properties of coordination compounds. It was after its introduction quickly combined with MO theory to render Ligand Field Theory (LFT), in which covalent interactions, and therefore chemical bonding could be described as well.[102] The concept remains to the day of today very useful in describing the bonding in transition metal complexes. Figure 2.3 displays the MO obtained for an octahedral complex with 6 identical ligands in T_h symmetry. The Mulliken symbols represent the Symmetry Adapted Linear Combinations (SALCs) of the atomic orbitals. The figure represents a 12 electron (*12e*) complex, in which the 12 electrons come from the 6 ligands that form the coordinate covalent bonds. Any additional electrons, whether initially present in the valence shell of the metal ion, or donated by *π-basic* ligands (such as oxido) that can undergo side-on overlap fill the three $1T_g$ orbitals. This forms the basis of the 18-electron rule, a *d*-block analogue of the octet rule. Any additional electrons then fill the $2E_g$ antibonding orbital, destabilizing the complex. Whereas this is possible, it becomes increasingly unlikely for *π-acid* ligands that engage into backdonation since these increase the $1T_g$-$2E_g$ gap. An important observation here is that LFT defines three *3c4e* bonds ($1T_u$).

In constructing an MO for a main-group metal-based octahedral cluster of O_h symmetry *without* metal *d*-orbitals, one ends up with the MO in figure 2.4. The two doubly-occupied $1E_g$ orbitals are nonbonding, but can potentially overlap with metal *d*-orbitals if these lie low enough in energy.

The MO diagram describes an octahedral complex with partially ionic bonding. The metal and ligand *p*-orbitals play a central role. They form three bonding orbitals ($1T_u$), and two non-bonding orbitals ($1E_g$), so 4 out of 12 electrons entirely located ligand *p*-orbitals (with *s*-*p* mixing neglected). Comparing figures 2.3 and 2.4 as Canonical Molecular Orbitals, one can thus draw the conclusion that the MO σ bond order is 6 for the transition metal, and 4 for the main group metal.

Methods

General procedure

All calculations were performed using the Amsterdam Density Functional (ADF) program,[103-106] using the BLYP functional. The numerical integration was performed using the procedure developed by Boerrigter, te Velde, and Baerends.[107-108] The MOs were expanded in a large uncontracted set of Slater type orbitals (STOs) containing diffuse functions, which is of triple-ζ quality for all atoms and has been augmented with two sets of polarization functions: 2p and 3d for H, 4d and 4f for O, B and Al, 4d and 4f for Ga, 5d and 4f for In, 6d and 5f for Tl. The core shells of all atoms were treated by the frozen-core (FC) approximation.[109]

Energies and geometries were calculated using the generalized gradient approximation (GGA) of DFT at the BLYP level.[110,111] GGA proceeds from the local density approximation (LDA) where exchange is described by Slater's X_α potential and correlation is treated in the Vosko-Wilk-Nusair (VWN) parametrization[112] which is augmented with nonlocal corrections to exchange due to Becke[110] and correlation due to Perdew[113] added self-consistently.[114] Relativistic effects, expected for thallium in particular, are accounted by Zeroth-Order Regular Approximation (ZORA).[115,116] Grimme's latest dispersion correction, D3, is implemented,[117] with Becke-Johnson damping.[118]

Bond Energy Decomposition

The overall bond energy is made up of two major components:

$$\Delta E = \Delta E_{prep} + \Delta E_{int}$$

In this formula, the preparation energy ΔE_{prep} is the amount of energy required to deform the separate molecular fragments that are connected by the chemical bond from their equilibrium structure to the geometry that they acquire in the overall molecular system. The interaction energy ΔE_{int} corresponds to the actual energy change when the prepared fragments are combined to form the overall molecule. It is analyzed for our model systems in the framework of the Kohn-Sham MO model using a Morokuma-type decomposition of the bond into electrostatic interaction, exchange repulsion (or Pauli repulsion), and (attractive) orbital interactions.

$$\Delta E_{int} = \Delta V_{elstat} + \Delta E_{Pauli} + \Delta E_{Oi}$$

The term ΔV_{elstat} corresponds to the classical electrostatic interaction between the unperturbed charge distributions of the prepared (i.e. deformed) fragments and is usually attractive. The Pauli repulsion ΔE_{Pauli} comprises the destabilizing interactions between occupied orbitals. It arises as the energy change associated with going from the superposition of the unperturbed electron densities of two fragments, here H_2O: and M, i.e. $\rho_{H2O(\alpha)} + \rho_{M(\beta)}$, to the wave function

$\Psi^0 = N\ A\ [\Psi_{H2O(\alpha)}\ \Psi_{M(\beta)}]$, that properly obeys the Pauli principle through explicit antisymmetrization (*A* operator) and renormalization (*N* constant) of the product of fragment wave functions. It consists of the four-electron destabilizing interactions between occupied orbitals and is responsible for steric repulsion. The orbital interaction ΔE_{Oi} in any MO model, and thus also in Kohn-Sham theory, accounts for electron-pair bonding, charge transfer (donor-acceptor interactions) and polarization (empty-occupied orbital mixing on one fragment due to the presence of another fragment). This term is of our major interest and is decomposed in:

$$\Delta E_{Oi} = \Delta E_s + \Delta E_p + \Delta E_{d\sigma} + \Delta E_{d\pi}$$

Theoretical set-up.

In this chapter, the hexaaqua complex is chosen as benchmark molecule, for it is frequently synthesized, used and observed for both transition metal and main group metal chemistry. Apart from that, it is highly symmetric, and can participate in π-bonding, making the aqua ligand archetypal for most ligands used in coordination chemistry. An analysis is carried out, in which a M^{3+} (M = B, Al, Ga, In, Tl, Sc) fragment is allowed to interact with a $(H_2O)_6$ fragment (figure 2.5).

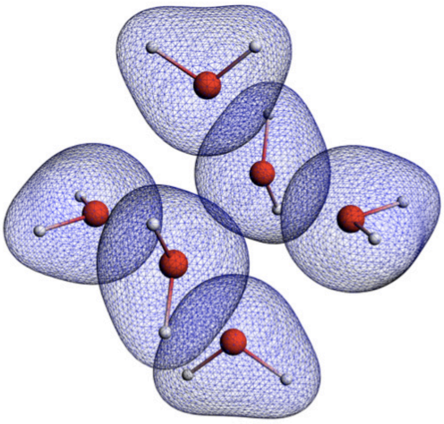

Figure 2.5 The strained $(H_2O)_6$ fragment. The blue grid displays the Self-Consistent Field (SCF) density.

This $(H_2O)_6$ fragment is constructed from 6 geometrically optimized H_2O molecules, that undergo certain strain ΔE_{prep}, to make up the fragment displayed in figure 2.5. In this strained $(H_2O)_6$ fragment, we find the six aqua ligands in the same geometry as in geometrically optimized $[M(H_2O)_6]^{3+}$. Naturally, this geometry depends on the metal ion radius and is thus calculated for all six complexes defined above.

Apart from Al, Ga, In and Tl, for which hexaaqua complexes are readily synthesized,[119] the nonexisting $[B(H_2O)_6]^{3+}$ molecule is treated as well. The group 13 based complexes are compared with $[Sc(H_2O)_6]^{3+}$. Sc^{3+} is chosen as transition metal ion since it contains an empty valence shell – just as the group 13 ions do[†††] – and can form the same MOF topologies, such as MIL-53, MIL-100 and MIL-101.

Whereas the hexaaqua complex carries T_h symmetry (not tetrahedral which is T_d), analysis was carried out at lower D_{2h} symmetry, since the former was not available in the ADF software package.

The major consideration of this lower symmetry is that the metal *s*, d_{z2} and d_{x2-y2}, and thus the corresponding SALCs of the aqua ligand orbitals are all *totally symmetric* (A_g) within this point

---

[†††] In the 'short form' of the periodic table, the original form proposed by Mendeleev, Sc is in the same group as B, Al, Ga etc.

group, with ligand *$4A_g$* suitable for overlap with the metal *s* orbital, and ligand *$5A_g$* and *$6A_g$ to* d_{z2} and $d_{x2\text{-}y2}$ *(*figure 2.6). MOs belonging to the latter two are analogues of the *$1E_g$* orbitals of figure 2.3, and are of major focus in this study since they involve potential *σ* bonding with metal *d*-orbitals. Further, the *$1T_u$* and *$1T_g$* orbitals of figure 2.3, responsible for the hypervalent 3c4e, and *π* bonding respectively, carry *$B_{1u}/B_{2u}/B_{3u}$* and *$B_{1g}/B_{2g}/B_{3g}$* symmetry (figure 2.6).

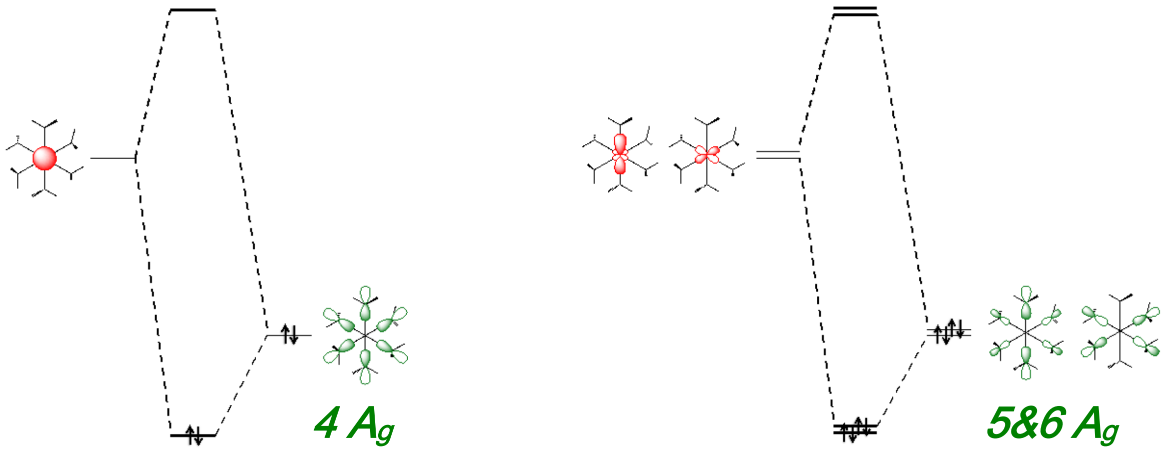

Figure 2.5 Schematic MO diagrams of the M^{3+}---$(H_2O)_6$ interaction for the totally symmetric irreducible representations of the *D_{2h}* point group. *Left*: bonding with the metal *s* orbital, *right*: bonding with the metal d_{z2} and $d_{x2\text{-}y2}$ orbitals.

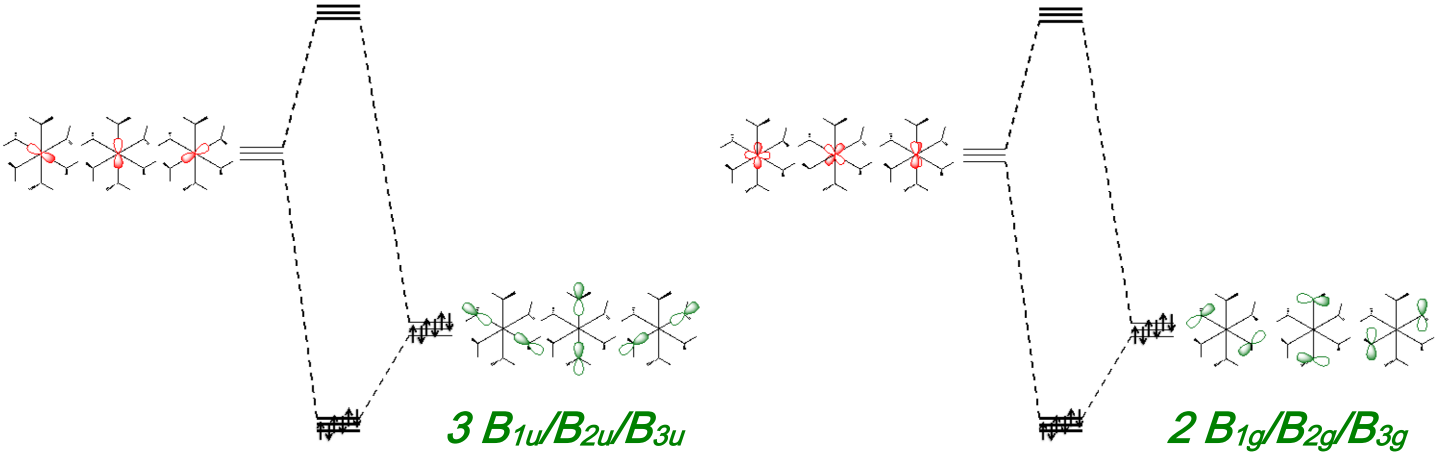

Figure 2.6 Schematic MO diagrams of M^{3+}---$(H_2O)_6$ interaction for *$B_{1u}/B_{2u}/B_{3u}$* and *$B_{1g}/B_{2g}/B_{3g}$* irreducible representations of the *D_{2h}* point group. The former provides the *3c4e* bonding, the latter metal-ligand side-on overlap.

Results

Table 1 summarizes the results of the calculations on the clusters. It lies within line of expectation that the small, unstable B^{3+} fragment undergoes the largest stabilization upon reaction with $(H_2O)_6$, and the deformation of the six aqua ligands to the final complex geometry, with ΔE_{prep}, is largest here for the smallest cation. Exchange interaction/Pauli repulsion increases for increasing metal ion radius, yet is largest for the transition metal ion Sc^{3+}. This is an inverse trend towards calculations on single-atoms, where in moving up and to the right in the periodic table, exchange increases, due to smaller electron-electron distances.[121,122] In terms of making new bonds with an empty valence shell: repulsion due to exchange is expected to be the smallest for small ions, where inner-shell electrons are pulled in strongly by the nucleus. Scandium, which carries the lowest electronegativity of the treated

	B-(H_2O)$_6$	Al-(H_2O)$_6$	Ga-(H_2O)$_6$	In-(H_2O)$_6$	Tl-(H_2O)$_6$	Sc-(H_2O)$_6$
Bond Energy Decomposition (in kcal/mol)						
ΔE_{OI}	-813.9	-461.9	-469.0	-355.7	-372.3	-383.4
ΔE_{Pauli}	41.8	76.5	97.6	108.4	121.5	149.8
ΔV_{ElStat}	-312.8	-341.3	-367.1	-356.3	-351.1	-340.2
ΔE_{int}	-1089.8	-734.7	-746.7	-613.4	-611.9	-583.7
ΔE_{prep}	67.2	30.6	25.3	17.6	16.3	18.7
Fragment Orbital Overlaps (normalized, absolute)						
$\langle 4\mathbf{A_g} \mid k\mathbf{s} \rangle$[a]	0.52	0.53	0.49	0.46	0.40	0.21
$\langle 3\mathbf{B_{iu}} \mid k\mathbf{p}_\sigma \rangle$[b]	0.39	0.46	0.42	0.40	0.38	0.12
$\langle (5,6)\mathbf{A_g} \mid k\mathbf{d}_\sigma \rangle$[c]	0.02	0.48	0.31	0.25	0.46	0.20
$\langle 2\mathbf{B_{ig}} \mid m\mathbf{d}_\pi \rangle$[b]	0.21	0.25	0.35	0.38	0.38	0.08
Fragment Orbital Populations (in electrons)						
(H_2O)$_6$						
$4\mathbf{A_g}$	1.28	1.58	1.38	1.39	1.26	1.88
$3\mathbf{B_{iu}}$	1.58	1.74	1.68	1.78	1.81	1.92
$(5,6)\mathbf{A_g}$	1.91	1.84	1.86	1.91	1.92	1.69
$2\mathbf{B_{ig}}$	1.98	1.96	1.95	1.97	1.98	1.87
M						
$k\mathbf{s}$	0.63	0.32	0.57	0.57	0.69	0.03
$k\mathbf{p}_\sigma$	0.38	0.17	0.24	0.16	0.15	0.03
$m\mathbf{d}_\sigma$	0.06	0.14	0.08	-0.02	0.06	0.25
$m\mathbf{d}_\pi$	0.02	0.05	0.07	0.03	0.02	0.10

Fragment Orbital Overlap Populations (in electrons)

σ_s[d]	0.34	0.23	0.29	0.27	0.26	~ 0
σ_p	0.16	0.14	0.17	0.11	0.10	0.04
σ_d	~ 0[e]	0.10	0.05	0.01	0.05	0.10
π_d	0.04	0.02	0.04	0.03	0.01	0.03
Total	0.94	0.91	1.02	0.71	0.69	0.41

Table 2.1 Central atom–water bonding analysis in D_{2h}-symmetric M–(H2O)$_6$ complexes.#

*# Computed at ZORA-BLYP-D3(BJ)/TZ2P. **a**: k=2(B), 3(Al), 4(Sc, Ga), 5 (In), 6 (Tl) **b**: i = 1-3 for the three energy-degenerate orbitals **c:** 5A_g and 6A_g are energy- **d:** the subscripts s,p,d correspond to the ligand orbitals ks, kp$_\sigma$* etc. ***e:** Population smaller than 0.001*

elements, has its electrons relatively far from the nucleus and therefore experiences largest exchange in coordination.

If the Mulliken fragment orbital populations after interaction are considered in more detail, it is of no surprise that the *d*-orbital population for Scandium outnumbers the main group *d*-orbital populations by far. However, whereas populational numbers for boron, gallium, indium and thallium could be reasonably ascribed to Mulliken artifacts from the TZ2P basis set, the population of 0.14 electron for aluminium seems a too large to be explained in this way. Moreover, Mulliken orbital overlap populations also appear to indicate that aluminium *d*-orbitals are involved in holding the complex together.

From table 2.2, we conclude that aluminium *d*-orbitals do not lie much lower than the other main-group metals, and the large population must thus be an orbital overlap effect. Therefore, an explanation for the large populations and overlaps associated with *d*-orbitals could be related to the diffusivity of the orbitals in the TZ2P basis set and the small, charged Al^{3+} fragment.

	B^{3+}	Al^{3+}	Ga^{3+}	In^{3+}	Tl^{3+}	Sc^{3+}
***E* / eV**	-5.74	-16.40	-15.49	-15.74	-12.27	-32.19

Table 2.2 Metal ion *d*-orbital energies

Now, *d*-orbitals clearly improve the wavefunction ψ, but are they also significant in controlling molecular geometry? In order to investigate this, a geometry optimization was performed on a distorted 6-coordinate complex, using a modified basis set for Al^{3+} from which the *d*-functions were deleted. The calculated metal-ligand bond length in the resulting $[Al(H_2O)]^{3+}$ complex turns out barely elongated at 195.7 with respect to the original value of 194.0 pm. To put this into context: this difference is considerably smaller than the one associated with inclusion/exclusion of electron correlation: a similar geometry optimization at the Hartree-Fock/TZ2P level results in a bond length of 199.7. We thus conclude that for the group 13 based clusters, *d*-orbitals are not required for canonical description of the bonding, which is represented by scheme B.

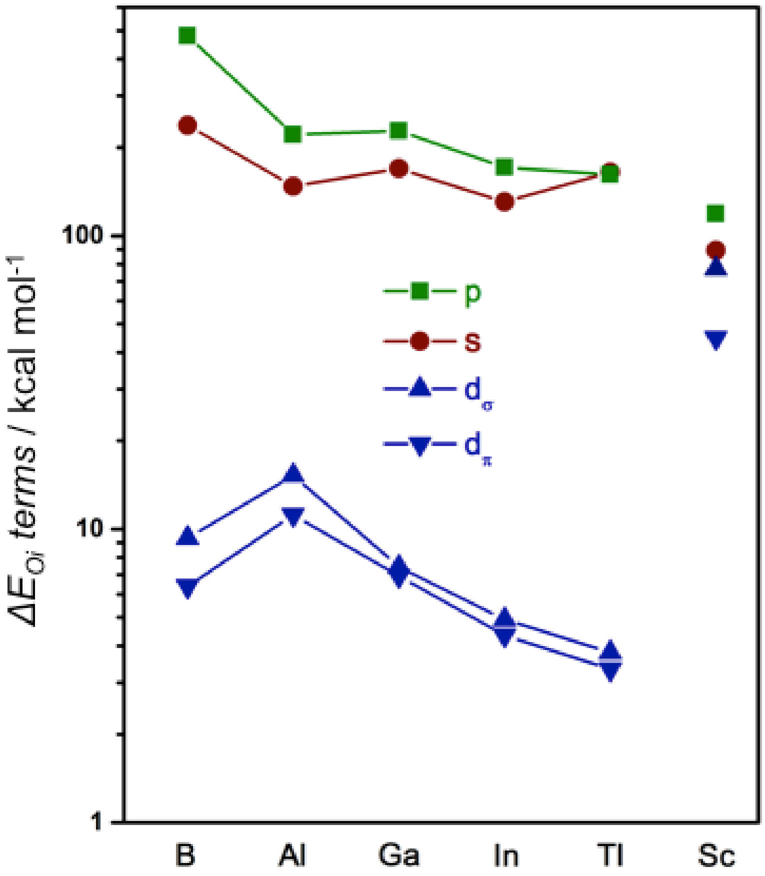

Figure 2.7 Energetic contribution of metal orbitals in interaction with $(H_2O)_6$.

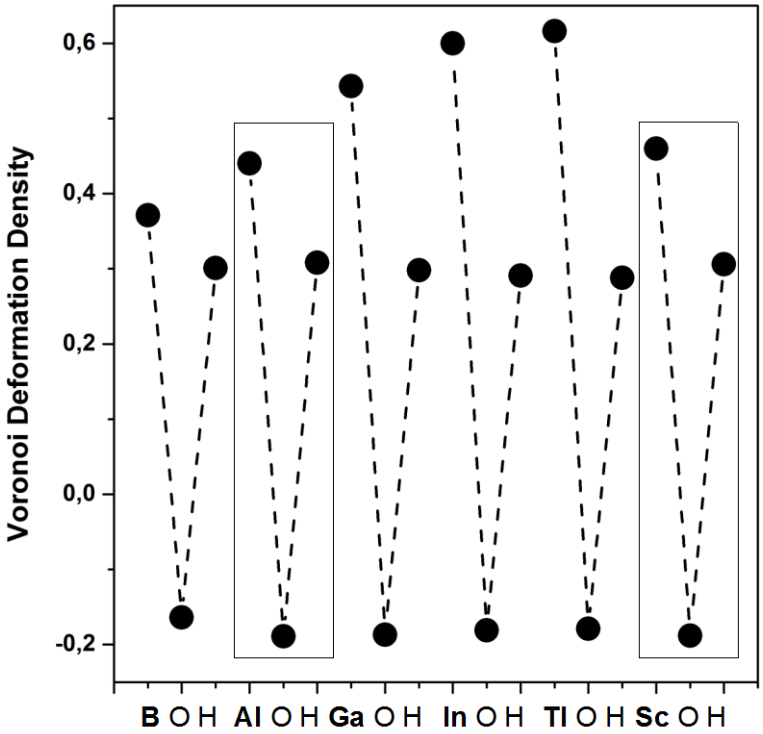

Figure 2.8 Atomic Voronoi charges within the complexes for the cation, oxygen and hydrogen. Charges for aluminium and scandium hexaaqua complexes are highlighted with a rectangle.

Energy terms corresponding to electron-pair charge transfer to the metal ion *s (*1 × *σ* overlap)*,* *p (*3 × *σ*-overlap) and *d* orbitals (2 × *σ*- and 3 × *π*-overlap) were calculated; these are displayed in figure 2.7 It is evident here that *d*-orbital contributions to bonding, being an order of magnitude smaller than the *s* and *p*-orbital counterparts, don't significantly add to the total bond energy for the group 13 cations. This contrasts with Sc^{3+}, for which all orbital contributions are at comparable levels. Further, in line with the orbital populational and overlap analysis, a positive 'kink' is produced for aluminium, but the graph also indicates that this energetic 'deviation' should not be overestimated, attributing to a few kcal/mol at maximum. It is noteworthy that the slightly increased contribution of the *d*-orbitals goes at the cost of the hypervalent contribution of the *p*-orbitals. Further, the energetic stabilization by the metal *s* orbital electron acceptance increases when moving to thallium, which is in line with the *inert-pair effect*, i.e. the difficulty to remove electrons from the valence *s*-orbital of Tl.

Having elucidated this, we focus our attention to the consequences of this result. Hypervalent 6-coordinate complexes (and frameworks) are expected to carry typical bonding properties, predicted by the electron-rich *7c-10e* pattern, such as *(1)* 'elongated' metal-ligand bond lengths and *(2)* considerable charge-polarization across these bonds.[100] As 'elongated' we define bonds that considerably exceed the bond length predicted by the sum of the covalent radii of the M^{3+} and oxygen atom that are engaged in the interaction. Taking this as measure, the 6-coordinate clusters based on group 13 cations are indeed held together by elongated bonds, as can be seen in table 1. Using the equilibrium bond length as measure for bond strength, the comparatively shorter bond length for the Sc^{3+} complex is in good agreement with the total MO bond orders of 6 and 4 from Scheme A and B, respectively.

	B^{3+}	**Al^{3+}**	**Ga^{3+}**	**In^{3+}**	**Tl^{3+}**	**Sc^{3+}**
***Sum Covalent Radii* / pm**[122]	150 ± 5	187 ± 6	188 ± 5	208 ± 7	211 ± 9	233 ± 9
***Bond Length* / pm**	172.8	194.0	201.9	221.2	230.5	216.2

Table 2.3 Sum of the covalent radii of the cation and aqua oxygen and calculated bond lengths in the hexaaqua complex for the different elements.

If we consider the Voronoi Deformation Density (VDD) charges, based on integrating the deformation density over Voronoi cells,[123] Figure 2.8 expectedly indicates that the increasing metal radius renders an increase in local positive charge as the polarizing ability of the cation diminishes. However, the charge polarization pattern across the M-O-H (M=metal) bond path is virtually equal between aluminium and scandium whilst their respective atomic vdWaals radii differ considerably (Al: 184 pm, Ga: 187pm, In: 193 pm Tl: 196pm, Sc: 211 pm). This is a typical consequence of electron-rich bonding in hypervalent compounds, where 'excess' electrons reside on the ligands (the $1E_g$ orbitals in Scheme B).

Concluding remarks

The initial question was: how do 6-coordinate main group clusters compare to their transition metal analogues from the perspective of bonding and what is the role of hypervalence? Based on the results treated above, it is concluded that 6-coordinate group-13 based clusters should be treated as classic hypervalent moieties in which bonding is mainly structured by an electron-rich *7c10e* centre; *d*-orbitals lie too high in energy to be significantly involved. Importantly, this is of direct explanatory value for some general features of MIL-53 (and probably, MOFs in general) based on 6-coordinate clusters constructed by group-13 metals; it has been shown that MIL-53(Al) is more stable thermally, yet less stable chemically with respect to analogues based on transition metals.[124,125] This is in line of expectation for a solid structured by ionic, electron-rich bonds. Our calculations also indicate increased bond lengths with respect to transition metals. However, this holds for isolated clusters; extended networks based on such clusters experience lattice enthalpy and long-range electrostatic effects for which this non-classical result on electron-rich bonding becomes less significant. The isolated Al cluster has an Al-(μ_2-OH) bond length of 181 pm in MIL-53(Al) vs. a Sc-(μ_2-OH) bond length of 209; the Al-O/Sc-O bond length ratio here is 0.87, which is close to our computationally obtained ratio of 0.90, yet one needs to be careful in a discussion on bond lengths in extended networks.

Summarizing, this chapter treats a long unexplored field; it presents the first theoretical treatment of bonding in 6-coordinate group-13-based clusters, and a rationale is presented for several observations on the coordination chemistry of Metal-Organic Frameworks.

References

[1] M. Simard, D. Su, J. D. Wuest, *J. Am. Chem. Soc.* **1991**, *113*, 4696–4698.

[2] J. V. Smith, *Chem. Rev.* **1988**, *88*, 149–182.

[3] X. Wang, M. Simard, J. D. Wuest, *J. Am. Chem. Soc.* **1994**, *116*, 12119–12120.

[4] A. I. Cooper, *Angew. Chem. - Int. Ed.* **2012**, *51*, 7892–7894.

[5] B. F. Hoskins, R. Robson, *J. Am. Chem. Soc.* **1989**, *111*, 5962–5964.

[6] N. W. Ockwig, O. Delgado-Friedrichs, M. O'Keeffe, O. M. Yaghi, *Acc. Chem. Res.* **2005**, *38*, 176–182.

[7] O. M. Yaghi, M. O'Keeffe, N. W. Ockwig, H. K. Chae, M. Eddaoudi, J. Kim, *Nature* **2003**, *423*, 705–714.

[8] *Metamorphosis II, © 2015* The M.C. Escher Company B.V.- Baarn - Holland. All rights reserved. www.mcescher.com

[9] M. Eddaoudi, J. Kim, N. Rosi, D. Vodak, J. Wachter, M. O'Keeffe, O. M. Yaghi, *Science* **2002**, *295*, 469–472.

[10] A. R. Millward, O. M. Yaghi, *J. Am. Chem. Soc.* **2005**, *127*, 17998–17999.

[11] O. K. Farha, I. Eryazici, N. C. Jeong, B. G. Hauser, C. E. Wilmer, A. A. Sarjeant, R. Q. Snurr, S. T. Nguyen, A. O. Yazaydin, J. T. Hupp, *J. Am. Chem. Soc.* **2012**, *134*, 15016–15021.

[12] D. Liu, H. Wu, S. Wang, Z. Xie, J. Li, W. Lin, *Chem. Sci.* **2012**, *3*, 3032–3037.

[13] B. Moulton, J. Lu, R. Hajndl, S. Hariharan, M. J. Zaworotko, *Angew. Chem. - Int. Ed.* **2002**, *41*, 2821–2824.

[14] T. Loiseau, L. Lecroq, C. Volkringer, J. Marrot, G. Férey, M. Haouas, F. Taulelle, S. Bourrelly, P. L. Llewellyn, M. Latroche, *J. Am. Chem. Soc.* **2006**, *128*, 10223–10230.

[15] S. R. Batten, *J. Solid State Chem.* **2005**, *178*, 2475–2479.

[16] M. O'Keeffe, O. M. Yaghi, *Chem. Rev.* **2012**, *112*, 675–702.

[17] K. S. Park, Z. Ni, A. P. Côté, J. Y. Choi, R. Huang, F. J. Uribe-Romo, H. K. Chae, M. O'Keeffe, O. M. Yaghi, *Proc. Natl. Acad. Sci.* **2006**, *103*, 10186–10191.

[18] J. Cravillon, C. A. Schröder, R. Nayuk, J. Gummel, K. Huber, M. Wiebcke, *Angew. Chem. - Int. Ed.* **2011**, *50*, 8067–8071.

[19] J. Juan-Alcañiz, R. Gielisse, A. B. Lago, E. V. Ramos-Fernandez, P. Serra-Crespo, T. Devic, N. Guillou, C. Serre, F. Kapteijn, J. Gascon, *Catal. Sci. Technol.* **2013**, *3*, 2311–2318.

[20] M. G. Goesten, J. Juan-Alcañiz, E. V. Ramos-Fernandez, K. Gupta, E. Stavitski, H. van Bekkum, J. Gascon, F. Kapteijn, *J. Catal.* **2011**, *281*, 177-187

[21] M. G. Goesten, K. Gupta, E. V. Ramos-Fernandez, H. Khajavi, F. Kapteijn, J. Gascon, CrystEngComm **2012**, 14, 4109-4111

[22] K. M. L. Taylor-Pashow, J. Della Rocca, Z. Xie, S. Tran, W. Lin, *J. Am. Chem. Soc.* **2009**, *131*, 14261–14263.

[23] Z. Wang, S. M. Cohen, *Chem. Soc. Rev.* **2009**, *38*, 1315–1329.

[24] J. R. Gispert, *Coordination Chemistry* **2008**, Wiley-VCH, New York

[25] M. Kondo, T. Yoshitomi, K. Seki, H. Matsuzaka, S. Kitagawa, *Angew. Chem. - Int. Ed.* **1997**, *36*, 1725–1727.

[26] P. Ayyappan, O. R. Evans, W. Lin, *Inorg Chem* **2002**, *41*, 3328–3330.

[27] R. Vaidhyanathan, S. S. Iremonger, K. W. Dawson, G. K. H. Shimizu, *Chem. Comm.* **2009**, 5230–5232.

[28] H. Li, M. Eddaoudi, T. L. Groy, O. M. Yaghi, *J. Am. Chem. Soc.* **1998**, *120*, 8571–8572.

[29] C. Serre, N. Stock, T. Bein, G. Férey, *Inorg Chem* **2004**, *43*, 3159–3163.

[30] B. Q. Ma, D. S. Zhang, S. Gao, T. Z. Jin, C. H. Yan, G. X. Xu, *Angewandte Chemie - International Edition* **2000**, *39*, 3644–3646.

[31] A. Violante, P. M. Huang, *Clays and Clay Minerals* **1985**, *33*, 181–192.

[32] A. Violante, P. M. Huang, *Clays and Clay Minerals* **1993**, *41*, 590–597.

[33] M. Haouas, C. Volkringer, T. Loiseau, G. Férey, F. Taulelle, *Chem. Mater.* **2012**, *24*, 2462–2471.

[34] G. Férey, C. Serre, C. Mellot-Draznieks, F. Millange, S. Surblé, J. Dutour, I. Margiolaki, *Angew. Chem. - Int. Ed.* **2004**, *43*, 6296–6301.

[35] A. Martiñez-Joaristi, J. Juan-Alcañiz, P. Serra-Crespo, F. Kapteijn, J. Gascon, *Crystal Growth & Design* **2012**, *12*, 3489–3498.

[36] R. Mondal, T. Basu, D. Sadhukhan, T. Chattopadhyay, M. K. Bhunia, *Crystal Growth & Design* **2009**, *9*, 1095–1105.

[37] H. M. Park, I. H. Hwang, J. M. Bae, Y. D. Jo, C. Kim, H. Y. Kim, Y. Kim, S. J. Kim, *Bull. Korean Chem. Soc.* **2012**, *33*, 1517–1522.

[38] B. Notash, N. Safari, H. R. Khavasi, *CrystEngComm* **2012**, *14*, 6788–6796.

[39] W. Wei, H. Yu, F. Jiang, B. Liu, J. Ma, M. Hong, *CrystEngComm* **2012**, *14*, 1693–1700.

[40] D. Louër, L. F. Ma, H. H. Zou, Y. G. Wang, H. Liang, M. H. Zeng, *Dalton Trans.* **2011**, *40*, 11402–11409.

[41] H. M. Hao, F. P. Huang, H. D. Bian, Q. Yu, X. L. Sun, H. Liang, *Polyhedron* **2011**, *30*, 2099–2105.

[42] T. Loiseau, G. Férey, *J. of Fluorine Chem.* **2007**, *128*, 413–422.

[43] K. S. Min, M. P. Suh, *J. Am. Chem. Soc.* **2000**, *122*, 6834–6840.

[44] Y. S. Li, H. Bux, A. Feldhoff, G. N. Li, W. S. Yang, J. Caro, *Adv. Mater.* **2010**, *22*, 3322–3326.

[45] E. Stavitski, M. Goesten, J. Juan-Alcañiz, A. Martiñez-Joaristi, P. Serra-Crespo, A. V. Petukhov, J.

Gascon, F. Kapteijn, *Angew. Chem. - Int. Ed.* **2011**, *50*, 9624–9628.
[46] L. Carlucci, G. Ciani, D. M. Proserpio, *J. Chem. Soc. - Dalton Trans.* **1999**, 1799–1804.
[47] H. P. Wu, C. Janiak, L. Uehlin, P. Klufers, P. Mayer, *Chem. Comm.* **1998**, 2637–2638.
[48] Y. Zhang, P. S. Cremer, *Current Opinion in Chemical Biology* **2006**, *10*, 658–663.
[49] R. Custelcean, B. A. Moyer, *Eur. J. of Inorg. Chem.* **2007**, 1321–1340.
[50] V. Trukil, L. Fábián, D. G. Reid, M. J. Duer, G. J. Jackson, M. Eckert-Maksić, T. Friić, *Chemical Communications* **2010**, *46*, 9191–9193.
[51] B. C. Tzeng, H. T. Yeh, T. Y. Chang, G. H. Lee, *Crystal Growth & Design* **2009**, *9*, 2552–2555.
[52] C. P. Li, M. Du, *Chem. Comm.* **2011**, *47*, 5958–5972.
[53] I. Senkovska, S. Kaskel, *Eur. J. of Inorg. Chem.* **2006**, 4564–4569.
[54] M. Dincă, J. R. Long, *J. Am. Chem. Soc.* **2005**, *127*, 9376–9377.
[55] C. A. Williams, A. J. Blake, C. Wilson, P. Hubberstey, M. Schröder, *Crystal Growth & Design* **2008**, *8*, 911–922.
[56] S. I. Noro, S. Horike, D. Tanaka, S. Kitagawa, T. Akutagawa, T. Nakamura, *Inorg Chem* **2006**, *45*, 9290–9300.
[57] N. N. Adarsh, D. K. Kumar, P. Dastidar, *CrystEngComm* **2008**, *10*, 1565–1573.
[58] S. Couck, J. F. M. Denayer, G. V. Baron, T. Rémy, J. Gascon, F. Kapteijn, *J. Am. Chem. Soc.* **2009**, *131*, 6326–6327.
[59] S. Couck, T. Rémy, G. V. Baron, J. Gascon, F. Kapteijn, J. F. M. Denayer, *Phys. Chem. Chem. Phys.* **2010**, *12*, 9413–9418.
[60] A. Boutin, S. Couck, F. X. Coudert, P. Serra-Crespo, J. Gascon, F. Kapteijn, A. H. Fuchs, J. F. M. Denayer, *Microporous Mesoporous Mater.* **2011**, *140*, 108–113.
[61] P. Serra-Crespo, M. A. Van Der Veen, E. Gobechiya, K. Houthoofd, Y. Filinchuk, C. E. A. Kirschhock, J. A. Martens, B. F. Sels, D. E. De Vos, F. Kapteijn, et al., *J. Am. Chem. Soc.* **2012**, *134*, 8314–8317.
[62] P. Serra-Crespo, E. V. Ramos-Fernandez, J. Gascon, F. Kapteijn, *Chem. Mater.* **2011**, *23*, 2565–2572.
[63] M. Schubert, U. Mueller, C. Kiener, *Patent WO 2008061958 A1* **2008**.
[64] A. F. Gualtieri, *Phys. Chem. Miner.* **2001**, *28*, 719–728.
[65] F. Millange, R. El Osta, M. E. Medina, R. I. Walton, *CrystEngComm* **2011**, *13*, 103–108.
[66] F. Millange, R. El Osta, M. E. Medina, R. I. Walton, *CrystEngComm* **2011**, *13*, 7318.
[67] A. C. Sudik, A. P. Côté, O. M. Yaghi, *Inorg Chem* **2005**, *44*, 2998–3000.
[68] M. G. Goesten, E. Stavitski, J. Juan-Alcañiz, *Catal. Today* **2013**.
[69] M. G. Goesten, P. C. M. M. Magusin, E. A. Pidko, B. Mezari, E. J. M. Hensen, F. Kapteijn, J. Gascon, *Inorg Chem* **2014**, *53*, 882–887.
[70] J. Juan-Alcañiz, M. G. Goesten, E.V. Ramos-Fernandez, J. Gascon, F. Kapteijn, J *New J. Chem.* **2012**. 36, 977-987
[71] M. R. Lohe, M. Rose, S. Kaskel, *Chem. Comm.* **2009**, 6056–6058.
[72] S. K. Nune, P. K. Thallapally, B. P. McGrail, *J. Mater. Chem.* **2010**, *20*, 7623–7625.
[73] G. Férey, *Chem. Soc. Rev.* **2008**, *37*, 191–214.
[74] M. Jansen, J. C. Schön, *Angewandte Chemie - International Edition* **2006**, *45*, 3406–3412.
[75] R. F. Lobo, S. I. Zones, M. E. Davis, *Journal of Inclusion Phenomena and Molecular Recognition in Chemistry* **1995**, *21*, 47–78.
[76] S. L. Burkett, M. E. Davis, *Journal of physical chemistry* **1994**, *98*, 4647–4653.
[77] M. Choi, K. Na, J. Kim, Y. Sakamoto, O. Terasaki, R. Ryoo, *Nature* **2009**, *461*, 246–249.
[78] X. D. Do, V. T. Hoang, S. Kaliaguine, *Microporous and Mesoporous Materials* **2011**, *141*, 135–139.
[79] L. G. Qiu, T. Xu, Z. Q. Li, W. Wang, Y. Wu, X. Jiang, X. Y. Tian, L. D. Zhang, *Angew. Chem. - Int. Ed.* **2008**, *47*, 9487–9491.
[80] L. Peng, J. Zhang, J. Li, B. Han, Z. Xue, G. Yang, *Chem. Comm.* **2012**, *48*, 8688–8690.
[81] S. R. Bajpe, C. E. A. Kirschhock, A. Aerts, E. Breynaert, G. Absillis, T. N. Parac-Vogt, L. Giebeler, J. A. Martens, *Chemistry - A European Journal* **2010**, *16*, 3926–3932.
[82] J. Juan-Alcañiz, M. Goesten, A. Martiñez-Joaristi, E. Stavitski, A. V. Petukhov, J. Gascon, F. Kapteijn, *Chem. Comm.* **2011**, *47*, 8578–8580.
[83] C. Serre, F. Millange, C. Thouvenot, M. Noguès, G. Marsolier, D. Louër, G. Férey, *J. Am. Chem. Soc.* **2002**, *124*, 13519–13526.
[84] P. Serra-Crespo, E. Gobechiya, E. V. Ramos-Fernandez, J. Juan-Alcañiz, A. Martinez-Joaristi, E. Stavitski, C. E. A. Kirschhock, J. A. Martens, F. Kapteijn, J. Gascon, *Langmuir* **2012**, *28*, 12916–12922.
[85] J. P. S. Mowat, V. R. Seymour, J. M. Griffin, S. P. Thompson, A. M. Z. Slawin, D. Fairen-Jimenez, T. Düren, S. E. Ashbrook, P. A. Wright, *Dalton Trans.* **2012**, *41*, 3937–3941.
[86] M. Anbia, S. Sheykhi, *J. Natural Gas Chem.* **2012**, *21*, 680–684.
[87] J. I. Musher, *Angew. Chem. Int. Ed.* **1969**, *8*, 54–68.
[88] L. Pauling, *J. Am. Chem. Soc.* **1932**, *54*, 3570–3582.
[89] G. C. Pimentel, *J. Chem. Phys.* **1951**, *19*, 446–448.
[90] L. C. Cusachs, *Int. J. Quantum Chem.* **1975**, *9*, 75–81.
[91] E. Magnusson, *J. Am. Chem. Soc.* **1990**, *112*, 7940–7951.
[92] A. E. Reed, P. V. R. Schleyer, *J. Am. Chem. Soc.* **1990**, *112*, 1434–1445.
[93] M. L. Munzarová, R. Hoffmann, *J. Am. Chem. Soc.* **2002**, *124*, 4787–4795.
[94] B. Braïda, P. C. Hiberty, *Nat Chem.*, *5*, 417–422.

[95] S. C. A. H. Pierrefixe, S. J. M. van Stralen, J. N. P. van Stralen, C. Fonseca Guerra, F. M. Bickelhaupt, *Angew. Chem. Int. Ed.* **2009**, *48*, 6469–6471.

[96] W. C. McKee, J. Agarwal, H. F. Schaefer, P. V. R. Schleyer, *Angew. Chem. Int. Ed.* **2014**, *53*, 7875–7878.

[97] S. C. A. H. Pierrefixe, F. M. Bickelhaupt, *Structural Chemistry* **2007**, *18*, 813–819.

[98] S. C. A. H. Pierrefixe, C. F. Guerra, F. M. Bickelhaupt, *Chemistry - A European Journal* **2008**, *14*, 819–828.

[99] S. C. A. H. Pierrefixe, J. Poater, C. Im, F. M. Bickelhaupt, *Chemistry - A European Journal* **2008**, *14*, 6901–6911.

[100] K. Akiba, *Chemistry of Hypervalent Compounds*, **1999**, Wiley-VCH, New York,

[101] M. B. Hay, S. C. B. Myneni, *J. Phys. Chem. A* **2008**, *112*, 10595–10603.

[102] J.S. Griffith, L.E. Orgel, *Q. Rev. Chem. Soc.* **1957**, 11, 381-383

[103] *www.scm.com*

[104] G. te Velde, F. M. Bickelhaupt, E. J. Baerends, C. Fonseca Guerra, S. J. A. van Gisbergen, J. G.Snijders, T. Ziegler, *J. Comput. Chem.* **2001**, *22*, 931–967.

[105] J. G. Snijders, P. Vernooijs, E. J. Baerends, *Atomic Data and Nuclear Data Tables*, *26*, 483–509.

[106] C. Fonseca Guerra, J. G. Snijders, G. te Velde, E. J. Baerends, *Theoretical Chemistry Accounts* **1998**, *99*, 391–403.

[107] P. M. Boerrigter, G. te Velde, J. E. Baerends, *Int. J. Quantum Chem.* **1988**, *33*, 87–113.

[108] G. te Velde, E. J. Baerends, *J. of Comput. Phys.***1992**, *99*, 84–98.

[109] E. J. Baerends, D. E. Ellis, P. Ros, *Chem. Phys.* **1973**, *2*, 41–51.

[110] A. D. Becke, *Physical Review A* **1988**, *38*, 3098–3100.

[111] C. Lee, W. Yang, R. G. Parr, *Phys. Rev. B* **1988**, *37*, 785–789.

[112] S. H. Vosko, L. Wilk, M. Nusair, *Can. J. Phys.* **1980**, *58*, 1200–1211.

[113] J. Perdew, *Phys. Rev. B* **1986**, *33*, 8822–8824.

[114] L. Fan, T. Ziegler, *J. Chem. Phys.* **1991**, *94*, 6057–6063.

[115] E. Van Lenthe, R. Van Leeuwen, E. J. Baerends, J. G. Snijders, *Int. J. Quantum Chem.* **1996**, *57*, 281–293.

[116] Johnson, E. R.; Becke, A. D. J Chem Phys 2006, 124, 174104.

[117] E. Van Lenthe, J. G. Snijders, E. J. Baerends, *J. Chem. Phys.* **1996**, *105*, 6505–6516.

[118] S. Grimme, J. Antony, S. Ehrlich, H. Krieg, *J. Chem. Phys.* **2010**, *132*, DOI 10.1063/1.3382344.

[119] S. S. A. Iqbal, *Chemistry of P-Block Elements*, Discovery Publishing House Pvt. Limited, **2003**.

[120] S. Shaik, H. Chen, D. Janardanan, *Nature Chemistry* **2011**, *3*, 19–27.

[121] S. Shaik, H. Chen, D. Janardanan, *Nature Chemistry* **2012**, *4*, 511.

[122] B. Cordero, V. Gómez, A. E. Platero-Prats, M. Revés, J. Echeverría, E. Cremades, F. Barragán, S. Alvarez, *Dalton Trans.* **2008**, 2832.

[123] C. Fonseca Guerra, J.-W. Handgraaf, E. J. Baerends, F. M. Bickelhaupt, *J. Comput. Chem.* **2004**, *25*, 189–210.

[129] R. Vaidhyanathan, S. S. Iremonger, K. W. Dawson, G. K. H. Shimizu, *Chem. Comm.* **2009**, 5230–5232.

[130] I. J. Kang, N. A. Khan, E. Haque, S. H. Jhung, *Chemistry* **2011**, *17*, 6437–6442.

PART II

Molecular pathways in MOF crystallisation

In Chapter 1, the significance of *in-situ* studies on the formation of MOFs has been underlined. This second part deals with that very subject and aims at answering the question: how do MOFs form? Naturally, it is impossible to fill this thesis with a large overview of MOFs for which this question is answered, also because dedicated studies on MOF crystallisation are relatively rare in an otherwise impressively covered field of 'modern' coordination chemistry. It is for this reason that certain model systems are selected to be investigated, of which the analytic results would count for general scientific interest. In this chapter, three model systems are treated, all of which deal with 'popular' MOFs that have attracted great scientific interest due to their high stability and attractive properties.

The first system is the competitive synthesis of NH_2-MIL-53(Al) and NH_2-MIL-101(Al) from identical precursors. Both MOFs are aminated versions of two very well-studied MOF topologies, MIL-53 and MIL-101. This system is chosen for (i) their thermal and chemical stability that make them frontrunners among MOF materials, (ii) they are made from identical precursors yet form under very different conditions, (iii) these structures can be synthesized with aminated ligands. The aminated ligands are used as they are readily soluble in most solvents, which facilitates *in-situ* spectroscopic study. MIL-53 is a microporous MOF topology, in all likelihood the most famous example of a *breathing* porous coordination polymer. MIL-101 is a mesoporous material possessing huge cages, making it a material highly suitable for catalytic applications. The chapter is divided into three parts, 3A, 3B and 3C, where the supramolecular, full crystal and atomic scale are highlighted, respectively.

The second system is zinc based ZIF-7, in chapter 4, a stable, microporous MOF that can separate paraffins over olefins via a 'gate-opening' mechanism. The influence of diethyl amine, a modulator, and $ZnCl_2$, a combination that yields rod-shaped crystals with high aspect ratios, is investigated.

The third system is zirconium and hafnium based UiO-66, the thermally most stable MOF available, which is constructed by large inorganic clusters of high nuclearity (and a connectivity of 24 bonds!). Here, in chapter 5, it will be shown that there's evidence for a *solid-state clock reaction* in the growth of UiO-66.

As stated in the first line, the use of *in-situ* studies is very important. As the reader will find out, *in-situ* X-ray Scattering and *in-situ* NMR are the preferred techniques in this part. It will be demonstrated these techniques, backed up by DFT, can portrait events in MOF formation from the atomic to the full crystal scale.

This part is based on the following publications:

Chapter 3A: *Kinetic control of Metal–Organic Framework crystallization investigated by time-resolved in situ X-Ray scattering*

E. Stavitski,* M.G.Goesten, J. Juan-Alcañiz, A. Martinez-Joaristi, P. Serra-Crespo, A.V. Petukhov, J. Gascon,* F. Kapteijn. *Angew. Chem. Int. Ed.* 50, **2011**, 9624–9628

Chapter 3B: *Small-angle X-ray scattering documents the growth of Metal-Organic Frameworks.*

M.G. Goesten,* E. Stavitski, J Juan-Alcañiz, A. Martinez-Joaristi, A.V. Petukhov, F. Kapteijn, J. Gascon.* *Catal. Today*, 205, **2013**, 120-127

Chapter 3C: *Molecular promoting of aluminum metal-organic framework topology MIL-101 by N,N-dimethylformamide*

M.G. Goesten,* P.C.M.M. Magusin, E.A. Pidko, B. Mezari, E.J.M. Hensen, F. Kapteijn, J. Gascon* *Inorg Chem*, 53(2), **2014**, 882-887

Chapter 4: *The molecular pathway to ZIF-7 microrods revealed by in situ time-resolved small- and wide-angle X-ray scattering, quick-scanning extended X-ray absorption spectroscopy, and DFT calculations*

M.G. Goesten, E. Stavitski, E.A. Pidko, C. Gücüyener, B. Boshuizen, S.N. Ehrlich, E.J.M. Hensen, F. Kapteijn, J. Gascon,* *Chem. Eur. J.* 19, **2013**, 7809-7816.

Chapter 5 *Evidence for a solid-state clock reaction in the formation of UiO-66(Zr/Hf)*

M.G. Goesten,* M. de Lange, A. Olivos-Suarez, A. Bavykina, P. Serra-Crespo, C. Krywka, F.M. Bickelhaupt, F. Kapteijn, J. Gascon,* *submitted*

The interested reader is further referred to the following works on this subject by the author, not included in this thesis:

{Title in preparation}

M.G. Goesten & X. Zhu, R. Rohling, B. Szyja, G. Filonenko, N. Kosinov, F. Kapteijn, J.Gascon, E.J.M. Hensen* *in preparation*

Live encapsulation of a Keggin polyanion in NH_2-MIL-101(Al) observed by in situ time resolved X-ray scattering

J. Juan-Alcañiz, M.G. Goesten, A. Martinez-Joartisti, E. Stavitski,* A.V. Petukhov, J. Gascon,* F. Kapteijn, *Chem. Comm.* 47, **2011**, 8578-8580

3A

Kinetic pathways of Metal–Organic Framework crystallisation investigated by *in-situ* medium- and wide-angle X-ray scattering

Using X-ray Scattering at medium and wide angles, the chain of events leading to the formation of several MOF phases synthesized from identical precursors has been clarified. Our findings underline the complexity of the process and the multitude of factors governing the mechanism. One important result is, that the stabilization of the NH_2-MOF-235(Al) phase by DMF is essential for the successful synthesis of NH_2-MIL-101(Al). Further, it was the first time that the MOF-235 phase had been identified for a metal other than iron. Based on the kinetic results of this chapter, the optimal solvent composition for NH_2-MIL-53(Al) was determined to be DMF : H_2O = 10 : 90, instead of the original synthesis protocol using only H_2O. This led to the yield increase by 75% under the same conditions of time, temperature and concentration of precursors

Introduction

In 2010, Millange and co-workers reported the first *in-situ* diffraction study on the crystallisation of different MOFs (CuBTC, MIL-53(Fe), and MOF-14) under hydrothermal conditions.[1,2] The authors emphasized the importance of *in-situ* methods, the necessity of tackling more complex MOF systems, and the use of combined techniques that allow crystallisation to be followed over several length scales. Diffraction data provide information about crystalline phases; however, important primary processes, such as reactions occurring in solution or gel formation stages and nucleation, cannot be directly probed.[3-5]

In this chapter, we will discuss the first *in-situ*, combined medium- and wide-angle scattering (MAXS/WAXS) study on the crystallisation of two topical metal–organic frameworks synthesized from identical inorganic and organic precursors, NH_2-MIL-101(Al)[6] and NH_2-MIL-53(Al).[7,8] These two structures differ in the connectivity of the metal nodes and organic linkers: The former contains supertetrahedral (ST) building units formed by 2-aminoterephthalate ligands and trimeric Al^{III} octahedral clusters, whereas the latter consists of $AlO_4(OH)_2$ octahedra connected by the same linker. X-ray scattering is shown to be an indispensible tool for studying the synthesis process of zeolites and zeotypes,[9-12] mesoporous materials,[13] nanoparticles and colloids,[14] and interfaces.[15] This approach is especially valuable when combined with other methods such as XRD, NMR, X-ray absorption, and Raman spectroscopy.[16-19]

Experimental

Synchrotron analysis

Time resolved medium- and wide-angle x-ray scattering (MAXS/WAXS) experiments were performed at beamline BM16 of the European Synchrotron Radiation Facility, ESRF (Grenoble, France), equipped with Roper Scientific CCD camera PI SCX90-1300 mounted on a Newport RV240PE goniometer, and X-Ray Research marCCD detector for WAXS and MAXS/MAXS measurements, respectively.

With the high-intensity synchrotron radiation and position-sensitive detectors, we were able to collect MAXS and WAXS patterns simultaneously with an excellent signal to noise ratio, at every twenty seconds at different points of the crystallisation cell. The data were normalized for

the intensity of the X-ray beam and corrected for detector sensitivity prior to background correction. The background scattering from the solvent (DMF or water) at the given reaction temperature was subtracted.
An in-house developed synthesis cell was used for the experiments (Figure 3A.1). In this cell, the synthesis solution is loaded between two mica windows (10 mm diameter) separated by PTFE spacers (1.5 mm thickness). Heating was provided by four electrical cartridges and temperature was controlled at the external wall of the PTFE inserts.

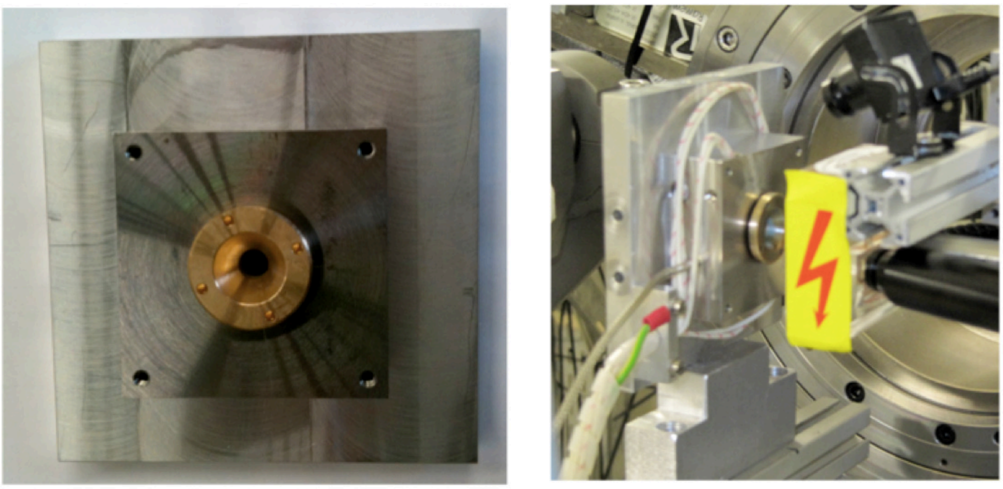

Figure 3A.1 *In-situ* X-ray Scattering measurement cell, left: backside, right: in operation at DUBBLE @ ESRF

Synchrotron analysis
Aluminium chloride ($AlCl_3 \cdot 6H_2O$, Fluka, purum p.a.), amino-terephthalic acid (Aldrich, 99%) and DMF (Sigma, 99.8% anhydrous) were used as received. Metal and organic precursors were first dissolved in DMF or water and then the solutions were mixed. After vigorous stirring for 5 min, 0.1 ml aliquot was transferred to the in situ cell, which is then heated to 130°C. For the experiments described in the main text the following concentration of the precursors were used.

Reaction products/Solvent	**$AlCl_3.6H_2O$ (g) : Solvent (ml)**	**2-aminoterephthalic acid (g) : Solvent (ml)**
NH_2-MIL-101(Al) / DMF	0.507 / 15 (DMF)[a]	0.564 / 15 (DMF)[a]
NH_2-MIL-53(Al) / H_2O	1.97 / 10 (H_2O)[b]	1.5 / 10 (H_2O)[b]
NH_2-MIL-53(Al) / DMF: H_2O = 0.70 : 0.30	1.97 / 6 (H_2O)[b]	1.5 / 14 (DMF)[b]
NH_2-MIL-53(Al) / DMF: H_2O = 0.90 : 0.10	1.97 / 2 (H_2O)[b]	1.5 / 18 (DMF)[b]
NH_2-MIL-53(Al) / DMF: H_2O = 0.95 : 0.30	1.97 / 1 (H_2O)[b]	1.5 / 19 (DMF)[b]
NH_2-MIL-53(Al) & NH_2-MIL-101(Al) / DMF	1.97 / 10 (DMF)[b]	1.5 / 10 (DMF)[b]

Table 3A.1: [a]: referred as to “low concentration of precursor” in the main text, [b] Referred to as “high precursor concentration”.

Kinetic modelling of Bragg-peak evolution
Analysis of the kinetic profiles was performed using the model developed by Gualtieri[20] and applied by Millange et al.[1] for the formation of several prototypical MOFs. This model is based on decoupling the nucleation and crystal growth processes. The extent of crystallisation (*C*) with time (*t*) can be simulated according to the following equation:

$$C = \frac{1}{1+\exp\left(-\left(\frac{t-a}{b}\right)\right)}\left(1-\exp\left(-\left(k_g t\right)^n\right)\right) \qquad \textbf{Eq. 3A.1}$$

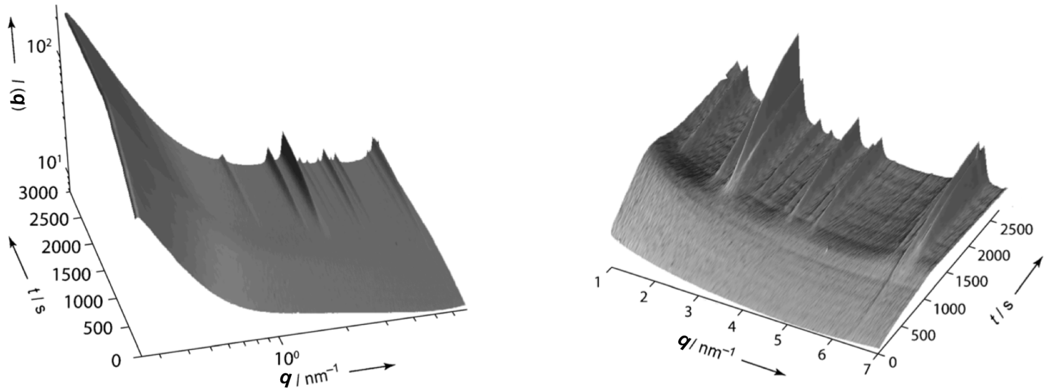

Figure 3A.2 left: time-resolved MAXS data recorded during crystallisation of NH_2-MIL-101(Al) at 403 K using DMF as solvent and low precursor concentrations ; b) Q = 1-7 nm^{-1} region of {left} focusing on the developing Bragg peaks.

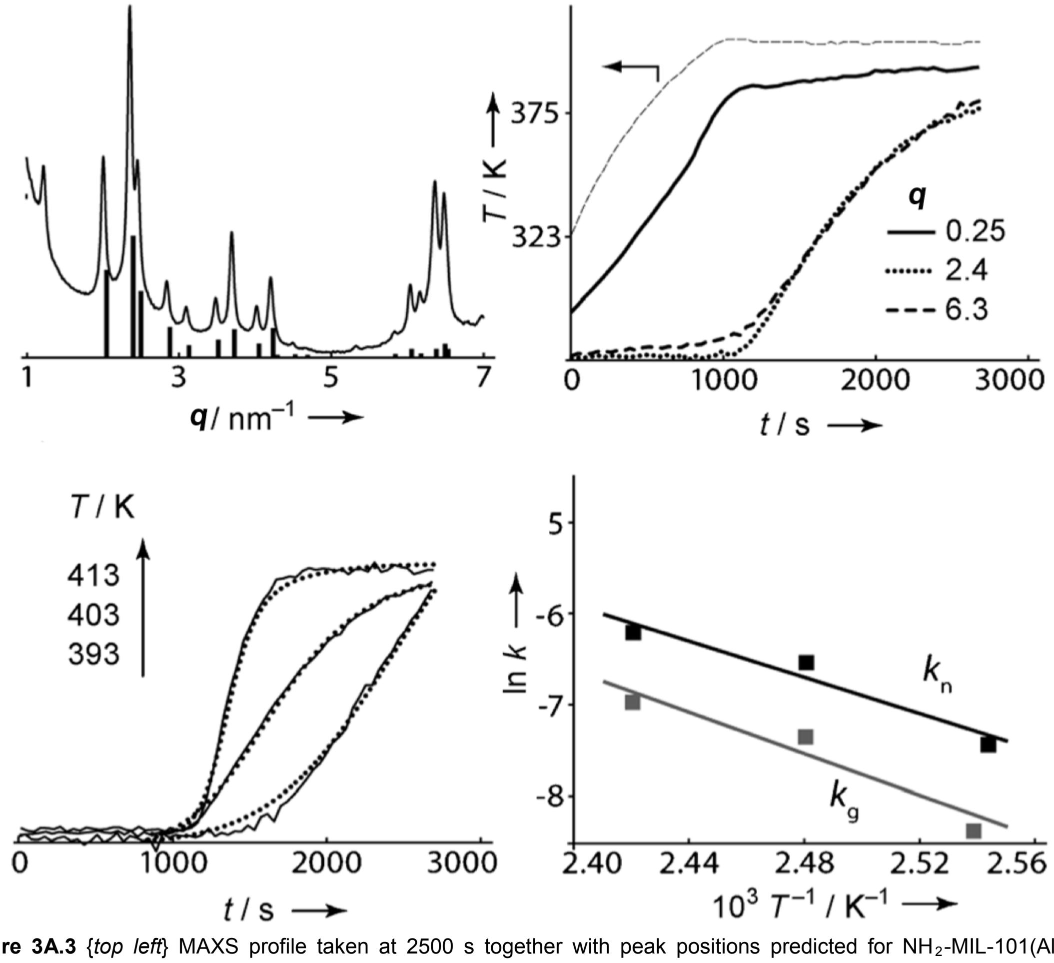

Figure 3A.3 {*top left*} MAXS profile taken at 2500 s together with peak positions predicted for NH_2-MIL-101(Al) structure (sticks) calculated from the data from references;[7-12,16-19,21-23] {*top right*} development of the scattering at different Q values. The Bragg peak at 6.3 nm^{-1} emerges earlier than the one at 2.4 nm^{-1}. The temperature profile in the in situ cell is represented on the vertical axis; {*down left*} experimental (solid) and calculated (smooth, dotted) profiles of the development of Bragg peak at Q = 2.4 nm^{-1} recorded at different temperatures. The Gualtieri model (vide supra) was used for kinetic fitting, {*down right*} Arrhenius plots for nucleation and crystal growth rate constants k_n and k_g.

Fitting a kinetic curve with this expression yields the parametrisation of a, b and k_g (growth rate constant) and indirectly the nucleation rate constant, $k_n = 1/a$. In this work, as inferred from MAXS data evaluation, and as suggested earlier by Millange *et al.*[1] it is assumed that MOF crystals grow in three dimensions (n=3) and that nucleation is heterogeneous (b = 15).

Results

The scattering patterns recorded during the formation of NH_2-MIL-101(Al) at 403 K are shown in Figure 3A.2. Scattering at low Q values (< 1 nm^{-1}) develops immediately at the start of heating, well before the formation of most Bragg peaks. The obtained diffraction pattern corresponds to the NH_2-MIL-101 structure (Fd3m, cubic, a = 88.87 Å; [21,22] Figure 3A.3 {top left}). Increasing scattering at low Q-values is likely to be due to the formation of amorphous primary particles that subsequently assemble into crystalline structures. Remarkably, the reflection at Q = 6.3 nm^{-1}, corresponding to a d-spacing of 9.7 Å, develops first. It exhibits a high multiplicity factor of 72: 24 sets of {119} planes and 48 sets of {357} planes, contributing to this reflection. From the FWHM of the reflections, the size of the first crystallites was estimated to be about 60 nm, increasing to about 90 nm after 2500 s. Intensity at low Q remains constant in the remaining stage of the synthesis owing to the cumulative scattering by particles of different sizes and due to scattering by imperfectness of the crystals (such as defects and voids).

Figure 3A.3 {top right} shows normalized crystallisation curves produced by integration of the Bragg peak at Q = 2.4 nm^{-1} (plane 357) recorded at different temperatures. Analysis of the kinetic profiles was performed using the model developed by Gualtieri[20] and applied for the MOF formation.[2] This model (vide supra) allows for decoupling the nucleation and crystal growth processes. The fitting of the kinetic profiles (Figure 3A.3 {down left}) yielded nucleation and growth rate constants, k_n and k_g, which are given in Table 3A.1. From the Arrhenius plot (Figure 3A.3 {down right}), activation energies for nucleation and growth were found to be (82 ± 4) and (94 ± 6) kJ mol^{-1} respectively, which is in the range of values reported previously for HKUST-1 and MOF-14.[2]

***T* / K**	**k_g (10^{-4} s^{-1})**	**k_n (10^{-4} s^{-1})**
393	2.3	5.8
403	6.3	14
413	9.3	20

Table 3A.1 Crystal growth and nucleation rate constants for NH_2-MIL-101(Al) crystallization extracted from the fitting of experimental profiles recorded at different temperatures. Syntheses were carried out in DMF with low precursor concentrations. All rate constants are determined with ±10% accuracy.

To obtain further insight into the factors governing crystallisation, the influence of the synthesis conditions was investigated. Either the increase of concentration of the precursors or replacing DMF by water as solvent leads to the formation of a different topology, namely NH_2-MIL-53(Al).[8] Figure 3A.4 shows the scattering patterns obtained during the crystallisation process. Similar to the above case, formation of primary particles could be detected from the scattering at low Q, which appears without any detectable induction period (3A.4, top left). MAXS data shows development of the Bragg peak at Q = 6.2 nm^{-1} that is characteristic of NH_2-MIL-53 (I*mma* (no. 74), orthorhombic, a = 6.9, b = 17.6, c = 12.1 Å).[24] It should be noted that owing to the higher concentrations of 2-aminoterephthalic acid and its low solubility, the linker is not dissolved completely in water at room temperature, leading to turbid solutions. This is also seen in the WAXS patterns (see 3A.4, bottom right), where Bragg reflections of the linker can be observed at early times; these features disappear upon dissolution of the linker.

To study the observed substantial solvent effect, the synthesis of NH_2-MIL-53(Al) was performed in DMF/water mixtures. As slow dissolution of the linker can significantly hinder the rate of MOF formation, we adjusted the DMF concentration to fully dissolve the precursors

(DMF/H_2O = 0.70:0.30). This synthesis resulted exclusively in the formation of the MIL-53 framework (Figure 3A.5, {top left and top right}). As anticipated, the growth rate constant increased up to tenfold (Table 3A.2). The nucleation rate constant remained unchanged and significantly higher than that determined for NH_2-MIL-101(Al). A further increase of the DMF/water ratio resulted in the decrease of both k_g and k_n.

Strikingly, when the synthesis was carried out in DMF, both MIL-53 and MIL-101 phases could be observed. Curiously, we identified a broad Bragg peak at Q =6.3nm^{-1}, which appears almost instantaneously from the start of the synthesis (Figure 3A.2 {right}). The structure of the intermediate phase formed prior to the crystallization of MIL-53(Fe) was reported[1] and identified as an analogue of MOF-235,[25] which is composed of Fe^{III} trimers linked by terephthalate linkers in a structurally similar fashion to MIL-101. The main Bragg reflection of this structure is predicted to appear at a *d*-spacing of 9.4 Å, corresponding to Q = 6.3 nm^{-1}.

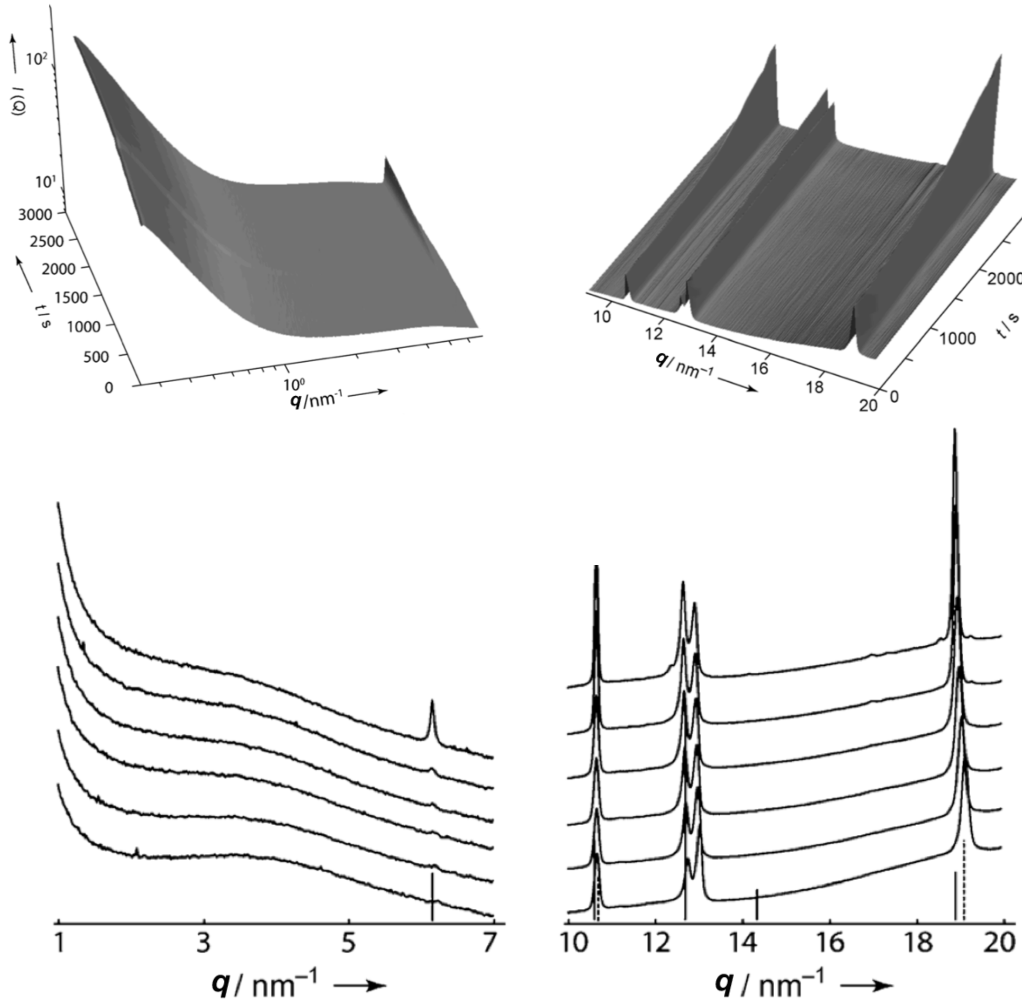

Figure 3A.4 Time-resolved MAXS {*top left*} and WAXS {*top right*} patterns showing the development of the scattering during NH_2-MIL-53(Al) crystallisation at 403 K using water as solvent and at high precursor concentrations; {*bottom left, bottom right*} patterns recorded every 200 s, together with the Bragg reflection positions, for NH_2-MIL-53 (solid sticks)[24] and the 2-aminoterephthalic acid linker (dashed sticks). The doublet reflection at Q = 12.5–13 nm^{-1} that overlaps with the Bragg peaks originates from the mica windows.

Above findings enable for identification of the major events taking place during M^{3+}/terephthalate MOF crystallization. The hypothetical chain of events is displayed in a scheme in figure 3A.6. This scheme is prone to refinement and leaves several questions unanswered, all of which are treated in **chapter 3B** and **3C** in this thesis, but does provide the main lines of the formation pathway for the complete system. The scheme reads as follows: when DMF is present as solvent or co-solvent, formation of the disordered MOF-235 phase rapidly occurs in the intermediate temperature regime. This phase appears to be kinetically favored. In pure DMF, the assembly of MOF-235 clusters into a MIL-101 phase follows as temperature rises. This is a rate-limiting step, as the nucleation rate for MIL-101 is concentration-independent (compare Table 3A.1 and table 3A.2 for results at the same temperature). In DMF/water mixtures, NH_2-MIL-53(Al) crystallisation takes place at high temperatures. In the presence of water, the MIL-235 phase is hydrolyzed as temperature rises and MIL-53, the thermodynamically favoured phase, is formed. A larger amount of DMF in the

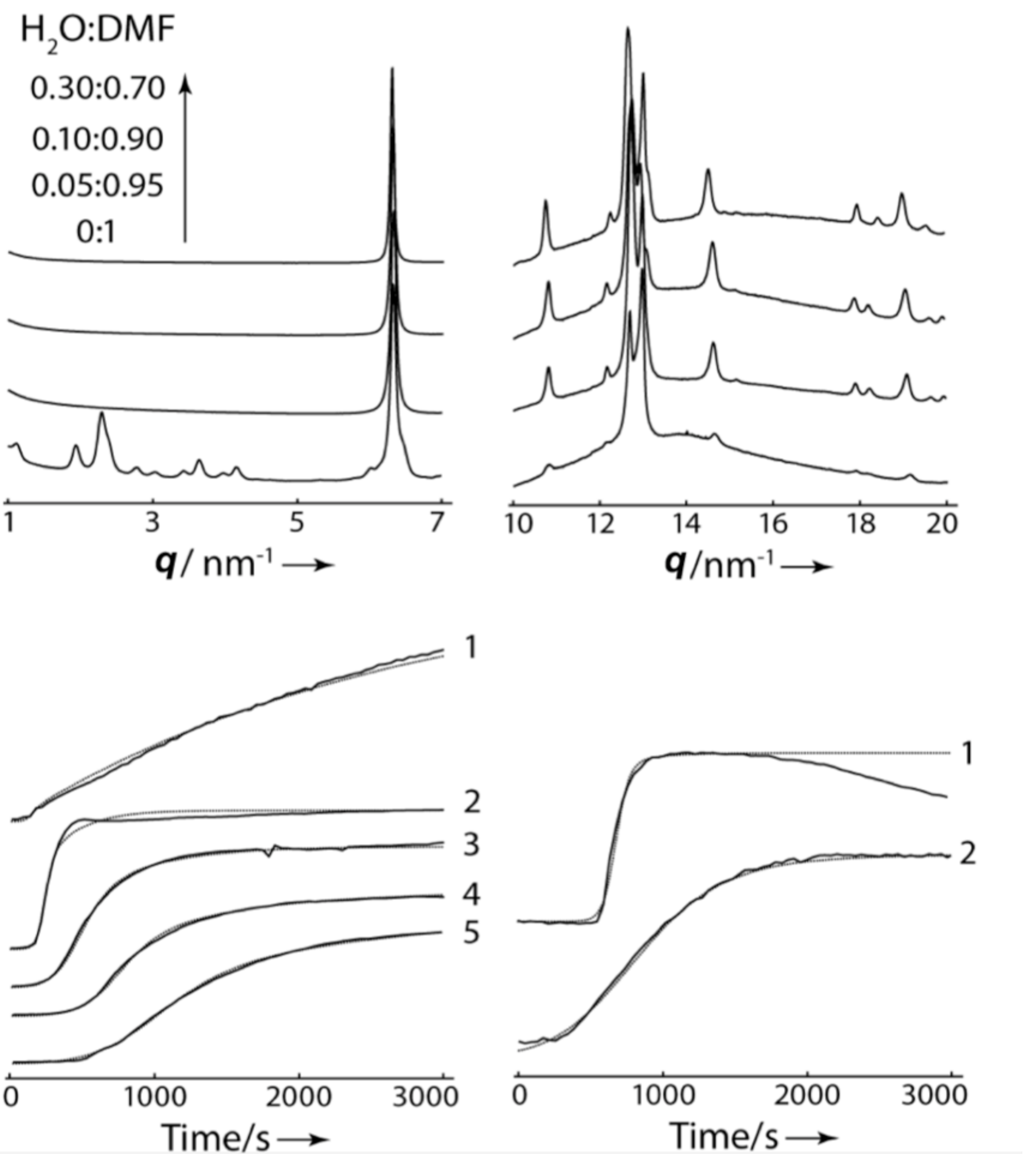

Figure 3A.5 Top, MAXS (*left*)/WAXS(*right*) profiles taken during crystallization in various solvent mixtures. Note the formation of the NH_2-MIL-101 phase in pure DMF, *bottom left*: temporal development of the MIL-53 Bragg peak at Q = 6.5 nm^{-1} with H_2O/DMF ratios of 1) 1:0, 2) 0.30:0.70, 3) 0.10:0.90, 4) 0.05:0.95, and 5) 0:1; *bottom right*: temporal development of the MIL-101 Bragg peak at Q = 2.3 nm^{-1} in DMF at 1) high and 2) low precursor concentrations. The Gualtieri model was used for kinetic fitting. Note that t = 0 for kinetic fitting (smooth lines in {*bottom left*} and {*bottom right*}) is chosen when the temperature reaches 90% of the setpoint.

Solvent composition (H_2O:DMF)	Product	k_g / 10^{-4} s^{-1}	k_n / 10^{-4} s^{-1}
1 : 0	NH_2-MIL-53(Al)	1.2	45
0.3 : 0.7	NH_2-MIL-53(Al)	14	43
0.1 : 0.9	NH_2-MIL-53(Al)	7.0	23
0.05 : 0.95	NH_2-MIL-53(Al)	4.1	14
0 : 1[a]	NH_2-MIL-53(Al)	2.7	11
0 : 1[a]	NH_2-MIL-101(Al)	13	15

Table 3A.2 Crystal growth and nucleation rate constants for NH_2-MIL-53(Al) and NH_2-MIL-101(Al) crystallisation in different solvent mixtures at 403 K. These syntheses are all performed using the high precursor concentrations, [a]: both phases are observed during synthesis.

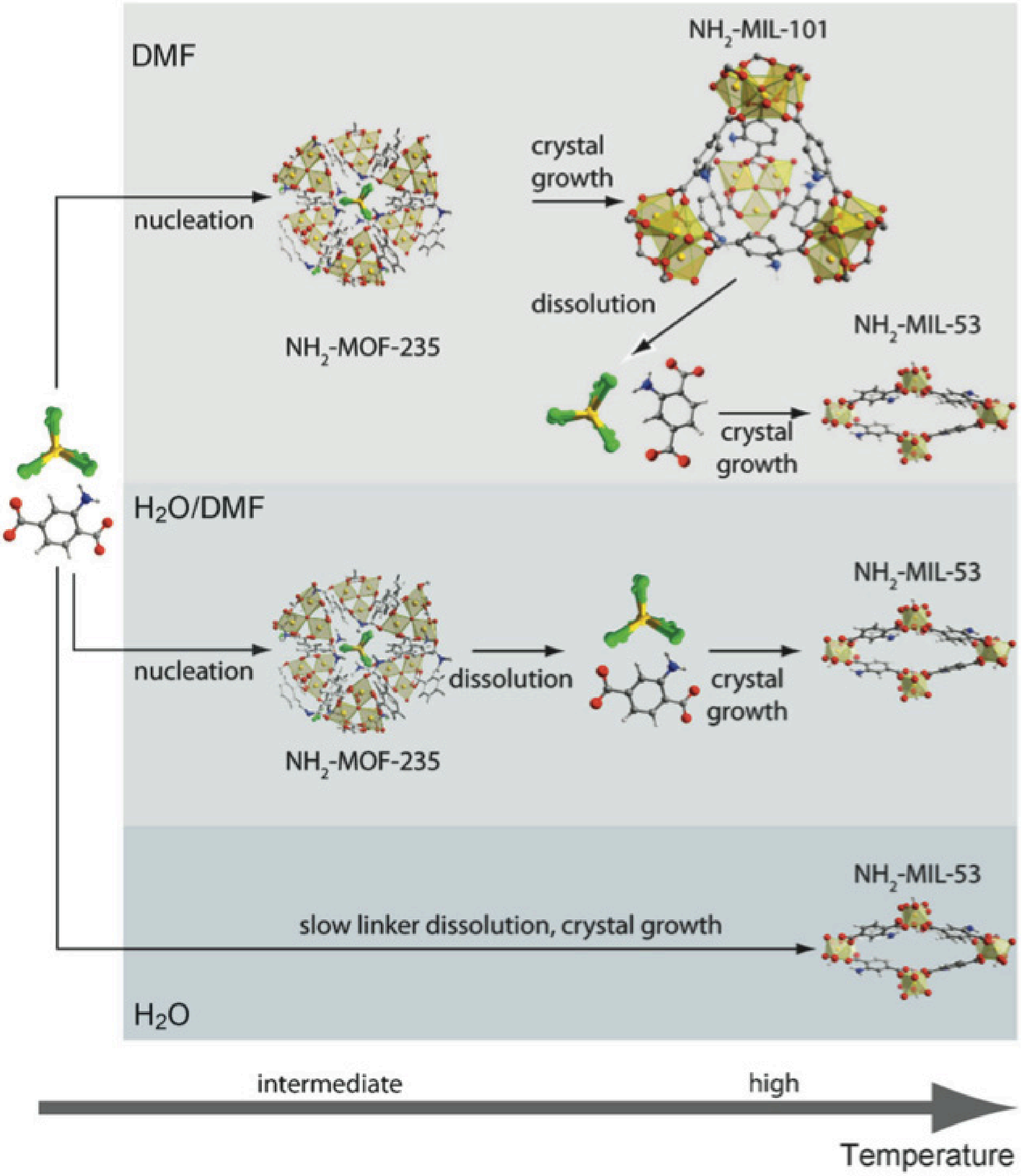

Figure 3A.6 The sequence of events during the crystallization of NH_2-MIL-101(Al) and NH_2-MIL-53(Al) in different media: Low precursor concentrations (DMF); high precursor concentrations (H_2O/DMF or H_2O). C grey, H white, N blue, O red, Al yellow, Cl green. $AlCl_3$ is depicted in a simplified manner.

synthesis is seen to favour formation of MOF-235. At this phase of the research, we attributed this observation to increased solubility of the linker in the solvent system, increasing availability of the building blocks in the media, thus favoring MOF-235. Later, we found out that DMF, as terminal ligand in comparison with H_2O, also favours synthesis of μ_3-O-centered Al_3 building blocks, which form MOF-235. This will be treated in detail in **Chapter 3C**.

Another observation of importance is that the relation between growth and nucleation constants follows E_a (growth) > E_a (nucleation), which is opposite to that observed for other MOFs.[2] This implies that in overall crystallisation the end product formation (MIL-101 and/or MIL-53) from MOF-235 is rate-determining. Higher nucleation rate constants (Table 3A.1 and Table 3A.2) also indicate that crystal growth is the limiting step.

To further corroborate involvement of the NH_2-MOF-235(Al) as the intermediate product, we successfully isolated and characterized this phase quenching the synthesis at intermediate temperatures. The position of the most intense XRD reflection agrees with the one found in the *in situ* experiments. Figure 3a.5 {*down right*} also indicates that at high precursor concentrations, the MIL-101 phase decomposes over time, accentuating that (at least for aluminium) MIL-53 is the thermodynamic product. This result is not necessarily extended to transition-metal based analogues of MIL-53 and MIL-101, in which bonding is different, as treated in **Chapter 2**.

Conclusions

From the analysis of X-ray scattering data on different length scales, the chain of events leading to the formation of several MOF phases synthesized from identical precursors has been clarified. Our findings underline the complexity of the process and the multitude of factors governing the mechanism. It appears that the stabilization of the NH_2-MOF-235(Al) phase by DMF is essential for the successful synthesis of NH_2-MIL-101(Al), this is confirmed by an *in-situ* NMR study in **Chapter 3C**. Notably, this was also the first time that this metastable phase has been identified for a metal other than iron. Finally, establishing how synthesis conditions direct the formation of a given topology and how these competing phases are assembled may ultimately permit some fine-tuning of synthesis conditions to test and realize the ideas of design in synthesis, including the synthesis of MOF-based coatings or membranes.[26] As an example, based on the kinetic results of this chapter, the eventually determined optimal solvent composition for NH_2-MIL-53(Al) was determined to be DMF : H_2O = 1 : 9, instead of the original synthesis protocol using only H_2O. This led to the yield increase by 75% under the same conditions of time, temperature and concentration of precursors.

3B

A Small-Angle X-ray Scattering study on the growth of MOF crystals

This chapter presents an *in-situ* Small-Angle X-ray Scattering (SAXS) study on the crystallisation of the two topical Metal-Organic Frameworks (MOFs) of **Chapter 3A**, which are synthesized from identical precursors: NH_2-MIL-53(Al) and NH_2-MIL-101(Al). A thorough analysis of SAXS data reveals important phenomena occurring during crystallisation and further unravels the effect of the synthesis solvent. Crystallisation of NH_2-MIL-53(Al) follows two routes: *(i)* through direct hydrolysis of $AlCl_3 \cdot 6H_2O$ in water, and *(ii)* via the intermediate species NH_2-MOF-235(Al), which forms in pure DMF or DMF/H_2O mixtures. In the case of pure H_2O as solvent, formation of NH_2-MIL-53(Al) crystals proceeds through steady growth in all three dimensions. The addition of DMF to the synthesis mixture results in amorphous scattering entities forming very rapidly and subsequently arranging into an intermediate phase, NH_2-MOF-235(Al). In DMF/H_2O mixtures, amorphous precursors develop in rapid fashion with surface fractal character appearing, followed by densification, crystallisation of NH_2-MOF-235(Al) and slow transformation into NH_2-MIL-53(Al). Crystallisation of NH_2-MIL-101(Al) only occurs when pure DMF is used as solvent, and it always proceeds through the formation of the intermediate NH_2-MOF-235(Al). In this case a smooth scatterer surface is observed, with morphology and size constant in time.

Introduction

In-situ scattering techniques are capable of providing detailed information about crystal growth and nucleation, as well as information on crystal size and morphology. The most powerful scattering techniques for this purpose are Small-Angle X-ray Scattering (SAXS) and Small-Angle Neutron Scattering (SANS). Synchrotron SAXS provides high-resolution scattering profiles for systems and events occurring at a wide scale range (1–200 nm). Moreover, simultaneous recording of scattering at small and medium/wide angles (SAXS/MAXS/WAXS) is possible through using multiple detectors. The formation and morphology of particles or crystals, i.e. scattering entities, can then be investigated by SAXS, and their crystalline properties by MAXS/WAXS, both in time-resolved fashion.

Although the number of SAXS based studies on MOFs is small, interesting investigations have been published in recent years. Tsao *et al.* were the first to apply SAXS for the study of MOF systems, more specifically, MOF-5, mainly providing detailed nanostructural information about the material. [27,28] Further topological study, in line with the work of Tsao, was presented by Klimakow *et al*. on mechanosynthesis; the authors extended structural analysis with qualitative use of SAXS.[29] A most interesting work, which attempts at resolving the mechanism of MOF growth, also the scope of this work, was done by Cravillon *et al.*, who studied the formation of ZIF-8 to obtain time-resolved structural information, and demonstrated that nucleation governs the growth of this material.[30]

In this chapter, a thorough analysis is presented of *in-situ* SAXS data supported by simultaneously recorded MAXS data – obtained during the crystallization of NH_2-MIL-101(Al) and NH_2-MIL-53(Al). The formation of MOF precursors and their transformation to small MOF crystals is studied in detail at a length scale of the order 1–70 nm. Several parameters are determined describing particle morphology, i.e. radius of Gyration, Porod volume and surface-to-volume as a function of time, demonstrating that the crystallisation of two phases follows very different chemical and morphological pathways.

Experimental

The experimental conditions and recipes follow those from **Chapter 3A**, but the SAXS measurements were carried out at beamline X9, NSLS, Brookhaven, which utilizes the marCCD SAXS detector and Photonic Science MAXS/WAXS detector. SAXS/MAXS spectra were recorded every 20 seconds. The data were normalized for the intensity of the X-ray beam and corrected for detector sensitivity prior to background correction. The background scattering was subtracted, and the physical parameters, which are discussed below were calculated in MATLAB. MAXS is used to follow crystallization during SAXS analysis.

Theory

Herein, we briefly focus on mathematically deriving the important physical parameters in the experimental set-up.

The definition of scattering vector q is $q=(4\pi/\lambda)\sin\theta$ (dimension in nm^{-1}), where θ is the Bragg angle that is usually used in XRD. The physical meaning of q is that all electrons in a plane perpendicular to q are in phase with respect to incoming light. The location of a particular electron with respect to an electron in the origin (spherical coordinates (0,0,0)) is defined by r. Therefore the phase of the electron is qr and the outcoming *phase factor* as recorded is given by e^{-iqr}, which is the complex representation that is convenient for Fourier Transformation (FT). The magnitude of q is representative for the size of the scattering entities; the typical scale of the scatterer is of the order $2\pi/q$.
Now, the recorded amplitude is the sum of all recorded waves, which in our case is defined using an *electron density* $\rho(r)$, integrated over all three dimensions:

$$A(q) = \iiint dV \cdot \rho(r)e^{-iqr} \qquad \textbf{Eq. 3B.1}$$

This is a Fourier Integral. Mathematically speaking, we need to square the amplitude by multiplying it by its complex conjugate to yield intensity. Physically speaking, only a *pair* of electrons can be responsible for interference, and therefore the diffraction pattern. The result of both interpretations is the same and yields a six-fold integral over two volume elements and two local spaces, with the distance between the electron pair defined as r_1-r_2. Rather than evaluating this integral, every pair of electrons is defined by one single, fictitious point $r=r_1-r_2$. This transformation is a FT in itself, and yields a new relation for $I(q)$:

$$I(q) = \iiint dV\langle\rho(r)\rangle^2 e^{-iqr} \qquad \textbf{Eq. 3B.2}$$

Here, the angular brackets denote the auto-correlation, the summarizing of all electron pairs.

An additional advantage to mathematical simplification is that this –new- electron density is averaged over all electrons in the structure, and is highly characteristic for the morphology of the scatterer.
When we take into account the isotropy in space, the problem becomes one-dimensional in r, and Debye formulated an orientationally averaged term for the phase factor.[31]

$$\langle e^{-iqr}\rangle = \frac{\sin(qr)}{qr} \qquad \textbf{Eq. 3B.3}$$

Then, making use of the absence of long-range order in a solute or dispersed system of scatterers, one measures only fluctuation relative to the background:

$$\eta = \rho - \bar{\rho} \qquad \textbf{Eq. 3B.4}$$

For which:

$$\tilde{\eta}^2 = V \cdot \gamma(r) \qquad \textbf{Eq. 3B.5}$$

that has defined an *auto-correlation* by:

$$\gamma(r) = \langle \eta(r_1)\eta(r_2)\rangle, r = r_1 - r_2 \qquad \textbf{Eq. 3B.6}$$

γ(r) is therefore the average of the two fluctuations occurring at a distance *r* (the distance between the electron pair. This auto-correlation function is very distinct for the geometry of scattering entity. In our case we don't have very well defined crystals and we use the *pair-distance distribution p(r)* instead, which is derived below.
First, one must summarize the simplifications and formulations of eq. 3B.3 to eq. 3B.6, in which the equation for intensity is made one-dimensional in spherical coordinates, the phase factor is simplified by the Debye equation, and electron density is transformed into an auto-correlation which is a deviation from the background and is directly characteristic for the geometry of the scatterer.
One can now write eq. 3B.2 as:

$$I(q) = V\int_0^\infty 4\pi r^2 dr \cdot \gamma(r)\frac{\sin(qr)}{qr} \qquad \textbf{Eq. 3B.6}$$

This functional describes the shape of the intensity decay obtained in the SAXS experiment. The Inverse Fourier Transform of *I(q)* yields the function for *γ(r)*, which by multiplication with r^2 yields *p(r)*, carrying dimension [nm]:

$$p(r) = \frac{r^2}{V}\frac{1}{2\pi^2}\int_0^\infty q^2 dq \cdot I(q)\frac{\sin(qr)}{qr} \qquad \textbf{Eq. 3B.7}$$

The *p(r)* function describes the paired-set of all distances between points within an object, and is used here to detect conformational changes in time within the growing MOF particles.

Before continuing, we must first consider that in order to perform FT analysis, a smooth dataset spanning from 0 to ∞ is needed. Experimental SAXS data have a cut-off at the beam stop at a small *q*-value (the value *q* = 0 can't be measured), plus a nonzero background value at large *q*, resulting in infinite values for the Fourier integral.
The first problem can be solved by extrapolating SAXS data to *q* = 0 by using an approximation derived by Guinier in 1939 for single-particle scattering.[32] The derivation is briefly discussed here. Two major criteria – which are not always met in literature – but which are required for the Guinier approximation to be valid are the following: (1) the particles must be well-separated in solution (2) there scatterer must have a centre of symmetry. In other words, the solution in which the MOF crystallises ought to be (at least relatively) dilute, and the MOF crystals and agglomerates should possess an axis of symmetry. The first criterium is met since – even though not all 2-aminoterephthalic acid is dissolved at the start of synthesis – crystallisation occurs from clear solutions. The second criterium also holds for the NH_2-MIL-53(Al) and NH_2-MIL-101(Al) frameworks, which on average, and to reasonable extent, possess a centre of symmetry.
With condition (1), one can focus on the scattering by a single particle, and condition (2) simplifies the phase factor e^{-iqr}, which has now become real for any orientation, and can be replaced by *cos(qr).* Now, eq. 3B.1, for the amplitude, becomes:

$$A_1(q) = \Delta\rho \int dV \cdot \cos(qr) \qquad \textbf{Eq. 3B.9}$$

Where $\Delta\rho=\rho-\rho_0$, ρ_0 being the scattering from solution. This is implied by condition (1) and *Δρ,* which is independent of *r*, replaces *ρ(r)* of Eq. 3B.1. Now, *cos(qr)* can be expanded via:

$$\cos(qr) = 1 - \frac{(hr)^2}{2} + \cdots \qquad \textbf{Eq. 3B.10}$$

Which leads to the *Guinier Approximation*

$$I_1(q) = (\Delta n_e)^2 e^{-q^2 R_g^2/3} \qquad \textbf{Eq. 3B.11}$$

Where $\Delta n_e = (\Delta \rho V)^2$ and R_g is the *Radius of gyration.*

In the data treatment R_g is used to extrapolate data to $q = 0$.
The second problem, the subtraction of the background and infinite integration can be treated using the approximation for the final slope as derived by Porod.[32] For this, a scaled version of the correlation function is defined, such that:

$$\gamma_0(r) = \frac{\gamma(r)}{(\Delta\rho)^2} \qquad \textbf{Eq. 3B.12}$$

This function was called the *characteristic* by Porod and is analytically derivable for most well-defined, constant morphologies, which opens the door to modeling

This is done to obtain a parameter, $\gamma_0(r)$, which is related to the electronic structure (read: morphology) of the scatterer, and scaled by the electron density difference, which is usually assumed constant. $\gamma_0(r)$ plays an important role in modeling with SAXS, by defining a *correlation length,* but this is not considered in our data treatment, and will not be further considered (the interested reader is referred to the standard works of Glatter & Kratky and Feigin & Svergun). [32,33]

For the *Porod regime* of the decay in SAXS (the higher q-values), $\gamma_0(r)$ can be expanded into a power series

$$\gamma_0(r) = 1 - ar + br^2 + cr^3 \ldots \qquad \textbf{Eq. 3B.13}$$

Now, it is possible to define $\gamma_0(r)$ as the volumetic overlap of a particle and a new particle moved by a distance r. For small r, it is obvious that $\gamma_0(r)$ is determined by the surface of the particle. This leads to the derivation of the fourth power law (see again: Glatter and Kratky), defined as:

$$\frac{S}{V} = \pi \cdot \lim_{q\to\infty} I(q) q^4 / Q^{inv} \qquad \textbf{Eq. 3B.14}$$

Here S/V is the Porod surface-to-volume ratio of the scatterer, and Q^{inv} is the Porod *Invariant.* The latter needs consideration, as it is a fundamental parameter in SAXS. Setting $r = 0$ in $\gamma(r)$ leads to:

$$\gamma(0) = \frac{1}{2\pi^2 V} \int_0^\infty q^2 dq \cdot I(q) = \overline{\eta^2} \qquad \textbf{Eq. 3B.15}$$

The final statement is easily derived from the definition of the auto-correlation (eq. 3B.6), for which:

$$\lim_{r\to\infty} \gamma(r) = 0 \qquad \textbf{Eq. 3B.16}$$

$$\gamma(0) = \overline{\eta^2} \qquad \textbf{Eq. 3B.17}$$

Eq. 3B.16 follows from the fact that, at large electron-pair distances, ‘correlation is lost’, i.e. the average local scattering is equal to the scattering of the background. It must be stated that, although here the limit of r to infinity is taken, in reality, $\gamma(r)$ goes to zero for very finite values that lie well within colloidal dimensions. Eq. 3B.17 follows directly from the definition of the correlation function in eq. 3B.6. The result is important as it means that the integral factor in Eq.3B.15 is only directly proportional to the mean square fluctuation of electron density, meaning that it is fully independent of temperature, crystallinity and/or crystal morphology, and is therefore called the *Porod Invariant* Q^{inv}:

$$Q^{inv} = \int_0^\infty q^2 dq \cdot I(q) \qquad \textbf{Eq. 3B.17}$$

Using this definition, Eq. 3B.11 and Eq. 3B.14 are used to extrapolate the pattern obtained by synchrotron SAXS data (figure 3B.1). Here the power law in Eq. 3B.14 is used to extrapolate the *q*-space to infinity, using $I(q) = x_1 q^{-4} + x_2$. Here, x_1 represents $SQ/\pi V$ while x_2 corrects for incomplete subtraction of the background from experimental data. This data treatment yields a smooth dataset without Bragg peaks suitable for the application of eqs 3B.11 and 3B.14. Functions and parameters that can thus be calculated in this time-resolved experiment are: $p(r)$, R_g, V, and S/V. The first and the third are of most importance in this chapter, and therefore leaves us with the definition of V, the *Porod Volume*. Using the condition that for a single scatterer:

$$I_1(0) = (\Delta\rho)^2 \cdot V^2 = (\Delta n_e)^2 \qquad \textbf{Eq. 3B.19}$$

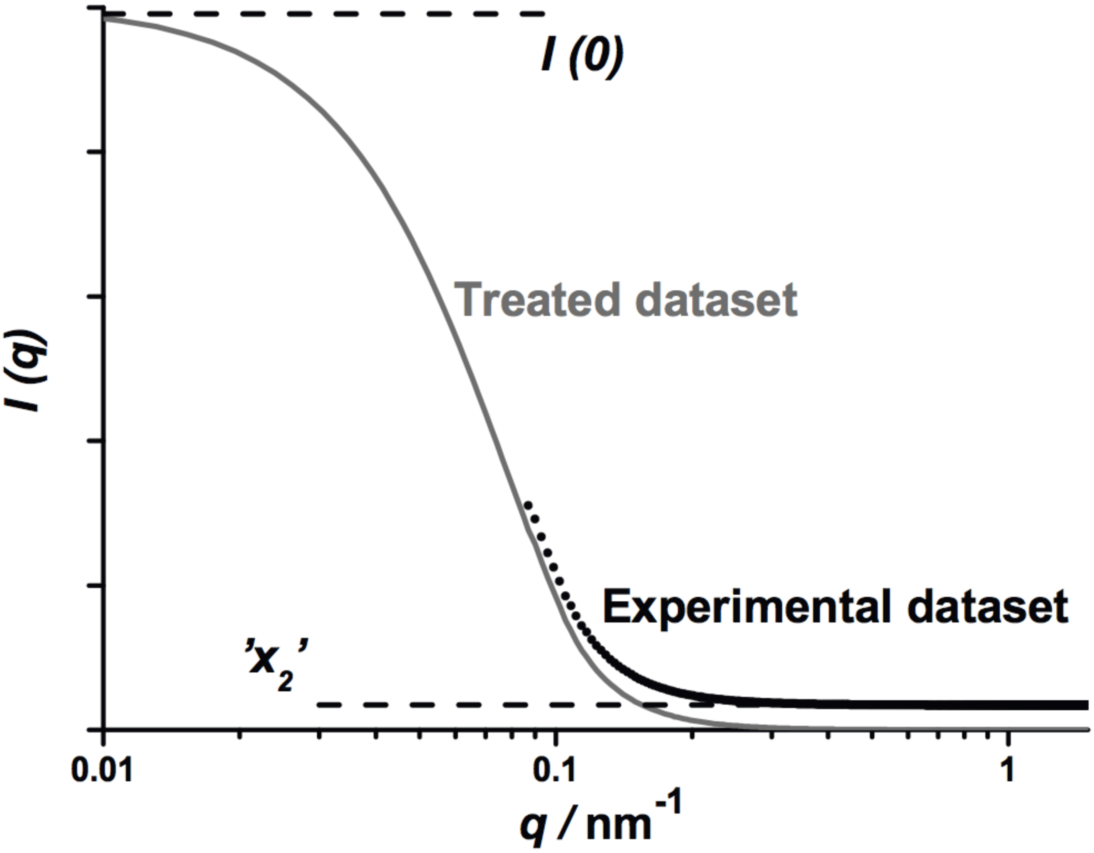

Figure 3B.1 Experimental and treated SAXS dataset of NH_2-MIL-101(Al), in an *I(q) vs. log(q)* plot. The treated dataset (gray) is the same as the experimental dataset, but has additional extrapolated values for *q* going to zero and for *q* going to infinity, background values are subtracted. Values for *I(0)* and background parameter x_2 are indicated.

This is the condition that $I_1(0)$ must be equal to the square of the number of excess electrons presented by the scatterer. From this follows that:

$$Q_1^{inv} = \int_0^\infty q^2 dq \cdot I_1(q) = 2\pi^2 \cdot (\Delta\rho)^2 \cdot V \qquad \textbf{Eq. 3B.20}$$

Here it was used that for a single particle

$$\overline{\eta^2} = (\Delta\rho)^2 \qquad \textbf{Eq. 3B.21}$$

Combination of Eq.3B.19 with Eq.3B.18 yields the expression for the Porod Volume, *V*, of the scatterer:

$$V = I_1(0)/Q_1^{inv} \cdot 2\pi^2 \qquad \textbf{Eq. 3B.22}$$

As it is deduced for a single-scatterer, the same condition as for the radius of gyration holds, in the sense that the equation does not hold well for very densely packed systems of scatterers. When dealing with crystals that do not possess any high aspect ratios, deviation from the fourth power law of Porod might occur when the surface of the scatterer is not smooth. In that case $I(q)$ obeys behaviour of the form q^{6-D_s} with D_s representing the dimensionality of the surface fractal of the scatterer. Power law decay of the form $q^{-\alpha}$ with $\alpha = 4$ indicates a scatterer with a smooth surface. When $\alpha < 4$, one deals with rougher surfaces. As α approaches 3, one deals with surfaces of dominant fractal character. Fractal surface development is an important concept for MOFs, which are built up from smaller building blocks (e.g. trinuclear clusters) that have their influence on full crystal scale. More information on this topic by the author of this thesis can be found in the article by Juan-Alcaniz *et al.* on polyoxometalate templation of metal-organic frameworks.[34]

Apart from this qualitative analysis, the main text of the chapter lays the focus on the calculation of *p(r)* and *V*, in time. These are informative of particle morphology, and size, respectively. Notice that R_g can be calculated from Eq. 3B.11, but can also be deduced from the *p(r)* function in the text, of which it is the value of *r* at maximum.

Results

Fig. 3B.2 {*top*} presents time-resolved SAXS and MAXS data recorded at 130°C during crystallisation using high precursor concentrations in pure water (for the stoichiometric values, see **Chapter 3A**). Under these conditions, only NH_2-MIL-53(Al) is formed, as inferred from the Bragg peak at q = 6.2 nm^{-1} which corresponds to the (2 0 0) plane of NH_2-MIL-53(Al) in its narrow pore form.[35] First evidence for formation of the MIL-53 phase formation can be observed at ~700s. The SAXS decay, as shown in Fig. 3B.2, follows power law behaviour $q^{-\alpha}$ with α increasing from 3.55 to 3.95 with time. These values are typical for growth of porous phases, as described for porous zeolites, indicating two processes, i.e. smoothening of the surface of the scattering particles and densification of the internal structure. [36-38] Porod volume development (Eq. 3B.20), is displayed in Fig. 3B.2 {*bottom left*}. The initial (first 200s) drop in volume is linked to dissolution of residual linker crystallites during temperature stabilization in the crystallization cell. Linker dissolution is followed by steady particle growth occurring in parallel with the development of the (2 0 0) reflection. Crystallite morphology can be deduced from the calculated electron distance distribution function *p(r)* (Fig. 3B.2 {*bottom right*}). The particle size growth is clearly reflected by an increase in scattering, while the maximum electron pair distance gives information about the shape of the particles. NH_2-MIL-53(Al) crystals possess elongated character, in good agreement with the asymmetric curve shape of the *p(r) function*.[32] The intensity grows in time as new crystals are created in a process of continuous nucleation. The maximum of the curve at $r = R_g$ corresponds to the radius of gyration. The highest value of *r* corresponds to the maximum length of the scatterer, i.e. the particle size. The increase in scatterer volume can be associated with nucleative crystal growth, in which the formation of the first primary units is the rate-limiting step.[39] The constant shape of the *p(r)* function with time (SI) is attributed to the fact that during growth, on average, the particle

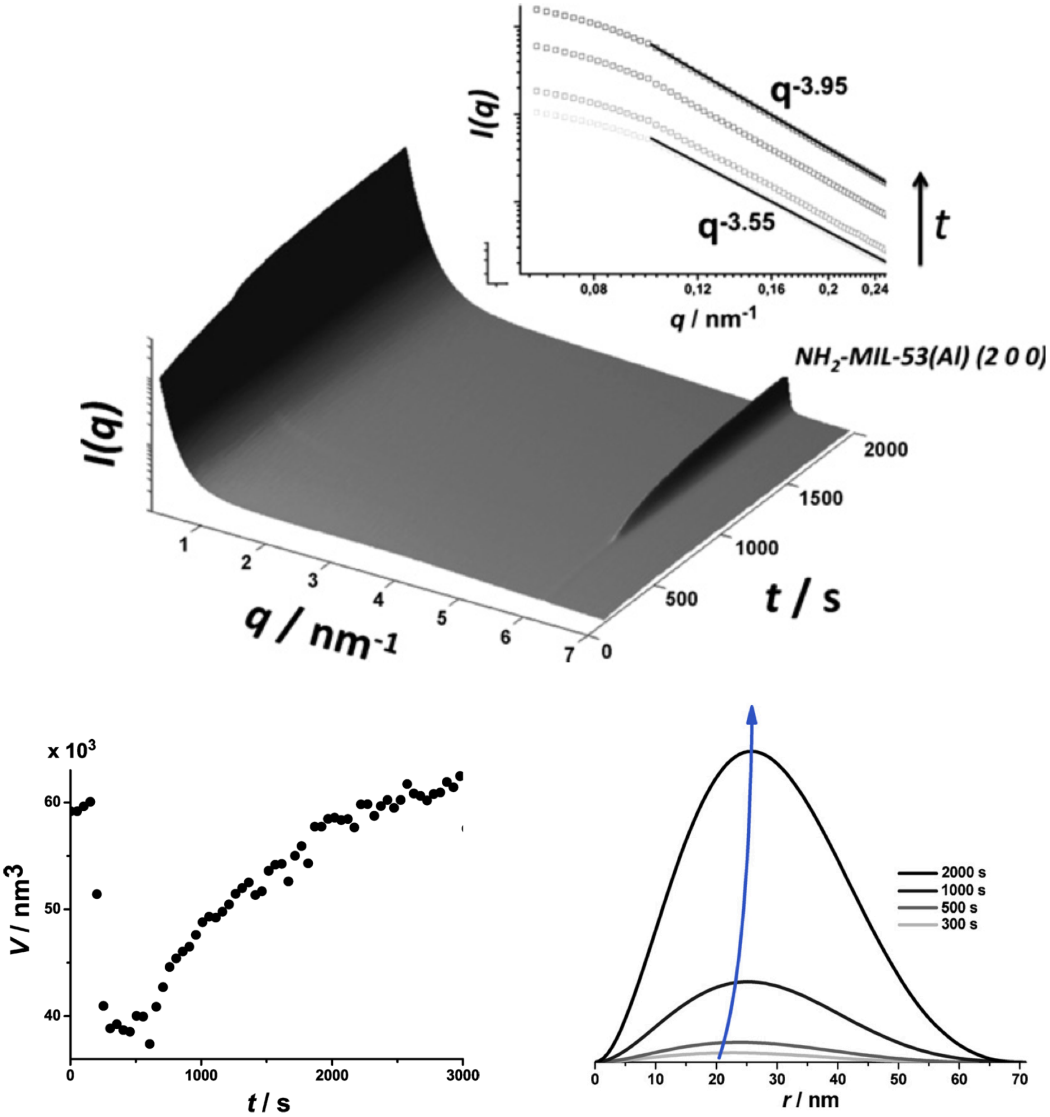

Figure 3B.2 {*top*} Temporal evolution of the MAXS pattern during the in-situ synthesis of NH_2-MIL-53(Al) in H_2O with corresponding SAXS decays in log–log form in the inset at 300s, 500s, 1000s and 2000s, {*bottom left*} evolution of the Porod Volume of NH_2-MIL-53(Al) crystals in time, notice the drop in the beginning, which corresponds to dissolution of 2-aminoterephthalic acid crystals, {*bottom right*} calculated *p(r)* curves for 300s, 500s, 1000s and 2000s

morphology does not change. It is emphasized however, that the average size of crystals observed during our experiments is always smaller than 90 nm because of the detection limits of the detector (the maximum detectable particle size follows $2\pi/q$).

Contrary to aqueous media, synthesis in pure DMF with low precursor concentrations yields the NH_2-MIL-101(Al) phase. The time evolutions of the SAXS and MAXS patterns are shown in figure 3B.3 {*top*}. Before the MIL-101 crystalline planes, with dominant contributions by (111) and (113) planes,[40] start to develop around 500s, evidence for the early formation of NH_2-MOF-235(Al) phase is clearly observed (**Chapter 3A**). Surprisingly, SAXS decay does not vary in time exhibiting a constant slope with $\alpha = 3.8$. This value is indicative for scatterers possessing smooth surface. The Porod Volume development (figure 3B.3 {*bottom left*}) initially displays (little) dissolution of the linker, but thereafter the volume of the scatterers remains constant, in agreement with calculated values for R_g and S/V (see SI). *The p(r) function* – also in strong contrast to MIL-53–shows constant intensity and shape, implying that scattering entities with ~25 nm radius are rapidly formed before the measurements begin, with diffraction peaks of

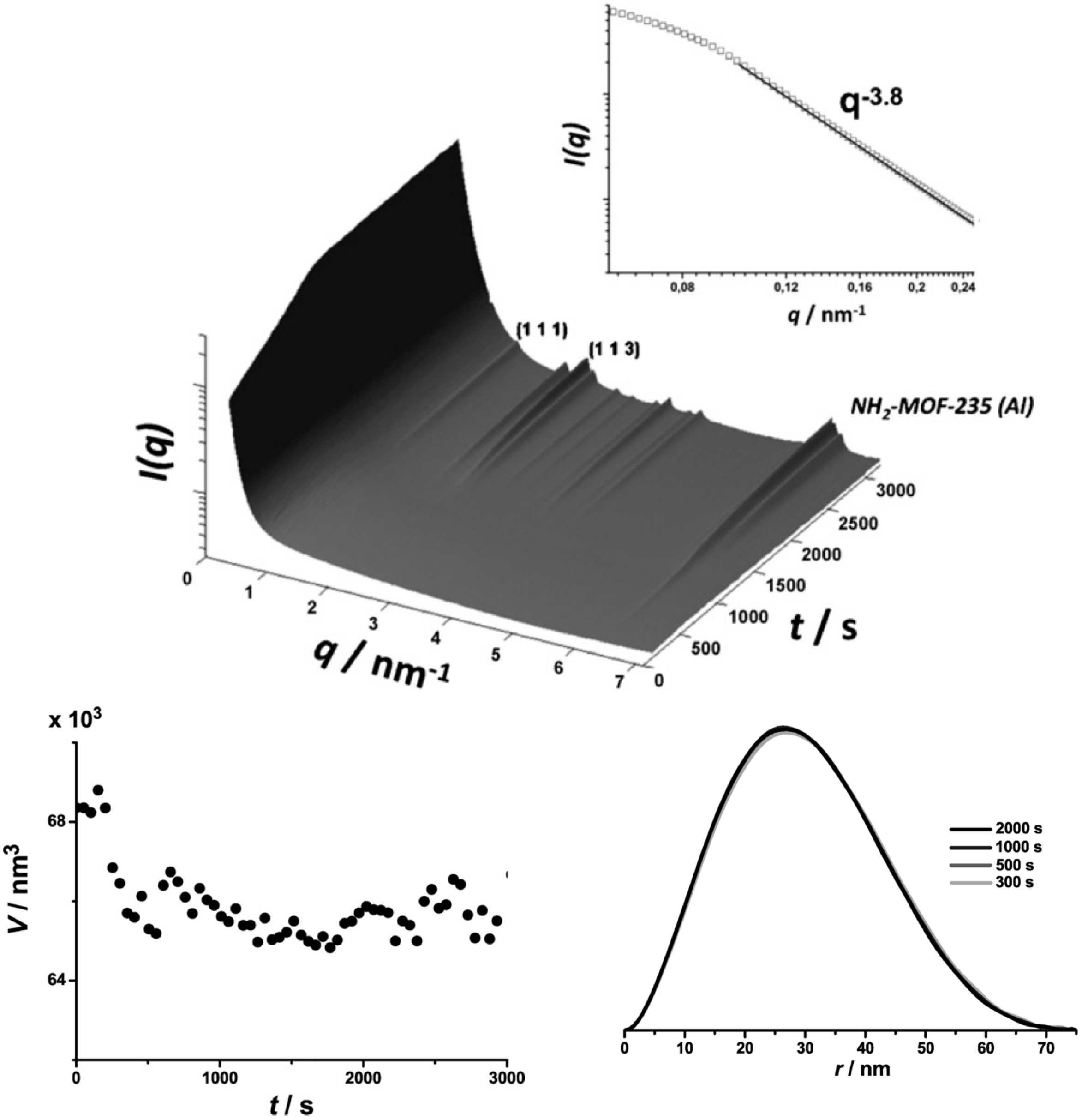

Figure 3B.3 {*top*} Temporal evolution of the MAXS pattern during the in-situ synthesis of NH_2-MIL-101(Al) in dry DMF with corresponding SAXS decays in log–log form in the inset at 300s, 500s, 1000s and 2000s, {*bottom left*} evolution of the Porod Volume of NH_2-MIL-101(Al) crystals in time, {*bottom right*} calculated *p(r)* curves for 300s, 500s, 1000s and 2000s.

NH_2-MOF-235(Al) and NH_2-MIL-101(Al) developing at about 500 s and 1500 s, respectively. Figure 3B.4 {*top*} depicts the evolution in the SAXS and MAXS patterns for syntheses performed in DMF : H_2O = 9:1 mixtures at high precursor concentrations. The Bragg peak of NH_2-MOF-235(Al) is clearly visible, right from the beginning of the synthesis and its fast appearance is ascribed to the higher precursor concentrations.

Decay parameter values initially increase, but then decrease from α = 3.55 to 3.00, pointing

The maximum of the *p(r)* function (Figure 3B.4 {*bottom right*}) increases whilst showing a shif to larger sizes, and then a shift to smaller sizes, pointing again at growth and shrinkage, without undergoing any significant morphologic change. The intensity, i.e. number of scattering entities keeps increasing during this process.

Discussion

The experimental results reported above demonstrate that important information can be extracted from SAXS decays. It has to be considered that we deal with a poorly defined system, from the perspective of scattering entities, and therefore only part of the information obtained from the SAXS pattern is quantitative. That said, SAXS certainly adds value to our previous kinetic analysis of **Chapter 3B** and allows for chemical interpretation of the results, as discussed below.

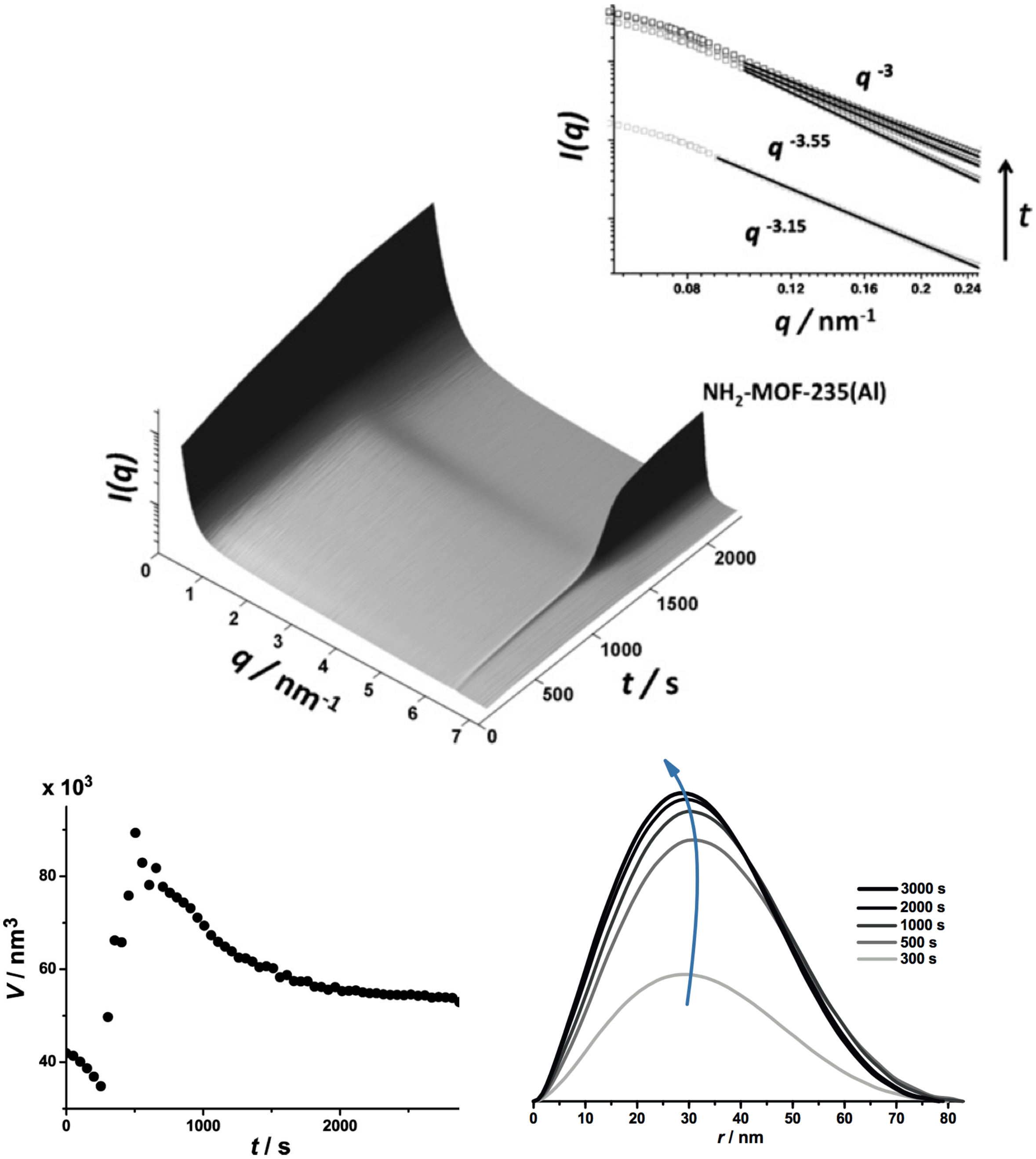

Figure 3B.4 {*top*} Temporal evolution of the MAXS pattern during the in-situ synthesis of NH_2-MOF-235(Al) in dry DMF with corresponding SAXS decays in log–log form in the inset for 300s, 500s, 1000s, 2000s and 3000s., {*bottom left*} evolution of the Porod Volume of NH_2-MIL-235(Al) crystals in time, {*bottom right*} calculated *p(r)* curves for 300s, 500s, 1000s, 2000s and 3000s.

It is herewith proposed that NH_2-MIL-53(Al) forms via hydrolysis of $AlCl_3 \cdot 6H_2O$. The formation of μ_2-OH bridged Al polymorphs via hydrolysis of the hexaaqua aluminium complex in water has been thoroughly studied. [41-44] It is claimed that equilibrium exists between the monomeric complex and the polymers it forms, favouring the former in non-basic solutions. The latter fact explains the relatively low yield and slow kinetics when pure water is used as solvent.[39]

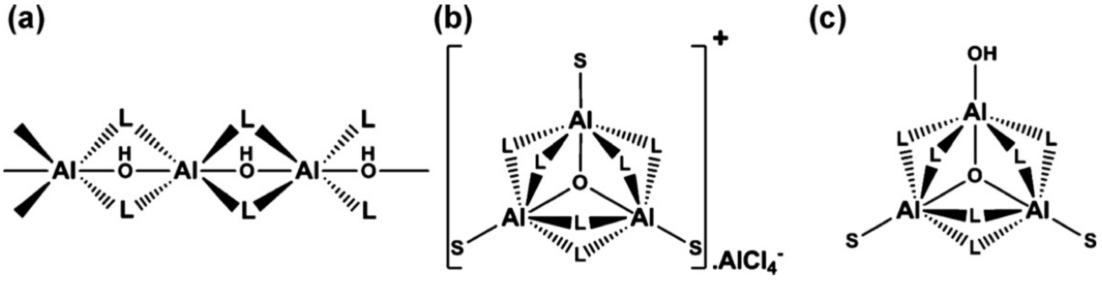

Figure 3B.5 Simplified coordination-chemical representation of aluminium MIL-53(a), MOF-235 (b) and MIL-101 (c) topologies. S denotes solvent and L denotes ligand, in this case 2-aminoterephthalic acid, the metal-ligand bonding is simplified and more extensively shown in **Chapter 3C**.

As expected for this mechanism, in which Al-OH-Al chains steadily grow with 2-aminoterephthalic acid acting as cross-linker, one observes growth dominated by nucleation, densification of the porous phase and smoothening of the crystallite surface in SAXS. A similar nucleation control was earlier reported for ZIF-8,[30] and also observed during the electrochemical synthesis of NH_2-MIL-53(Al).[45]

Whenever DMF is present, the intermediate phase NH_2-MOF-253(Al) appears. This framework consists of μ_3-O bridged, trigonal SBUs. This cluster is well known for *d*-block metals, but was only recently reported for *p*-block metals.[46-48] DMF seems to stabilize this cluster and an immediate result is a change in crystal growth and kinetics in comparison with the synthesis in water. It was already shown by Yaghi *et al.* that DMF acts as terminal ligand for Fe-based MOF-235.[49] This observed solvent-induced stabilization of the phase remained at this point unknown, and will be revealed and discussed in **Chapter 3C**.

With SAXS, we observe unusually fast growth of scattering particles of an amorphous phase. But as these particles then slowly shrink, the phase changes into crystalline NH_2-MOF-235(Al). It is here proposed that the amorphous phase consists of stacked (possibly π-stacked) SBUs which arrange into NH_2-MIL-253(Al) as $AlCl_4^-$ anions diffuse into the voids, balancing the charge of the cluster (figure 3B.5 {b}) and creating the crystalline phase. During this process, the fractal character of the crystals and their roughness increases, as indicated by the change in slope in the SAXS decay (figure 3B.4 {*top*}). NH_2-MOF-253(Al) is then only slowly transformed into NH_2-MIL-53(Al) over a long period of time (+48 h) (**Chapter 3A**). In any case, yield improves tremendously after an extended period of synthesis. It appears that the equilibrium between NH_2-MOF-235(Al) and NH_2-MIL-53(Al) structure is favourable towards the latter.

Pure, dry, DMF has to be used to obtain NH_2-MIL-101(Al). From the perspective of local coordination chemistry, only removing the terminal aqua ligand is required to convert NH_2-MOF-235(Al) into NH_2-MIL-101(Al) (figure 3B.5), which might be the reason for the observation that scatterer volume, morphology and surface are constant in time. This could be rationalized by a crystal rearrangement, rather than a formation–dissolution–formation mechanism as suggested in **Chapter 3A**, figure 3A.6. More evidence for such a solid-state rearrangement will be provided in **Chapter 3C**. The synthesis in anhydrous DMF is unique as it is the only reported route towards NH_2-MIL-101(Al). It seems that only in pure DMF, reaction of the aqua ligand and aluminium tetrachloride anion to form a hydroxyl ligand and hydrochloric acid, is favourable. Enhanced stability of hydrochloric acid in DMF had been demonstrated in literature before,[50] and sparked the study presented in the next part (**3C)**.

Conclusion

In this chapter, synchrotron-based SAXS was presented as method for the *in-situ* study of MOF growth. It was possible to monitor the temporal development of size, morphology (and crystallinity, with MAXS) of two of the important MOF topologies, MIL-53 and MIL-101. Based on the information obtained, description of the formation of these frameworks nears completion. The macroscopic developments on full crystal scale are now documented for the synthesis in water, *N,N*-dimethylformamide and their mixtures. The chemistry behind MOF-235 and its transformation into MIL-53 and/or MIL-101 are discussed in **Chapter 3C**.

3C

Molecular promotion of a MOF topology by an appropriate solvent

In-situ NMR and DFT modeling demonstrate that *N,N*-dimethylformamide (DMF) promotes the formation of metal−organic framework NH_2−MIL-101(Al). It is demonstrated that upon dissociation of an aluminium-coordinated aqua ligand in NH_2−MOF-235(Al), DMF forms a H−Cl−DMF complex during synthesis. This reaction induces a transformation from the MOF-235 topology into the MIL-101 topology. Density Functional Theory (DFT) calculations show that the use of DMF instead of water as the synthesis solvent decreases the energy gap between the kinetically favored MIL-101 and thermodynamically favored MIL-53 products.
DMF therefore promotes MIL-101 topology both kinetically and thermodynamically.

Introduction

The seemingly promotional role of DMF and its interplay with $AlCl_3 \cdot 6H_2O$, which was described at the end of **Chapter 3B**, will be cleared up in this chapter. This is done by carrying out a study at the molecular level, using *in-situ* ^1H NMR and ^{27}Al NMR, supported by DFT calculations. It is seen in this chapter that the role of DMF in synthesis is remarkably versatile; apart from acting as solvent, it is directly involved in promoting formation of NH_2-MIL-101(Al) both thermodynamically and kinetically.

Experimental

In-situ NMR experiments

In-situ NMR spectra were recorded on a Bruker DRX200 spectrometer, operating at ^1H and ^{27}Al NMR frequency of 200 and 52 MHz, respectively. The NMR experiment is in essence a liquid-state experiment, but in order to extend the NMR detectability of larger chemical structures in confined space (such as Al−DMF complexes) that are normally beyond the typical limits of detection in solution NMR, the synthesis solutions were rotated under the magic angle at a sample rotation rate of 1.1 kHz. For these magic angle spinning (MAS) experiments a Bruker 7 mm MAS WVT (wide variable temperature) probe head with temperature was used. The temperature was controlled via a temperature controller. Control proceeds using a heated and cooled nitrogen flow. The temperature controller was calibrated using the melting of polyethylene glycol (61 °C). To contain the pressure buildup at 130 °C, specially designed home-constructed PEEK (polyether ether ketone) inserts with screwable caps were used inside the standard zirconia 7 mm MAS rotors. This PEEK insert was filled with the precursor solution for NH_2−MIL-101(Al), which was prepared in the following way: in one beaker, 0.507 g of $AlCl_3 \cdot 6H_2O$ was mixed with 15 mL of (dried) DMF; in another beaker, 0.564 g of 2-aminoterephthalic acid was mixed with in 15 mL of DMF (this follows the lines of **Chapter 3A**). Both solutions were stirred ultrasonically and then mixed and quickly loaded into the insert.
^1H and ^{27}Al MAS NMR spectra were recorded alternating in time. For ^1H NMR spectra, the number of scans was 16, and the relaxation delay between the scans was 10 s. For ^{27}Al NMR spectra, the number of accumulated scans was 256, relaxation delay was 1 s.

DFT Calculations.

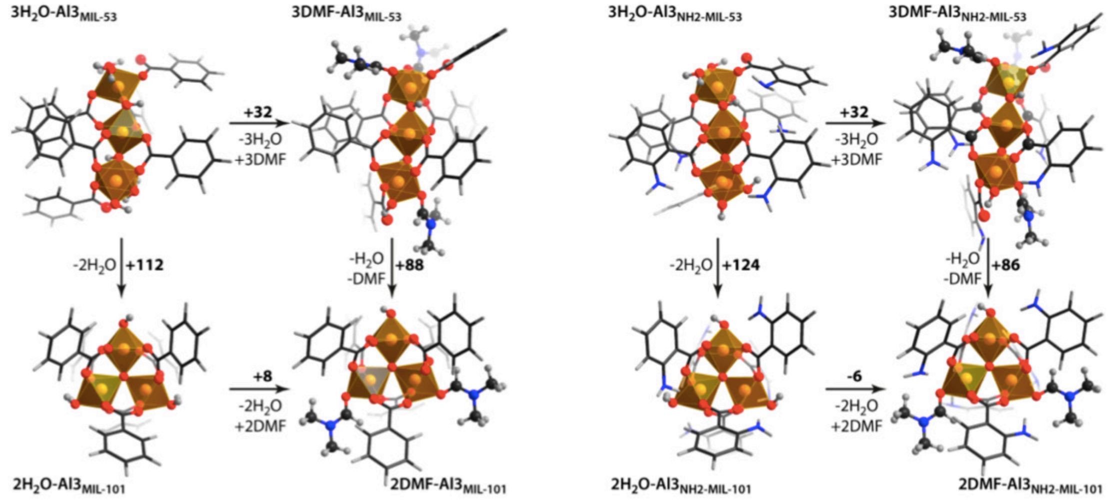

Figure 3C.1 Solvent−ligand-induced transformations of trinuclear Al clusters representing structure-forming units of MIL-53 and MIL-101 topologies. DFT-computed reaction energies are given in kJ/mol above the arrows indicating respective chemical transformations. *Left*: MIL-53(Al) and MIL-101(Al). *Right*: NH_2-MIL-53(Al) and NH_2-MIL-101(Al).

Density Functional Theory (DFT) calculations were performed with the meta-GGA M06 L exchange-correlation functional by Zhao and Truhlar[51] and a full electron *6-31G(d,p)* basis se All calculations were performed with the Gaussian 09 software.[52] The initial structures of MOF precursors were constructed by cutting an appropriate charge-neutral structural motif containing three Al centers from crystal structures of MIL-53 and MIL-101.

Terephthalate and 2-aminoterephthalate ligands were simplified with benzoate and meta-amino benzoate ligands. The octahedral coordination of Al centers in the models was ensured by introducing H_2O or DMF ligands at the unsaturated sites.

Results

In computationally examining the stabilizing role of DMF on the μ_3-O-centered cluster, we built four representative clusters of MIL-53(Al), MIL-101(Al), NH_2-MIL-53(Al), and NH_2-MIL-101(Al). Each cluster contains three aluminium centers and coordinated benzoic and 2-aminobenzoic acid to mimic terephthalic acid and 2-aminoterephthalic acid, respectively. The results of DFT calculations (Figure 3C.1) are in good agreement with experimental observations as they indicate that MIL-53(Al) is the thermodynamically preferred topology in both H_2O and DMF, but stabilization of the linear Al_3 MIL-53 cluster is more pronounced in water. Exchanging the aqua ligands for DMF ligands leads to an increase in energy of 32 kJ/mol. This energy increase is smaller in the case of the μ_3-O-centered Al_3 MIL-101 cluster, 8 kJ/mol, but enough to obstruct formation of MIL-101(Al), which has not been isolated in literature yet at the time of writing. When the amino-functionalized carboxylic acid is considered as the ligand, energetics of the ligand exchange for the MIL-53 clusters remain effectively unchanged (ΔE = +31 kJ/mol), depicted in Figure 3C.1 at the right. However, the exchange of two aqua ligands in the μ_3-O-centered Al_3 NH_2−MIL-101(Al) cluster for two DMF molecules becomes exothermic (ΔE = −6 kJ/mol). The origin of this small but important stabilization is not clear and requires a separate theoretical study.

We thus see that the combination of DMF and the aminated ligand stabilizes the μ_3-O-centered cluster of NH_2-MOF-235(Al) and NH_2−MIL-101(Al), yet it does not explain the transition of the former phase into the latter. An *in-situ* NMR study was performed in order to demystify this. *In-situ* NMR was used only once before in a study on the crystallization of metal−organic frameworks. Haouas *et al.* demonstrated the existence of several intermediate solid phases

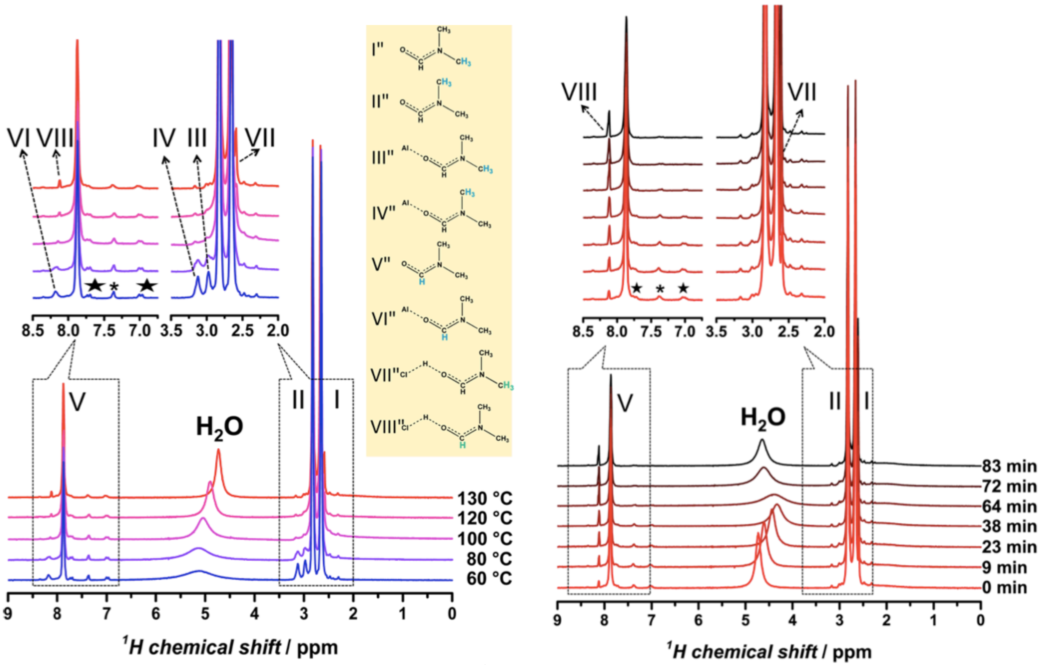

Figure 3C.2 {*left*} Temperature-programmed in situ ^{1}H NMR spectra of NH_2-MIL-101(Al) synthesis. Species are identified in the legend on the right, ★ marks peaks of dissolved 2-aminoterephthalic acid, and ∗ marks a $^{13}C-^1H$ satellite, {*right*} *In-situ* ^{1}H NMR spectra of NH_2−MIL-101 (Al) synthesis at 130 °C, following up on {*left*}.

during the syntheses of aluminium trimesates MIL-96, MIL-100, and MIL-110 and proposed corresponding reaction pathways.[53] *In-situ* NMR is a most powerful tool for the study of small complexes; it can reveal the subtle changes in coordination chemistry around the metal ion during MOF synthesis and is able to clearly identify previously unknown chemical events and/or structures.[54]

In the current case, we must first note that delocalization of the lone-pair electrons in the DMF molecule does not only cause it to preferentially coordinate via its oxygen atom, it also causes the two methyl groups to be chemically nonequivalent, and six signals corresponding to coordinated and uncoordinated DMF are observed in a ^{1}H NMR experiment of a DMF/ $AlCl_3{\cdot}6H_2O$ solution at room temperature.[55] The NH_2−MIL-101(Al) precursor solution shows these six peaks next to a broad water peak, originating from the metal chloride hydrate, as well as small peaks in the aromatic region that belong to the 2- aminoterephthalic acid linker. Figure 3C.2 {*left*} shows the temperature-controlled *in-situ* 1H spectra of the precursor solution as it is heated to the MOF synthesis temperature of 130 °C. A first observation is that the three signals corresponding to DMF coordinated to aluminium vanish as the complex dissociates, and aluminium is left free for coordination to the MOF linker. Linker signals disappear concurrently as the framework crystallizes, and the linker is consumed from the solution. The water signal is seen to shift to a higher field and sharpens strongly during this process. This combination of line sharpening and shift to higher field is a normal observation during the heating of water. It is caused by the weakening of the hydrogen-bonding interactions during the heating process. Protons are as a result more effectively shielded from the magnetic field, causing the upfield shift, with better defined electron density, causing the sharper resonance.[56] An interesting observation is the appearance of two extra visible proton resonances, suggesting the presence of a previously unknown moiety in solution (VII and VIII, Figure 3). Because of the use of $AlCl_3{\cdot}6H_2O$, moiety was soon suspected to be an H−Cl−DMF complex; in literature described as a highly stable species that is readily formed in HCl−DMF mixtures.[57] In support of this claim, additional ^{1}H NMR experiments were carried out on DMF−HCl mixtures to confirm that the additional peaks are indeed caused by this complex.

Figure 3C.2 {*right*} displays the time-resolved development at 130 °C for which we know NH_2−MOF-235(Al) forms almost instantaneously, and NH_2−MIL-101(Al) forms after approximately 25−30 min (**Chapter 3B**). One can first of all see that the concentration of the H−Cl−DMF complex rapidly increases as the solution is kept at 130 °C.

Further, the water signal undergoes several changes. At the early stages at 130 °C, we see that the water signal keeps moving upfield long after the synthesis temperature of 130 °C had been reached. We attribute this effect to the "consumption" of water in solution. Water dissociates into protons and the μ_3-O ligands that make up the NH_2−MOF-235(Al) framework. Integration of the water signal confirms that over the whole time−space, 16% of water is lost, which lies within the expected range of 11−28% (this range is spanned by the terminal aqua ligand parameter. When looking at Figure 3C.2, the minimum assumes that zero terminal (solvent) ligands of the μ_3-O cluster are aqua; ergo all consumed water goes to the μ_3-O ligand. The maximum assumes two terminal ligands of the trigonal cluster are aqua. These extremes correspond to 11.11% and 27.80%, respectively, and the reality lies somewhere in the middle, as confirmed by NMR experiments. We can conclude from the integration that every trigonal cluster has on average 0.58 aqua ligands and 1.42 DMF ligands in this synthesis). The upfield effect can be explained as follows: a lower concentration of water in DMF leads to less pronounced hydrogen bonding between water molecules and a shift to higher fields.

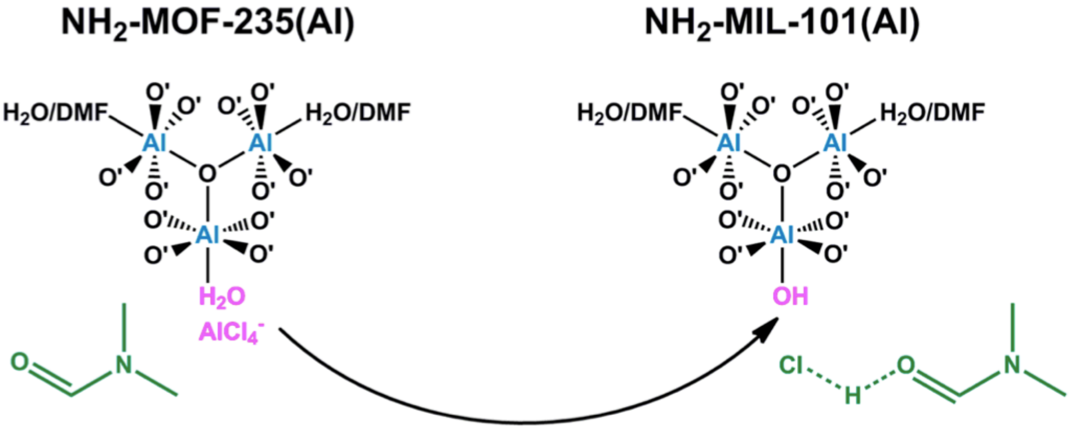

Figure 3C.3 Promoting effect of DMF in formation of NH_2−MIL-101(Al). $AlCl_3$ dissociates and is rapidly taken up in the new framework.

Interestingly, after approximately 30 min, the reverse phenomenon is visible; the water signal broadens, indicating rapid exchange, and promptly shifts to a lower field. This remarkable "shifting" of the water signal was a fully reproducible observation that was eventually rationalised with the help of DFT. Initially proposed was, that the very stable H−Cl-DMF complex molecularly promotes the formation of NH_2−MIL-101(Al). It does so by providing the required hydroxido ligand, which distinguishes NH_2−MIL-101(Al) from NH_2−MOF-235(Al), through a water dissociative mechanism. This reaction would lead to a sudden increase in the concentration of solvated protons, which would explain the observed exchange line broadening as well as the "acidic" downfield shift of the water signal. Such a reaction is usually highly unfavorable, and our DFT study indeed indicated that such a reaction of the form **Cl^- + H_2O + DMF → OH^- + H−Cl-DMF** is strongly endothermic (+272 kJ/mol) due to the insufficient stabilization of the hydroxide anions. However, when considering the exchange of Cl^- by the OH^- anion in the coordination sphere of the Al^{3+} center, which would be the case in an NH_2−MOF-235(Al) to NH_2−MIL-101(Al) rearrangement, energetics are much more favorable (+2 kJ/mol). NH_2−MIL−101(Al) is expected to be the entropically and thermodynamically preferred lattice as the noncoordinate charge separation is eliminated, and this is likely to be the driving force behind the observed transition.

It can thus be stated with confidence that DMF acts as a molecular promoter, providing required hydroxido ligands to selectively form the kinetic MIL-101 phase (Figure 3C.3). Finally, the same in situ NMR experiment was carried out, but for the ^{27}Al nucleus. The ^{27}Al spectrum displays one peak, corresponding to dissolved octahedrally coordinated Al^{3+}, which decays in time as aluminium is consumed during crystallization of the framework. The concentration of Al^{3+} in solution in time was calculated, which is displayed in Figure 3C.4, along with the chemical shift of H_2O. During temperature ramping, aluminium is consumed in the formation of larger structures that are not crystalline yet. This can be concluded from the fact that no Bragg peaks are observed in this time domain of crystallization, though structures carry enough Chemical Shift Anisotropy (CSA) to prevent peaks from occurring in FT liquid-state NMR experiments. From 130 °C onward, Al^{3+} concentration decays steadily. The trend resembles the one of a reactant concentration decaying in a first-order reaction, and this is fitted correspondingly, though rather to provide a guide to the eye than a kinetic rationale. An important result is that the trend is maintained throughout the remainder of the synthesis, including the time domain where NH_2−MOF- 235(Al) rearranges into NH_2−MIL-101(Al).

Discussion and conclusion

Summarizing, we demonstrate that the combination of the amine functionality in 2-aminoterephthalic acid and DMF stabilizes the formation of the μ_3-O-centered cluster that builds NH_2−MOF-235(Al) and NH_2−MIL-101(Al). Furthermore, the role of DMF is very versatile as *in-situ* 1H NMR shows that upon dissociation of an aluminium-coordinated aqua ligand in NH_2−MOF-235(Al) DMF forms a H-Cl-DMF complex during synthesis. The formation of this complex induces a transformation from the MOF-235 topology into the MIL-101 topology because it leaves a terminal hydroxido ligand. This ligand is required for formation of MIL-101. We thus see that a combination of the metal chloride precursor and DMF is required for successful synthesis of NH_2−MIL-101(Al), which fits laboratory observation.

The physical transformation of NH_2-MOF-235(Al) into NH_2-MIL-101(Al) is very interesting. In the preceding **Chapter 3B**, using *in-situ* small-angle X-ray scattering, it was observed that the transformation from NH_2−MOF-235(Al) into NH_2−MIL-101(Al) proceeds without any change in morphology or size of the crystals.[58] As we now see from NMR experiments, the aluminium concentration decays steadily over the entire time domain, and a reaction between a terminal aqua ligand and DMF in the aluminium coordination sphere induces the transformation. We conclude that the (earlier in **Chapter 3A**) suggested hypothesis of a predominating dissolution−recrystallization mechanism should be rejected (although a solid-to-solid rearrangement will involve interaction with the solvent).

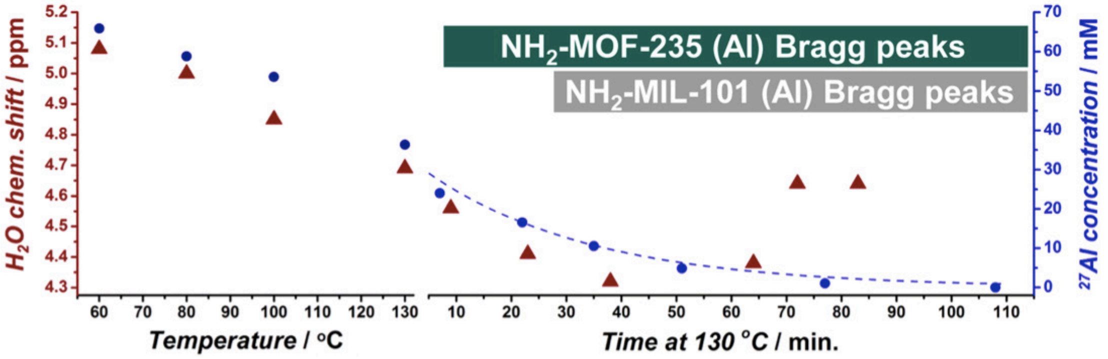

Figure 3C.4 Promoting effect of DMF in formation of NH_2−MIL-101(Al). $AlCl_3$ dissociates and is rapidly taken up in the new framework. The two rectangles indicate the time-space of Bragg peak development of the denoted frameworks, discussed in Chapters 3A and 3B.

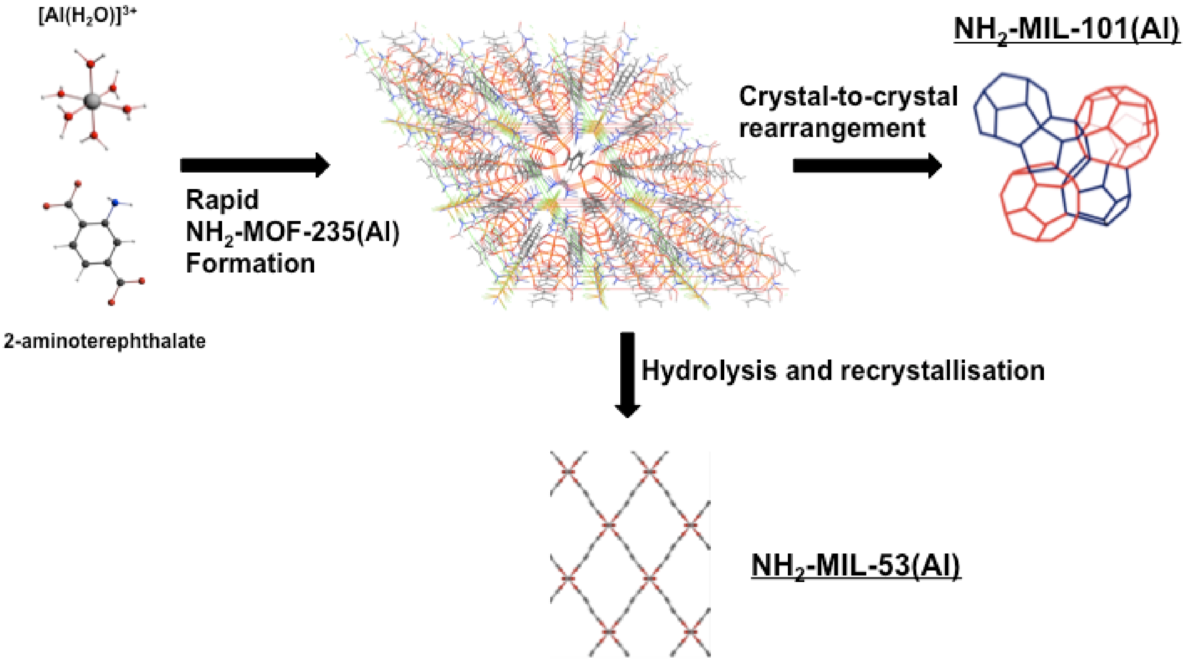

Figure 3C.5 Schematic, concluding view of the formation of NH_2-MIL-101(Al) and NH_2-MIL-53(Al) in DMF and DMF/H_2O respectively: NH_2-MOF-235(Al) forms rapidly in the presence of DMF, after which slow crystal-to-crystal rearrangement takes place in pure DMF, and hydrolysis followed by recrystallization to NH_2-MIL-53(Al) in the presence of H_2O.

The transformation of NH_2−MOF-235(Al) into NH_2−MIL-101(Al) thus occurs in the solid state and is induced by the reaction displayed in Figure 3C.3. Similar types of solid-state transformations have been reported in MOF literature before[59] and owe their existence to MOFs being coordination compounds, in which a process of dative bond breakage and reformation is continuously present (see also: **Chapter 1**).[60] This phenomenon has been associated to the large crystallinity of MOFs in general[61] but also provides the possibility of solvent-assisted ligand exchange,[62] and here, topologic transformations occur within the solid state. NH_2−MIL-53(Al) was earlier identified as the thermodynamic product of the synthesis mixture and is seen to be the only product in syntheses over much longer periods of time. The promoting role of DMF also affects NH_2−MIL-53(Al) synthesis, which is evident from the observation that already small (10%) additions of DMF to the H_2O synthesis mixture of NH_2−MIL-53(Al) yield a 3-fold increase of the latter (**Chapter 3A**). The isolated Al-(μ_2-OH) chains are more efficiently obtained when there is a hydroxido ligand-generating solvent like DMF, yet the solvent is not required to obtain the framework. For NH_2−MIL-101(Al) synthesis, DMF can be seen as an indispensable moiety, which is required to promote the kinetic product.

It is possible that similar solvent-promotional effects can also be observed with other widely used chemicals such as DMSO, which is, among others, also known to form complexes with HCl. A last but important remark is that this work deals with aluminium-based MOFs, and this chemistry is not necessarily to be extrapolated to MOFs based on transition metals. Haouas *et al.* but also Ribas in his textbook on coordination chemistry discussed how similar μ_3-O-based building blocks form easily (*ergo*, early in synthesis) for *d*-metals, but assembly is more complicated when dealing with aluminium (*p*-block) chemistry. Underlying theory for this observation is discussed in **Chapter 2**. That stated, aluminium MOFs are among the most interesting MOF materials due to stability and catalytic inertness from an application point of view, which makes the study on their formation significant.

In conclusion, in this chapter it was shown how the choice of an appropriate solvent can lead to specific MOF topologies and/or large improvements in yield by acting as a versatile promoter in MOF synthesis while demonstrating the power of in situ NMR to unravel underlying molecular mechanisms. Yield and topology dependence on solvents has been commonly observed by other groups, but these are barely explained at the molecular scale in literature. The information presented in this chapter may allow for synthesis of new MOF topologies and/or higher yields of existing ones.

Finally, in figure 3C.5 a definitive, corrected version of figure 3A.6 is displayed of the molecular proceedings, in the presence of DMF. We have seen that only a combination of techniques can lead to the right conclusion.

4

Atomic-to-crystal scale documentation of the growth of ZIF-7 nanorods

In this chapter, an *in-situ* Small- and Wide-angle X-ray Scattering (SAXS/ WAXS) and Quick-Scanning Extended X-ray Absorption Fine-Structure (QEXAFS) spectroscopy study on the crystallization of the Metal–Organic Framework ZIF-7 is presented. In combination with DFT the self-assembly and growth of ZIF-7 microrods together with the chemical function of the crystal growth modulator (diethylamine) are revealed at all relevant length scales, from the atomic to the full crystal size

Introduction

An important aspect of crystal engineering is the ability to control particle morphology. In many cases it allows properties to be tuned without changing the material composition. For instance, the performance of gold or silver nanoparticles for surface plasmon resonance,[63] semiconductor nanodots for quantum confinement,[64] and metal or metal oxides for catalysis[65,66] can be substantially improved through tailoring of the crystal morphology. The morphology and particle size (distribution) of MOFs can be controlled by proper choice of the synthesis conditions. Microwave and electrochemical protocols are powerful synthesis tools for the manufacture of homogeneous MOF nanocrystals, [67,68] whereas the precise use of biphasic synthesis mixtures allows for the shaping of hollow MOF particles.[69] A different method towards controlled particle morphology is the so-called modulator approach. [70-74] Often, monofunctional carboxylic acids, which compete with linkers for coordination to the metal cations, or Brønsted bases such as amines that can directly deprotonate the organic ligand, thereby affecting nucleation kinetics and particle morphology, are used as modulators.[75] Unfortunately, little is known about the detailed mechanism of MOF assembly and even less about the effect of modulators on crystallization and nucleation, thus hampering further systematic progress towards *"crystal design".*

This chapter presents an *in-situ* study on MOF crystallisation influenced by a modulator. By applying SAXS/WAXS *in situ*, the growth of ZIF-7 microrods could be studied over different length scales. SAXS studies on crystal morphology were stretched to the molecular scale with *in-situ* quick-scanning extended X-ray absorption fine-structure spectroscopy (QEXAFS) and Density Functional Theory (DFT). ZIF-7, one of the most promising MOFs for applications in adsorptive separation,[76,77] was selected as the MOF model for this study.

Experimental

Synthesis

Zinc chloride ($ZnCl_2$, Fluka, purum p.a.), benzimidazole (Sigma, 98%), diethylamine (Sigma, 99.5%), and DMF (Sigma, 99.8% anhydrous) were used as received and handled under ambient atmospheric conditions. Metal and organic precursors were first dissolved in DMF before mixing the solutions. To promote crystallization at room temperature, diethylamine (DEA) was added to the synthesis mixture right before starting the experiment. Synthesis solutions were prepared with the molar ratios given in Table 4.1. Experiments in the absence of diethylamine did not result in the formation of ZIF-7 at room temperature.

Synchrotron measurements and kinetic modeling

The conditions for the in situ measurement cell and the kinetic modeling are described in **Chapter 3A** with the equation for the modeling being eq. 3A.1.

SAXS/WAXS measurements

Time-resolved SAXS/WAXS experiments were performed at the X9 beamline at the National Synchrotron Light Source (NSLS) at Brookhaven National Laboratory (NY, USA). The undulator-based X9 at NSLS utilized the marCCD SAXS detector and Photonic Science WAXS detector. The high-flux synchrotron radiation allowed us to collect SAXS and WAXS patterns simultaneously with an excellent signal-to-noise ratio and a 20 s time resolution. The data were normalized for the intensity of the X-ray beam and corrected for detector sensitivity prior to background correction. The background scattering was subtracted.

Solution	**DMF**	**Diethyl Amine**	**Benzimidazole**	**$ZnCl_2$**
1	4.2	3.5	1.5	1
2	4.2	7	1.5	1
3	4.2	14	1.5	1
4	4.2	28	1.5	1

Table 4.1 Molar composition of the different crystallization solutions studied.

QEXAFS

Time-resolved QEXAFS experiments were performed at the X18A beamline at the NSLS at Brookhaven National Laboratory (NY, USA). Beamline X18A is a bending magnet line, which used a home-built Si-(111) channel-cut monochromator and a rhodium-coated toroidal focusing mirror to provide an approximately 1.0 mm (horizontal) and approximately 0.5 mm (vertical) spot size with a flux of approximately $2.5 \bullet 10^{11}$ photons per second at 10 keV. An XAS scan could be completed in 0.5 s with 1000 equally spaced data points, so that either a XANES or a full EXAFS scan with good resolution and quality were obtained.[78] Usually, twelve consecutive scans were averaged after alignment by using the spectra obtained from the Zn foil in the reference ion chamber, recorded simultaneously with those of the sample. Data reduction of Zn K-edge EXAFS data were performed using the computer program Athena 0.8.041.[79] The EXAFS scattering curves were simulated using FEFF included with the Artemis program for the atomic model to determine the number/identity of atoms bonded to Zn in the first coordination shell. Zinc K-edge EXAFS data were processed using the IFEFFIT package. [80,81] Since Zn-O and Zn-N bond lengths are similar, the sum of two contributions is reported. Back-scattering paths and phase corrections were calculated by the FEFF6 program. EXAFS data were Fourier transformed across a q range of 0–12.0 Å^{-1} for an *R*-space fitting between 0 and 5.0 Å, which was conducted in the Artemis program. When fitting the data in Artemis, weighing factors k = 1, 2, and 3 were selected to optimize the fits. When constructing the model, all paths with a computed amplitude of <20% were discarded because these paths were not needed to fit spectral features across the chosen *k*- space and *R*-space fitting ranges. An amplitude reduction factor (*s*) was determined from the analysis of the ZnO EXAFS spectrum.

DFT

Quantum chemical calculations were performed with density functional theory (DFT) using the B3LYP[82] hybrid exchange-correlation functional in combination with the full-electron 6-31+G(d,p) basis set for all atoms. Full geometry optimizations and saddle-point searches were performed using the Gaussian 09 program.[83] The nature of the stationary points was evaluated from the harmonic modes. To account for solvent effects, the polarizable continuum model (PCM) that employed the reaction field with the integral equation formalism model[84] was used during the geometry optimizations and frequency calculations. Standard parameters for DMF solvent as implemented in Gaussian 09 were used. Zero-point, finite temperature, and entropic energy contributions were computed using the results of the normal-mode analysis within the ideal gas approximation at a pressure of 1 atm and a temperature of 298 K. The reaction ΔG^{O}_{298} values were calculated for these conditions.

Results

The WAXS patterns recorded during the formation of ZIF-7 at room temperature are shown in Figure 4.1. Diffraction patterns obtained correspond to the ZIF-7 structure (trigonal, R3 (148), *a*=22.9(3), *c*=15.8(3) Å; *c/a*=0.7). Figure 4.2 shows normalized crystallization curves produced by integration of the most intense Bragg reflection at Q = 5.1 nm^{-1} (plane {-120}) recorded at different amine concentrations. Analysis of the kinetic profiles using the Gualtieri model yielded the nucleation and growth-rate constants, k_n and k_g, respectively, given in Table 4.2 (*next page*). The rate of formation of ZIF-7 is clearly dependent on the concentration of the amine modulator used. For low amine concentrations, a certain induction time is observed, as represented by $1/k_n$. For the experiment at the highest amine concentration, crystallization seems to be instantaneous. The kinetic parameters, k_n and k_g, are of the same magnitude and both vary with amine concentration, whereas crystallisation becomes more heterogeneous (decreasing *b* values) as amine concentration increases.

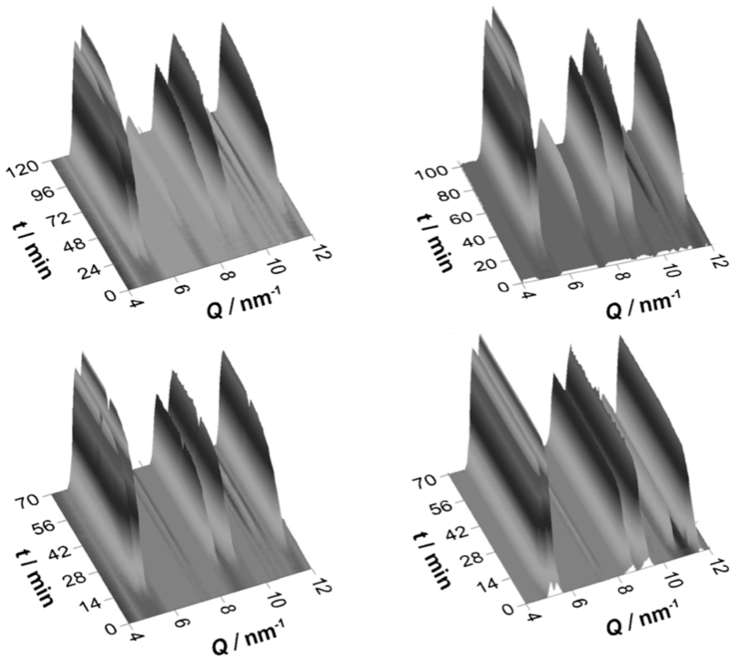

Figure 4.1 3D WAXS data recorded during crystallization of ZIF-7 at room temperature at increasing DEA/Zn molar ratios, *top left:* 3.5 *top right:* 7 *bottom left:* 14 and *bottom right:* 28.

In addition to the faster growth kinetics, preferential growth of certain crystalline planes occurs upon increasing the concentration of diethyl amine (DEA). Through the addition of DEA, preferential growth in the (101), (012), (030), and (-132) planes is observed, in agreement with microscopy characterization of the reaction products (Figure 4.3). In the case of the synthesis with the lowest DEA concentration, rods of 500nm size can be distinguished. Doubling the DEA amount in the synthesis causes formation of regular cubes of 1–2 μm size formed by agglomeration of smaller rods. Increasing the DEA concentration further leads to the formation of rods with higher aspect ratios (up to 50 μm length by 2 μm width).

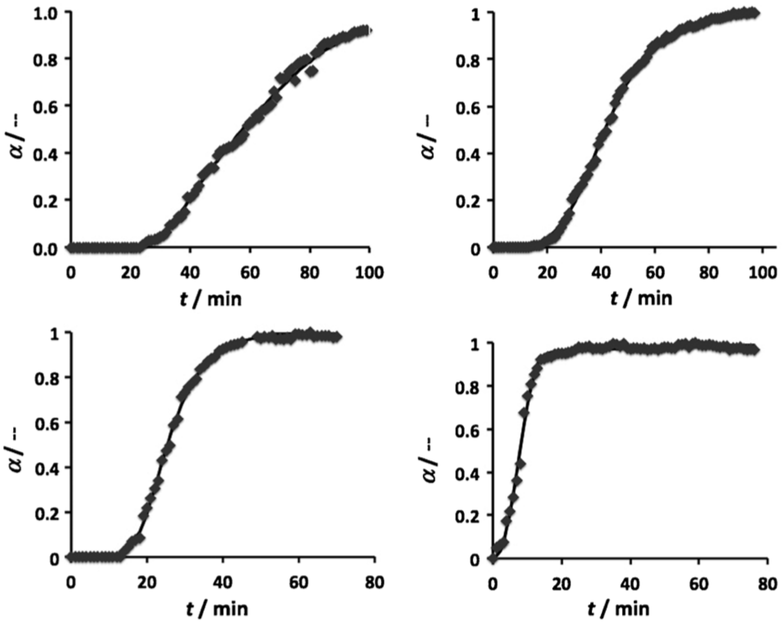

Figure 4.2 Experimental (solid) and calculated (line) profiles of the development of the Bragg peak at Q = 5.1 nm^{-1} at increasing DEA/Zn molar ratios: 3.5 {*top left*}, 7{*top right*}, 14 {*bottom left*}, and 28 {*bottom right*}. Note that different timescales have been used in the different plots.

DEA/Zn molar ratio	**3.5**	**7**	**14**	**28**
k_n / min^{-1}	0.0175 ± 0.0003	0.027 ± 0.002	0.0414 ± 0.002	-
k_g / min^{-1}	0.028 ± 0.002	0.031 ± 0.003	0.0500 ± 0.0008	0.105 ± 0.003
b / min^{-1})	16.8 ± 0.8	12.5 ± 1.3	5.90 ± 0.03	6.7 ± 0.6

Table 4.2 Molar composition of the different crystallisation solutions studied.

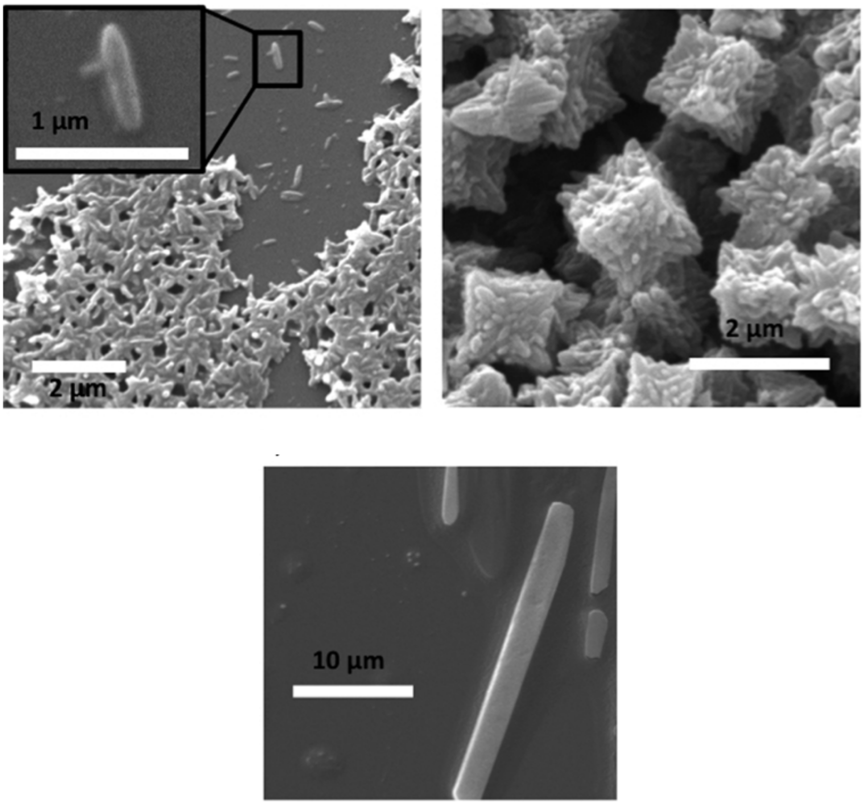

Figure 4.3 SEM images of the ZIF-7 crystals collected on the quartz window with DEA/Zn molar ratios: 3.5 {*top left*}, 7 {*top right*}, and 14 {*bottom*} after 3 h of synthesis.

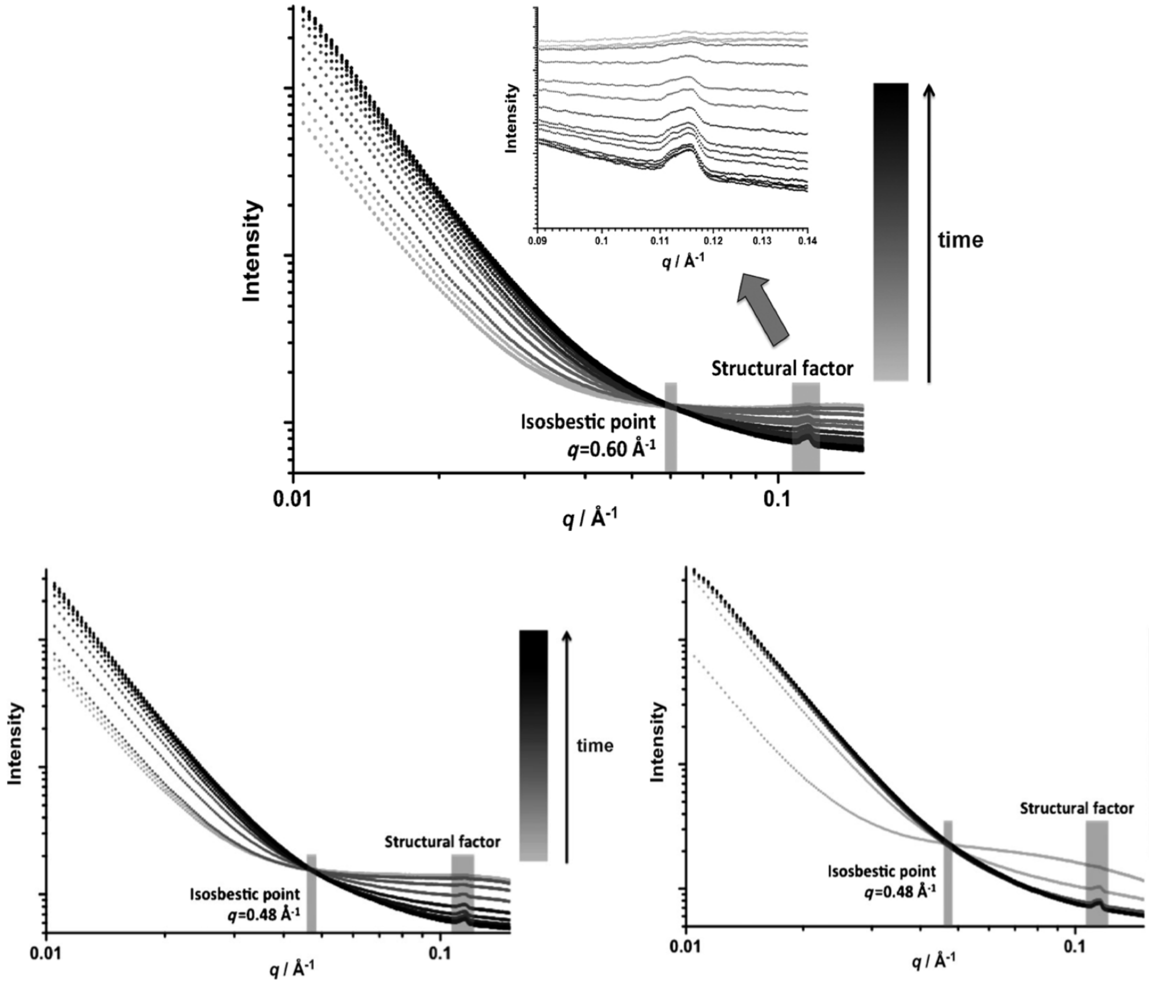

Figure 4.4 {*top*} Time-resolved intensity of scattered X-rays as a function of scattering vector *q,* recorded at small angles (SAXS), with a magnified view of the structural factor observed, during growth of ZIF-7 at low DEA concentrations (solution 1, Table 4.1). The time space between each curve is 500 s. SAXS intensities for intermediate (DEA/Zn = 14, *bottom left*) and high (DEA/Zn = 28, *bottom right*) DEA concentrations. The time space between each curve is 500 s.

Whereas WAXS provides information about crystallisation, the formation, growth, and SAXS provides high-resolution scattering profiles on a larger scale: 2–60 nm in this case, ideal for a study on early crystals. SAXS profiles during the growth of ZIF-7 at low amine concentrations (Figure 4.4) indicate steady, 3D growth with $I(q)$ following $q^{-3.8}$ ($q = 0.01–0.02$ Å^{-1}). An isosbestic (or isoscattering) point at q = 0.6 Å^{-1} indicates that only two solid states dominate the scattering during growth: smaller scatterers, to the right-hand side of the isosbestic point, and larger ones, to the left-hand side.[81,86] Expectedly, the concentration of the large scatterers increases in time, whereas the opposite occurs for the small ones. A structural factor at q = 0.11–0.12 Å^{-1} develops analogously. Structural factors are caused by interparticle interference owing to regularly packed scattering entities of isoelectronic composition. The size of these entities follows $2\pi/q$, ultimately leading to 5.3– 5.7 nm in this case.[32] Altogether, the combination of the isosbestic point and the structural factor suggests the formation of large crystals from well-defined building blocks of approximately 5.3–5.7 nm in size.

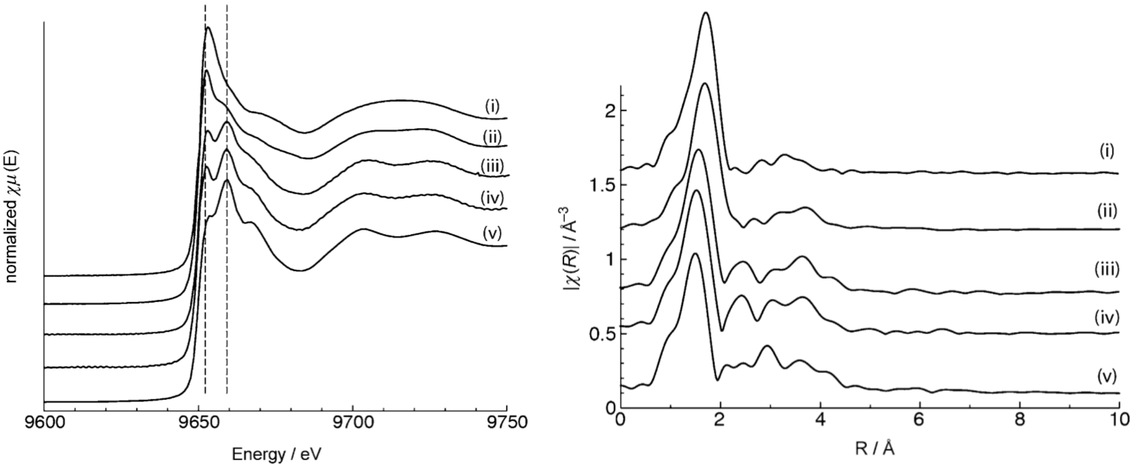

Figure 4.5 {*left*} XANES region of the XAS spectra for (i) $ZnCl_2$ in DMF ii) $ZnCl_2$ /Bim in DMF, iii) $ZnCl_2$/Bim/DEA in DMF before reaction (Solution 3, Table 4.1); iv) same as (iii) after reaction; and v) ZIF-7 isolated product. Dashed lines indicate first and second XANES peaks as discussed in the text, {*right*} Fourier transforms (FT) of EXAFS spectra (k_2-weighed) corresponding to the systems as marked {*left*}. Note that the FT EXAFS shown are not phase-shift-corrected.

As shown before, increasing amine concentration leads to faster crystallisation and to higher aspect ratios. The small to large crystal transformation clearly occurs more rapidly, as shown in Figure 4.4 (bottom left and bottom right). Physically, the Porod slope is similar to the one at low amine concentrations, and so is the lineshape of the structure factor; the size of the primary building units proves to be independent of the amine concentration, which further suggests that differences in particle morphology (Figure 4.3) are due to differences in self-assembly of the smaller units.

The isosbestic point is also seen to shift to the left from low to intermediate amine concentrations, thus indicating a larger average volume between the two (crystal size) states, which is to say that - although primary units remain the same size - they cluster together more efficiently, and the large scatterers become larger as amine concentration increases, thereby supporting the heterogeneous crystallisation analysis. The amine clearly plays a role in connecting the smaller units.

Development of the ZIF-7 phase from the solute Zn species should be reflected in the change of Zn coordination. The Zn X-ray absorption near-edge structure (XANES) spectra recorded at different steps of the synthesis are shown in figure 4.6. The intensity of the white line related to the 1*s*→4*p* transition is dependent on the coordination number (CN) and geometry.[87] When Zn is coordinated by oxygen atoms in ZnO or aqueous solutions, the first XANES peak (9652 eV) dominates the spectrum, thereby resembling the spectrum obtained in pure DMF.[88] Zinc imidazole complexes, in which four nitrogen atoms coordinate the metal ion, show significant increase in the second XANES peak intensity (9660 eV), which is consistent with the spectrum obtained for a ZIF-7 product.[89] Interestingly, upon addition of the benzimidazole (Bim) ligand to the solution in DMF (spectrum ii in Figure 4.5), a minor change of the line shape can be observed, which indicates that, in the absence of amine, a small fraction of imidazole is incorporated into the Zn coordination sphere at room temperature. In spite of this coordination, formation of ZIF-7 does not take place.

EXAFS analysis allowed us to determine the structural transformation of the metal complexes during the reaction in a more accurate fashion. It has been shown that in DMF Zn assumes coordination number 6, thereby suggesting a six-coordinate octahedral structure.[90] With chloride ions present in solution, tetrahedral structures with two Cl and two DMF ligands have been reported.[91] In the present case, analysis of EXAFS data for the $ZnCl_2$/DMF system shows

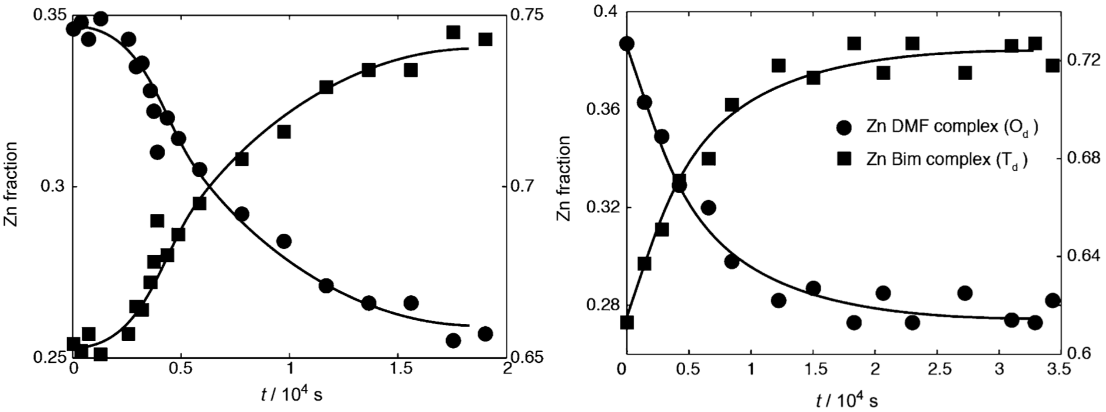

Figure 4.6 Result of a linear combination fitting of the in situ XANES lineshapes, using $ZnCl_2$/DMF and ZIF-7 spectra as principal components for, {*left*} low- (solution1, Table 4.1) and {*right*} high-concentration (solution 4, Table 4.1) DEA mixtures. The right axis represents the fraction of Zn in octahedral coordination (unreacted Zn in solution) and the left axis represents the fraction of Zn in tetrahedral coordination (forming part of the ZIF-7 product).

that the average total CN equals 5.5, which suggests an equilibrium between hexa- and tetracoordinated complexes. We attribute this equilibrium to traces of water in the metal precursor and solvent.[88] Upon addition of Bim to the $ZnCl_2$/DMF solution, the total coordination number decreases to 5.1, and a shortening of the Zn first-neighbor distance relative to the $ZnCl_2$/DMF case is observed. One can see that the first peaks in the spectra shown in Figure 4.5i–iv contain two contributions, consistent with coexistence of Cl and O/ N in the first coordination sphere. Unfortunately, attempts to distinguish O and N on the basis of the EXAFS analysis were not successful. Due to the significant number of possible structures, the EXAFS analysis was limited to the first coordination sphere.

The changes in spectral lineshapes over the course of the reaction are not as significant as the effect of amine addition to the $ZnCl_2$/DMF/Bim solution (see spectra ii and iii in Figure 4.5). The changes in the intensities of the first and second maxima in the XANES spectra that occur in the course of the reaction are consistent with increased Zn-N coordination, as well as a shift of the EXAFS FT peak that corresponds to the first coordination shell. Upon apparent reaction completion (i.e., when no changes in the WAXS patterns occur), the XAS spectra are not identical to the one of the isolated product, as one might expect, since only a fraction of Zn in solution is consumed in the reaction and incorporated into the MOF structure. As the final ZIF-7 product should be exclusively four-coordinated, we used its XANES spectrum for linear combination analysis of the in situ spectra. The other principal component was $ZnCl_2$/DMF. The evolution of these two principal component contributions to the total XANES spectra is depicted in Figure 4.6. These are in very good agreement with the kinetic data extracted from WAXS (Figure 4.2) (notice the activation period in the case of low DEA concentration).

On the basis of the QEXAFS analysis, several conclusions can be drawn. Upon addition of linker to the Zn solution in DMF, a small fraction of the Bim molecules replaces solvent molecules in the Zn coordination sphere, thereby resulting in the shift in the equilibrium towards four-coordinated complexes. In spite of this coordination, formation of ZIF-7 is not observed. Amine addition triggers this process without penetrating the metal coordination sphere and results in the formation of ZIF-7. To gain more insight into the chemical processes that take place at the early stage of ZIF-7 assembly, the transformation of the initial $ZnCl_2 \cdot 2DMF$ (1) to multinuclear Bim-containing Zn complexes was studied by DFT calculations (B3LYP/6-31+G(d,p)). Dimethylamine (DMA) was used as a model base to reduce the configurational complexity of the system. The optimized geometrical parameters for complex 1 (Figure 4.7, vide infra) are in good agreement with those derived from EXAFS data ($ZnCl_2$/DMF, Table 4.2). In the presence of the Bim ligand and DMA ($NHMe_2$) three alternative transformations can take place. DMF ligands can exchange with either DMA or Bim (reactions **1 → 1a** and **1 → 2,** respectively, in Figure 4.7).

	Neighbours	CN	R / Å	$\sigma^2 \times 10^3$
$ZnCl_2$/DMF	O	3.8 (3)	2.05(3)	13(7)
	Cl	1.7 (6)	2.22(6)	5(1)
$ZnCl_2$/DMF/Bim	O/N	3.4 (7)	2.03(9)	8(6)
	Cl	1.7 (8)	2.24(6)	5(7)
ZIF-7 product	N	4^a	1.98(2)/1.99^b	4(2)
	C	4^a	2.99(9)/2.95^b	12(6)
	C	4^a	3.42(10)/3.53^b	5(8)
	N	2^a	4.20(12)/4.21^b	10(2)
	C	2^a	4.38(14)/4.23^b	13(7)
$ZnCl_2$/DMF/Bim/DEA (2.0) *t*=0s	O/N	3.5 (6)	2.02(1)	25(12)
	Cl	1.5 (7)	2.24(6)	11(8)
$ZnCl_2$/DMF/Bim/DEA (2.0) *t*=60s	O/N	3.4 (6)	2.02(8)	11(7)
	Cl	1.5 (5)	2.24(10)	18(8)

Table 4.2 Structural parameters extracted from the EXAFS data fits. a: CN values were fixed at crystallographic values, b: Values obtained from XRD pattern refinement are shown for comparison

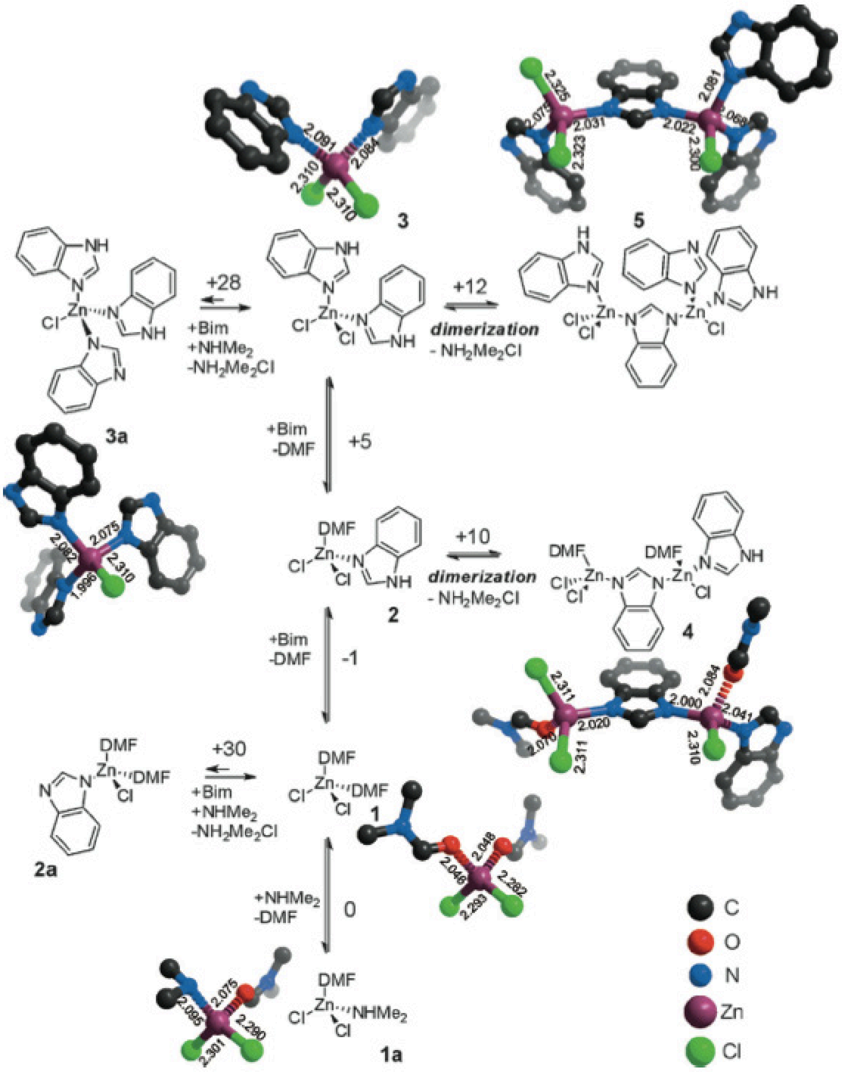

Figure 4.7 DFT-computed reaction free energies (ΔG°_{298k} [kJ mol^{-1}]) and optimized geometries of selected reaction intermediates (bond lengths in Å, hydrogen atoms not depicted) for the potential transformation pathways of initial $ZnCl_2 \cdot 2DMF$ (1) during the early stages of ZIF-7 synthesis in DMF in the presence of DMA.

Both reactions are characterized by very small values of ΔG^{o}_{298k} [kJ mol^{-1}]; furthermore, subsequent exchange of the neutral ligands within both **1a** and **2** shows very similar energetics. Negligible ΔG^{o}_{298k} values were computed for the formation of such adducts as Bim·ZnCl$_2$·DMA and ZnCl$_2$·2DMA, as well as ZnCl$_2$·2Bim (**3**). An alternative reaction (**1 → 2a**) proceeds by substitution of one of the Cl$^-$ ions in the coordination sphere of Zn by a deprotonated Bim ligand. In the absence of a base, the computed free-energy change is prohibitively large (> 100 kJ mol^{-1}). Therefore, we assume that the main role of the amine is to neutralize HCl generated during ZIF-7 assembly. When this reaction is taken into account, the free energy change for Cl$^-$ substitution reactions is lowered by 78 kJ mol^{-1}.

Nevertheless, the direct exchange of Cl$^-$ with Bim$^-$ in mononuclear Zn complexes (Figure 4.7, reactions **1 → 2a** and **3 → 3 a**) is very unlikely in view of the computed high ΔG^{o}_{298k} values. In contrast, the substitution of the strongly bound Cl$^-$ ions can be achieved by the dimerization of mononuclear Zn complexes that contain neutral Bim ligands (reactions **2 → 4** and **3 → 5**, Figure 4.7). The Zn-N bonds in dimers **4** and **5** are similar and considerably shorter than those formed upon complexing with neutral Bim. This is in line with the differences in the coordination properties in ZIF-7 and the reaction medium. The preference for self-organization of Bim-ZnCl$_2$ adducts over the direct ion exchange is most likely associated with the increased acidity of the -NH moiety in the imidazole fragments that are (mono)coordinated to Lewis acidic Zn^{2+} cations. The main finding of the DFT calculations is that the substitution of the stronger-bound Cl$^-$ ions and the actual assembly of ZIF-7 precursors proceeds through the condensation of Zn species with lower nuclearity. This process will show a considerable degree of directionality because it leads to the formation of 2D Zn-Bim clusters decorated with Zn-Cl moieties that are very likely to form rodlike structures.[75] In contrast, when Zn salts that fully dissociate upon dissolution (e.g., NO$_3^-$) are used as a metal source for ZIF-7 synthesis, an alternative uniform 3D evolution of Zn-Bim aggregates is envisaged upon cluster growth and involves the direct exchange of both neutral and anionic ligands.[76]

Conclusion

The crystallization of the metal–organic framework ZIF-7 was studied in the presence of a DEA modulator by using *in-situ* Small- and Wide-Angle X-ray Scattering and Quick-Scanning Extended X-ray Absorption Fine-Structure spectroscopy in combination with DFT calculations. The addition of DEA to the synthesis mixture (ZnCl$_2$/Bim in DMF) results in the formation of ZIF-7 rods at room temperature; the aspect ratio of the obtained rods varies with the concentration of DEA. WAXS analysis reveals that the rate of formation of ZIF-7 is clearly dependent on the concentration of the amine modulator used. QEXAFS analysis in combination with DFT calculations demonstrate that the use of ZnCl$_2$ as Zn precursor promotes the formation of 2D Zn-Bim clusters decorated with Zn-Cl moieties. The use of a base such as DEA is crucial for the formation of MOF crystals, since it neutralizes the HCl generated upon ZIF-7 assembly. DEA does not coordinate to Zn and has therefore an indirect role. SAXS analysis shows that once the first 2D Zn-Bim/Zn-Cl decorated clusters are formed, growth of ZIF-7 proceeds through near-ideal growth with the formation of “nano-building blocks” approximately 5.5 nm in size that further assemble to larger particles. The self-assembly of such primary units determines the final morphology of the particles. It is speculated here that, in the presence of large concentrations of DEA, a high concentration of nanoblocks would promote the formation of particles with high aspect ratios, whereas moderate amine concentrations result in smaller rods that further agglomerate into fractal structures (see Figure 4.3 {*top left* and *top right*}).

Altogether, these results demonstrate that the modulating MOF assembly proceeds through a rather complex mechanism, and that both theoretical and *in-situ* crystallization studies are of the highest importance for a better understanding of the mechanism(s) that control MOF assembly.

5

Evidence for a solid-state clock reaction in the formation of UiO-66(Zr/Hf)

In this chapter it is demonstrated that the synthesis of zirconium and hafnium based UiO-66 proceeds via a *solid-state clock reaction.*
In-situ Small-Angle X-ray Scattering shows that during precipitation, UiO-66 crystal number density and dimensions *oscillate* towards final values during synthesis. Extent of crystallisation matters an independent process from particle growth, and is devoid of these oscillations. Quantum chemical bonding- and energy decomposition analyses (EDA) based on relativistic DFT were carried out to determine the degree of covalency in Metal-Organic bond formation, pinpointing the interaction between the organic strut and the inorganic building block. Calculations indicate that HCl plays an autocatalytic role in UiO-66, consumed during precipitation and released in crystallisation. This is, to the best of our knowledge, the first time a clock reaction has been *in-situ* followed and rationalized for the synthesis of a solid material.

Introduction

In the previous chapters we dealt with hydrochloric acid, HCl, which is generated during crystallisation, using a metal chloride that serves as MOF precursor. As could be expected *a priori*, the neutralisation of HCl by addition of a base favourably shifted equilibrium towards MOF formation, yielding faster rates and higher yields, the base being DMF in chapter 3, and diethyl amine in chapter 4. A report suggesting that the addition of HCl to the precursor solution will lead to an improvement in the kinetics of MOF synthesis would thus seem counterintuitive, yet Farha and co-workers reported this very fact for the synthesis UiO-66 (from $ZrCl_4$).[92]
UiO-66 is the thermally most stable MOF available, only breaking down at a temperature of 540 °C.[93] It consists of high-coordinate oxoclusters of the form $M_6O_4(OH)_4$, M=Zr/Hf,[94] which each bind to 12 μ_4-terephthalato ligands. *As*-synthesized UiO-66 was shown to contain defects that render inherent Lewis acidity,[95,96] and several methods exist to increase the concentration of defects, such as thermal dehydroxylation and modulation during synthesis.[97,98] Since the ligand can be chemically and spatially tuned as well, and at minimal cost of thermal stability,[99] it is not surprising that UiO-66 finds itself at the very top of the shortlist of MOFs which carry promise for applications in catalysis.[100,101]
In this chapter, we use Small and Wide-Angle X-ray Scattering (SAXS/WAXS) to show that the UiO-66 particle dimensions, as well as the number of particles in solution, oscillate to final values in time during synthesis, reminiscent of a *clock reaction*. Meanwhile, the extent of crystallisation in time does not show these oscillations, whilst carrying some delay with respect to precipitation. Using high-level relativistic Density Functional Theory (DFT) bonding analyses, in which we pinpoint metal-organic interaction, we are able to show that the oscillations are the result of autocatalytic interplay between HCl and the precipitating framework.

Experimental

Synthetic procedures

The in-house developed SAXS/WAXS cell, described in chapter 3, was used for the experiments. For a typical solution, 0.75 mmol 2-aminoterephthalic acid (134 mg), 0.54 mmol $ZrCl_4$ (125 mg), 1 ml HCl (37%) and 15 ml dried DMF were mixed and injected in the synchrotron cell. 1 ml matters 1 eq. of HCl in the main text. The cell is heated via a temperature controller.

X-ray scattering

SAXS/WAXS measurements were carried out at the X9 beamline at the National Synchtrotron Light Source (NSLS), Brookhaven, NY. All datasets were azimuthally integrated, normalized for beam intensity, and background-subtracted to yield time-resolved 1D data which was processed to obtain temporal information on the following integral parameters: radius of gyration R_g [nm], number densiy N/V [-], Porod surface-to-volume S/V [nm^{-1}] and Porod volume, V_p [nm^3]. The definition of the number density N/V is:

$$\frac{N}{V} \propto \frac{Q^2}{I(q=0)} \qquad \textbf{Eq. 5.1}$$

With forward scattering, *I(q=0)* calculated by Eq. 3B.11. The other parameters are introduced and discussed in chapter 3B.

During the experiments, wide-angle X-ray scattering (WAXS) was used to follow the extent of crystallisation, Eq. 3A.1, *via* the development of Bragg peaks.

Density functional theory

All calculations were carried out with ADF at the ZORA-BLYP-D3(BJ)/TZ2P level of the generalized gradient approximation (GGA) of Kohn Sham Density Functional

Theory (DFT).[102-104] ZORA stands for Zeroth Order Regular Approximation and was used to take relativistic effects into account, expected to be present for calculations involving hafnium.[105,106]

Fragment analyses were carried out, very well suited for the study of MOF precipitation, since one can specify a ‘metal’ and ‘organic’ fragment, in order to pinpoint the interaction between them. In this case, a fragment of 12 geometrically optimized formate molecules is deformed to its final, crystallographic state in the UiO-66 framework, using the Activation-Strain Model.[107] The ‘final crystallographic state’ is derived from Rietveld refinement provided by Lamberti *et al.*[97,108] Formate, rather than terephthalate or benzoate, was chosen to make the high-level calculations less expensive. The specified $[formato]_{12}$ fragment is allowed to interact with an inorganic fragment of the form $M_6O_8H_x$, with M=Zr or Hf, and x =0 to 8, in total 2 × 9 isoelectronic (inorganic) fragments, and 18 metal-organic interactions with the degree of protonation as main parameter in the construction of Zr and Hf based UiO-66. Within this metal-organic interaction, an Energy Decomposition Analysis (EDA) is carried out to split the interaction energy into electrostatic, orbital and Pauli terms: $\Delta E_{int} = \Delta V_{elstat} + \Delta E_{oi} + \Delta E_{Pauli}$ (figure 2, I).[109] More information on EDA can be found in chapter 2. The EDA is required because we investigate MOF precipitation in a polar solvent, which is governed by the formation of bonds that carry significant covalent character. To illustrate this: AgF will not precipitate in a polar solvent in contrast to AgCl; a result of highly ionic bonding versus ionic bonding with some degree of covalency. Since clearly, electrostatic interaction between the (positively charged) inorganic fragment and the $[formato]_{12}$ fragment becomes stronger upon increasing the degree of protonation, it makes sense to define a ‘degree of covalency’, $\Delta E_{oi}/\Delta V_{elstat}$, within the frame of the EDA described above.

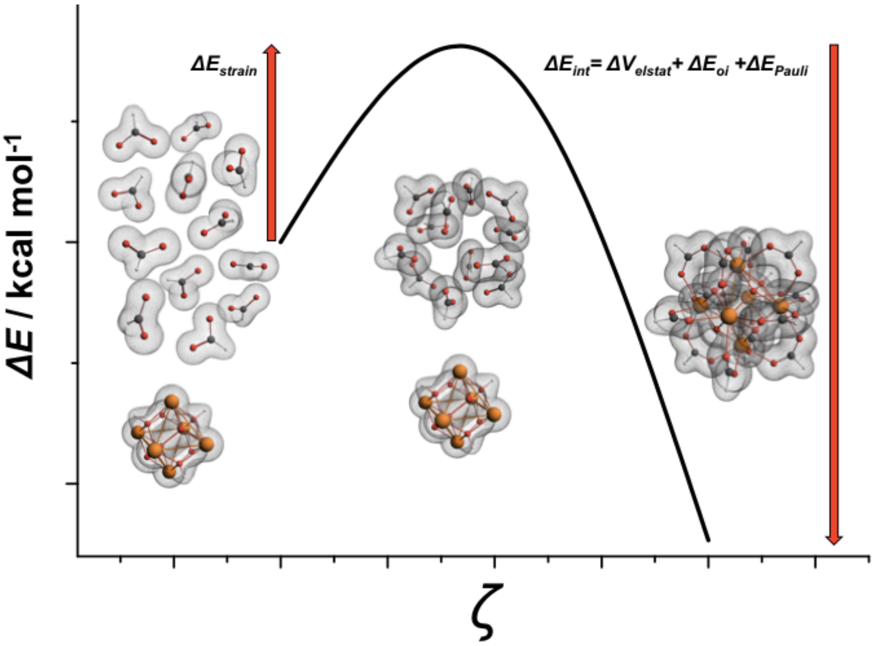

Figure 5.1 - Implementation of the Activation-Strain model and Energy Decomposition Analysis (EDA) in which the $[\text{formato}]_{12}$ fragment reacts with 18 isoelectronic $M_6O_8H_x$ fragments. **ζ** represents the reaction coordinate. The fragments deform towards their final state in the framework, and this metal-organic interaction is decomposed into energetic terms for electrostatic interaction, orbital interaction, and Pauli repulsion.

Results

Figure 1 displays the trends of both parameters for Zr and Hf based UiO-66. Remarkably, after a certain induction time and rapid precipitation thereafter, the crystal radius of gyration and number density are seen to *oscillate* to final values. This is mainly visible for the slower syntheses, where damping of the oscillations is least effective and secondary fluctuations are visible. It must be stressed that these oscillations were fully reproducible, and that the final value for R_g is independent of temperature and or HCl concentration, consistent with the SEM analysis by Farha et al.[92]

Interestingly, it appears that after start of precipitation, particle growth of hafnium-based UiO-66 takes slightly more time with respect to Zr to reach the maximum of the first oscillation (e.g. a difference of three points, corresponding to just over 3 minutes to reach the maximum, for the ‘HCl ½ eq’ synthesis). Oscillations were also present for the development of the Porod volume and surface-to-volume ratio, yet tellingly, no oscillatory behaviour was observed for the extent of crystallisation ε obtained from the WAXS data. This is in line with observations by Ragon *et al.* who studied formation of UiO-66 with *in-situ* synchrotron XRD.[110] It is further noteworthy that the start of bulk crystallisation, as observed by WAXS, was for all cases seen to carry a small delay whilst proceeding gradually with respect to the process of precipitation (this is graphically compared in the ESI, figure S3). This indicates that the precipitating coordination polymer is briefly amorphous before rearranging itself to a crystalline structure.

It is now important to explain this oscillatory behaviour, which is something expected for clock reactions such as the *iodine clock reaction*:[111]

$$H_2O_2 + 2\,I^- + 2\,H^+ \rightarrow I_2 + 2\,H_2O \qquad \{\text{reaction 1}\}$$
$$2\,S_2O_3^{2-} + I_2 \rightarrow S_4O_6^{2-} + 2\,I^- \qquad \{\text{reaction 2}\}$$

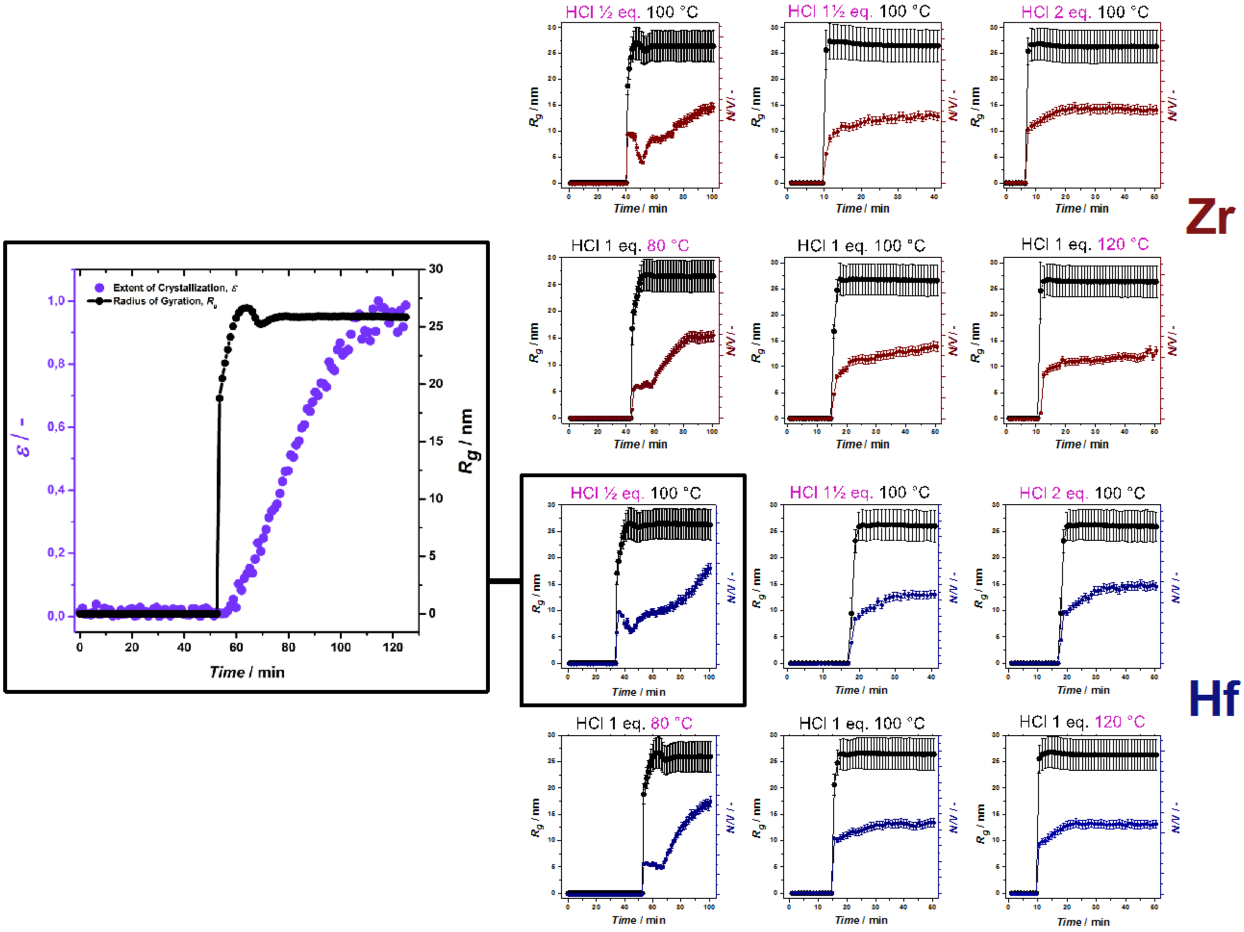

Figure 5.2 Development of radius of gyration, R_g (nm), and number density, N/V, as a function of time for Zr (top 6) and Hf (bottom 6) based UiO-66. *Left*: close-up and comparison with extent of crystallisation ε, which shows that precipitation and crystallisation are independent processes.

Many clock reactions exist, but this is the simplest and most exemplary; iodide is consumed in a slow, first reaction, slowing down the rate of reaction 1, but as it is generated in a second, fast reaction, the rate of reaction 1 finds itself again accelerated, resulting in oscillating values for the coupled concentrations. These oscillations then dampen to equilibrium. The autocatalytic species remains retained in this set of reactions; it is simply consumed in one step and produced in another whilst serving an overall reaction. The only species in the synthesis of UiO-66 that can hold such an autocatalytic role is HCl. A starting point in explaining such an autocatalytic role of HCl lies in the observation that *as*-synthesized UiO-66 contains four μ_3-OH ligands, next to four μ_3-O ligands. This is striking, because the proton acidity strongly increases in the sequence (μ_1-μ_2-μ_3)-OH, and this proton was indeed seen to play an active role in catalysis,[112] or be prone to exchange for other monovalent moieties in targeted functionalization of the inorganic node.[113] Whilst these protons are required to charge-stabilize the scaffold, they are expected to materialize in rather acidic local environments. This information logically implies that HCl might be actively protonating the inorganic cluster in the synthesis of UiO-66.

The results of the DFT calculations prove to be rather unambiguous as the ratio $\Delta E_{oi}/\Delta V_{elstat}$ is seen to increase linearly and significantly upon increasing the degree of protonation of the inorganic fragment (figure 5.3) Apparently, highly protonated clusters engage in stronger orbital interactions, and precipitate therefore more easily. In disclosing the nature of this covalency, we attempted to provide a Molecular Orbital (MO) picture of the metal-organic fragment interaction that turns out to be essential in understanding the formation of UiO-66.

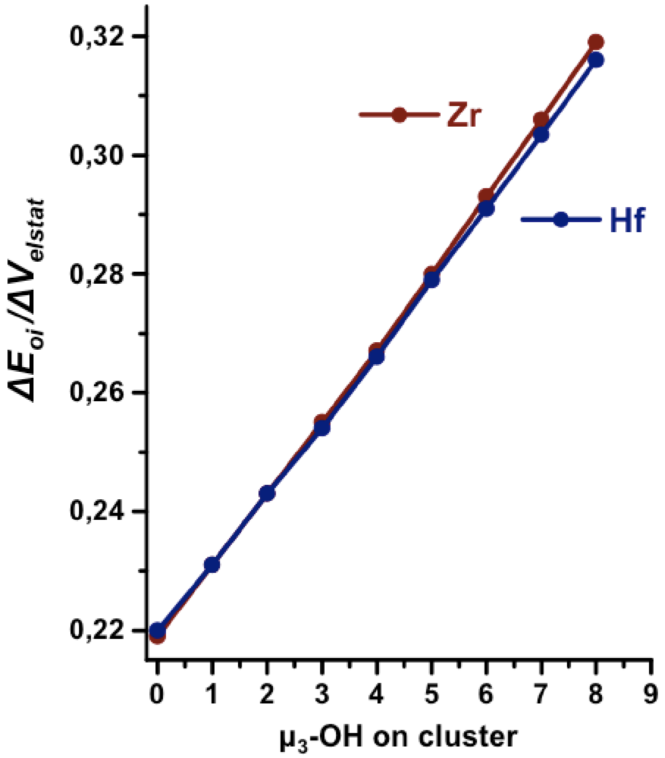

Figure 5.3 Degree of covalency defined as $\Delta E_{oi}/\Delta V_{elstat}$ as calculated for the 18 fragment interactions (9 for zirconium and 9 for hafnium based UiO-66).

The bonding between the two fragments involves 36 electron pairs (24 σ and 12 π, in line of expectation for μ_2-formato); in many cases the orbital interactions between the two fragments involve more than two Fragment Orbitals (FOs). This makes it rather challenging to construct a simple MO picture that provides a good qualitative picture of the influence of protonation on the covalent metal-organic bond order. However, if one only considers the interactions involving the inorganic fragments with 0 and 8 protons, one does not only consider the extremes that span the range of study, but also interactions in which all fragments carry O_h symmetry. This considerably facilitates the analysis: the use of group theory indicates that solely considering the high symmetries A_{1g}, A_{2g}, A_{2u}, thus three MO diagrams per model complex, a reasonably complete picture can be obtained. Only the four MOs of totally symmetric A_{1g} are displayed here, in figure 3, since they represent the most significant interactions. MO diagrams for A_{2g} and A_{2u} can be found in the ESI.

From the MO coefficients displayed in figure 3 and the other MO coefficients, it is clear that for both Zr and Hf based UiO-66, metal-organic bonding becomes decreasingly polar as the degree of protonation increases. Note that the stronger bonding is not a result of the metal-organic orbital overlap, which remains similar, if not slightly decreasing, for the 8-proton inorganic clusters with respect to their 0-proton analogues. The analysis of the metal-organic bonding thus indicates that, whilst bonds are spatially similar, covalent bond order increases. In a simple description of this phenomenon we consider the postulate of the Bond Order Conservation Principle, without the Morse Potential approach as frequently applied by Shustorovich and others,[114] and observe the inorganic cluster that undergoes protonation at μ_3-O. According to Shustorovich's theory, this weakens the metal-oxygen bond, and therefore increases the acidity of the metal ion, thus enhancing the metal-organic interaction in this case.

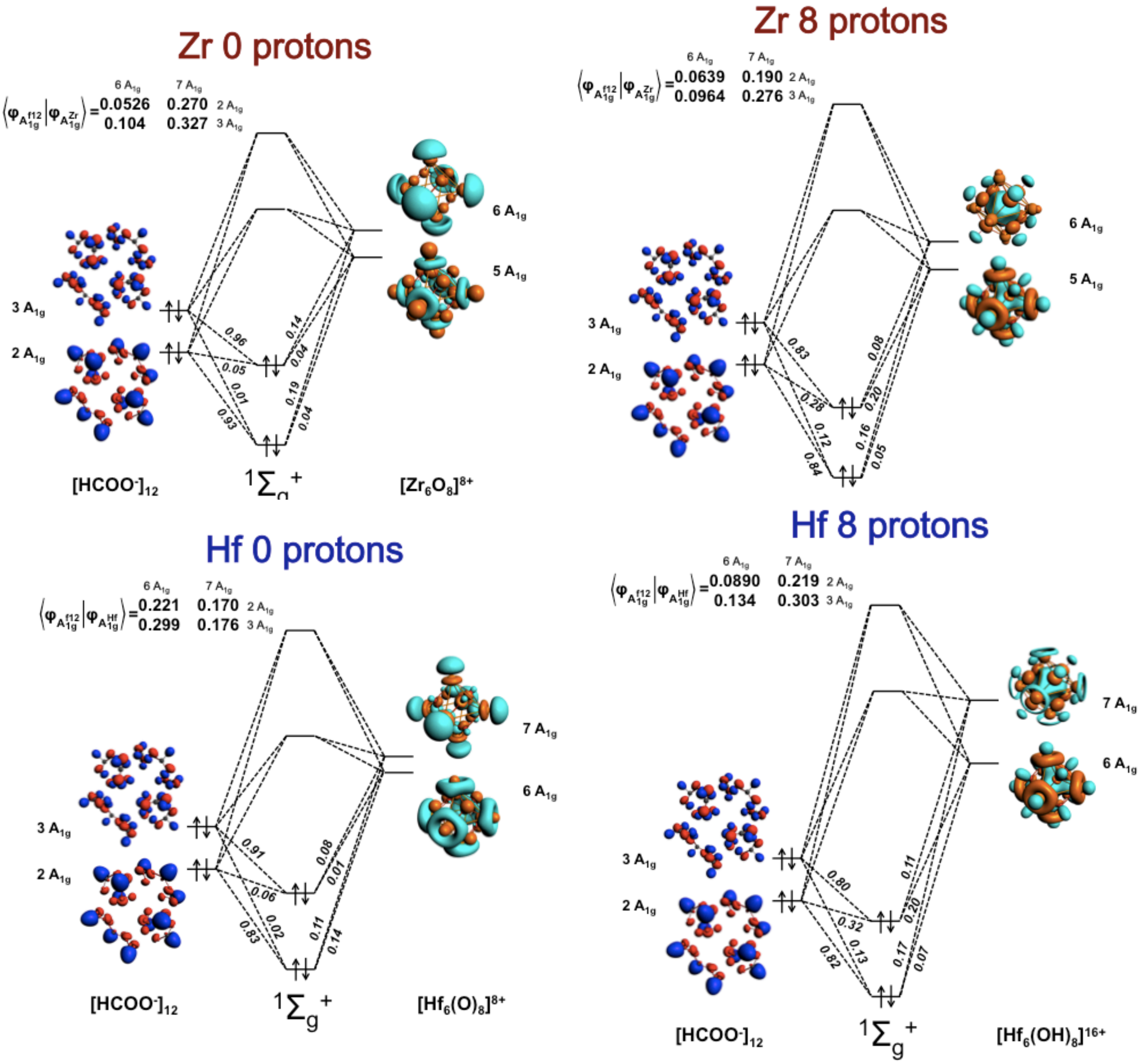

Figure 5.4 MO diagrams showing the Metal-Organic interaction between the totally symmetric (*A_{1g}*) fragment orbitals, with the inorganic fragment either carrying 0 or 8 protons, in *O_h* symmetry. The overlap matrices are depicted in the top left corner for each diagram.

Discussion and conclusion

Figure 5.5 displays a schematic pathway based on the observations in SAXS/WAXS and DFT analysis. **Step 1** in the scheme occurs in the preparation of the precursor solution and matters the hydrolysis of $ZrCl_4$ and formation of zirconyl chloride species, which are known to form tetranuclear species in solution, such as $[Zr_4(\mu_2\text{-}OH)_8]^{8+}$ depicted in the scheme.[115] The rearrangement of this cluster into the hexanuclear UiO-66 building block follows an unknown path, but what is certain is that the pathway to precipitation must be acid catalysed, since despite the appearance of μ_3-O(H) bridges, oxygens remain largely protonated. This is indeed observed by the groups of Serre and Farha.[92,110]

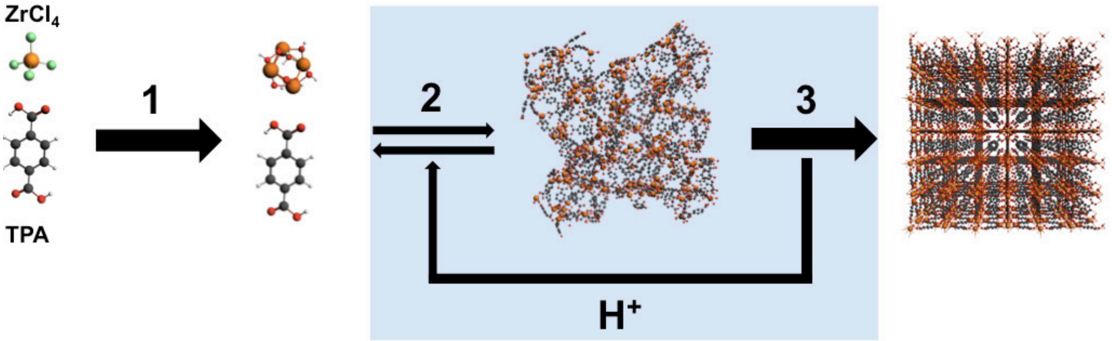

Figure 5.5 Schematic view of the formation of UiO-66 and the autocatalytic role of H^+. Step 1: formation of tetranuclear clusters, step 2: consumption of H^+ and fast precipitation, step 3: development of crystallinity upon release of H^+.

The highly protonated clusters then engage in metal-organic bond formation in **step 2** and fast precipitation of the solid coordination polymer occurs. The solid is not fully crystalline at this brief stage, and the network – due to the protonated oxido bridges - carries local positive charge, countered by chloride ions in solution. This situation is metastable, and reorganisation is rapid; the crystalline lattice is formed and the oxido bridges deprotonate, neutralizing the charge difference between the scaffold and solution (**step 3**). This process, likely to be driven by lattice enthalpy, was observed before in the crystal-to-crystal transformation of NH_2-MOF-235(Al) to NH_2-MIL-101(Al),[116] but is also seen in the formation of zeolites, where charged templates are squeezed out of the network during the process of crystallisation.[117] The release of protons in **step 3** is vital, since it accelerates **step 2**, which was slowed down, or even stopped by the consumption of protons, with staggering crystal number and dimensions as a result. This autocatalytic cycle leads to oscillations for the integral parameters R_g, V_p, N/V, S/V in a chemical clock reaction.

Clock reactions are common and even popular subjects in chemical education as they can be used to visualise the kinetics of coupled reactions, but oscillations are rarely directly observed for solid dimensions and/or numbers, and we were not able to find any example of a solid-state process that bears any resemblance to the one in this study.

In stating that, we do not rule out the possibility that similar clock reactions do occur in the formation of other MOFs; on the contrary, we might expect them to be present in the coordination of other high-coordinate oxoclusters. An interesting, additional observation in this work is that the coordination chemistry in forming UiO-66 is very similar for Zr and Hf, yet precipitation and corresponding oscillations were slightly slower for the latter. This is in line with observations made before by Christoph Marschner, who writes in an essay on its (coordination) chemistry that "*Hafnium imitates Zirconium in a sluggish way*".[118]

More than anything, this work demonstrates that in resolving molecular pathways of MOF crystallisation, a multiscale approach is required: in this work, the use of both SAXS and WAXS was required to separate the process of precipitation from that of crystallisation, frequently shown to exist as independent processes in MOF synthesis. At the molecular scale, high-level DFT approaches work in concert with X-ray scattering to provide necessary insight from the perspective of coordination chemistry. We further believe that in particular the use of fragment analysis and EDA should be encouraged in theoretical studies on MOF formation, since covalent interactions between the organic struts and inorganic nodes can be highlighted, essential in the understanding of metal-organic network formation. This work demonstrates that this is a viable theoretical approach.

Attempts at describing the oscillations with a kinetic model were in vain, since crystal size could not be linked to local concentrations, and the number density *N/V* is by definition a proportionality parameter, and therefore displayed in arbitrary units.

References

[1] F. Millange, M. I. Medina, N. Guillou, G. Férey, K. M. Golden, R. I. Walton, *Angew. Chem. - Int. Ed.* **2010**, *49*, 763–766.

[2] F. Millange, R. El Osta, M. E. Medina, R. I. Walton, *CrystEngComm* **2011**, *13*, 103–108.

[3] P. Norby, *Curr. Opin. Colloid Interface Sci.* **2006**, *11*, 118–125.

[4] P. P. E. A. De Moor, T. P. M. Beelen, R. A. van Santen, L. W. Beck, M. E. Davis, *J. Phys. Chem. B* **2000**, *104*, 7600–7611.

[5] C. J. Y. Houssin, C. E. A. Kirschhock, Magusin, P.C.M.M., B. L. Mojet, P. J. Grobet, P. A. Jacobs, J. A. Martens, R. A. van Santen, *Phys. Chem. Chem. Phys.* **2003**, *5*, 3518–3524.

[6] P. Serra-Crespo, E. V. Ramos-Fernandez, J. Gascon, F. Kapteijn, *Chem. Mater.* **2011**, *23*, 2565–2572.

[7] J. Gascon, U. Aktay, M. D. Hernandez-Alonso, G. P. M. van Klink, F. Kapteijn, *J. Catal.* **2009**, *261*, 75–87.

[8] T. Ahnfeldt, D. Gunzelmann, T. Loiseau, D. Hirsemann, J. Senker, G. Férey, N. Stock, *Inorg Chem* **2009**, *48*, 3057–3064.

[9] S. Yang, A. Navrotsky, D. J. Wesolowski, J. A. Pople, *Chem. Mater.* **2004**, *16*, 210–219.

[10] S. Nikitenko, A. M. Beale, A. M. J. Van Der Eerden, S. D. M. Jacques, O. Leynaud, M. G. O'Brien, D. Detollenaere, R. Kaptein, B. M. Weckhuysen, W. Bras, *J. Synchrotron Radiat.* **2008**, *15*, 632–640.

[11] T. P. Caremans, B. Loppinet, L. R. A. Follens, T. S. Van Erp, J. Vermant, B. Goderis, C. E. A. Kirschhock, J. A. Martens, A. Aerts, *Chem. Mater.* **2010**, *22*, 3619–3629.

[12] S. Kumar, T. M. Davis, H. Ramanan, R. L. Penn, M. Tsapatsis, *J. of Phys. Chem. B* **2007**, *111*, 3398–3403.

[13] K. Flodström, C. V. Teixeira, H. Amenitsch, V. Alfredsson, M. Lindén, *Langmuir* **2004**, *20*, 4885–4891.

[14] G. R. Patzke, Y. Zhou, R. Kontic, F. Conrad, *Angew. Chem. - Int. Ed.* **2011**, *50*, 826–859.

[15] D. Grosso, F. Ribot, C. Boissiere, C. Sanchez, *Chem. Soc. Rev.* **2011**, *40*, 829–848.

[16] C. Alétru, G. N. Greaves, G. Sankar, *J. Phys. Chem. B* **1999**, *103*, 4147–4152.

[17] A. M. Beale, A. M. J. Van Der Eerden, S. D. M. Jacques, O. Leynaud, M. G. O'Brien, F. Meneau, S. Nikitenko, W. Bras, B. M. Weckhuysen, *J. Am. Chem. Soc.* **2006**, *128*, 12386–12387.

[18] A. Aerts, L. R. A. Follens, M. Haouas, T. P. Caremans, M. A. Delsuc, B. Loppinet, J. Vermant, B. Goderis, F. Taulelle, J. A. Martens, et al., *Chem. Mater.* **2007**, *19*, 3448–3454.

[19] A. M. Beale, M. G. O'Brien, M. Kasunič, A. Golobič, M. Sanchez-Sanchez, A. J. W. Lobo, D. W. Lewis, D. S. Wragg, S. Nikitenko, W. Bras, et al., *J. Phys. Chem. C* **2011**, *115*, 6331–6340.

[20] A. F. Gualtieri, *Phys. Chem. Miner.* **2001**, *28*, 719–728.

[21] P. Serra-Crespo, E. V. Ramos-Fernandez, J. Gascon, F. Kapteijn, *Chem. Mater.* **2011**, *23*, 2565–2572.

[22] J. Juan-Alcañiz, M. Goesten, A. Martiñez-Joaristi, E. Stavitski, A. V. Petukhov, J. Gascon, F. Kapteijn, *Chem. Comm.* **2011**, *47*, 8578–8580.

[23] G. Férey, C. Serre, C. Mellot-Draznieks, F. Millange, S. Surblé, J. Dutour, I. Margiolaki, *Angew. Chem. - Int. Ed.* **2004**, *43*, 6296–6301.

[24] E. Stavitski, E. A. Pidko, S. Couck, T. Rémy, E. J. M. Hensen, B. M. Weckhuysen, J. Denayer, J. Gascon, F. Kapteijn, *Langmuir* **2011**, *27*, 3970–3976.

[25] A. C. Sudik, A. P. Côté, O. M. Yaghi, *Inorg Chem* **2005**, *44*, 2998–3000.

[26] J. Gascon, S. Aguado, F. Kapteijn, *Microporous Mesoporous Mater.* **2008**, *113*, 132–138.

[27] C. S. Tsao, M. S. Yu, T. Y. Chung, H. C. Wu, C. Y. Wang, K. S. Chang, H. L. Chen, *J. Am. Chem. Soc.* **2007**, *129*, 15997–16004.

[28] C. S. Tsao, M. S. Yu, C. Y. Wang, P. Y. Liao, H. L. Chen, U. S. Jeng, Y. R. Tzeng, T. Y. Chung, H. C. Wu, *J. Am. Chem. Soc.* **2009**, *131*, 1404–1406.

[29] M. Klimakow, P. Klobes, A. F. Thünemann, K. Rademann, F. Emmerling, *Chem. Mater.* **2010**, *22*, 5216–5221.

[30] J. Cravillon, C. A. Schröder, R. Nayuk, J. Gummel, K. Huber, M. Wiebcke, *Angew. Chem. - Int. Ed.* **2011**, *50*, 8067–8071.

[31] P. Debye, *Ann. Phys.* **1915**, *351*, 809–823.

[32] O. Glatter, O. Kratky, *Small Angle X-ray Scattering*. **1982**, Academic Press Inc. Ltd., London

[33] L. A. Feigin, D. I. Svergun, *Structure Analysis by Small-Angle X-ray and Neutron Scattering.* **1987** Plenum Press, NEw York

[34] J. Juan-Alcañiz, M. Goesten, A. Martiñez-Joaristi, E. Stavitski, A. V. Petukhov, J. Gascon, F. Kapteijn, *Chem. Commun.* **2011**.

[35] S. Couck, E. Gobechiya, C. E. A. Kirschhock, P. Serra-Crespo, J. Juan-Alcañiz, A. Martiñez-Joaristi, E. Stavitski, J. Gascon, F. Kapteijn, G. V. Baron, et al., *ChemSusChem* **2012**, *5*, 740–750.

[36] T. P. M. Beelen, W. H. Dokter, H. F. Van Garderen, R. A. van Santen, E. Pantos, *J. De Physique. IV : JP* **1993**, *3*, 393–396.

[37] P. P. E. A. De Moor, T. P. M. Beelen, R. A. van Santen, *Microporous Mater.* **1997**, *9*, 117–130.

[38] P. P. E. A. De Moor, T. P. M. Beelen, R. A. van Santen, L. W. Beck, M. E. Davis, *J. Phys. Chem. B* **2000**, *104*, 7600–7611.

[39] E. Stavitski, M. Goesten, J. Juan-Alcañiz, A. Martiñez-Joaristi, P. Serra-Crespo, A. V. Petukhov, J. Gascon, F. Kapteijn, *Angew. Chem. - Inter. Ed.* **2011**, *50*, 9624–9628.

[40] P. Serra-Crespo, E. V. Ramos-Fernandez, J. Gascon, F. Kapteijn, *Chem. Mater.* **2011**, *23*, 2565–2572.
[41] A. Violante, P. M. Huang, *Clays Clay Minerals* **1985**, *33*, 181–192.
[42] A. Violante, P. M. Huang, *Clays Clay Minerals* **1993**, *41*, 590–597.
[43] K. P. Prodromou, A. S. Pavlatou-Ve, *Clays Clay Minerals* **1995**, *43*, 111–115.
[44] M. Digne, P. Sautet, P. Raybaud, H. Toulhoat, E. Artacho, *J. Phys. Chem. B* **2002**, *106*, 5155–5162.
[45] A. Martiñez-Joaristi, J. Juan-Alcañiz, P. Serra-Crespo, F. Kapteijn, J. Gascon, *Crystal Growth & Design* **2012**, *12*, 3489–3498.
[46] C. Volkringer, D. Popov, T. Loiseau, G. Férey, M. Burghammer, C. Riekel, M. Haouas, F. Taulelle, *Chem. Mater.* **2009**, *21*, 5695–5697.
[47] H. Hatop, M. Ferbinteanu, H. W. Roesky, F. Cimpoesu, M. Schiefer, H. G. Schmidt, M. Noltemeyer, *Inorg Chem* **2002**, *41*, 1022–1025.
[48] P. Lemoine, A. Bekaert, J. D. Brion, B. Viossat, *Z. fur Kristallographie - New Crystal Structures* **2006**, *221*, 309–310.
[49] A. C. Sudik, A. P. Côté, O. M. Yaghi, *Inorg Chem* **2005**, *44*, 2998–3000.
[50] O. N. Temkin, *Homogeneous Catalysis with Metal Complexes: Kinetic Aspects and Mechanisms*, **2012** Wiley-VCH, New York
[51] Y. Zhao, D. G. Truhlar, *J. Chem. Phys.* **2006**, *125*.
[52] M. J. Frisch et al. (full: http://www.gaussian.com/g_tech/g_ur/m_citation.htm)
[53] M. Haouas, C. Volkringer, T. Loiseau, G. Férey, F. Taulelle, *Chem. Mater.* **2012**, *24*, 2462–2471.
[54] C. J. Y. Houssin, C. E. A. Kirschhock, Magusin, P.C.M.M., B. L. Mojet, P. J. Grobet, P. A. Jacobs, J. A. Martens, R. A. van Santen, *Phys. Chem. Chem. Phys.* **2003**, *5*, 3518–3524.
[55] H. H. Emons, M. Siedler, B. Thomas, A. Porzel, *Z. Anorg. Allg. Chem.* **n.d.**, *558*, 231–239.
[56] A. J. Hartel, P. P. Lankhorst, C. Altona, *Eur. J. Biochem.* **1982**, *129*, 343–357.
[57] I. S. Kislina, N. B. Librovich, V. D. Maiorov, E. G. Tarakanova, G. V. Yukhnevich, *Kinetics Catal.* **2002**, *43*, 671–674.
[58] M. G. Goesten, E. Stavitski, J. Juan-Alcañiz, A. Martiñez-Joaristi, A. V. Petukhov, F. Kapteijn, J. Gascon, *Catal. Today* **2013**, *205*, 120–127.
[59] K. S. Min, M. P. Suh, *J. Am. Chem. Soc.* **2000**, *122*, 6834–6840.
[60] M. C. Bernini, F. Gandara, M. Iglesias, N. Snejko, E. Gutierrez-Puebla, E. V. Brusau, G. E. Narda, M. A. Monge, *Chem. Eur. J.* **2009**, *15*, 4896–4905.
[61] D. Beaudoin, T. Maris, J. D. Wuest, *Nature Chemistry* **2013**, *5*, 830–834.
[62] T. Li, M. T. Kozlowski, E. A. Doud, M. N. Blakely, N. L. Rosi, *J. Am. Chem. Soc.* **2013**, *135*, 11688–11691.
[63] L. M. Liz-Marzán, *Langmuir* **2006**, *22*, 32–41.
[64] G. Q. Ding, W. Z. Shen, M. J. Zheng, W. L. Xu, Y. L. He, Q. X. Guo, *J. Crystal Growth* **2005**, *283*, 339–345.
[65] A. Quintanilla, M. Valvo, U. Lafont, E. M. Kelder, M. T. Kreutzer, F. Kapteijn, *Chem. Mater.* **2010**, *22*, 1656–1663.
[66] E. V. Ramos-Fernandez, C. Pieters, B. Van Der Linden, J. Juan-Alcañiz, P. Serra-Crespo, M. W. G. M. Verhoeven, H. Niemantsverdriet, J. Gascon, F. Kapteijn, *J. Catal.* **2012**, *289*, 42–52.
[67] S. H. Jhung, J. H. Lee, J. W. Yoon, C. Serre, G. Férey, J. S. Chang, *Adv. Mater.* **2007**, *19*, 121–124.
[68] A. Martiñez-Joaristi, J. Juan-Alcañiz, P. Serra-Crespo, F. Kapteijn, J. Gascon, *Crystal Growth & Design* **2012**, *12*, 3489–3498.
[69] R. Ameloot, F. Vermoortele, W. Vanhove, M. B. J. Roeffaers, B. F. Sels, D. E. De Vos, *Nature Chemistry* **2011**, *3*, 382–387.
[70] T. Tsuruoka, S. Furukawa, Y. Takashima, K. Yoshida, S. Isoda, S. Kitagawa, *Angew. Chem. - Int. Ed.* **2009**, *48*, 4739–4743.
[71] S. Diring, S. Furukawa, Y. Takashima, T. Tsuruoka, S. Kitagawa, *Chem. Mater.* **2010**, *22*, 4531–4538.
[72] A. Schaate, P. Roy, A. Godt, J. Lippke, F. Waltz, M. Wiebcke, P. Behrens, *Chem. - Eur. J.* **2011**, *17*, 6643–6651.
[73] A. Umemura, S. Diring, S. Furukawa, H. Uehara, T. Tsuruoka, S. Kitagawa, *J. Am. Chem. Soc.* **2011**, *133*, 15506–15513.
[74] Y. S. Li, H. Bux, A. Feldhoff, G. N. Li, W. S. Yang, J. Caro, *Adv. Mater.* **2010**, *22*, 3322–3326.
[75] Y. S. Li, H. Bux, A. Feldhoff, G. N. Li, W. S. Yang, J. Caro, *Adv. Mater.* **2010**, *22*, 3322–3326.
[76] C. Gücüyener, J. Van Den Bergh, J. Gascon, F. Kapteijn, *J. Am. Chem. Soc.* **2010**, *132*, 17704–17706.
[77] M. Goesten, E. Stavitski, E. A. Pidko, C. Gücüyener, B. Boshuizen, S. N. Ehrlich, E. J. M. Hensen, F. Kapteijn, J. Gascon, *Chem. - Eur. J.* **2013**, *19*, 7809–7816.
[78] N. S. Marinkovic, Q. Wang, L. Barrio, S. N. Ehrlich, S. Khalid, C. Cooper, A. I. Frenkel, *Nuclear Instruments and Methods in Physics Research, Section A: Accelerators, Spectrometers, Detectors and Associated Equipment* **2011**, *649*, 204–206.
[79] B. Ravel, M. Newville, *J. Synchrotron Radiation* **2005**, *12*, 537–541.
[80] J. Van Den Bergh, C. Gücüyener, E. A. Pidko, E. J. M. Hensen, J. Gascon, F. Kapteijn, *Chem. - Eur. J.* **2011**, *17*, 8832–8840.
[81] S. Kler, R. Asor, C. Li, A. Ginsburg, D. Harries, A. Oppenheim, A. Zlotnick, U. Raviv, *J. Am. Chem. Soc.* **2012**, *134*, 8823–8830.
[82] A. D. Becke, *Phys. Rev. A* **1988**, *38*, 3098–3100.

[83] M. J. Frisch et al. (see reference 52)

[84] J. Tomasi, B. Mennucci, R. Cammi, *Chem. Rev.* **2005**, *105*, 2999–3093.

[85] M. G. Goesten, E. Stavitski, J. Juan-Alcañiz, *Catal. Today* **2013**.

[86] B. L. Caetano, C. V. Santilli, F. Meneau, V. Briois, S. H. Pulcinelli, *J. Phys. Chem. C* **2012**, *116*, 4404–4412.

[87] M. Takahashi, H. Tanida, S. Kawauchi, M. Harada, I. Watanabe, *J. of Synchrotron Radiation* **1999**, *6*, 278–280.

[88] S. J. Borg, W. Liu, *Nuclear Instruments and Methods in Physics Research, Section A: Accelerators, Spectrometers, Detectors and Associated Equipment* **2010**, *619*, 276–279.

[89] M. C. Feiters, A. P. A. M. Eijkelenboom, H. F. Nolting, B. Krebs, F. M. I. Van den Ent, R. H. A. Plasterk, R. Kaptein, R. Boelens, *J. Synchrotron Radiation* **2003**, *10*, 86–95.

[90] K. Ozutsumi, M. Koide, H. Suzuki, S. I. Ishiguro, *J. Phys. Chem.* **1993**, *97*, 500–502.

[91] H. Suzuki, N. Fukushima, S. I. Ishiguro, H. Masuda, H. Ohtaki, *Acta Crystallographica Section C: Crystal Structure Commun.* **1991**, *47*, 1838–1842.

[92] M. J. Katz, Z. J. Brown, Y. J. Colón, P. W. Siu, K. A. Scheidt, R. Q. Snurr, J. T. Hupp, O. K. Farha, *Chem. Commun.* **2013**, *49*, 9449.

[93] J. H. Cavka, S. Jakobsen, U. Olsbye, N. Guillou, C. Lamberti, S. Bordiga, K. P. Lillerud, *J. Am. Chem. Soc.* **2008**, *130*, 13850–13851.

[94] K. E. Dekrafft, W. S. Boyle, L. M. Burk, O. Z. Zhou, W. Lin, *J. Mater. Chem.* **2012**, *22*, 18139–18144.

[95] S. Øien, D. Wragg, H. Reinsch, S. Svelle, S. Bordiga, C. Lamberti, K. P. Lillerud, *Crystal Growth & Design* **2014**, 141003125543007.

[96] G. C. Shearer, S. Chavan, J. Ethiraj, J. G. Vitillo, S. Svelle, U. Olsbye, C. Lamberti, S. Bordiga, K. P. Lillerud, *Chem. Mater.* **2014**, *26*, 4068–4071.

[97] L. Valenzano, B. Civalleri, S. Chavan, S. Bordiga, M. H. Nilsen, S. Jakobsen, K. P. Lillerud, C. Lamberti, *Chem. Mater.* **2011**, *23*, 1700–1718.

[98] F. Vermoortele, B. Bueken, G. Le Bars, B. Van De Voorde, M. Vandichel, K. Houthoofd, A. Vimont, M. Daturi, M. Waroquier, V. Van Speybroeck, et al., *J. Am. Chem. Soc.* **2013**, *135*, 11465–11468.

[99] M. Kandiah, M. H. Nilsen, S. Usseglio, S. Jakobsen, U. Olsbye, M. Tilset, C. Larabi, E. A. Quadrelli, F. Bonino, K. P. Lillerud, *Chem. Mater.* **2010**, *22*, 6632–6640.

[100] F. Vermoortele, R. Ameloot, A. Vimont, C. Serre, D. De Vos, *Chem. Comm.* **2011**, *47*, 1521–1523.

[101] M. B. Lalonde, O. K. Farha, K. A. Scheidt, J. T. Hupp, *ACS Catalysis* **2012**, *2*, 1550–1554.

[102] G. te Velde, F. M. Bickelhaupt, E. J. Baerends, C. Fonseca Guerra, S. J. A. van Gisbergen, J. G. Snijders, T. Ziegler, *J. Comput. Chem.* **2001**, *22*, 931–967.

[103] *www.scm.com*,

[104] C. Fonseca Guerra, J.-W. Handgraaf, E. J. Baerends, F. M. Bickelhaupt, *J. Comput. Chem.* **2004**, *25*, 189–210.

[105] E. Van Lenthe, E. J. Baerends, J. G. Snijders, *J. Chem. Phys.* **1994**, *101*, 9783–9792.

[106] E. Van Lenthe, R. Van Leeuwen, E. J. Baerends, J. G. Snijders, *Int. J. Quantum Chem.* **1996**, *57*, 281–293.

[107] I. Fernández, F. M. Bickelhaupt, *Chem. Soc. Rev.* **2014**, *43*, 4953–4967.

[108] S. Jakobsen, D. Gianolio, D. S. Wragg, M. H. Nilsen, H. Emerich, S. Bordiga, C. Lamberti, U. Olsbye, M. Tilset, K. P. Lillerud, *Phys. Rev. B* **2012**, *86*, 125429 EP –.

[109] U. Radius, F. M. Bickelhaupt, A. W. Ehlers, N. Goldberg, R. Hoffmann, *Inorg Chem* **1998**, *37*, 1080–1090.

[110] F. Ragon, P. Horcajada, H. Chevreau, Y. K. Hwang, U. H. Lee, S. R. Miller, T. Devic, J. S. Chang, C. Serre, *Inorg Chem* **2014**, *53*, 2491–2500.

[111] H. Landolt, *Ber. Dtsch. Chem. Ges.* **1886**, *19*, 1317–1365.

[112] M. Vandichel, J. Hajek, F. Vermoortele, M. Waroquier, D. E. De Vos, V. Van Speybroeck, *CrystEngComm* **2014**, DOI 10.1039/C4CE01672F.

[113] C. Larabi, E. A. Quadrelli, *Eur. J. Inorg. Chem.* **2012**, 3014–3022.

[114] E. Shustorovich, *Surf. Sci.* **1985**, *163*, L645–L654.

[115] R. Nielsen, in *Ullmann's Encyclopedia of Industrial Chemistry*, **2000**, Wiley-VCH, New York

[116] M. G. Goesten, P. C. M. M. Magusin, E. A. Pidko, B. Mezari, E. J. M. Hensen, F. Kapteijn, J. Gascon, *Inorg Chem* **2014**, *53*, 882–887.

[117] B. Szyja, A. Jansen, T. Verstraelen, R. Van Santen, *Phys. Chem. Chem. Phys.* **2009**, *11*, 7605–7610.

[118] C. Marschner, *Angew. Chem. Int. Ed.* **2007**, *46*, 6770–6771.

PART III

Post-Synthetic Functionalisation

MOFs offer a vast amount of possibilities for the inclusion of catalytically active moieties. Due to the hybrid (inorganic-organic) nature of the materials, new functionalities can be introduced at the inorganic metal cluster, or at the organic bridging ligand. For the latter case, three approaches have been successfully demonstrated: (1) synthesis of the MOF with a pre-functionalised linker (2) post-synthetic chemical functionalization of the framework and (3) post-synthetic ligand exchange in an appropriate solvent. When looking at covalently attached moieties of choice on the bridging ligand to obtain acid-functionality, options (1) and (3) are not always attractive, since functionalized ligands might coordinate at undesired sites (see: the sulfonic acid or sulfate moiety as discussed in **Chapter 6**), or hamper coordination and corresponding crystallization for reasons that are not always clear (**Chapter 1**). Option (2) matters post-synthetic functionalization (sometimes dubbed post-modification, post-synthetic modification abbreviated by PSM) is a very field in itself within the crystal engineering community, populated by chemists looking for suitable reactions aiming at targeted functionalities.

Many such functionalities can in principle be realized with classical organic chemistry, but this is not in all cases straightforward, as MOFs cannot withstand harsh reaction conditions, and are often constructed from deactivated struts (most exemplary, the terephthalate ligand). This field thus offers the unique challenge of finding, or even developing, mild yet efficient reactions towards targeted chemical functionality.

The third part of this thesis deals with this particular field within crystal engineering, namely the targeted chemical modification of the porous MOF crystals *after crystallisation.* **Chapter 6** deals with the implementation of an acidic sulfoxy group on the terephthalic acid linker of MIL-53(Al) and MIL-101(Al) via a new, mild sulfation procedure. The resulting MOFs, named S-MIL-53(Al) and S-MIL-101(Cr) were highly active in acid-catalysed esterification of *n*-butanol and acetic acid, apart from being efficient proton conductors. In **Chapter 7**, a chloromethyl group is introduced through a mild, non-toxic treatment of NH_2-MIL-53(Al) and MIL-101(Cr) crystals. The chloromethyl group is a popular, intermediate substitutent for further covalent substitution, and its use is demonstrated by the simple covalent attachment of a diphenylphosphine moiety.

This part is based on the following publications:

Chapter 6:	*Sulfation of Metal-Organic Frameworks: opportunities for acid catalysis and proton conductivity* M.G.Goesten, J. Juan-Alcañiz, E.V. Ramos-Fernandez, K. B. Sai Sankar Gupta, E.Stavitski, H. van Bekkum, Gascon,[*] F. Kapteijn, *J. Catal.* 281, **2011**, 177-178
Chapter 7:	*Chloromethylation as functionalisation pathway for Metal-Organic Frameworks* M.G. Goesten,[*] K. B. Sai Sankar Gupta, E.V. Ramos-Fernandez, H. Khajavi, J. Gascon,[*] F.Kapteijn, *CrystEngComm*, 14, **2012**, 4109–4111

The interested reader is also referred to the following co-authored papers on this subject, not included in this thesis:

Enhancing optical absorption of metal-organic frameworks for improved visible light photocatalysis

M.A. Nasalevich,* M.G.Goesten, Tom J. Savenije, F. Kapteijn, J. Gascon,* *Chem. Comm.* 49, **2013**, 10575-10577

Induced chirality in a metal–organic framework by post-synthetic modification for highly selective asymmetric aldol reactions

A.L.W. Demuynck, M.G. Goesten, E.V. Ramos-Fernandez, M. Dusselier, J. Vanderleyden, F. Kapteijn, J. Gascon* and B.F. Sels,* *ChemCatChem,* **2014**, 6, 2211-2214

6

Mild sulfation of MIL-101 and MIL-53 to obtain Brønsted-acid functionality

A new post-functionalization method for metal–organic frameworks (MOFs) has been developed to introduce Brønsted acidity. Upon treatment with a mixture of triflic anhydride and sulfuric acid, the chemically stable MOF structures MIL-101(Cr) and MIL-53(Al) can be sulfated, resulting in a Brønsted sulfoxy acid group attached to up to 50% of the aromatic terephthalate linkers of the structure. The sulfated samples, named S-MIL-53(Al) and S-MIL-101(Al) were extensively characterized by solid-state NMR, XANES, and FTIR spectroscopy. The functionalized acidic frameworks show catalytic activity similar to that of acidic polymers like Nafion® in the esterification of *n*-butanol with acetic acid (*TOF* ~ 1 min^{-1} @ 70ºC). Water adsorbs strongly up to 4 molecules per sulfoxy acid group, and an additional two water molecules are taken up at lower temperatures in the 1D pore channels of S-MIL-53(Al). The high water content and Brønsted acidity result in high proton conductivity up to moderate temperatures, for the case of S-MIL-53(Al).

Introduction

The limited chemical stability of MOFs does not allow for functionalization reactions requiring harsh conditions. Classical sulfonation, using concentrated sulfuric acid at 160ºC is thus not an option. Furthermore, terephthalato, perhaps the most used bridging ligand in MOF construction, is deactivated towards electrophilic substitution at the aromatic ring. Sulfonation or sulfation[1] of the aromatic ring therefore presents the tough challenge of substitution at a deactivated aromatic ring under mild conditions. Several groups have attempted at overcoming this challenge: Burrows *et al.* pioneered the incorporation of secondary sulfone moieties by using thiol-tagged linkers followed by a post-synthetic oxidation,[2] and Neofotistou *et al.* used a pre-modified linker already containing secondary sulfones: the ligand 4,4'-bibenzoic acid-2,2'-sulfone.[3] This last approach, however, does not introduce acid functionality. Along the same line, Britt *et al.* reported the post-synthetic modification of an amine containing MOF (IRMOF- 3) with sultones, resulting in the opening of the sultone ring and the formation of terminal sulfonic acid groups.[4] In spite of the elegance of this method, sultones are among the most hazardous chemicals, and therefore forbidden in most countries. Juan-Alcañiz *et al.* developed a pre-modified linker, introducing sulfonic acids, but the catalyst requires acid treatment after every step in order to be functional.[5]

In this chapter, a different approach is followed. Here, we report a room-temperature, homogeneously activated method to post-synthetically incorporate sulfoxyacid moieties into chemically and thermally stable MOFs (MIL-101(Cr)[6] and MIL-53(Al)[7]). Characterization demonstrates that the treatment of these stable MOFs with a mixture of sulfuric acid and trifluoromethanesulfonic anhydride (triflic anhydride), sulfoxyacid moieties are covalently bonded to the aryl carbons of the organic linker. The resulting functionalized MOFs (denoted as S-MIL-101(Cr) and S-MIL-53(Al)) display excellent acid-catalytic properties and high proton conductivity.

Experimental

Preparation of catalysts

All chemicals were obtained from Sigma–Aldrich and were used without further purification. MIL-53(Al) and Nafion® R50 (0.5 mm pellets) were also purchased from Sigma–Aldrich, while MIL-101(Cr) was synthesized following the procedure described elsewhere.[6] Stoichiometric sulfation was carried out with sulfuric acid in the presence of trifluoromethanesulfonic anhydride (triflic anhydride, Tf_2O), using nitromethane (CH_3NO_2) as solvent. The molar ratio used was: MOF-incorporated terephthalate : H_2SO_4 : Tf_2O = 1:1:1.5. The mixture was continuously stirred in a water bath at room temperature. After 60 min, the solid product was filtered off, rinsed with ultrapure water and acetone, soaked in ethanol for 24 h at 70ºC, and stored at 160 °C.

General characterization

Nitrogen sorption at 77 K was measured in a Quantachrome Autosorb-6B unit gas adsorption analyzer. The BET surface area was calculated between 0.05 and 0.15 relative pressure, and the pore volume at 0.95 relative pressure.

Water adsorption isotherms were measured using a Quantachrome Aquadyne DVS gravimetric water sorption analyzer.

X-ray diffraction (XRD) was done using a Bruker-AXS D5005 with Cu $K\alpha$ radiation.

Thermogravimetric analysis (TGA) of the MOFs was performed by means of a Mettler Toledo TGA/SDTA851e, under an airflow of 60 ml/min, at a heating rate of 5ºC/min up to 600 ºC (starting from room temperature).

The carbon and sulfur mass percentages (elemental analysis) in the MOF were measured in a Leco CS induction oven. The samples were burnt in a continuous stream of O_2, with the gases being analyzed by IR upon formation. The analysis is performed in duplicate after which the average concentration is obtained.

The infrared spectra were obtained using a Thermo Nicolet Nexus FTIR spectrometer. The samples (1 mg) were mixed with KBr and pressed into self-supporting pellets (50 mg/cm^2). Spectra were taken in transmission mode, using an in situ cell equipped with CaF_2 windows. Prior to the measurements, the samples were degassed in vacuum (10^{-5} mbar), at 200 ºC for 30 min to remove adsorbents.

Solid-state ^{27}Al, ^{13}C, and ^{1}H NMR studies were performed on a Bruker AV-750 spectrometer with a 17.6 T magnetic field, in which these nuclei resonate at 195.46, 188.64, and 750.13 MHz, respectively. A H/X/Y 2.5 mm MAS probe-head and a standard ZrO_2 were used. The rotor was spun at 20 kHz.

For the acquisition of ^{27}Al MAS spectra, the RF field frequency, pulse duration, number of scans, and repetition time were 55 kHz, 1.5 µs, 1024 scans, and 1 s, respectively. The corresponding parameters were 78.1 kHz, 3.2 µs, 32 scans, and 1s for ^{1}H MAS spectra. For ^{1}H to ^{13}C CPMAS with TPPM decoupling, we used 62.5 and 89 kHz RF field frequencies in the ^{13}C and ^{1}H channels, respectively for cross-polarization (CP). The contact time was 3 ms, and the repetition time was 2 s for 1024 scans. Chemical shift references (0 ppm) are $Al(NO3)3$ in aqueous nitric acid solution for ^{27}Al and TMS for ^{1}H and ^{13}C. ^{27}Al spectra were fitted with the DMFIT software package[8] to obtain approximations for quadrupolar coupling constant C_q and the asymmetry factor η.

The sulfur *K*-edge experiments were carried out at beamline X19b, National Synchrotron Light source (NSLS) at Brookhaven National Laboratory (Upton, New York). Powder samples were grinded to prevent scattering and then mounted on a 2.5-µm Mylar film to reduce the self-absorption effect that commonly occurs for thick samples with S content higher than 0.3 wt.%. The incident X-ray energy was scanned over the range from 2430 to 2500 eV with a step size of 0.25 eV. Elemental sulfur (99.998%, Sigma–Aldrich, USA) was used as reference. Sample fluorescence was measured using a PIPS (passivated implanted planar silicon) detector (Canberra Industries, CT).

Proton conductivity of S-MIL-53(Al) pellets was measured by AC impedance spectroscopy, using an Autolab PGSTAT302N over a range of 10^1–10^7 Hz with controlled voltage. The pellets, pressed at 5 ton/cm^2, approximately 13.5mm ± 0.9mm thick, were clamped between two pairs of electrodes and placed in a chamber under controlled humidity and temperature. Parent MIL-53(Al) was not analysed with impedance spectroscopy as this material could not be pelletized.The resistance R of the membrane was derived from the low intersection of the high-frequency semicircle on a complex impedance plane with the real Re(Z) axis. The conductivity is calculated using the relationship $\sigma = d/(R \times S)$, where σ is the conductivity in S cm^{-1}, σ the measured resistance of the membrane in Ω, d the distance between the two electrodes in cm, and S the contact surface, in cm^2. The values reported for σ are an average of at least three measurements.

The esterification of acetic acid and *n*-butanol was performed without solvent using a mixture with a molar ratio acetic acid/*n*-butanol = 1:1. The mixture was introduced in a roundbottom flask while being stirred under reflux. A ratio of 3 g catalyst per mol of acetic acid was used. After recovering the catalyst, it was filtered, stored at 150 °C, and reused without further activation procedure.

Results and discussion

Elemental analysis

After treatment of two spatially different MOF structures, MIL-101(Cr) and MIL-53(Al), using stoichiometric amounts of reactant H_2SO_4 for 60 minutes, a C/S weight ratio of 6 was determined by elemental analysis for MIL-53(Al). Assuming mono-sulfation, this would correspond to successful sulfation of a 50% of the aromatic terephthalato ligands. In the case of MIL-101(Cr), up to 20% of the linking terephthalate were mono-sulfated (one sulfoxyacid moiety per terephthalate linker) under similar reaction conditions. No sulfation was observed of MOFs treated only with Tf_2O or with H_2SO_4 under similar reaction conditions.

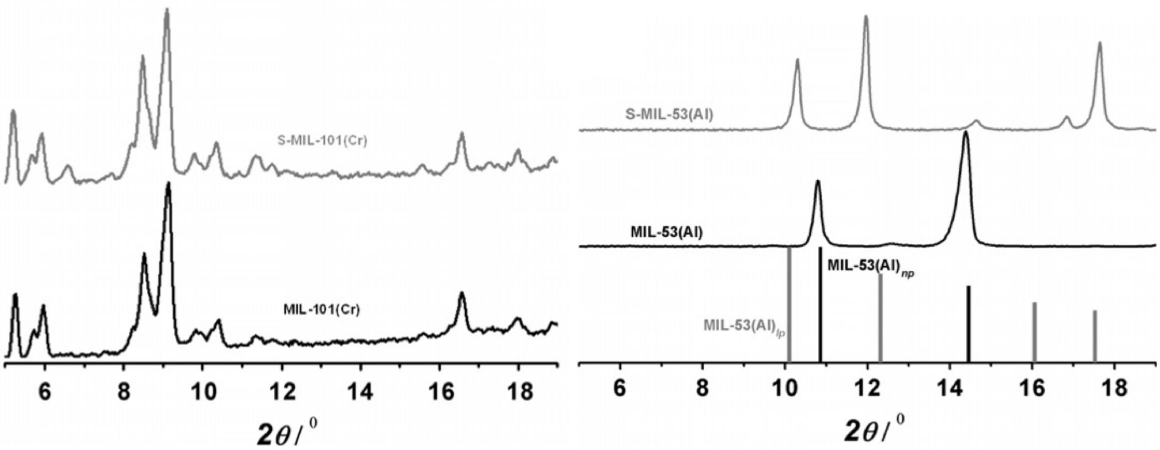

Figure 6.1 XRD patterns of MIL-101(Cr)/S-MIL-101(Cr), *left*, and MIL-53(Al)/S-MIL-53(Al), *right*. The bars on the image on the right are XRD simulations for the large-pore (*grey*) and narrow-pore (*black*) forms of MIL-53(Al).

X-ray diffraction (XRD)

XRD patterns of the sulfated samples (Figure 6.1) demonstrate that the framework integrity is preserved after this mild post-treatment. For the case of S-MIL-53(Al), the structure mainly resides in the large-pore form, attributed to a steric effect induced by the sulfoxy groups.

Thermogravimetric analysis (TGA)

TGA results indicate high thermal stability in air for the sulfated materials (Figure 6.2). Different profiles are obtained for Tf_2O-(MIL-53(Al)/MIL-101(Cr)) and H_2SO_4-(MIL-53(Al)/MIL-

101(Cr)), the species as-treated with triflic anhydride and sulfuric acid, respectively. Differential ThermoGravimetry (DTG) on S-MIL-53(Al)/MIL-53(Al) shows particular weight loss occurring at 282 °C, which matters the desorption step of water tightly bound to sulfoxyacid groups (this will be further discussed).

N_2 physisorption

Figure 5.3 depicts a comparison between the N_2 sorption isotherms of MIL-53(Al)/S-MIL-53(Al) and MIL-101(Cr)/S-MIL-101(Cr). The case of MIL-101(Cr) displays a decrease in specific surface area from ca. 2750 m^2/g to 2230 m^2/g, whilst the shape of the isotherm remains unchanged after the modification. In the case of MIL-53(Al), the framework is not open for N_2 at 77 K after sulfation, even after placement in high vacuum at 240 °C for 12h. This result points at a large decrease in the pore size of the MIL-53(Al) caused by the volume of the sulfoxy acid groups and their stacking after dehydration, together with the presence of residual water enclosed by the framework, as also shown in the TGA analyses (*vide infra).*

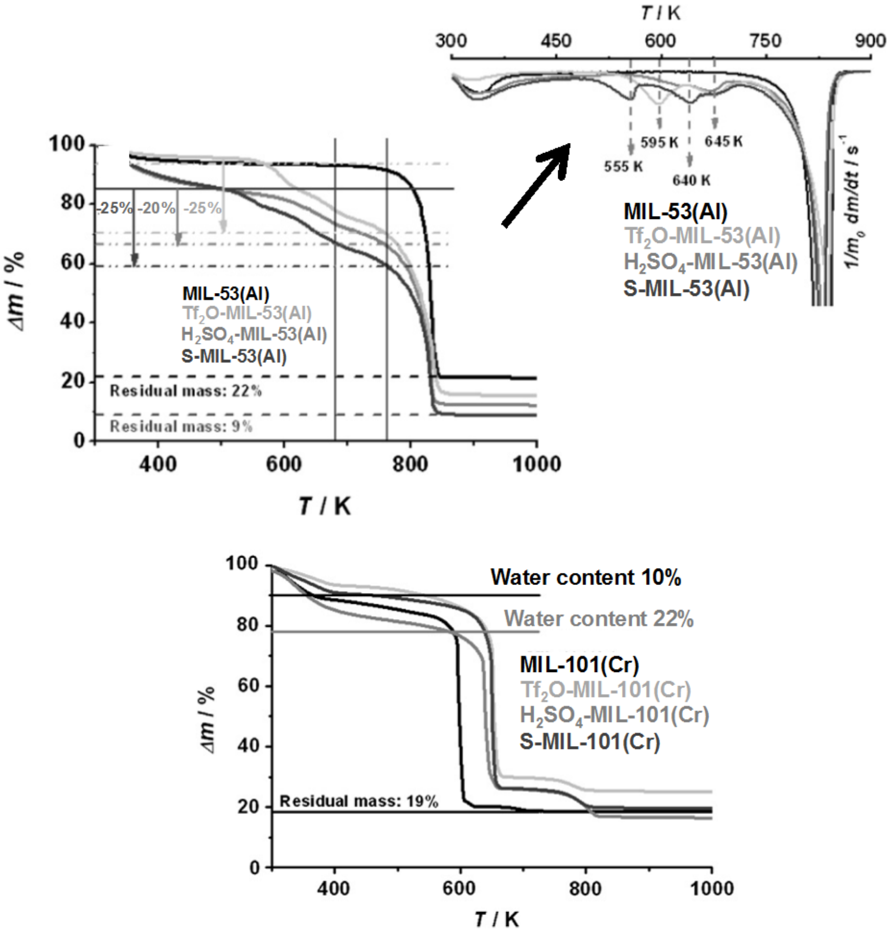

Figure 6.2 TGA analysis of the same samples in air at a heating rate of 5 K/min: samples as-treated with Tf_2O or H_2SO_4 are also shown for comparison. *Top*: MIL-53(Al)/S-MIL-53(Al)/Tf_2O-MIL-53(Al)/H_2SO_4-MIL-53(Al), *bottom*: MIL-101(Cr)/S-MIL-101(Cr)/Tf_2O-101(Cr)/H_2SO_4-101(Cr). The TGA of the MIL-53(Al) species is further analysed using DTG (Differential ThermoGravimetry), shown in the middle of the image and highlighted by the arrow.

H_2O vapour sorption

In order to demonstrate that after sulfation the MIL-53 framework retains its porosity, vapour sorption isotherms of H_2O at different temperatures were measured (figure 6.4). The sulfated sample did not show any N_2 uptake at -196 °C, a temperature in which molecular diffusion in microporous materials is often severely hampered, but water is able to access the pores at

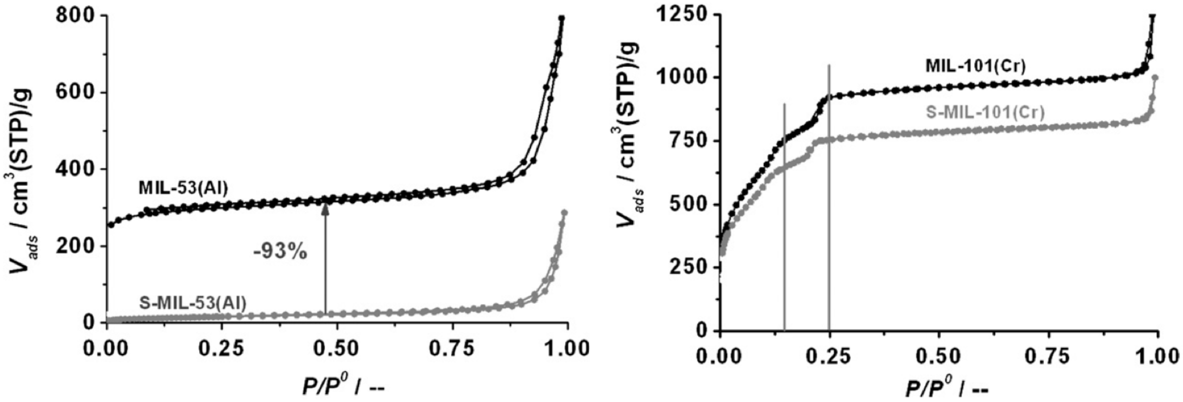

Figure 6.3 N_2 sorption isotherms at 77 K for MIL-53(Al)/S-MIL-53(Al), *left*, and MIL-101(Cr)/S-MIL-101(Cr), *right*.

higher temperatures. Adsorption/Desorption curves are obtained for 25 °C, 50 °C and 85 °C. Two steps are observed during water adsorption: the onset of the first step clearly depends on the temperature and shifts to lower relative humidities (*RH*) with increasing temperature, whilst the adsorbed amount decreases in the case of T = 85 °C. The second step occurs close to 100% RH for all cases, indicative of water condensation in the inter-particular voids.

In every case, a remarkable adsorption–desorption hysteresis occurs. The whole set of isotherms was determined with the same sample, demonstrating the chemical stability of the framework upon (de)hydration. These water isotherms are arguably unique for microporous materials and entirely different from the ones reported for non- or differently functionalized MIL-53(Al).[9] Interestingly, the sulfated sample adsorbs twice as much water as parent MIL-53(Al) and more than four times as much as amino-functionalised MIL-53(Al).[9]

InfraRed Spectroscopy (IR)

An intense IR study on the sulfated structures confirms the successful functionalization of both MOFs and shows up several interesting properties. Figure 5.5 displays a comparison

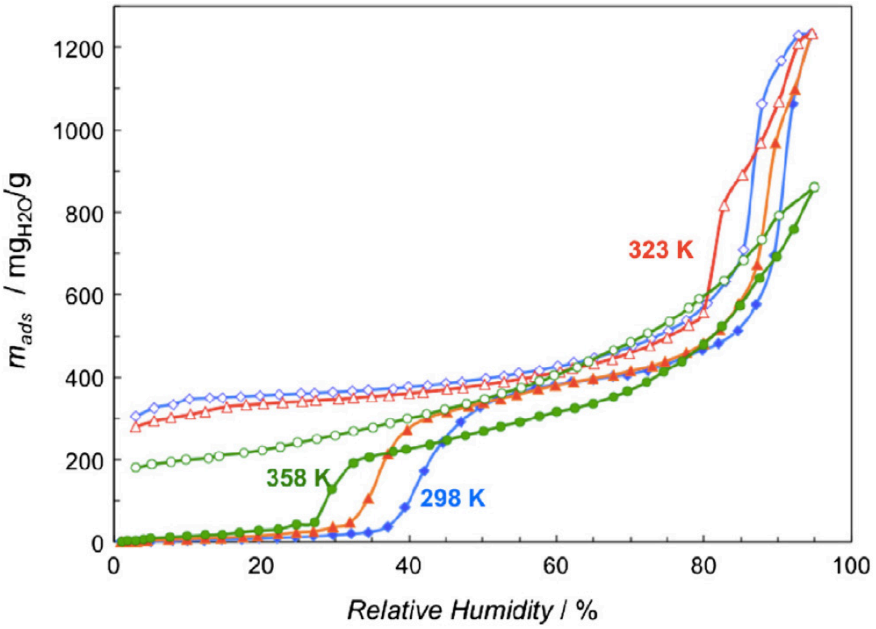

.

Figure 6.4 H_2O vapour sorption isotherms at 298K (blue), 323K(red) and 358K (green) for S-MIL-53(Al). Filled symbols form the adsorption path, open symbols the desorption path between parent and sulfated samples. Each material was pretreated under vacuum at 300 °C for 60 min. Clear differences are already revealed when observing the full spectra (4000–1000 cm^{-1}). The σ(OH) region (4000–3000 cm^{-1}) exhibits a broad band centered at 3400 cm^{-1} for the sulfated materials, which is absent in the parent samples. This vibration corresponds to water molecules held in the pores through strong hydrogen bond connections with the sulfoxyacid. Specific sulfoxyacid stretchings can be observed when zooming in at the region between 1800 and 1000 cm^{-1}. [10,11] In the case of MIL-101(Cr), new bands appear at 1170 and 1260 cm^{-1} alongside a shoulder at 1430 cm^{-1}, which can be attributed to the O=S=O symmetric and asymmetric stretching modes. [10,11] The peak at 1100 cm^{-1} corresponds to the in-plane skeletal vibration of the benzene rings substituted by a sulfoxyacid group, whereas the 1030 cm^{-1} band can be assigned to the S-O stretching vibration. [10,12]

In the case of S-MIL-53(Al), double and single S-O bond vibrations of sulfoxyacid groups are observed in the 1350–1000 cm^{-1} region. Upon pretreating the sample, the presence of large amounts of remaining water within the S-MIL-53(Al) framework is evident from the bands appearing in the 3500–2750 cm^{-1} region. The broad band at 3000–2900 cm^{-1} is related to the O-H vibration mode of sulfoxyacid groups associated with cyclic dimers.[12] It is straightforward to envisage that within the channel structure of S-MIL-53(Al), sulfoxyacid groups attached to opposite walls might interact with each other via hydrogen bonds, as reported for polymers with a high density of sulfonic acid groups.[12] When comparing the IR results with the TGA curves of S-MIL-53(Al) above, this strongly adsorbed water in the framework corresponds to the third desorption step at 555 K; water that is strongly coordinated to the sulfoxyacid moieties.

Figure 5.6 shows the comparison between the IR spectra of samples treated with Tf_2O/H_2SO_4 mixtures and samples treated with only one of the reactants (Tf_2O or H_2SO_4), focusing on two specific regions of the spectra, namely, 3800–3600 and 1550–950 cm^{-1}. Before recording, the samples were pretreated at 573 K for 60 min in order to remove weakly adsorbed water and to better differentiate between the spectral features. In the σ(OH) region, two main bands can be observed: MIL-53(Al) (Figure 6.6, left) reveals only one sharp stretching band at 3700 cm^{-1} related to ν(OH). This result is in line with previous reports, where this peak has been assigned to µ-hydroxido groups.[13] In the case of the modified samples, the stretching band at 3700 cm^{-1} remains, but its intensity decreases dramatically. Some µ-hydroxido groups are free, whilst others interact with guest molecules. Hydrogen bond formation between the µ-hydroxido groups and S=O or -OH moieties (of the sulfoxy groups, H_2SO_4 and Tf_2O) is thought to be the cause of a broad band between 3700 and 3660 cm^{-1} observed in the modified materials. The Tf_2O sample shows a higher intensity at 3660 cm^{-1} indicating a higher density of S=O bonds (four per (initial) molecule, whilst only two per moiety in the sulfated and H_2SO_4 samples).

In the 1550–950 cm^{-1} region, where several sulfoxyacid stretchings can be found, similar features are observed for the modified materials. The absorption maxima at 1290 and 1165 cm^{-1} are due to the symmetric and asymmetric S=O stretching vibrations, respectively. In contrast, the band at 1110 cm^{-1}, only appearing in the sulfated sample, is related to the benzene rings substituted with a sulfoxyacid group. These results are in agreement with the data obtained for S-MIL-101(Cr).

On basis of the catalytic activity (as discussed later) and the fact the sulfated, hydrated materials contain hydrated protons (hydronium ions),[14] IR spectroscopy was applied *in-situ* during dehydration for the various materials. At this point, it is of primary importance to show the main differences and similarities between samples sulfated and those treated only with H_2SO_4 or Tf_2O. Figure 5.7 shows the IR spectra recorded during the dehydration of the modified and parent materials. The samples were treated at specified temperature at vacuum for 10 min before spectra were collected. For the case of MIL-53(Al), one observes a breathing phenomenon upon hydration/dehydration, which involves atomic movements of ~5

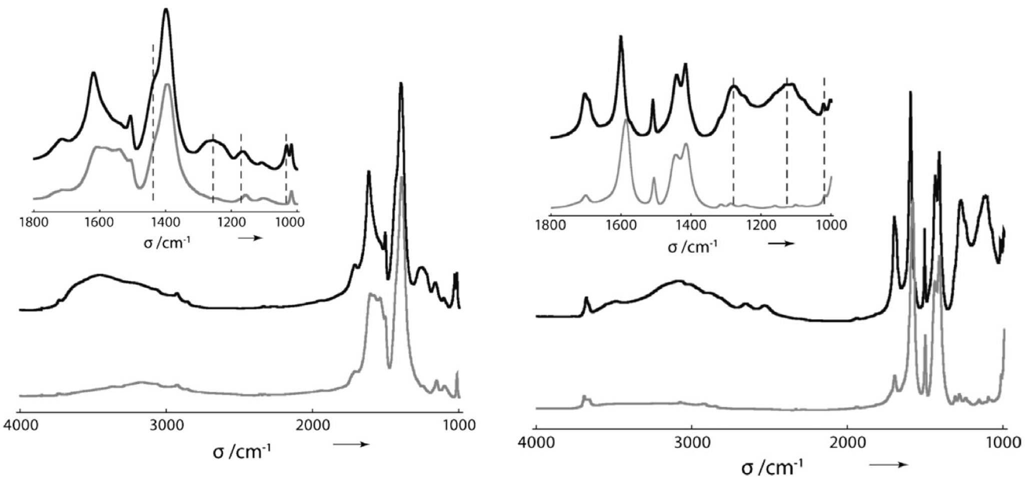

Figure 6.5 Transmission-IR spectra (T-IR) of MIL-53(Al)/S-MIL-53(Al), *left*, and MIL-101(Cr)/S-MIL-101(Cr), *right*. The 1000-1800 cm^{-1} regions with characteristic sulfate stretchings are magnified for both cases.

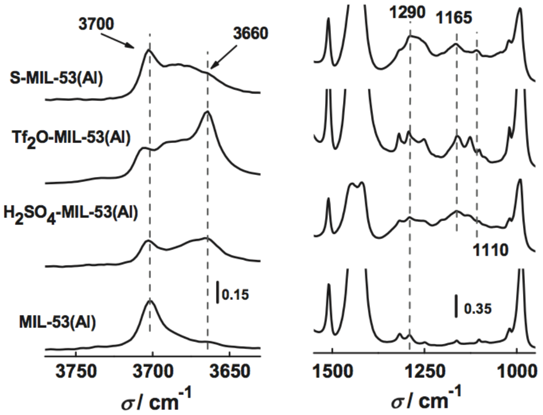

Figure 6.6 Infrared spectra in the regions 3800–3600 and 1500–1000 cm^{-1} for MIL- 53(Al) (sulfated, Tf_2O, and H_2SO_4) treated under vacuum.

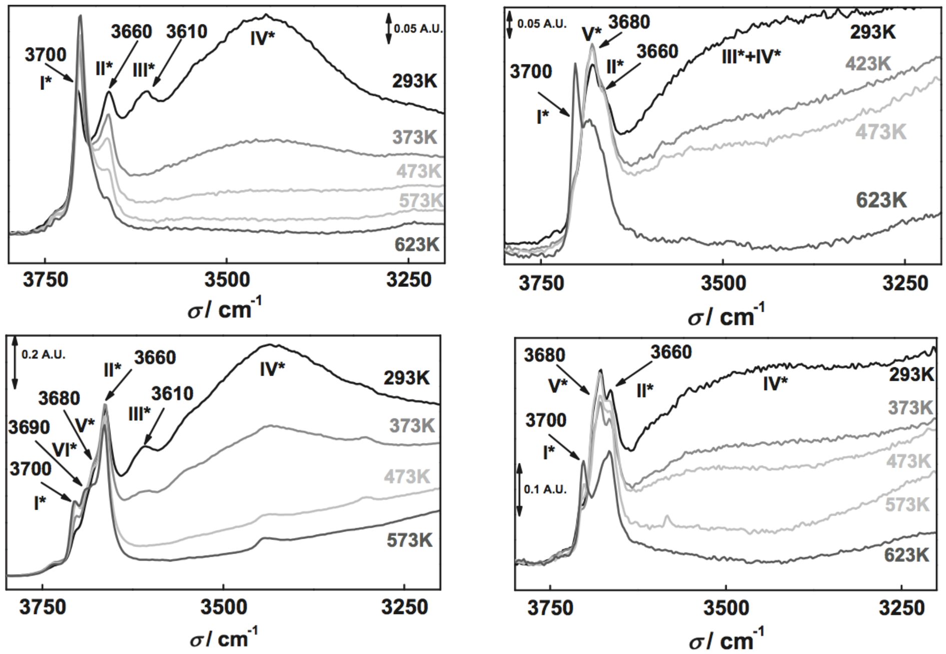

Figure 6.7 T-IR spectra of the *v*(OH) (3800–3200 cm^{-1}) region. IR study on dehydration by vacuum treatment and heating at at different temperatures. Running clockwise: Parent MIL-53(Al), S-MIL-53(Al), Tf_2O-MIL-53(Al) and H_2SO_4-MIL-53(Al).

Å. In the hydrated form, the pores are slightly deformed due to interactions between the hydrogen atoms of adsorbed water and the *μ*-hydroxido groups.[15] In vacuum at room temperature, three different types of –OH groups (I*, II* and III*) are present in the sample, apart from physisorbed water (IV*). The bands at 3660 (II*) and 3610 cm^{-1} (III*) can be assigned to interaction between the *μ*-hydroxido groups and water molecules in the pores.[16] In addition, the peak at 3700 cm^{-1} shows the ν(OH) of the μ-hydroxido group. In this situation, the pores of the structure are closed. After heating at 373 K under vacuum, the type III* groups have already disappeared with most of the broad water band. As pretreatment temperature increases, strongly adsorbed water moieties desorb (disappearance of the 3660 cm^{-1} band). At reaching 623 K under vacuum, only the 3700 cm^{-1} band (μ-hydroxido groups) remains. The second graph in figure 5.7 (clockwise), shows the spectra obtained upon dehydration of S-MIL-53(Al). At room temperature, two main bands appear: the –OH group at 3680 (type V*) and 3660 cm^{-1} (type II*). In addition, a shoulder is present at 3700 (type I*) related to the free μ-hydroxido group. Upon heating, type I* dominates the spectrum, whereas type II* and V* bands decrease drastically.

The third image (clockwise) of figure 5.7 displays the dehydration study of the H_2SO_4-MIL-53(Al) sample, showing similar behavior to S-MIL-53(Al). At room temperature, the main -OH bands observed are V* (at 3680 cm^{-1}) and II* (at 3660 cm^{-1}), with a shoulder at 3700 cm^{-1} (type I*) corresponding to free μ-hydroxido groups. When the pretreatment temperature increases, the absorbance at 3680 cm^{-1} decreases significantly, whilst the band at 3700 cm^{-1} is again visible, displaying a similar intensity as the also remaining band at 3660 cm^{-1}. Free μ-hydroxido groups are detectable again when most of the water is desorbed by dehydration (which is the third peak in the DTA in figure 5.2). Remaining -OH types V* and II* might be associated with -OH groups of H_2SO_4 interacting with water molecules and μ-hydroxido groups.

The fourth image shows the dehydration study of Tf_2O-MIL-53(Al). The main stretching band is observed at 3660 cm^{-1} (type II*) with a shoulder at 3680 cm^{-1} (type V*). No free μ-hydroxido groups at 3700 cm^{-1} (type I*) are observed. When the sample is heated, the band at 3680 cm^{-1} is shifted to 3690 cm^{-1}, while the 3660 cm^{-1} (type II*) band decreases in intensity and again the vibration at 3700 cm^{-1} (type I*) appears.

For the parent MIL-53(Al) and Tf_2O-MIL-53(Al) materials, the absorbance at 3610 cm^{-1} disappears upon heating at 373 K under vacuum. In addition, the broad band (centered at 3400 cm^{-1}) associated with ν(OH) of water moieties almost disappears.

For the case of H_2SO_4 and S-MIL-53(Al), the interaction of water with the hydroxyl groups exhibits different behavior. The peak at 3610 cm^{-1} is not visible due to a broader band centered at 3500 cm^{-1}, associated with the ν(OH) of adsorbed water. After pretreating the samples at 473 K under vacuum, the broad band centered at 3500 cm^{-1} is still visible, in contrast to the bare and Tf_2O-MIL-53(Al) samples, showing a much stronger interaction (red shift and desorption at higher temperatures) between water and -OH groups of sulfuric acid and sulfated groups.

NMR

In Figure 6.8, ^{13}C CPMAS NMR, ^{1}H MAS NMR, and ^{27}Al MAS NMR spectra of S-MIL-53(Al) and unfunctionalized MIL-53(Al) are shown. Similar analyses could not be performed on MIL-101(Cr) due to the paramagnetic nature of chromium. Because of this, relaxation is too fast to obtain an acquisition FID.

The ^{13}C CPMAS NMR spectrum shows the removal of free terephthalic acid by the disappearance of the peak at 174 ppm present in the commercial sample. An additional aromatic carbon peak, or rather, an extra shoulder at 132–133 ppm is visible.[17] Whether this signal is caused by the aromatic carbon bonded to the sulfate group remains unclear, since Loiseau *et al.* have reported a similar shoulder for as-synthesized MIL-53(Al).[7] In their paper, this shoulder only occurs for as-synthesized MIL-53(Al) as does the terephthalic acid peak at

173–174 ppm, which would suggest it is terephthalic acid giving rise to this signal, but in our case of the S-MIL-53(Al) no free terephthalic acid carbon signal is found. Peaks at 130 and 137 ppm are unfunctionalized aryl carbons bonded to protons.

The ^{1}H MAS NMR spectrum is much more relevant, with an acidic proton signal at 13–14 ppm. Theoretically, this proton signal could be attributed to free terephthalic acid, but ^{13}C

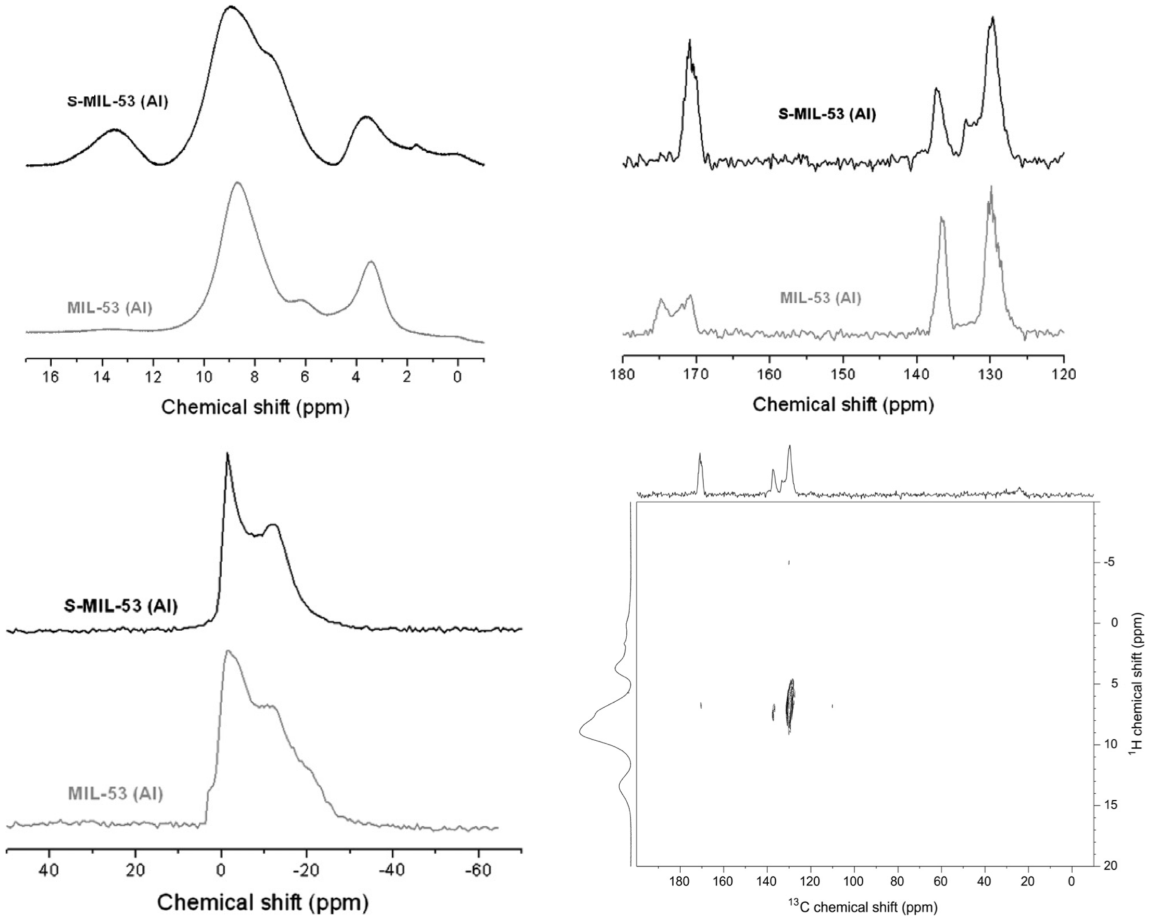

Figure 6.8: *Clockwise*: ^{1}H MAS NMR of MIL-53(Al)/S-MIL-53(Al), ^{13}C CPMAS NMR of MIL-53(Al)/S-MIL-53(Al), ^{27}Al MAS NMR of MIL-53(Al)/S-MIL-53(Al) and ^{1}H-^{13}C HETCOR NMR of S-MIL-53(Al).

CPMAS experiments and ^{1}H-^{13}C HETCOR experiments (the third image in Figure 6.8) rule this out.

As convincingly shown with XANES, *vide infra*, it is most probable that that we deal with a sulfate proton. In ^{1}H MAS NMR, an extra proton peak at 1.7–1.8 ppm is visible too, which is in perfect correspondence with Al-OH-Al proton signals for heated MIL-53(Al) in Loiseau's work. Apart from that, the peak caused by framework-coordinated water, at 6 ppm, for the unfunctionalized sample, is more intense and shifted to a higher chemical shift (~8 ppm) for the sulfated sample. This can be explained by the sulfated sample coordinating more water with respect to the unfunctionalised sample; sulfate-coordinated water protons are slightly more deshielded, giving rise to a larger chemical shift.

^{27}Al MAS NMR shows interesting results as well as a duplet of peaks is obtained, due to quadrupolar coupling. The line shape can be fitted in order to yield values for the quadrupolar coupling constant (and asymmetry factor). Upon fitting, a quadrupolar coupling constant of 12.6 MHz is obtained which is significantly larger than the 8.5 and 9.2 MHz coupling constants reported by Lieder *et al.*[18] in their NMR analysis of MIL-53(Al) with different adsorbents. Quadrupolar coupling constants for solids are correlated with electronic field gradients within the crystal, and it would be reasonable to suppose that sulfoxyacid groups, binding in a non-symmetric way from the crystallographic perspective, enlarge electric field gradients and therefore quadrupolar coupling constants.

Finally, ^{1}H-^{13}C HETCOR NMR (Figure 6.8, right bottom) shows that the acidic proton signal is not coming from terephthalic acid, since no cross coupling-peak is visible in that region. The distance between aryl carbons and sulfoxy acid protons is too large to transfer magnetization and obtain cross-correlation.

XANES – X-ray absorption at the sulfur *K*-edge

So far, we have shown the successful functionalization of two frameworks with sulfur-containing acidic species. However, the real nature of these sulfur species is not clear yet; it must now be stated that our initial aim was electrophilic aromatic sulfonation of the bridging ligand, (formal oxidation state of sulfur +5) rather than electrophilic aromatic sulfation (formal oxidation of sulfur +6). Sulfur *K*-edge absorption spectra were recorded in the samples with the higher degree of functionalization: S-MIL-53(Al). Sulfur *K*-edge absorption spectra are very sensitive to electronic structure, oxidation state, and the symmetry of the absorbing site. In particular, the position of the white line is a very accurate indicator for the oxidation state, spanning from ~11 eV from 2469 eV for cystine (S^{2-}) to 2483 eV for inorganic sulfates (S^{6+}).[19]* The line shape (features in the pre-edge and post-edge regions) may also be used for the identification of the sulfur-containing compounds. The traditional approach for speciation of multicomponent mixtures involves creation of a spectral library of the possible components and analysing the experimental spectra as their linear combination.[19,20] We, however, limit ourselves to determination of the sulfur oxidation state in the sulfated MOF. The XANES region of the *K*-edge absorption spectra for S-MIL-53(Al) is shown in Figure 6.9. Comparison of the white line position (2483 eV) with results reported in the literature[19,20] points out the +6 oxidation state of sulfur (sulfate). This assumption is supported by experimental spectra of $(NH_4)_2SO_4$ obtained under similar conditions (Figure 6.9b) as well as the spectrum of the relevant organic compound chondroitine sulfate, fig 6.9c.[21] In all three cases, the absorption maximum appears at nearly the same position. For the organic sulfonate group

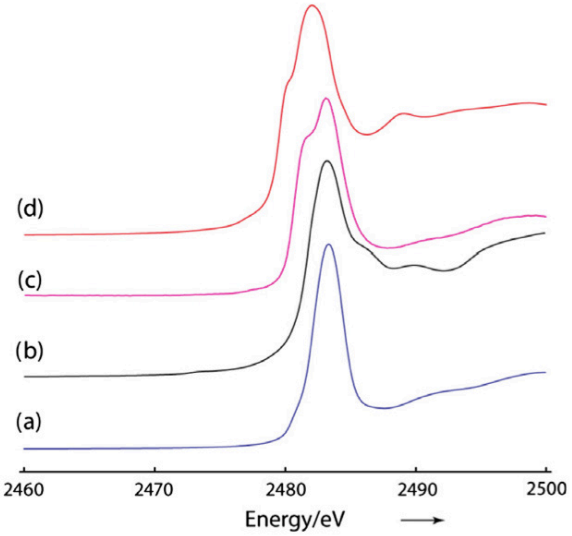

Figure 6.9: Sulfur *K*-edge XANES spectra of (a) S-MIL-53, (b) $(NH_4)_4SO_4$, (c) chondroitine sulfate and (d) Amberlyst®. Spectra (a), (b) and (d) are recorded in this work, spectrum (c) is adapted from Cuif et al.[21] All data had been normalized to the height of the white line.

---

[*] Please bear in mind that this is a *formal* oxidation state, determination of the real oxidation state matters a specialised study. Sulfur is in almost all cases in this chapter *hypervalent*, the chemistry of hypervalent compounds is to limited extent discussed in Chapter 2 in this thesis, but will be treated by the author in more detail in the future, for more elements to come.

C-SO_3H, one would expect a shift to lower energy by ~1.5 eV. This is confirmed, as the spectrum of Amberlyst-15 (sulfonic-acid-functionalized polystyrene) shows a shift of 1.3 eV (Figure 6.9d).

Proton conductivity

Impedance spectroscopy was performed on S-MIL-53(Al) to characterize its proton conduction properties and to compare them with those of acidic polymers. It turned out that the conductivity of a pellet as a function of temperature in the presence of N_2 saturated with H_2O at room temperature (Figure 6.9) lies in the order of magnitude of Nafion® and is several orders of magnitude higher than those reported for other proton-conducting MOFs, although those were measured under dry conditions.[22] Above 80°C, however, the conductivity drops considerably. This suggests that, if water is only adsorbed at the bisulfate groups and not filling up the rest of the framework space, the proton conductivity decreases dramatically. Arguably, in this case, protons can only be conducted through the grain boundaries but not through the dry framework.

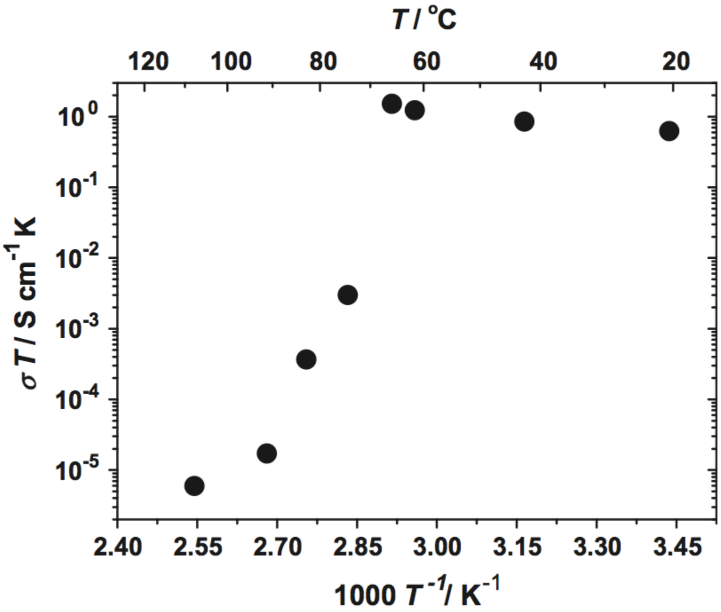

Figure 6.10: Conductivity of HSO_4-MIL-53(Al) framework as measured by impedance spectroscopy at different temperatures in the presence of *humid* N_2 (1.5 wt.% H_2O).

Esterification of *n*-butanol and acetic acid

The catalytic activity of the functionalized frameworks was benchmarked against Nafion® with the liquid-phase, stoichiometric esterification of *n*-butanol and acetic acid at low temperatures (70 °C). The yield of the only reaction product, butyl acetate, is obtained using the same weight ratio (3 g/mol reactant) of S-MIL-53(Al) and S-MIL-101(Cr) and Nafion® NR50. The functionalised samples show high catalytic activity in the first run, due to adsorbed Tf_2O and/or H_2SO_4, which are very difficult to eliminate except for reaction conditions. Hence, the performance shown in Figure 6.11 is related to the second use of the catalysts in case of the sulfated MOFs and compared with the first use of Nafion® NR50 as standard acid resin. Functionalized S-MIL-53(Al) displays outstanding performance as acid catalyst and can be recycled without significant loss of activity (Figure 6.11).

Experiments with unfunctionalised MIL-53(Al) show the same conversion profile as the blank run, demonstrating that the catalysis can be attributed to the presence of sulfoxyacid groups within the framework, and not the framework itself.

The second image in figure 6.11 compares the second use (first re-use) of S-MIL-53(Al) of the same material treated with only one of the reactants (Tf_2O or H_2SO_4). Whilst S-MIL-53(Al) maintains its outstanding performance, Tf_2O and H_2SO_4-MIL-53(Al) drop in activity due to desorption of the active species. These results underline the presence of stable active sites in S-MIL-53(Al) formed by the combination of Tf_2O and H_2SO_4 in the sulfation procedure. A slightly higher turnover frequency (*TOF*) per acid group is found for the MOF: 1.0 mol of acetic acid reacts per mol of sulfur per minute against 0.6 for the acidic resin (Table 1). This *TOF* is maintained even after 5 re-uses of the S-MIL-53(Al) catalyst. In the case of S-MIL-101(Cr), a lower *TOF* and activity on a weight basis are obtained, while for samples treated only with Tf_2O or H_2SO_4 , no permanent activity was found at all.

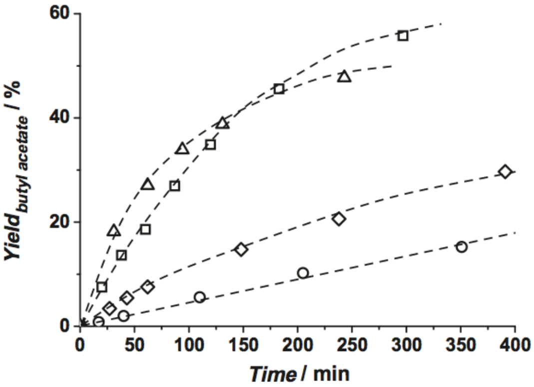

Catalyst	*TOF* $mol^{react}\ mol_S^{-1}\ min^{-1}$
NAFION NR50	0.63
S-MIL-53(Al) 2nd	1.04
S-MIL-53(Al) 3rd	0.98
S-MIL-53(Al) 4th	0.72
S-MIL-53(Al) 5th	0.85
S-MIL-101(Al) 2nd	0.55

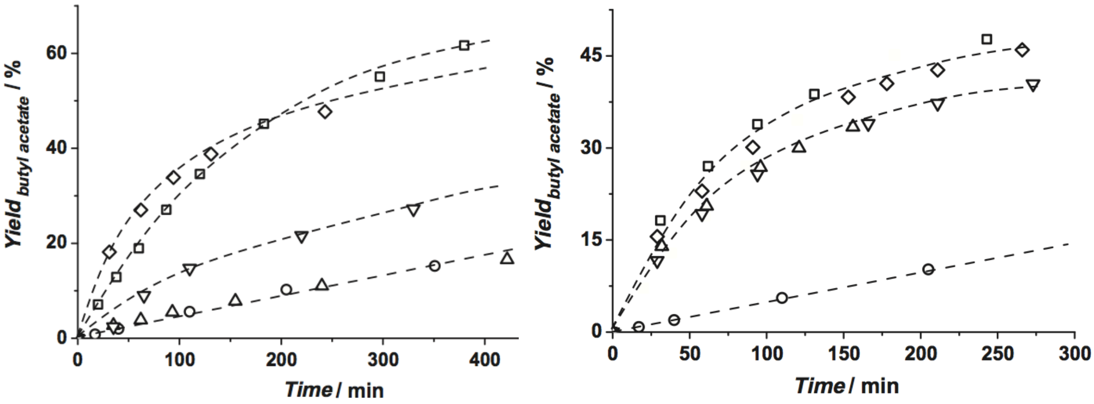

Figure 6.11: Top left: esterification of acetic acid with n-butanol (molar ratio 1:1) at 70 ºC with 3 g of catalyst per mol of acetic acid, (*rectangle*) Nafion NR50; (*triangle*) S-MIL-53(Al); (*diamond*) S-MIL-101(Cr) and (*circle*) blank run (*no catalyst*).

Top right: table Summary of *TOF* values obtained in esterification of acetic acid with n-butanol (molar ratio 1:1) at 70 ºC with 3 g of catalyst per mol of acetic acid. *TOFs* are based on butyl acetate production after 30 reaction minutes and per mol sulfur for the different samples and reuses.

Down right: esterification of acetic acid with *n*-butanol (molar ratio 1:1) at 70 ºC with 3 g of catalyst per mol of acetic acid. Yield of butyl acetate as a function of time. (*rectangle*) First reuse S-MIL-53(Al); (*diamond*) second reuse (*triangle upside down*); third reuse; (*triangle*) fourth reuse and (*circle*) blank run (no catalyst).

Down left: Esterification of acetic acid with *n*-butanol (molar ratio 1:1) at 70 ºC with 3 g of catalyst per mol of acetic acid. Yield of butyl acetate as a function of time. (*rectangle*) Nafion NR50; (*diamond*) first reuse S-MIL-53(Al); (*triangle upside down*) first reuse H_2SO_4-MIL-53(Al); (*triangle*) first reuse Tf_2O-MIL-53(Al) and (*circle*) blank run (no catalyst).

Discussion

The extensive characterization of the functionalized samples demonstrates that it is possible to sulfate stable MOF scaffolds under relatively mild conditions. It has to be stressed that the applicability of this method is limited to MOFs with high chemical stability, similar treatment performed on chemically less stable MOFs as UiO-66[23] or MIL-68[24] resulted in the destruction of the MOF.

The presence of sulfoxyacid moieties attached to the aromatic ring within the functionalized frameworks after post-synthetic treatment is demonstrated by NMR and XANES analyses supported by IR evidence (from O=S=O and S-O stretching vibrations).

From dehydration and IR experiments it appeared that the interaction of sulfated samples and samples with adsorbed H_2SO_4 with H_2O and the -OH groups of the structure is, as expected, very similar. However, the new band at 1100 cm^{-1} only appearing in the case of S-MIL-53(Al), together with the NMR results and the fact that for samples only treated with H_2SO_4, catalytic activity disappears after thorough washing of the material demonstrates that aryl carbon functionalization only takes place when a mixture of Tf_2O and H_2SO_4 is used.

As derived from comparison between the sulfur *K*-edge absorption spectra of the S-MIL-53(Al) sample and the different standards, it is clear that the formal oxidation state of sulfur in the MOF sample is +6 rather than +5. The XANES line shape (featuring in the pre-edge and post-edge regions) is similar to those reported for aryl sulfates (chondroitine sulfate). Together with the absence of any terephthalic acid species in the functionalized material, which is confirmed by ^1H-^{13}C HETCOR and ^1H NMR, this points at sulfoxy acidity. ^{27}Al MAS NMR shows that no aluminium salt residue is present in the sulfated framework and hence no sulfated aluminium oxide clusters. Partial destruction of the framework and possible sulfation of the linker at the carboxylic group should also be also discarded since it would result in partially coordinated aluminium that should be well visible in the MAS NMR spectra.

The mechanistic side of the reaction deserves some special care since we in all likelyhood deal with the implementation of a non-ordinary electrophile, OSO_3H^+. The first step is likely to matter traditional triflic anhydride chemistry in which triflic anhydride reacts with sulfuric acid to produce the mixed anhydride $HOSO_2$-O-SO_2CF_3. This mixed anhydride then rearranges to leave the electrophile via an unknown pathway.

The most common approach for the construction of aryl sulfoxyacids is sulfation of hydroxyl group-containing aromatics using sulfur trioxide–amine complexes or chlorosulfuric acid.[25] Due to high reactivity of the hydrogen sulfoxy acid proton, sulfated organics are usually produced in the form of alkaline sulfates and it is not common to find sulfate-containing organic compounds. In contrast, when such groups are anchored to porous solids, like inorganic oxides, it has been shown that both SO_4^{2-} and HSO_4^- species are present at the catalyst surface, resulting in a mixed Lewis–Brønsted acid. For example, in the case of sulfated zirconia, the positive charge of exposed Zr^{4+} cations is enhanced by the electron–acceptor nature of adjacent SO_4^{2-} groups and results in stronger Lewis acid centers, while hydrogen sulfate/sulfoxy groups and OH^- groups interacting with electron acceptors such as adjacent Zr^{4+} cations have been identified as Brønsted acid sites.[26] In the functionalisation of the MOFs, the combination of Tf_2O and sulfuric acid allows for direct formation of sulfoxyacid moieties covalently attached to the aromatic linkers, while the porosity of the material stabilizes the acidic proton of the sulfoxyacid groups, by interacting and stabilizing its charge in the spatial environment. The sulfoxyacid groups in the MOFs present good thermal stability. TGA analysis indicates that such functionalities are stable up to 282 °C. However, their chemical stability needs attention; a S-MIL-53(Al) sample was boiled in water at pH 10 for 12 h leaving only OH groups after hydrolysis.

When it comes to the properties of the sulfated materials, the effect of functionalization on the MIL-53(Al) framework is specifically interesting. MIL-53 is the best-known example of flexible MOFs, which, depending both on the presence of guests and temperature, transforms from a narrow pore (‘closed’) to a large pore (‘open’) form with a variation of the cell volume without any bond breaking.[13] The adsorption of water (Figure 6.4) is responsible for the switch between the open and the closed structure, with hydrogen bonding interactions playing the primary role.[7] The difference between this ‘breathing’ behavior among differently functionalized MIL-53 frameworks and the consequences for separation have recently been reported, demonstrating that the presence of functional organic sites at the aromatic rings strongly disturbs the framework breathing.[27,28] In the case of S-MIL-53(Al), strong hydrogen bonding already occurs in the absence of water. This is in line with the TGA and IR results showing desorption of water at high temperatures and with the XRD pattern depicted in figure 5.1: after pretreating the sulfated sample at 373 K in inert atmosphere, most of the structure remains in the narrow pore form, as concluded from the half-open/half-closed crystallographic pattern.[29] Only Kusgens *et al.*[30] reported a somewhat similar isotherm for the metal–organic framework DUT-4, but in that case, the shape of the isotherm was related to the irreversible collapse of the framework through the addition of water. We attribute the first step in the isotherm to the breathing of the framework: in the low-temperature isotherm, up to six molecules of water are reversibly adsorbed per sulfoxyacid group. The uptake at the highest temperature (85 °C) corresponds to ca. four water molecules per sulfoxyacid moiety. This demonstrates that at lower temperatures, water is adsorbed both at the sulfoxyacid sites, but also in the remaining pore space,[31] as seen before by de Lange et al., while at increased temperatures, only the sulfoxyacid groups are able to attract water. These adsorption results match the TGA data very well, where similar amounts of released water were observed after sample exposure to ambient conditions. In both cases, the framework has to expand to accommodate for the water. In the case of samples treated only with H_2SO_4 or Tf_2O, slightly different TGA profiles are found: none of them show the first H_2O desorption step at around 282 °C, related to strongly bonded water to sulfoxyacid moieties. The proton conduction mechanism in hydrated S-MIL-53(Al) may be understood as dissociation of the proton from the sulfoxy acid site, transfer of the proton to the aqueous medium, screening by water of the hydrated proton from the conjugate base (sulfoxyanion), and diffusion of the proton in the confined water within the MOF. Regrettably, when the presence of water within the pores of the material decreases, the proton conductivity is lost as the continuous water phase is broken up.

The catalytic results presented in Figure 6.11 demonstrate the high activities of the sulfated MOFs, specifically those of the MIL-53(Al) framework, where similar activities to those of Nafion® are found. These results demonstrate that, when anchored to an ordered structure, sulfoxy acid groups are stable and display high acidity. Whether the breathing behavior of S-MIL-53(Al) affects the catalytic performance is not clear. For instance, MIL-53(Fe) breathes through adsorption of different solvents, but the extent of breathing varies upon the nature of the solvent.[32] With regard to the pore opening observed through water adsorption (Figure 6.4), it is reasonable to assume that the S-MIL-53(Al) framework will be in it's large-pore form, in the reaction mixture, ensuring full accessibility of sulfoxyacid groups within the channels.

Conclusion

A new post-synthetic functionalization method for metal–organic frameworks has been developed. Upon treatment at room temperature with a stoichiometric mixture of triflic anhydride and sulfuric acid, it is possible to sulfate the aromatic ring of the terephthalic linker in stable MOF structures. The applicability of this method is limited to MOFs with high chemical stability like MIL-53(Al) and MIL-101(Cr).

The functionalized frameworks, of which up to 50% of their aromatic ligands are sulfated, show outstanding acid-catalytic activity in esterification and thermal stability superior to those of popular acidic resins. Furthermore, S-MIL-53(Al) displays high proton conductivity up to moderate temperatures with adsorbed water acting as conductor in a continuous phase.

7

Chloromethylation as generic post-synthetic functionalisation pathway

A mild and safe chloromethylation of terephthalate-based metal-organic frameworks is presented. After this post-synthetic functionalization, the chlorine of the chloromethyl group can be substituted by a wide range of moieties to obtain various multifunctional materials. The method can in principle be extended to other coordination polymers with exposed aromatic rings.

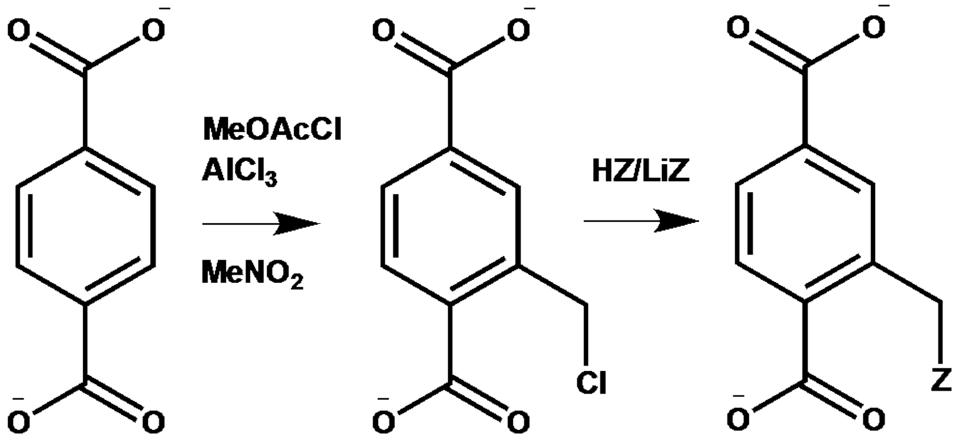

Figure 7.1: Concept of chloromethylation, Z represents a nucleophilic functionality of choice.

Introduction

Much of the work in post-synthetic modification of Metal-Organic Frameworks relies on modification of amine groups on the linker, and despite the effectiveness of these methods, potential amine activity is lost and some of the resulting functionalities are likely to be unstable in protonating environments.[33]

In this chapter, a chloromethylation (CM) procedure for aromatic MOFs and other coordination polymers is presented as a generic route to implement functionalities; CM leaves a reactive chlorine atom, which can be exchanged by virtually any nucleophilic group of choice through an S_n reaction. This can be used to synthesize materials with stable C_{aryl}–CH_2–Z based functionalities, with Z being the functionality of choice (figure 7.1).

Chloromethylation (CM) is a widely applied route towards implementation of functionalities in polymers.[34] Traditional CM methods are based on formaldehyde/hydrochloric acid mixtures, which may not only be too violent for the integrity of metal–organic frameworks, but also proceed through formation of highly carcinogenic intermediates.[35]

In this chapter, a mild and safe route is used to introduce chloromethylene groups in NH_2-MIL-53(Al) and MIL-101(Cr) through reaction of MOF-incorporated terephthalate or 2-aminoterephthalate with methoxyacetyl chloride and aluminium chloride. The use of this reactant system was earlier proposed and applied to a selected group of aromatics in homogeneous phase by McKillop et al.[36] Here, CM is carried out on MOF crystals. NH_2-MIL-53(Al) is used as a target framework for analysis as it allows for sound solid-state NMR analysis[37] and can act as target material in demonstrating the possibility of introducing multifunctionality (in having both CM and amino moieties attached to the MOF strut).

As proof of concept, chloromethylation is carried out on MIL-101(Cr) followed by the introduction of diphenylphosphine (PPh_2).

Experimental

MOF Synthesis

All chemicals were obtained from Sigma-Aldrich and used without further purification. Amino MIL-53 (Al) was synthesized mixing 1.97 g aluminium chloride hexahydrate, 1.50 g 2-aminoterephthalic acid, and 20.00 g distilled water in a Teflon insert, which is placed in an autoclave. The closed autoclave is heated for 8 h at 150°C. The resulting yellow powder is filtered off and washed in the same autoclave with DMF at 150°C overnight.

MIL-101(Cr) was synthesized mixing 1.63 g chromium nitrate hexahydrate, 0.97 g terephthalic acid, 0.20 g hydrofluoric acid (60%) and 12 g water in a Teflon insert, which is placed in a microwave autoclave. The mixture is heated in a microwave to 210°C within 4 min and kept for 45 min at that temperature. The resulting green powder is filtered off and washed in DMSO at 80°C overnight.

Chloromethylation

	NH_2-MIL-53(Al)	MIL-101(Cr)
$AlCl_3\cdot 6H_2O$ (g)	1.1	1.9
Methoxyacetyl chloride (g)	0.7	0.4
Nitromethane (g)	80	80
Temperature/duration (°C/h)	75/3	100/5

Table 7.1 Reactant/solvent amounts and conditions of chloromethylation

The reaction is carried out under reflux with continuous stirring. It is necessary to use the hexahydrate form of aluminium chloride as it offers protons required for initiation; dry conditions with dry $AlCl_3$ did not yield chloromethylated MOF. The reason MIL-101(Cr) has to be chloromethylated under harsher conditions lies in the absence of activating amino species in the aromatic ring to be chloromethylated. Any solid product of chloromethylation was washed overnight with boiling, distilled water and followed by washing in boiling THF for three hours, after which the MOF is activated in a furnace at 100 °C in air.

Diphenylphosphination

Before reaction, MIL-101(Cr) was dispersed in THF at -78 °C under nitrogen Schlenk conditions. 2 eq. of $LiPPh_2$ per eq. terephthalate in the MOF, in THF solution, was added dropwise before the reaction was carried out under slow stirring for 12 h. The resulting product was washed in THF at 50 °C before being activated in vacuum.

Solid-state NMR

Solid-state ^{27}Al, ^{13}C, and ^{1}H NMR studies were performed on a Bruker AV-750 spectrometer using a 17.6 Tesla magnetic field, in which these nuclei resonate at 195.46, 188.64, and 750.13 MHz, respectively. A H/X/Y 2.5 mm MAS probe-head was used and a standard ZrO_2 was spun at 20 kHz. For the acquisition of ^{27}Al MAS spectra, the RF field frequency, pulse duration, number of scans, and repetition time were 55 kHz, 1.5 μs, 1024 scans and 1 s, respectively. The corresponding parameters were 78.1 kHz, 3.2 μs, 32 scans, and 1 s for ^{1}H

MAS spectra. For ^{1}H to ^{13}C CPMAS with TPPM decoupling, we used 62.5 and 89 kHz RF field frequencies in the ^{13}C and ^{1}H channels, respectively. For cross-polarization (CP), the contact time was 3 ms, and the repetition time was 2 s for 1024 scans. Chemical shift references (0 ppm) are $Al(NO_3)_3$ in aqueous nitric acid solution for ^{27}Al, TMS for ^{1}H, Glycine for ^{13}C. ^{27}Al spectra were fitted with the DMFIT software package to obtain approximations for quadrupolar coupling constant C_q and asymmetry factor η_q. ^{31}P MAS NMR studies were performed on a Bruker DMX-400 spectrometer with a 9.6 Tesla magnetic field, in which ^{31}P and ^{1}H resonate at 161.69 and 399.42 MHz, respectively. A triple resonance 4 mm MAS probe with standard ZrO_2 rotor with spinning frequency of 12 kHz was used. A single pulse of 78.12 kHz was applied with a repetition time of 2 s, 5120 scans were collected. The chemical shift reference for ^{31}P was 85 % H_3PO_4. All the spectra were processed with Bruker Topspin 1.3.

XRD

XRD was carried out using a Bruker-AXS D5005 with Cu$K\alpha$ radiation.

Diffuse Reflectance IR Spectroscopy (DRIFTS)

DRIFT spectra of the chloromethylated and phosphinated samples were recorded on a Nicolet model 8700 spectrometer, equipped with a high-temperature DRIFT cell, DTGS-TEC detector and a 633 nm laser. The spectra were registered from 4000 to 600 cm^{-1} after accumulation of 128 scans and a resolution of 4 cm^{-1}. A flow of helium at 20 mL min^{-1} was maintained during the measurements. Before collecting the spectra, the different samples were pretreated in the same helium flow at 120 ^{o}C for 30 min. KBr was used to perform background experiments.

Transmission FTIR

IR analysis on the chloromethylated samples was carried out using a Thermo Nicolet Nexus FTIR spectrometer. The samples (1 mg) were mixed with KBr and pressed into self-supported pellets (50 mg/cm^{2}). The spectra were taken in an in-situ cell equipped with CaF_2 windows. Prior to the measurements, the samples were degassed under vacuum (10^{-5} mbar) at 200 ^{o}C for 30 min to remove adsorbents.

Temperature programmed desorption (TPD)

The thermal decomposition of the modified MOFs was followed by mass spectrometry. The sample, about 0.05 g, was heated in a quartz reactor at a rate of 5 ^{o}C min^{-1} under a helium flow of 50 cm^{3} min^{-1}. The released gases were analyzed by a mass spectrometer.

CO_2 sorption

High-pressure adsorption isotherms of pure CO_2 (purity > 99.995%), were determined volumetrically using an apparatus from BEL Japan (Belsorp HP). 0.5 g adsorbent was placed in the sample container. Before every measurement, the adsorbent was pretreated or regenerated by increasing the temperature to 200 ^{o}C at a rate of 10 ^{o}C /min under vacuum and maintaining this temperature for two hours.

N_2 sorption

Nitrogen adsorption at -195 ^{o}C was measured in a Quantachrome Autosorb-6B unit gas adsorption analyzer. The specific BET surface area was calculated between 0.05-0.15 relative pressure and the pore volume at 0.95 relative pressure.

Elemental analysis

Elemental analysis was carried out by means of Inductively Coupled Plasma Optical Emission Spectroscopy (ICP-OES). The samples were digested in a mixture of 1% HF and 1.25% H_2SO_4 and were analyzed with an ICP-OES Perkin Elmer Optima 3000 dv in order to determine the amount of phosphorus present in the structure. The procedure was carried out in duplo with the average taken as result.

Results

The lone pair electrons of the amine group activate the aromatic ring for electrophilic substitution and direct substitution to the aromatic carbon in the *ortho*- and *para*-position with

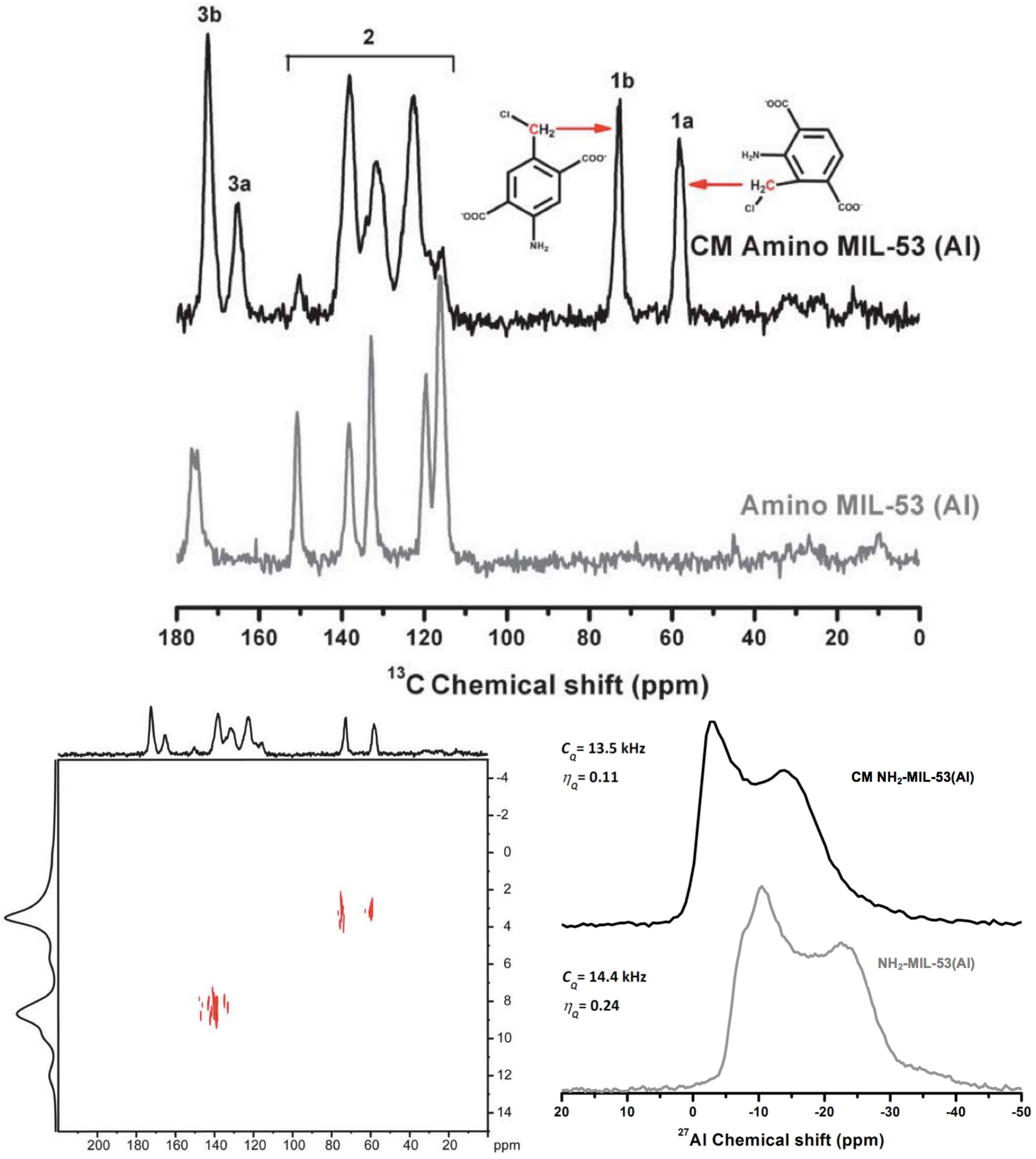

Figure 7.2: *Top*: ^{13}C CPMAS spectra of NH_2-MIL-53(Al)/CM-NH_2-MIL-53Al). *Down left*: ^{1}H-^{13}C HETCOR NMR spectrum of CM-NH_2-MIL-53(Al). *Down right*: ^{27}Al MAS NMR spectra of NH_2-MIL-53(Al)/CM-NH_2-MIL-53Al).

respect to the aminoaryl carbon. This is confirmed by the ^{13}C CPMAS NMR where *ortho*- and *para*-substituted methylene carbons give rise to different signals in the upfield region of the spectrum (figure 7.2, top), suggesting a large intramolecular framework interaction between the amine group and the *ortho*-substituted chloromethylene carbon.

A special class of MOF materials describes solids that reversibly change their framework when guest molecules are introduced or through functionalization. This results in special properties like the breathing effect and the gate phenomenon where pores contract or open, as also discussed in the previous chapter. Interestingly, the NH_2-MIL-53(Al) structure changes from its very narrow pore (*vnp*) configuration to the large pore (*lp*) form after CM. This is clearly visible in XRD (figure 6.3) and in NMR with a clear downfield shift for the aryl protons.[38] Heteronuclear correlation between ^1H and ^{13}C nuclei, in addition to the expected correlation between non-substituted aromatic carbons (130–140 ppm) and aromatic protons (10 ppm), clearly demonstrates a correlation between the $–CH_2Cl$ protons (3 ppm) and methylene carbons (60–80 ppm, Figure 7.2), as expected for CM structures. Finally, in combination with XRD and TPD,[39] ^{27}Al MAS NMR confirms the integrity of the framework after CM and the removal of reactant $AlCl_3{\cdot}6H_2O$ from the pores of the functionalized framework (figure 7.2, right bottom).[8] Further, the decrease of both the quadrupolar coupling constant C_Q and the asymmetry factor η_Q also indicated the *vnp* → *lp* transition after CM through decrease, pointing at an increase of symmetry around the aluminium nucleus from the perspective of the electric field gradient.

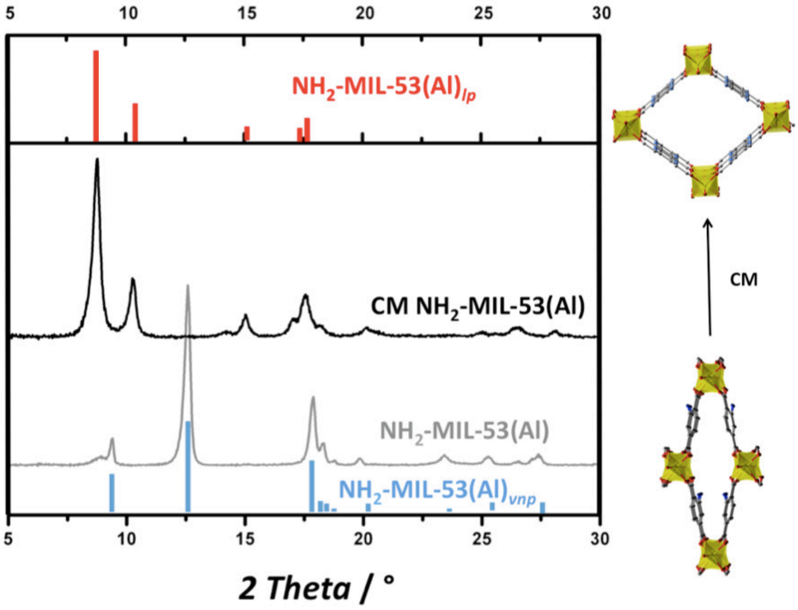

Figure 7.3 XRD patterns of NH_2-MIL-53(Al) and CM-NH_2-MIL-53(Al) together with the simulated XRD patterns for NH2-MIL-53(Al) in the *vnp* and *lp* configurations.

Further evidence for this structure transition and the absence of breathing after CM follows from the CO_2 sorption isotherms (figure 7.4). Whilst the unfunctionalized NH_2-MIL-53(Al) displays a significant breathing behavior,[27,39-42] CM-NH_2-MIL-53(Al) is clearly open from the beginning, displaying an isotherm similar to the one of its non-breathing analogue MIL-47.[41] The fact that the system behaves like a completely open framework whilst less than 100% of the linkers are chloromethylated leaves room for speculation that opening a large—chloromethylated—part of the channel opens the rest of the channel as well. Earlier, a combination of DFT and spectroscopic work from our group demonstrated that the breathing effect in NH_2-MIL-53(Al) is strongly affected by the interaction between the amine groups and the aluminium-bridging OH groups.[43] Chloromethylene groups are likely to exert steric influence on this interaction as they interact with the amino groups and reduce their interaction with OH groups, resulting in the opening of the framework.

InfraRed studies (Figure 7.5) also indicate new amine interactions as new symmetric and asymmetric amine stretchings are visible, a result of interaction between the amine nitrogen and the chloromethylene group.

To illustrate the functionalization concept, diphenylphosphine is attached to MIL-101(Cr) after chloromethylation (Figure 7.6, *vide infra*). This terephthalate-based, highly stable framework was chosen as it carries mesopore cavities, which are likely to preserve sufficient remaining guest accessibility after functionalization with a bulky group.[6]

The new material, named PPh_2-MIL-101(Cr), has ca. 7.7% of its terephthalate linkers functionalized (as quantified by elemental analysis). ^{31}P MAS NMR (Figure 7.7, *vide infra*) confirms the substitution and complete removal of the reactant, $LiPPh_2$. No paramagnetic relaxation—usually a problem for Cr-based MOFs—is observed since the methylene group acts like an ‘‘insulator’’. The chemical shift of the phosphorus peak is in the range of typical chemical shift values for benzyl diphenylphosphines.[44] However, as expected for uncoordinated trivalent methylene-bound phosphorus species, oxidation readily occurs in air, and this was visible in the solid-state NMR experiment by an increasing chemical shift signal at 48 ppm.

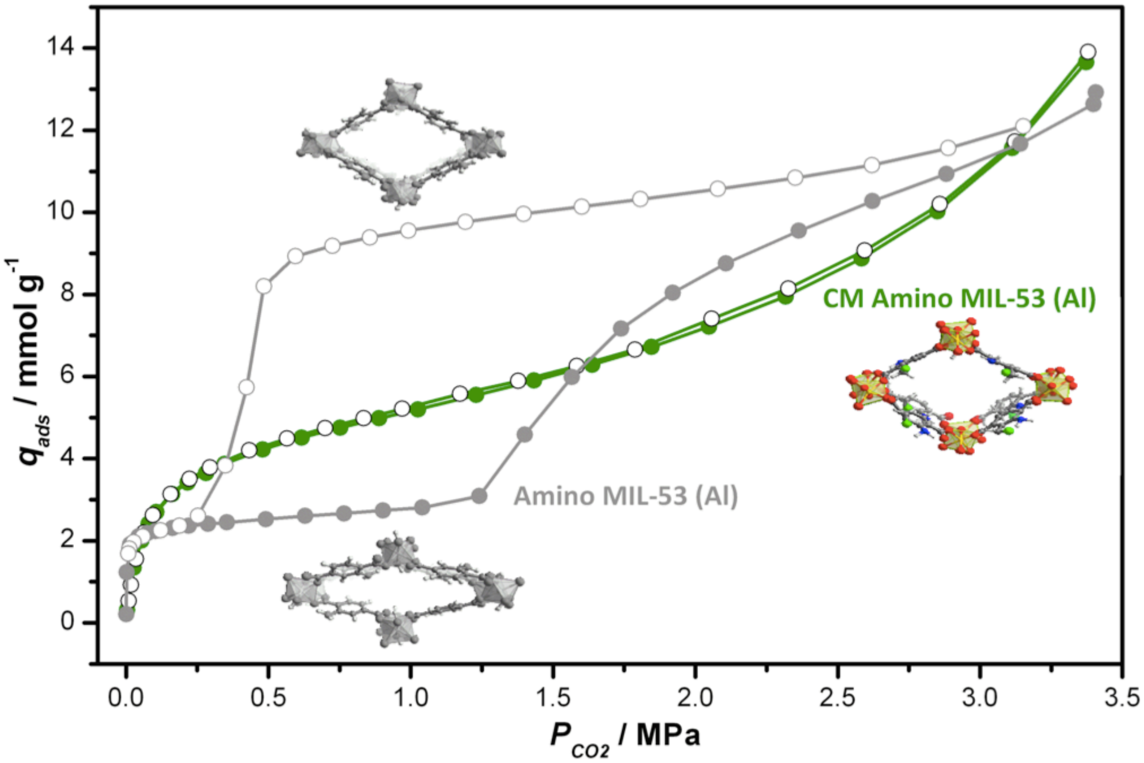

Figure 7.4: High-pressure CO_2 isotherm recorded at 0 °C of CM-NH_2-MIL-53(Al) {*green*} and NH_2-MIL-53(Al) {*grey*}.

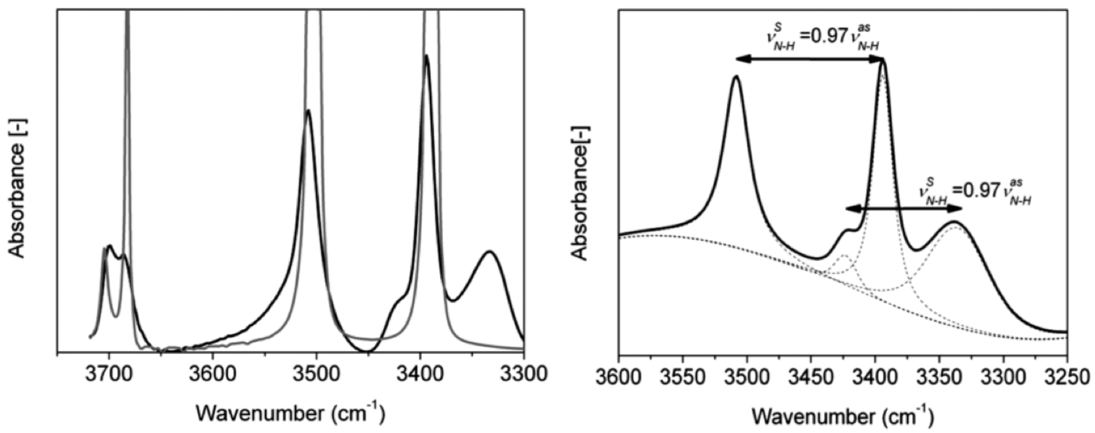

Figure 7.5: *Left*: IR spectra of NH$_2$-MIL-53(Al) and CM-NH$_2$-MIL-53(Al) (black). *Right*: zoom of the amine region for CM-NH$_2$-MIL-53(Al) and spectrum deconvolution.

The DRIFT spectrum reveals new, typical aryl phosphine stretchings at 2800–3000 cm,[45] overlapping the chloromethylene stretching. The non-oxidized material, PPh$_2$-MIL-101(Cr), is still highly porous (BET area: 1800 m^2 g^{-1}) and is thus an attractive candidate for catalysis.

Conclusion

In this chapter, a mild chloromethylation route for MOFs with terephthalic and aminoterephthalic linkers is introduced, which avoids the use of carcinogens. After chloromethylation, one can substitute the chlorine with a nucleophilic substituent of choice to obtain various multifunctional features. This is demonstrated by covalently attaching a diphenylphosphine moiety to the linker of NH$_2$-MIL-53(Al) and MIL-101(Cr). This method can be extended to coordination polymers that contain accessible aromatic units.

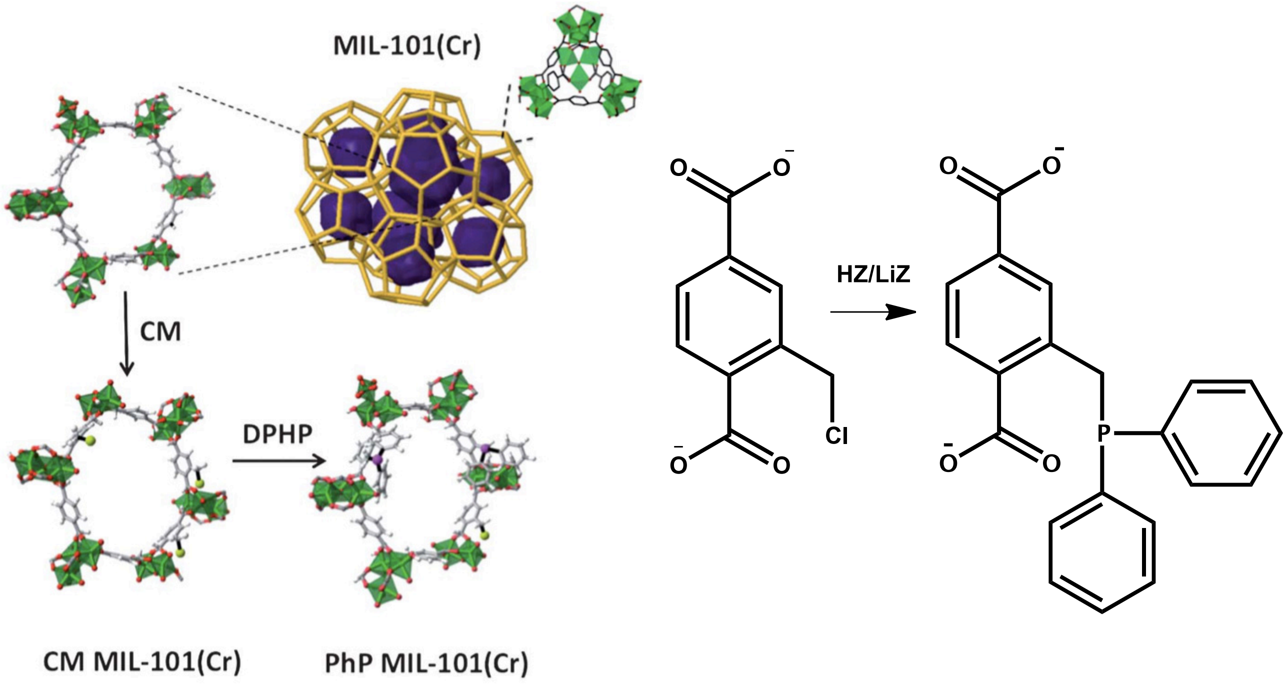

Figure 7.6: *Left*, three-dimensional structural representation of chloromethylation, and *right* followed up by diphenylphosphination of MIL-101(Cr)

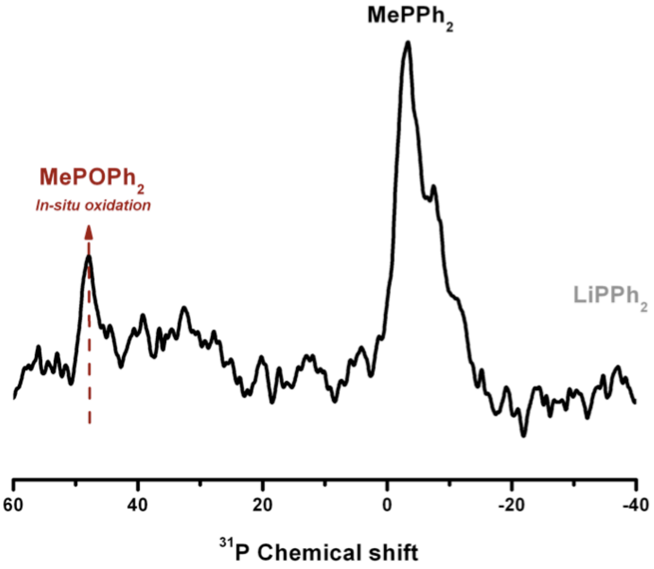

Figure 7.7: ^{31}P MAS NMR spectrum of PPh$_2$-MIL-101(Cr).

References

[1] F. Kučera, J. Jančář, *Polymer Eng. Sci.* **1998**, *38*, 783–792.

[2] A. D. Burrows, C. G. Frost, M. F. Mahon, C. Richardson, *Chem. Comm.* **2009**, 4218–4220.

[3] E. Neofotistou, C. D. Malliakas, P. N. Trikalitis, *Chem. Eur. J.* **2009**, *15*, 4523–4527.

[4] D. Britt, C. Lee, F. J. Uribe-Romo, H. Furukawa, O. M. Yaghi, *Inorg Chem* **2010**, *49*, 6387–6389.

[5] J. Juan-Alcañiz, R. Gielisse, A. B. Lago, E. V. Ramos-Fernandez, P. Serra-Crespo, T. Devic, N. Guillou, C. Serre, F. Kapteijn, J. Gascon, *Catal. Sci.Tech.* **2013**, *3*, 2311–2318.

[6] C. Férey, C. Mellot-Draznieks, C. Serre, F. Millange, J. Dutour, S. Surblé, I. Margiolaki, *Science* **2005**, *309*, 2040–2042.

[7] T. Loiseau, C. Serre, C. Huguenard, G. Fink, F. Taulelle, M. Henry, T. Bataille, G. Férey, *Chem. Eur. J.* **2004**, *10*, 1373–1382.

[8] D. Massiot, F. Fayon, M. Capron, I. King, S. Le Calvé, B. Alonso, J. O. Durand, B. Bujoli, Z. Gan, G. Hoatson, *Magn. Reson. Chem.* **2002**, *40*, 70–76.

[9] M. Tagliabue, D. Farrusseng, S. Valencia, S. Aguado, U. Ravon, C. Rizzo, A. Corma, C. Mirodatos, *Chem. Eng. J.* **2009**, *155*, 553–566.

[10] P. Atorngitjawat, R. J. Klein, J. Runt, *Macromolecules* **2006**, *39*, 1815–1820.

[11] D. S. Warren, A. J. McQuillan, *J. Phys. Chem. B* **2008**, *112*, 10535–10543.

[12] B. Ostrowska-Gumkowska, J. Ostrowska-Czubenko, *Eur. Polymer J.* **1994**, *30*, 869–874.

[13] C. Serre, F. Millange, C. Thouvenot, M. Noguès, G. Marsolier, D. Louër, G. Férey, *J. Am. Chem. Soc.* **2002**, *124*, 13519–13526.

[14] A. Zecchina, G. Spoto, S. Bordiga, *Phys. Chem. Chem. Phys.* **2005**, *7*, 1627–1642.

[15] P. L. Llewellyn, S. Bourrelly, C. Serre, Y. Filinchuk, G. Férey, *Angew. Chem. - Int. Ed.* **2006**, *45*, 7751–7754.

[16] C. Serre, S. Bourrelly, A. Vimont, N. A. Ramsahye, G. Maurin, P. L. Llewellyn, M. Daturi, Y. Filinchuk, O. Leynaud, P. Barnes, et al., *Adv. Mater.* **2007**, *19*, 2246–2251.

[17] M. J. Cánovas, I. Sobrados, J. Sanz, J. L. Acosta, A. Linares, *J. Membrane Sci.* **2006**, *280*, 461–469.

[18] C. Lieder, S. Opelt, M. Dyballa, H. Henning, E. Klemm, M. Hunger, *J. Phys. Chem. C* **2010**, *114*, 16596–16602.

[19] G. Sarret, J. Connan, M. Kasrai, G. M. Bancroft, A. Charrié-Duhaut, S. Lemoine, P. Adam, P. Albrecht, L. Eybert-Bérard, *Geochim. Cosmochim. Acta* **1999**, *63*, 3767–3779.

[20] J. Prietzel, J. Thieme, M. Salome, H. Knicker, *Soil Biol. Biochem.* **2007**, *39*, 877–890.

[21] J. P. Cuif, Y. Y. Dauphin, J. Doucet, M. Salome, J. Susini, *Geochim. Cosmochim. Acta* **2003**, *67*, 75–83.

[22] J. A. Hurd, R. Vaidhyanathan, V. Thangadurai, C. I. Ratcliffe, I. L. Moudrakovski, G. K. H. Shimizu, *Nature Chemistry* **2009**, *1*, 705–710.

[23] J. H. Cavka, S. Jakobsen, U. Olsbye, N. Guillou, C. Lamberti, S. Bordiga, K. P. Lillerud, *J. Am. Chem. Soc.* **2008**, *130*, 13850–13851.

[24] C. Volkringer, M. Meddouri, T. Loiseau, N. Guillou, J. Marrot, G. Férey, M. Haouas, F. Taulelle, N. Audebrand, M. Latroche, *Inorg Chem* **2008**, *47*, 11892–11901.

[25] Y. Liu, I. F. F. Lien, S. Ruttgaizer, P. Dove, S. D. Taylor, *Organic Lett.* **2004**, *6*, 209–212.

[26] M. Marczewski, A. Jakubiak, H. Marczewska, A. Frydrych, M. Gontarz, A. Śnieguła, *Phys. Chem. Chem. Phys.* **2004**, *6*, 2513–2522.

[27] S. Couck, J. F. M. Denayer, G. V. Baron, T. Rémy, J. Gascon, F. Kapteijn, *J. Am. Chem. Soc.* **2009**, *131*, 6326–6327.

[28] S. Couck, T. Rémy, G. V. Baron, J. Gascon, F. Kapteijn, J. F. M. Denayer, *Phys. Chem. Chem. Phys.* **2010**, *12*, 9413–9418.

[29] F. Millange, N. Guillou, R. I. Walton, J. M. Grenèche, I. Margiolaki, G. Férey, *Chem. Comm.* **2008**, 4732–4734.

[30] P. Küsgens, M. Rose, I. Senkovska, H. Fröde, A. Henschel, S. Siegle, S. Kaskel, *Microporous Mesoporous Mater.* **2009**, *120*, 325–330.

[31] M. F. De Lange, J.-J. Gutierrez-Sevillano, S. Hamad, T. J. H. Vlugt, S. Calero, J. Gascon, F. Kapteijn, *J. Phys. Chem. C* **2013**, *117*, 7613–7622.

[32] F. Millange, C. Serre, N. Guillou, G. Férey, R. I. Walton, *Angew. Chem. - Int. Ed.* **2008**, *47*, 4100–4105.

[33] M. B. Smith, J. March, *March's Adv.Org. Chem.* **2001**.

[34] M. Camps, M. Chatzopoulos, J.-M. Camps, J.-P. Montheard, *J. Macromolecular Sci. - Rev. Macromolecular Chem. Phys.* **1987**, *C27*, 505–557.

[35] F. C. Roe, *The Lancet* **1985**, *326*, 268.

[36] A. McKillop, F. A. Madjdabadi, D. A. Long, *Tetrahedron Lett.* **1983**, *24*, 1933–1936.

[37] T. Ahnfeldt, D. Gunzelmann, T. Loiseau, D. Hirsemann, J. Senker, G. Férey, N. Stock, *Inorg Chem* **2009**, *48*, 3057–3064.

[38] T. Loiseau, C. Serre, C. Huguenard, G. Fink, F. Taulelle, M. Henry, T. Bataille, G. Férey, *Chem. - Eur. J.* **2004**, *10*, 1373–1382.

[39] S. Couck, T. Rémy, G. V. Baron, J. Gascon, F. Kapteijn, J. F. M. Denayer, *Phys. Chem. Chem. Phys.* **2010**, *12*, 9413–9418.

[40] A. Boutin, S. Couck, F. X. Coudert, P. Serra-Crespo, J. Gascon, F. Kapteijn, A. H. Fuchs, J. F. M. Denayer, *Microporous Mesoporous Mater.* **2011**, *140*, 108–113.

[41] S. Bourrelly, P. L. Llewellyn, C. Serre, F. Millange, T. Loiseau, G. Férey, *J. Am. Chem. Soc.* **2005**, *127*, 13519–13521.

[42] L. Hamon, P. L. Llewellyn, T. Devic, A. Ghoufi, G. Clet, V. Guillerm, G. D. Pirngruber, G. Maurin, C. Serre, G. Driver, et al., *J. Am. Chem. Soc.* **2009**, *131*, 17490–17499.

[43] E. Stavitski, E. A. Pidko, S. Couck, T. Rémy, E. J. M. Hensen, B. M. Weckhuysen, J. Denayer, J. Gascon, F. Kapteijn, *Langmuir* **2011**, *27*, 3970–3976.

[44] M. F. Cain, R. P. Hughes, D. S. Glueck, J. A. Golen, C. E. Moore, A. L. Rheingold, *Inorg Chem* **2010**, *49*, 7650–7662.

[45] S. Berger, S. Braun, H. O. Kalinowski, *NMR Spectroscopy of the Non-Metallic Elements* **1997**, Wiley-VCH, New York

About the author

Maarten Goesten was born in Johannesburg, the Republic of South Africa, at the 10th of February 1987. In The Netherlands, he studied at the *Old Music* department, Royal Conservatory in the Hague under supervision of Dorothea Winter, and obtained his high-school diploma at the Stedelijk Gymnasium in Schiedam in 2004.
After this, he moved to the Delft University of Technology where he studied Chemical Engineering. He performed his *BSc.* thesis in 2007 on the topic of isopropylated naphthalenes under the supervision of prof. Wim Buijs, and his *MSc.* thesis in 2010 on the topic of acid-catalysis with Metal-Organic Frameworks, under the supervision of prof. Freek Kapteijn and prof. Jorge Gascon. In the same year, he started his PhD, on the topic of crystal engineering with Metal-Organic Frameworks. During his PhD, he was a guest researcher at the Inorganic Materials group, TU Eindhoven, of prof. Emiel Hensen, where he developed a methodology on studying the hierarchical stacking of zeolite nanosheets by Paracrystalline Theory and Small-Angle X-ray Scattering, and he is since December 2013 also a guest at the department of Theoretical Chemistry of prof. Matthias Bickelhaupt, Vrije Universiteit Amsterdam, where he develops concepts on chemical bonding.

As of December 2014, he works as researcher in the group of prof. Emiel Hensen, where his research interests focus on physical chemistry.

List of publications during PhD period

1. **M.G. Goesten,** J. Juan-Alcaniz, E.V. Ramos-Fernandez, K.B. Sai Sankar Gupta, E. Stavitski, H. van Bekkum, J. Gascon,* F. Kapteijn. Sulfation of Metal-Organic Frameworks: opportunities for acid catalysis and proton conductivity. J. Catal. 281 (2011) 177-187.

2. E. Stavitski,* **M.G. Goesten**, J. Juan-Alcañiz, A. Martinez-Joaristi, P. Serra-Crespo, A.V. Petukhov, J. Gascon* and F. Kapteijn. Kinetic control of metal organic framework crystallization investigated by time resolved in-situ X-ray scattering. Angew. Chem. Int. Ed. 50 (2011) 9624-9628

3. J. Juan-Alcaniz, **M.G. Goesten,** A. Martinez-Joaristi, E. Stavitski,* A.V. Petukhov, J. Gascon* and Freek Kapteijn. Live encapsulation of a Keggin polyanion in NH2-MIL-101(Al) observed by in-situ time resolved X-ray scattering. Chem. Comm. 47 (2011) 8578-8580

4. **M.G. Goesten,*** K.B.S. Sankar-Gupta, E.V. Ramos-Fernandez, H. Khajavi, J. Gascon* and F. Kapteijn. Chloromethylation as Functionalisation Pathway for Metal-Organic Frameworks. CrystEngComm 14, (2012), 4109-4111

5. J. Juan-Alcañiz, **M.G. Goesten,** E.V. Ramos Fernandez, J. Gascon * and F. Kapteijn. Towards efficient polyoxometalate encapsulation in MIL-100(Cr): influence of synthesis conditions. New J. Chem. 36 (2012), 977-987

6. **M.G. Goesten,*** E. Stavitski, J. Juan-Alcañiz, A. Martiñez-Joaristi, A.V. Petukhov, F. Kapteijn and J. Gascon.* Small-Angle X-ray Scattering Documents The Growth of Metal-Organic Frameworks. Catal. Today 205 (2013) 120-127

7. **M.G. Goesten,*** E. Stavitski, E. A. Pidko, C. Gücüyener, B. Boshuizen, S.N. Ehrlich, E.J.M. Hensen, F. Kapteijn and J. Gascon. * The molecular pathway to ZIF-7 microrods revealed by in situ time resolved SAXS/WAXS/QEXAFS and DFT. Chem. – Eur. J. 19 (2013) 7809-7816

8. M.A. Nasalevich, * **M.G. Goesten**, T.J. Savenije, F. Kapteijn and J. Gascon. * Enhancing optical absorption of Metal-Organic Frameworks for improved visible light photocatalysis. Chem. Comm. 49 (2013) 10575-10577

9. **M.G. Goesten**,* F. Kapteijn and J. Gascon. * Fascinating chemistry or frustrating unpredictability: observations in crystal engineering of Metal-Organic Frameworks. CrystEngComm 15 (2014) 9249-9257

10. **M.G. Goesten,*** Pieter Magusin, Evgeny Pidko, Brahim Mezari, Emiel Hensen, Freek Kapteijn and Jorge Gascon. * Molecular promoting of aluminium metal-organic framework topology MIL-101 by N,N,-dimethylformamide. Inorg Chem 53 (2014) 882-887

11. A. Demuynck, **M.G. Goesten,** E. Ramos-Fernandez, M. Dusselier, J. Vanderleyden, F. Kapteijn, J. Gascon* and B. Sels.*
    ChemCatChem 6 (2014) 2211-2214

12. **M.G. Goesten** & X. Zhu,# N. Kosinov, B.Szyja, R. Rohling, G. Filonenko, F. Kapteijn, J. Gascon and E.J.M. Hensen*, *Submitted*

13. **M.G. Goesten**,* A. Sceszeny, K.B.S. Sankar-Gupta, F. Kapteijn and J. Gascon. Sulfonation of two new ultrastable porous aromatic polymers: high catalytic activities and remarkable sorption properties. *Submitted*

14. A.Bavykina, **M.G. Goesten**,* M. Makkee, F. Kapteijn and J. Gascon*
    ChemSusChem 8 (2015) 809-812

15. **M.G. Goesten**,* M. de Lange, A. Olivos-Suarez, A. Bavykina, P. Serra-Crespo, C. Krywka, M. Bickelhaupt, F. Kapteijn and J. Gascon.* Evidence for a solid-state clock reaction in the formation of UiO-66(Zr/Hf). *Submitted*

16. **M.G. Goesten**,* C. Fonseca Guerra, F. Kapteijn, J. Gascon and M. Bickelhaupt. The role of 'hypervalence' in octahedral group 13 element based clusters. *Submitted*

* Denotes corresponding author, # denotes equal contribution from both authors.

Lectures in chronological order

1. *Chloromethylation as versatile post-synthetic functionalization for Metal-Organic Frameworks*
   Hybrid Materials, Strasbourg, France, March 2011

2. *Chloromethylation of Metal-Organic Frameworks*
   Workshop International Research Training Group "Diffusion in Porous Materials", Leipzig, Germany, April 2011

3 *Applications of solid-state NMR in heterogeneous Catalysis*
Delft, Netherlands, March 2011

4 *Competition between NH_2-MIL-53(Al) and NH_2-MIL-101(Al)*
Utrecht, Netherlands, November 2011

5 *Studying the growth of Metal-Organic Frameworks by X-ray Scattering*
13th Netherlands' Catalysis and Chemistry Conference, Noordwijkerhout, Netherlands, March 2012

6 *SAXS/WAXS study on NH_2-MIL-53(Al) vs. NH_2-MIL-101(Al)*
Workshop International Research Training Group "Diffusion in Porous Materials", Leipzig, Germany, April 2012

7 *Applications of solid-state NMR in heterogeneous Catalysis*
Delft, Netherlands, May 2012

8 *Stacking of zeolitic MFI nanosheets modelled by paracrystalline theory*
14th Netherlands' Catalysis and Chemistry Conference, Noordwijkerhout, Netherlands, March 2013

9 *Molecular promotion of a Metal-Organic Framework topology by an appropriate solvent*
Workshop International Research Training Group "Diffusion in Porous Materials", Delft, Netherlands, April 2013

10 *Applications of solid-state NMR in heterogeneous Catalysis*
Delft, Netherlands, May 2013

11 *Crystal engineering with Metal-Organic Frameworks*
Delft, Netherlands, February 2014

12 *Porous aromatic frameworks as heterogeneous catalysts*
15th Netherlands' Catalysis and Chemistry Conference, Noordwijkerhout, Netherlands, March 2014

13 *Crystal engineering with Metal-Organic Frameworks: a coordination chemistry perspective*
4th International conference on Metal-Organic Frameworks and Open Framework Compounds, Kobe, Japan, October 2014

Awards

Lecture award NCCC, 2014
"Most cited paper" award in *Journal of Catalysis,* 2011 and 2012, for publication no.1, above.

Summary and outlook / Samenvatting en vooruitzicht

English

Crystal engineering is the *design* and synthesis of crystalline structures with predictive functionalities, based on a bottom-up approach from smaller building blocks. Metal-Organic Frameworks (MOFs), perhaps more than any other material, fulfill the concept of crystal engineering, and are therefore of great interest to chemical industry. Predictive morphology and functionality of MOF crystals are vital parameters for applications such as heterogeneous catalysis and membrane technology, which renders the realization of crystal engineering as elementary research topic.

In chapter 1, the very realization of crystal engineering is observed from a coordination-chemistry perspective. We arrived to the conclusion that self-assembly to crystals with predicted properties is in essence not viable, unless the coordination chemistry of the metal-organic system is well studied. We advocated a strategy in which *design* is only applied on well-studied systems, for which the chemistry is well documented.

Chapter 2 treats bonding in MOFs based on group 13 elements, which is compared to bonding in MOFs based on transition metals. We here concluded that despite forming geometrically comparable structures, octahedral MOF clusters based on group 13 elements follow a *7-centre-10-electron* scheme, making bonding in general more ionic compared to transition metal analogues.

In chapter 3, the aluminium 2-aminoterephthalate systems of NH_2-MIL-53(Al) vs. NH_2-MIL-101(Al) was studied. Both materials crystallise from the same precursors, yet under different circumstances. In chapter 3A it is demonstrated by medium and wide-angle X-ray scattering (MAXS/WAXS) that only synthesis in pure DMF leads to NH_2-MIL-101(Al), which is the kinetic product (prolonged heating leads to framework breakdown and transformation into NH_2-MIL-53(Al)). Syntheses carried out in H_2O and H_2O/DMF mixtures directly form NH_2-MIL-53(Al), but the presence of DMF (whether pure or in a mixture with water) leads to the formation of the intermediate NH_2-MOF-235(Al) which involves considerably better kinetics for NH_2-MIL-53(Al) crystal growth. The transformation of NH_2-MOF-235(Al) into NH_2-MIL-101(Al) is assumed to follow a crystallisation-dissolution-crystallisation mechanism. In Chapter 3B, it is seen with small-angle X-ray scattering (SAXS) that DMF/H_2O mixtures lead to surface fractals, after which NH_2-MOF-235(Al) rapidly forms and transforms into NH_2-MIL-101(Al). During this transition, no morphological change is observed within the crystal and a suspected crystal-to-crystal rearrangement (rather than a crystallisation-dissolution-crystallisation mechanism) is proposed. This is confirmed in chapter 3C by *in-situ* NMR experiments and DFT calculations, where it is also shown that DMF plays a non-innocent role as solvent, complexating H-Cl and promoting the MIL-101 topology.

In chapter 4, the synthesis of ZIF-7 nanorods was followed by SAXS/WAXS/QEXAFS (quick EXAFS), and supported by scanning electron microscopy (SEM) and DFT calculations. It is possible to selectively synthesize nanorods by addition of a modulator, diethyl amine, to the MOF synthesis mixture of benzimidazole and $ZnCl_2$ in DMF. $ZnCl_2$ is required; $Zn(NO_3)_2$ does not lead to nanorods. In this chapter, the combination of techniques leads to the resolution of the entire crystallization pathway, and at all relevant length scales (atomic to full crystal)

In chapter 5, evidence was provided for the first solid-state *clock reaction*. Synthesis of UiO-66(Zr/Hf) is promoted by the addition of HCl, which is counterintuitive for HCl is formed in the reaction of $ZrCl_2$ with terephthalic acid, the precursors of UiO-66. SAXS revealed that UiO-66 particle dimensions and number oscillate to final values, whereas precipitation proceeds independently, and faster than crystallization. This is explained by relativistic DFT calculations, which are implemented in the frame of a new molecular-orbital theory based point of view, in which the inorganic-organic interaction is pinpointed. It is concluded that HCl is required to protonate inorganic clusters during crystallisation, after which it is released during development of bulk crystallinity within the initially amorphous UiO-66 particles.

In chapter 6, a novel and mild sulfation reaction is introduced to implement inherent Brønsted acidity. Sulfated frameworks S-MIL-53(Al) and S-MIL-101(Cr) display comparable activities to Nafion® in the esterification of *n*-butanol with acetic acid. S-MIL-53(Al), further, proved highly proton conductive up to moderate temperatures.

In chapter 7, a mild chloromethylation procedure is introduced. The chloromethyl moiety can be used to introduce a functionality of choice by substitution of the chlorine. This is demonstrated in a proof-of-concept, in which a diphenylphosphine moiety is attached to the organic linker.

The first part of the thesis showed that coordination chemistry around the tectonic units of Metal-Organic Frameworks practically rules out *ab-initio* structure determination. By treating numerous examples, and by the theoretical study in chapter 2, the richness and unpredictability of coordination chemistry is demonstrated. The second part of the thesis shows that this chemistry leads to complex molecular pathways that govern MOF crystallization for every case studied (MIL-53 vs. MIL-101 in chapter 3, ZIF-7 in chapter 4 and UiO-66 in chapter 5). Despite the, perhaps gloomy, perspective sketched in chapter 1, this second part of the thesis shows that, although complex, molecular pathways can be resolved. The key here is a combination of techniques, each technique targeting a relevant length scale. The studies carried out have already generated understanding directly leading to several developments in the Delft laboratory varying from yield enhancement (an improvement of 300% reported in the synthesis of NH_2-MIL-53(Al))[1] to 'real' crystal engineering such as total control over ZIF-7 crystal morphology at room temperature synthesis[2] and controlled synthesis of nanosheet MOF-polymer membrane composites for gas separation.[3]
In the third part of the thesis, the post-synthetic strategy towards crystal engineering is introduced. By attaching functionalities to pre-assembled MOF crystals, one avoids undesired pathways in MOF synthesis, without losing the ability to implement pin-point functionality. Naturally, the possibilities in post-synthetic modification are limited: many organic struts are highly electron-deactivated and require the use of activated reagents, yet those cannot be too aggressive for MOFs only carry moderate chemical (and thermal) stability. Apart from chapters 6 and 7, the creativity of chemists has led to numerous possibilities, and the field of post-synthetic functionalisation of MOFs has truly become a field of its own.[4]
Now the field of MOFs is starting to endure the test of time, it is vital to select the MOF materials that could be useful in the future. Of the tenths of thousands of structures reported, only a fraction possesses the stability required for possible application. It is required that these structures be identified and their formation pathway resolved. In such manner, the combination of high crystallinity and high tunability, i.e. the main facet of crystal engineering, comes to its full right. This means that applications based on 'designed' MOF crystals can indeed play (a small) part in addressing some of the major challenges makind faces in the 21th century when it comes to energy and feedstock conversion. Herein, this thesis identifies several current challenges, and targets their resolution through a combination of theory, spectroscopy and synthetic methodologies.

Nederlands

Crystal engineering betreft het *ontwerp* en de synthese van kristallijne structuren met specifieke eigenschappen, door de eigenschappen van onderliggende bouwstenen te beïnvloeden. Metal-Organic Frameworks (MOFs) zijn wellicht meer dan welk ander materiaal geschikt voor Crystal Engineering, en hebben daarom wijdverbreide interesse van industrie getrokken. Het sturen van de morfologie en eigenschappen zijn van grote waarde voor toepassingen in heterogene katalyse en membraantechnologie, waardoor Crystal Engineering als een belangrijk onderzoeksgebied geldt.

In hoofdstuk 1 wordt de haalbaarheid van Crystal Engineering onder de loep genomen vanuit het perspectief van coördinatiechemie. Er wordt geconcludeerd dat self-assemblage van kristallen met gewenste eigenschappen feitelijk niet (geheel) mogelijk is, tenzij de coördinatiechemie van het metaal-organische system goed is bestudeerd. Er wordt een strategie gepresenteerd waarin *ontwerp* alleen wordt overwogen voor goed bestudeerde systemen, waarvan de chemie goed is gedocumenteerd.

Hoofdstuk 2 behandelt de chemische binding in MOFs die gebaseerd zijn op groep-13 elementen; dit wordt vergeleken met de chemische binding in MOFs gebaseerd op overgangsmetalen. Hoewel de structuren geometrisch vergelijkbaar zijn, volgen octaedrische MOF clusters gebaseerd op groep-13 elementen een 7-centre-10-electron schema; dit maakt de binding ionischer dan het overgangsmetaal analogon.

Hoofdstuk 3 presenteert een studie van de aluminium 2-aminotereftalaat systemen NH_2-MIL-53(Al) en NH_2-MIL-101(Al). Beide materialen worden gevormd uit dezelfde precursors, maar de syntheses vinden plaats onder verschillende omstandigheden. In hoofdstuk 3A wordt middels medium en wide-angle X-ray scattering (MAXS/WAXS) gedemonstreerd dat alleen de synthese in puur DMF tot NH_2-MIL-101(Al) leidt; het kinetisch bepaalde product. Syntheses uitgevoerd in een medium dat water bevat leiden tot de vorming van NH_2-MIL-53(Al). De aanwezigheid van DMF (ofwel in een mengsel met water, ofwel puur) hierbij leidt tot de vorming van NH_2-MOF-235(Al),, resulterend in een sterk verbeterde kinetiek van de NH_2-MIL-53(Al) kristalgroei. In dit hoofdstuk wordt de transformatie van NH_2-MOF-235(Al) in NH_2-MIL-101(Al) beschouwd als een kristallisatie-oplos-herkristallisatie mechanisme. In hoofdstuk 3B wordt middels SAXS aangetoond dat DMF/H_2O mengsels tot oppervlakte fractalen leiden, waarna NH_2-MOF-235(Al) zeer snel neerslaat en transformeert tot NH_2-MIL-101(Al). Gedurende deze transformatie wordt geen verandering in kristalmorfologie waargenomen, en een kristal-naar-kristal transformatie wordt voor het eerst voorgesteld. Deze stelling wint aan kracht in hoofdstuk 3C, waarin *in-situ* kernspinresonantie en kwantumchemische berekeningen laten zien dat DMF niet slechts een rol als oplosmiddel speelt, maar H-Cl bindt en hiermee vorming van de MIL-101 topologie bevordert.

In hoofdstuk 4 wordt de synthese van ZIF-7 nanostaafjes bekeken met SAXS/WAXS/QEXAFS (QEXAFS: Quick Extended X-ray Adsorption Fine Structure), elektronenmicroscopie en kwantumchemische berekeningen. Het is mogelijk om selectief nanostaafjes te synthetiseren door toevoeging van modulator diethylamine aan de standaardoplossing van benzimidazole en $ZnCl_2$ in DMF. In dit hoofdstuk laat de unieke combinatie van technieken zien dat het volledige moleculaire mechanisme van kristalvorming in kaart gebracht kan worden op alle relevante lengteschalen.

Hoofdstuk 5 presenteert bewijs voor de eerste in kaart gebrachte klok-reactie in het vormen van een vaste stof. De synthese van UiO-66(Zr/Hf) wordt tegen de verwachting in gepromoot door de additie van HCl, terwijl HCl ook gevormd wordt tijdens de synthese. SAXS onthult dat de populatie en morfologie van de UiO-66 deeltjes oscillerend naar finale waardes evolueren, terwijl het neerslaan zich sneller dan en onafhankelijk van kristallisatie ontwikkelt. Dit wordt onderbouwd door relativistische kwantumchemische berekeningen, die worden gepresenteerd en geïnterpreteerd vanuit het perspectief van moleculaire orbitaaltheorie. Aangetoond wordt dat HCl de anorganische clusters protoneert tijdens het neerslaan, en weer teruggevormd wordt wanneer de neergeslagen deeltjes kristalliseren; een vaste-stof proces.

Hoofdstuk 6 introduceert een nieuwe, en milde sulfateringsreactie waarmee Brønsted zuurheid aangebracht kan worden. De gesulfateerde MOFs S-MIL-53(Al) en S-MIL-101(Cr) vertonen een aan Nafion® vergelijkbare katalytische activiteit in de esterificatie van *n*-butanol met azijnzuur. S-MIL-53(Al) blijkt ook nog een uitstekende protongeleider te zijn, tot aan gematigde temperaturen.

In hoofdstuk 7 wordt een milde chloromethylering geintroduceerd. De chloromethyl groep kan gebruikt worden om een functionaliteit van keuze aan te brengen in de MOF door het chloor te substitueren. Dit wordt gedemonstreerd door difenylfosfine aan de MOF linker te binden.

Het eerste deel van dit proefschrift laat zien dat coördinatiechemie de *ab-initio* voorspelbaarheid van de te vormen structuur in de weg zit. De veelzijdigheid en complexiteit van coördinatiechemie wordt door talloze voorbeelden toegelicht, voornamelijk in het theoretische hoofdstuk 2. Het tweede deel van het proefschrift laat zien dat dit tot complexe chemische routes leidt in de kristallisatie van MOFs; dit geldt voor elk bestudeerd scenario: MIL-53 vs. MIL-101 in hoofdstuk 3, ZIF-7 in hoofdstuk 4 en UiO-66 in hoofdstuk 5. Ondanks het wellicht weinig optimistische beeld dat geschetst wordt in hoofdstuk 1, laat dit deel van het proefschrift zien dat deze complexe routes opgehelderd en beschreven kunnen worden. De crux is een combinatie van technieken, waarmee op verschillende lengteschalen de verschijnselen blootgelegd kunnen worden. Dit onderzoek heeft inmiddels geleid tot enkele ontwikkelingen in de laboratoria in Delft, variërend van een verbetering in opbrengst (300% verbetering in het geval van NH_2-MIL-53(Al))[1] tot een werkelijke realisering van wat Crystal Engineering genoemd kan worden: totale controle over de morfologie van ZIF-7 kristallen,[2] en gecontroleerde synthese van composietmembranen van plaatvormige MOFs en polymeren voor de scheiding van gassen.[3]

Het derde deel van het proefschrift behandelt de strategie van post-synthetisch Crystal Engineering: door moleculaire functionaliteit in gesynthetiseerde MOF kristallen aan te brengen kunnen ongewenste effecten, die gedurende de synthese van MOFs kunnen optreden, vermeden worden. De post-synthetische mogelijkheden zijn uiteraard gelimiteerd: veel organische linkers zijn elektron-arm en vereisen het gebruik van een sterk activerend reagens, maar deze mogen chemisch niet tè agressief zijn omdat de stabiliteit van MOFs gelimiteerd is. Los van de hierin gepresenteerde hoofdstukken 6 en 7, heeft de creativiteit van chemici wereldwijd geleid tot legio mogelijkheden, en post-synthetische modificatie is een op zichzelf staand specialisme geworden.[4]

Nu het vakgebied van MOFs de tand des tijds moet doorstaan, is het van groot belang MOF materialen te selecteren die werkelijk van belang kunnen zijn voor de toekomst. Van de tienduizenden inmiddels bekende structuren bezit slechts een fractie de stabiliteit vereist voor potentiële toepassing. Het is van belang dat juist deze structuren worden geïdentificeerd, en hun moleculair vormingsmechanisme wordt opgelost. Op deze manier kan de combinatie van hoge kristalliniteit en het eenvoudig introduceren van functionaliteiten optimaal worden benut, en wordt Crystal Engineering realiteit. Dit betekent dat de toepassing van deze 'ontworpen' MOF materialen wellicht een rol kunnen spelen in de aanpak van de uitdagingen waar de mensheid voor staat in deze eenentwintigste eeuw, met name op het gebied van energie- en grondstofconversie. Vanuit dat perspectief worden in dit proefschrift verschillende uitdagingen geïdentificeerd, en deze aan te pakken door middel van een combinatie van theorie, spectroscopie en synthetische methodologie.

References/referenties

[1] E. Stavitski, M. Goesten, J. Juan-Alcañiz, A. Martiñez-Joaristi, P. Serra-Crespo, A. V. Petukhov, J. Gascon, F. Kapteijn, *Angew. Chem.- Int. Ed.* **2011**, *50*, 9624–9628.

[2] M. Goesten, E. Stavitski, E. A. Pidko, C. Gücüyener, B. Boshuizen, S. N. Ehrlich, E. J. M. Hensen, F. Kapteijn, J. Gascon, *Chem. - Eur. J.* **2013**, *19*, 7809–7816.

[3] T. Rodenas, I. Luz, G. Prieto, B. Seoane, H. Miro, A. Corma, F. Kapteijn, F. X. Llabrés i Xamena, J. Gascon, *Nature Mater* **n.d.**, *14*, 48–55.

[4] S. M. Cohen, *Chem. Rev.* **2012**, *112*, 970–1000.

Acknowledgements

Naturally, this thesis would not have materialized without the help of a significant number of people. Most importantly, I want to thank prof. Jorge Gascon and prof. Freek Kapteijn for the help they have provided during my time in the Catalysis Engineering group. When I started, Jorge was an assistant professor, but his ability to direct an entire research group into making a large number of discoveries on porous materials (whether those may be inorganic, organic-inorganic, or purely organic) had seen him rise to the rank of full professor before I submitted this thesis. It was a great pleasure to work with you Jorge. Apart from your mind, you have a great eye for putting the right people onto the right projects. A great scientific career looms. Freek, many thanks for the freedom you have given me over the course of my PhD. Very often, your suggestions that initially appeared of marginal importance turned out to be vital near the end of writing a manuscript. I also enjoyed the way you countered my aggression in scientific discussion: whereas many group leaders would've had the tendency to stab a pencil in my forehead, you applied a rather sedate smile, probably knowing you were right.

Special thanks go to a number of people with whom I had discussions on frequent basis, which proved highly inspirational. Prof. em. Herman van Bekkum, I often descended down into your office to discuss organic chemistry, and I usually left with a useful piece of scientific literature, which you fished from underneath a Talmudic stack of books. Evgeny Pidko and prof. Emiel Hensen, I took great inspiration from our discussions on theoretical chemistry and zeolite synthesis. Prof. Matthias Bickelhaupt and Célia Fonseca Guerra, you taught me the arts of quantum chemistry that I'm now using on a daily basis. I want to thank Andrei Petukhov, who in the early stages of my PhD guided me through the dense forest of Small-Angle X-ray Scattering on porous materials. Karthick Babu of Leiden, and Pieter Magusin and Brahim Mezari of Eindhoven, I thank you for working with me on the application of solid-state NMR and in-situ NMR on Metal-Organic Frameworks.

I want to thank my MSc student Agi, with whom I worked on porous polymers. The work we performed is not covered in this thesis, but has led to a very nice publication that was well received at the NCCC of 2014. You started working in Delft and Eindhoven now, in the field of quantum chemistry, and I'm sure you'll have a very successful PhD.

I want to thank the entire Catalysis Engineering group in Delft, in particular the people with whom I have collaborated in scientific papers: Jana, Enrique, Eli, Alberto, Pablo, Canan, Bart Boshuizen, Maxim, prof. Michiel Makkee, Martijn and Alma, it was a pleasure to work with you. I would like to thank Els and Elly for their administrative support, which was in my case at times a highly complicated affair, and Bart, Willy, Harry and Kevin for their technical support.

I would like to thank my parents and sister for giving me the opportunity to obtain a university degree, entering the field of science thereafter and providing the necessary love and support, and last but not least Nastya, with whom I have spent the last 2 years of my life working and living together, and who has become part of my family.

Maarten Goesten, 11-02-2015